UNIVERSIDAD POLITÉCNICA DE MADRID

Escuela Técnica Superior de Ingenieros Aeronáuticos (ETSIA)

DYNAMIC INTERACTIONS BETWEEN SOLIDS AND VISCOUS LIQUIDS WITH FREE SURFACE

INTERACCIONES DINÁMICAS ENTRE SÓLIDOS Y LÍQUIDOS VISCOSOS CON SUPERFICIE LIBRE

Tesis Doctoral

Benjamin Bouscasse

Ingeniero de l'École Centrale de Nantes, France

Madrid, Junio 2015

DEPARTAMENTO DE MECÁNICA DE FLUÍDOS Y PROPULSIÓN AEROESPACIAL

ESCUELA TÉCNICA SUPERIOR DE INGENIEROS AERONÁUTICOS (ETSIA)

DYNAMIC INTERACTIONS BETWEEN SOLIDS AND VISCOUS LIQUIDS WITH FREE SURFACE

INTERACCIONES DINÁMICAS ENTRE SÓLIDOS Y LÍQUIDOS VISCOSOS CON SUPERFICIE LIBRE

Autor

Benjamin Bouscasse

Ingeniero de l'École Centrale de Nantes, France

Directores de Tesis

Prof. Antonio Souto-Iglesias
Doctor Ingeniero Naval

Dr. Andrea Colagrossi
Doctor Ingeniero Aeronáutico

Madrid, Junio 2015

Au grand Konfrère Florian Gastineau
A mes grand-pères

POLITÉCNICA

Tribunal nombrado por el Sr. Rector Magfco. de la Universidad Politécnica de Madrid, el día.....de.....de 20....

Presidente:_____

Vocal: _____

Vocal:_____

Vocal:_____

Secretario:_____

Suplente:_____

Suplente:_____

Realizado el acto de defensa y lectura de la Tesis el día.....de.....de 20 ... en la E.T.S.I. /Facultad.....

Calificación .....

EL PRESIDENTE LOS VOCALES

EL SECRETARIO

CONTENTS

1 INTRODUCTION 1
- 1.1 Motivation and background 1
  - 1.1.1 General 1
  - 1.1.2 Applications 1
  - 1.1.3 Smoothed Particle Hydrodynamics 2
  - 1.1.4 Theoretical aspects 2
  - 1.1.5 Numerical models for fluid/body interaction 7
  - 1.1.6 Open problems 9
- 1.2 Structure of the thesis 10

i THEORETICAL MODEL 11

2 PHYSICAL PROBLEM AND GOVERNING EQUATIONS 13
- 2.1 Physical problem 13
- 2.2 Navier Stokes equations 14
- 2.3 Boundary conditions (BCs) 15
  - 2.3.1 Velocity 15
  - 2.3.2 Stress 15

3 ENERGY EQUATIONS 17
- 3.1 Introduction 17
- 3.2 Energy Conservation 17
  - 3.2.1 Mechanical power 18
  - 3.2.2 Compressibility and energy dissipation 18
  - 3.2.3 Global balance 19
- 3.3 Detailed decomposition of the viscous dissipation term 19
  - 3.3.1 Complete expression of the dissipation term 21
  - 3.3.2 Note on the free-surface term 21
  - 3.3.3 Detailed balance of the conservation of energy 22
- 3.4 Rigid Body case 23

ii NUMERICAL MODEL 25

4 THE SPH MODEL FOR THE NAVIER–STOKES EQUATIONS 27
- 4.1 delta-SPH equations 27
- 4.2 Initial particle distribution 28
- 4.3 Presence of a body and enforcement of the solid-boundary condition through a ghost-fluid method 29
  - 4.3.1 Numerical treatment of the intersection between the free surface and the body 31
  - 4.3.2 In/outflow conditions 32

4.3.3 Evaluation of Forces and Torques using the ghost-fluid technique 33
4.4 Algorithm for handling fluid-body coupling 36
5 ENERGY CONSERVATION IN THE SPH MODEL 39
5.1 Introduction 39
5.2 SPH discretization of the energy equation 40
5.2.1 Ghost fluid treatment in the conservation of energy 41
5.3 Energy components through Moving Least Square interpolation on scattered data 42
5.3.1 Free-surface terms 44
III NUMERICAL TESTS AND VALIDATION 47
6 ATTENUATION OF A VISCOUS STANDING WAVE 49
6.1 Definition of the problem 49
6.2 Effects of the weakly compressibility on time evolution of the energy components 52
6.3 High viscosity & small amplitude: Re=125, $\epsilon = 0.1$ 53
6.4 High viscosity & large amplitude: Re=125, $\epsilon = 0.4$ 54
6.5 Low viscosity & large amplitude: Re=2000, $\epsilon = 0.4$ 56
6.6 Summary of the influence of the Reynolds number and the wave amplitude on the viscous dissipation 59
6.7 Details of the free-surface terms 59
6.7.1 Convergence and Mach effect on the compressible dissipative term in the case without breaking 60
6.7.2 Convergence and Mach effect on the compressible dissipative term in the case with the overturning wave 61
6.7.3 Check of the balance involving MLS interpolation 63
6.7.4 Check of the balance involving free-surface terms 63
7 DAM BREAK FLOWS IN A CONFINED DOMAIN 65
7.1 Definition of the problem 65
7.2 High viscosity, Re=100 66
7.2.1 Re=100, Convergence properties of the conservation of energy 66
7.2.2 Convergence of the total dissipation, effect of the ghost fluid, free-surface term 68
7.3 Low viscosity, Re=1000 68
7.4 Summary of the chapter 73
8 NONLINEAR WATER WAVE INTERACTION WITH FLOATING BODIES IN SPH 75
8.1 Introduction 75
8.2 Diffraction test on a semi-immersed triangular body 75
8.3 Floating body in rest condition 77
8.4 Drop of a complex floating body in a water tank 77

8.5 Oscillating floating box: convergence tests and energy conservation 79
8.6 Wave Packet interacting with a floating body 82
8.7 Summary of this chapter 83

iv PHYSICAL INVESTIGATIONS 87

9 FLOW PAST A CIRCULAR CYLINDER CLOSE TO A FREE SURFACE 89
9.1 Introduction 89
9.2 Physical model 91
9.2.1 Physical problem 91
9.2.2 Boundary conditions (BCs) 92
9.3 Computational model 93
9.3.1 Field equations 93
9.3.2 Enforcement of the boundary conditions 93
9.4 Numerical Investigation 94
9.4.1 General 94
9.4.2 List of case studies 95
9.5 Sequence 1: influence of submergence on flow characteristics at intermediate-high Froude number $Fr_d = 1$ 98
9.5.1 Large gap ratio (deep submergence), $h/d = 2.5$ (KSN) 98
9.5.2 Moderate gap ratio (intermediate submergence), $h/d = 1.5$ (KSI) 99
9.5.3 Small gap ratio (low submergence), $h/d = 0.5$ (CSV) 102
9.5.4 Null gap ratio (tangency), $h/d = 0$ (CFR) 105
9.5.5 Negative gap ratio (half-submerged cylinder), $h/d = -0.5$ (BSI) 105
9.5.6 Influence of submergence on flow characteristics: summary 107
9.6 Sequence 2: influence of Froude number on flow characteristics at moderate submergence: $h/d = 0.55$ 110
9.6.1 Low Froude number: $Fr_d = 0.3$ (KFI) 110
9.6.2 Intermediate Froude number: $Fr_d = 0.6$ (CFR) 112
9.6.3 Intermediate-high Froude number: $Fr_d = 1.2$ (CPV) 112
9.6.4 High Froude number: $Fr_d = 1.6$ (CPI) 114
9.6.5 Very high Froude number: $Fr_d = 2.0$ (KPI) 115
9.6.6 Froude number flow dependence summary 117
9.7 Sequence 3: influence of Froude number on flow characteristics for the half-submergence condition 119
9.7.1 Very high Froude number: $Fr_d = 2.0$ ((C/K)PI) 119
9.7.2 High Froude number: $Fr_d = 1.6$ ((B/C)PI) 121
9.7.3 Moderate Froude number: $Fr_d = 0.6$ (BFR) 122
9.7.4 Low Froude number: $Fr_d = 0.4$ (BFI) 123

9.7.5 Influence of Froude number on flow characteristics for the half-submergence condition: summary 124
9.8 Sequence 4: influence of submergence on flow characteristics at very high Froude number, $Fr_d = 2$. 126
9.8.1 Large gap ratio (deep submergence), $h/d = 2.5$ (KSN) 126
9.8.2 Moderate gap ratio (intermediate submergence), $h/d = 1.5$ (KSI) 126
9.8.3 Influence of submergence at very high Froude number $Fr_d = 2$ on flow characteristics: summary 128
9.9 Influence of the computational domain size and resolution on the results 131
9.9.1 Channel depth 131
9.9.2 Inflow and outflow boundaries 131
9.9.3 Numerical resolution 135
9.10 Summary of the chapter 136
10 NUMERICAL AND EXPERIMENTAL INVESTIGATION OF NONLINEAR SHALLOW WATER SLOSHING 139
10.1 Introduction 139
10.2 CNR-INSEAN experimental set-up 140
10.3 Numerical SPH simulation and tuning of the viscosity 141
10.4 Nonlinear shallow water sloshing inside a swaying tank 142
10.4.1 Present investigation 144
10.4.2 Summary of the sloshing scenarios 156
10.5 Summary of the chapter 159
11 MECHANICAL ENERGY DISSIPATION INDUCED BY SLOSHING AND WAVE BREAKING IN A FULLY COUPLED ANGULAR MOTION SYSTEM. I. THEORETICAL FORMULATION AND NUMERICAL INVESTIGATION 161
11.1 Introduction 161
11.2 A pendulum Tuned Liquid Damper 163
11.2.1 Angular momentum and energy balances 166
11.2.2 Analogies between the present system, a TLD and a HMLD 168
11.2.3 Definition of envelopes and phase lags functions 169
11.3 Dynamics of the system with the empty tank 171
11.3.1 General 171
11.3.2 Torque exerted by the sliding mass on the empty tank 173
11.4 Theoretical and Numerical predictions of the torque exerted by the fluid and the associated dissipation 174
11.4.1 General 174
11.4.2 Torque from Verhagen and Van Wijngaarden analysis 175
11.4.3 Theoretical fluid dissipation 176
11.4.4 Numerical predictions of the torque exerted by the fluid and the associated dissipation 177
11.5 The fully coupled angular motion system 179

11.5.1 General 179
11.5.2 Pendulum TLD: numerical simulation with SPH 180
11.5.3 Pendulum TLD: frequency behaviour 183
11.6 Summary of this chapter 185
12 MECHANICAL ENERGY DISSIPATION INDUCED BY SLOSHING AND WAVE BREAKING IN A FULLY COUPLED ANGULAR MOTION SYSTEM. II. EXPERIMENTAL INVESTIGATION. 187
12.1 Introduction 187
12.2 Experimental setup 188
12.3 Dynamics of the system with the empty tank 189
12.4 Analysis of the dynamical system: tank filled with water. 191
12.4.1 Roll angle 192
12.4.2 Phase lags analysis of the coupled system 193
12.4.3 Energy transfer from tank to fluid 195
12.4.4 Wave breaking and energy dissipation 196
12.4.5 Summary of results for the water case 198
12.5 Effects of the liquid adopted: viscosity and density. 198
12.5.1 Series 1 200
12.5.2 Series 2 202
12.5.3 Series 3 204
12.5.4 Series 4 206
12.5.5 Summary of dissipation results for the different liquids 207
12.6 Practical application 210
12.7 Summary of this chapter 211

V CONCLUSIONS AND PERSPECTIVES 215
13 CONCLUSIONS AND PERSPECTIVES 217
13.1 Major findings 217
13.1.1 Computing the energy dissipation using SPH 217
13.1.2 Explicit algorithm for fluid/body interaction using SPH 218
13.1.3 Flow past a submerged cylinder 218
13.1.4 Shallow water sloshing on a rectangular tank 219
13.1.5 Pendulum-TLD, and dissipation in a coupled fluid-body problem 220
13.2 Perspective 222
14 PUBLICATIONS LINKED WITH THIS THESIS 223
14.1 Refereed papers 223
14.2 Conference papers 223
14.3 papers under preparation 224
A USEFUL RELATIONS 225
B TRANSPORT THEOREM 227
C DETAILED CALCULATIONS 229
C.1 Detail 1 229

C.2 Detail 2 229
C.3 alternative decomposition 230
BIBLIOGRAPHY 247

ABSTRACT

The subject of the present thesis is the interaction between a viscous fluid and a solid body in the presence of a free surface. The problem is expressed first theoretically with a particular focus on the energy conservation and the fluid-body interaction. The problem is considered 2D and monophasic, and some mathematical development allows for a decomposition of the energy dissipation into terms related to the Free Surface and others related to the enstrophy.

The numerical model used on the thesis is based on Smoothed Particle Hydrodynamics (SPH): a computational method that works by dividing the fluid into particles. Analogously to what is done at continuum level, the conservation properties are studied on the discrete system of particles. Additionally the boundary conditions for a moving body in a viscous flow are treated and discussed using the ghost-fluid method. An explicit algorithm for handling fluid-body coupling is also developed.

Following these theoretical developments on the numerical model, some test cases are devised in order to test the ability of the model to correctly reproduce the energy dissipation and the motion of the body. The attenuation of a standing wave is used to compare what is numerically simulated to what is theoretically predicted. Further tests are done in order to monitor the energy dissipation in case of more violent flows involving the fragmentation of the free-surface. The amount of energy dissipated with the different terms is assessed with the numerical model. Other numerical tests are performed in order to test the fluid/body interaction method: forces exerted by waves on simple shapes, and equilibrium of a floating body with a complex shape.

Once the numerical model has been validated, numerical tests are performed in order to get a more complete understanding of the physics involved in (almost) realistic cases. First a study is performed on the flow passing a cylinder under the free surface. The study is performed at moderate Reynolds numbers, for various cylinder submergences, and various Froude numbers. The capacity of the numerical solver allows for an investigation of the complex patterns which occur. The wake from the cylinder interacts with the free surface, and some characteristical flow mechanisms are identified.

The second study is done on the sloshing problem, both experimentally and numerically. The analysis is restrained to shallow water and horizontal excitation, but a large number of conditions are studied, leading to quite a complete understanding of the wave systems involved.

The last part of the thesis still involves a sloshing problem but this time the tank is rolling and there is coupling with a mechanical system. The system is named pendulum-TLD (Tuned Liquid Damper). This kind of system is normally used for damping of civil structures. The analysis is then performed analytically, numerically and experimentally for using liquids with different viscosities, focusing on non-linear features and dissipation mechanisms.

RESUMEN

En esta tesis se investiga la interacción entre un fluido viscoso y un cuerpo sólido en presencia de una superficie libre. El problema se expresa teóricamente poniendo especial atención a los aspectos de conservación de energía y de la interacción del fluido con el cuerpo. El problema se considera 2D y monofásico, y un desarrollo matemático permite una descomposición de los términos disipativos en términos relacionados con la superficie libre y términos relacionados con la enstrofía.

El modelo numérico utilizado en la tesis se basa en el método sin malla Smoothed Particle Hydrodynamics (SPH). De manera análoga a lo que se hace a nivel continuo, las propiedades de conservación se estudian en la tesis con el sistema discreto de partículas. Se tratan también las condiciones de contorno de un cuerpo que se mueve en un flujo viscoso, implementadas con el método ghost-fluid. Se ha desarrollado un algoritmo explicito de interacción fluido / cuerpo.

Se han documentado algunos casos de modo detallado con el objetivo de comprobar la capacidad del modelo para reproducir correctamente la disipación de energía y el movimiento del cuerpo. En particular se ha investigado la atenuación de una onda estacionaria, comparando la simulación numérica con predicciones teóricas. Se han realizado otras pruebas para monitorizar la disipación de energía para flujos más violentos que implican la fragmentación de la superficie libre. La cantidad de energía disipada con los diferentes términos se ha evaluado en los casos estudiados con el modelo numérico.

Se han realizado otras pruebas numéricas para verificar la técnica de modelización de la interacción fluido / cuerpo, concretamente las fuerzas ejercidas por las olas en cuerpos con formas simples, y el equilibrio de un cuerpo flotante con una forma compleja.

Una vez que el modelo numérico ha sido validado, se han realizado simulaciones numéricas para obtener una comprensión más completa de la física implicada en casos (casi) realistas sobre los había aspectos que no se conocían suficientemente. En primer lugar se ha estudiado el el flujo alrededor de un cilindro bajo la superficie libre. El estudio se ha realizado con un número de Reynolds moderado, para un rango de inmersiones del cilindro y números de Froude. La solución numérica permite una investigación de los patrones complejos que se producen. La estela del cilindro interactúa con la superficie libre. Se han identificado algunos inestabilidades características.

El segundo estudio se ha realizado sobre el problema de sloshing, tanto experimentalmente como numéricamente. El análisis se restringe a aguas poco

profundas y con oscilación horizontal, pero se ha estudiado un gran número de condiciones, lo que lleva a una comprensión bastante completa de los sistemas de onda involucradas.

La última parte de la tesis trata también sobre un problema de sloshing pero esta vez el tanque está oscilando con rotacion y hay acoplamiento con un sistema mecánico. El sistema se llama pendulum-TLD (Tuned Liquid Damper - con líquido amortiguador). Este tipo de sistema se utiliza normalmente para la amortiguación de las estructuras civiles. El análisis se ha realizado analíticamente, numéricamente y experimentalmente utilizando líquidos con viscosidades diferentes, centrándose en características no lineales y mecanismos de disipación.

ACKNOWLEDGEMENTS

This thesis would not have been done without the help of a lot of people.

I have to first thank Prof Antonio "Chou" Souto-Iglesias who gave me the opportunity to come to Madrid to do this thesis and has been a constant help during the work, for technical and scientific advices, but also for the practical aspects. I am proud to have him as a friend after these years of collaboration. I extend the thank towards his wife Marta and the children.

My second director Andrea Colagrossi is equally important in this thesis. He has been the main inspiration for the technical development involving SPH, and it has been of great fortune to work at INSEAN Roma with him during all these years. His extensive knowledge goes well beyond the scientific themes. I have been lucky to have worked with him for a long time and also to have developed a strong friendship. Most of my work with Andrea would not have been the same without Salvatore Marrone and Matteo Antuono. They are coauthors of most of the papers associated with this work. I am very grateful to have been a part of this amazing group. It is far from easy to work as a team in research and I think we managed to profit from everyone's skills, and this has been really great.

Before joining the SPH group, I learned a lot about fluid dynamics and what it is to be a researcher with Claudio Lugni. Without him I would not have followed this career, so I would not have done this thesis. He has also technically played a great role in the sloshing-related part of this thesis. Together with Claudio, Marilena Greco explained to me loads of stuff, and has always been a constant, constructive and friendly support. I will not forget Giuseppina Colicchio, Luigi Fabbri and Tomaso Bazzi who have also been really important. In general, the whole staff at INSEAN have been helpful, and regretfully I can not cite everyone. I thank CNR-INSEAN Director Emilio Campana who allowed me go to Madrid, and to have a lot of freedom in the thematics and ways of conducting my work.

In Madrid, a special thanks goes out to Patricia Alcanda, who made the Phd possible with her great efficiency to overcome all of the difficulties. Pasquale Dinoi has been a great companion: I'd like to thank him for the help in particular for the 30 credits mission. In general, I had a very good time in Madrid in the Cecenia office and in the city. Thanks to Jose-Luis "Pepe" Cercos Pita, Leo Gonzalez, and all of the people involved in the office. I am also grateful to the seakeeping master Alexandre Simos, his wife Luciana Barros, Ramon Garcia-Arellano and the Rayo Vallecano.

A big thanks to my whole family, in particular my father Hervé and my mother Josiane who have given me ultimate freedom in all my endeavors. I would like to mention also “la Konfrerie” crew in France and UK, and in Rome, Riccardo and Massimiliano Mariani, Andrea Mancori and Dario Caruso.

Last but not least, thanks to Danielle Marie Melgoza who has been very motivating for this last part of the work, and is supporting me each day.

NOMENCLATURE

GENERAL RULES

- Only the most used symbols in the following sections are listed
- Meaning of symbols is given at least when introduced in the thesis
- Sometimes the same symbol can be used to indicate different things
- Symbols for vectors and matrices are generally written in boldface
- Symbols between angle brackets (e.g. $\langle f \rangle$) represent the *regularized* values, i.e. obtained through an integral interpolation

SYMBOLS

$\mathbf{r}$	Position vector
$\mathbf{u}$	Velocity vector
ρ_0	Density
p	Pressure
c	Speed of sound
e	Specific internal energy
μ	Dynamic viscosity
ν	Kinematic viscosity
$\mathbf{g}$	Vector of the external volume forces

Re	Reynolds number ($= UL/\nu$)
St	Strouhal number ($= fL/U$, where f is a characteristic frequency)
Fr	Froude number ($= U/\sqrt{(gL)}$)
Ma	Mach number ($= U/c$)

$\mathbb{T}$	the stress tensor
$\mathbb{D}$	the rate of strain tensor

$\mathbb{V}$	the viscous part of the stress tensor
$\mathcal{E}_M$	the mechanical energy
$\mathcal{E}_K$	the kinetic energy
$\mathcal{E}_P$	the potential energy
$\mathcal{E}_C$	the compressible energy
$\mathcal{E}_I$	the internal energy

$\mathcal{P}_{ext}$	External power
$\mathcal{P}_{NC}$	Non-conservative force
$\mathcal{P}_B^\lambda$	Quadratic dissipative term due to compressibility
$\mathcal{P}_D$	Dissipative power associated to strain tensor
$\mathcal{P}^{Deform}$	Dissipative power associated to viscosity and deformation of the Free Surface (Boundary term)
$\mathcal{P}_\omega$	Enstrophy
$\mathcal{P}_{FS}$	Total dissipative power associated to the free surface (Boundary term)
$\mathcal{P}_{Body}$	Total dissipative power associated to the solid surface (Boundary term)
$\mathcal{P}_F$	Disspative power associated to viscosity and compressibility (Volumic term)
$\mathcal{P}_E^{2\mu}$	Disspative power associated to viscosity and compressibility (Free Surface Boundary term)

$\Delta\mathcal{E}_X^Y(t)$	$= \int_{t0}^{t} \mathcal{P}_X^Y \, dt$
$\mathcal{P}_X^{SPH}$	^{S}PH indicates that the terms derives directly from particles SPH quantities
P_X^{MLS}	^{M}LS indicates a term evaluated using Moving Least Square interpolation on the scattered data
$\mathcal{P}_{D+B}^{SPH}$	Total dissipative power associated to viscosity in SPH
$\mathcal{P}_{\omega*}$	Dissipative term including enstrophy and viscous effect from the ghost fluid
$\mathcal{P}_{FS}^{sub}$	Boundary surface term obtained by substraction of essentially volumic terms

W	Weight function called *smoothing function* or *kernel*
h	Smoothing length
N_{part}	Total number of particles
$\mathcal{N}_i$	Number of neighbours of the i-th particle
$\mathcal{N}$	Average number of neighbours
Δx	Mean inter-particle distance

Δt	Numerical integration time step
$\mathbf{n}$	Unit normal vector
$\boldsymbol{\tau}$	Unit tangent vector
δ	Numerical coefficient to control the diffusive term in the continuity equation

ACRONYMS AND ABBREVIATIONS

B.C.	Boundary Conditions
BEM-MEL	Boundary Element Method Mixed Eulerian-Lagrangian
CFL	Courant–Friedrichs–Lewy condition
MLS	Moving Least Square Interpolation
SPH	Smoothed Particle Hydrodynamics
VOF	Volume Of Fluid
WCSPH	Weakly-Compressible Smoothed Particle Hydrodynamics

1 INTRODUCTION

1.1 MOTIVATION AND BACKGROUND

1.1.1 General

The present thesis investigates the interaction of energetic, mainly viscous free-surface flows with rigid structures. The Lagrangian numerical method Smoothed Particle Hydrodynamics (SPH) is used along the thesis. Some development and investigations are performed on the numerical method, but the focus of the thesis is more on the physical applications than what have been done in the two previous thesis: "A meshless Lagrangian method for free surface and interface flows with fragmentation" Colagrossi 2005; and "Enhanced SPH modeling of free-surface flows with large deformations" Marrone 2011.

Nature is made up of fluids and bodies, that interact in a complex way. There can be several solids, several liquids, several gases. Among all these distincts elements, and under certain environmental conditions, a lot of interactions may occur: they can mix, experience chemical reactions, change state...

In the present thesis, the interaction between elements is studied in the framework of Mechanics. No other physics is taken into account. The scales of the problems studied are the ones of the classical mechanics. There are no effects due to very large scales or very small scales. The subject treated involves one fluid and one body for the most. The fluid is always considered Newtonian. The subjects described in the thesis are all linked to a theme of viscous effects and energy conservation in presence of complex free surface behaviour and moving bodies.

The introduction is general to the thesis. A more detailed state of the art is given at the beginning of the chapters linked to a specific topic.

1.1.2 Applications

Understanding the mechanics of multifluid problems is crucial for a large number of engineering problems. The number of applications is potentially very large: food and medical industry; engines; environmental science; oil and gas industry , and many others. More specifically, considering the potential applications of the physical problems studied in the present research, a common liquid/gas interaction is that taking place between air and water. Thinking about these two elements, sea is the most natural example. The impredictability of

the sea has continually worried people. It has always been a huge danger and it still is. Ships, structures, platforms, are object of wave impacts and stability related accidents. The dynamic involved is often characterised by non-linear interactions, violent flows and violent water impacts. Furthermore, when a viscous fluid is set in motion, vortices are generated and this is source of energy dissipation. When a structure is set in motion under a certain seastate, it is not possible to know the motions without accurately estimating the damping associated to the motion. This estimation is still an important challenge for future hydrodynamic. Conservative choices are not always easy to define, because in complex problems underdamping or overdamping may both lead to bad results that could influence bad decisions and put people or environnement at risk.

1.1.3 Smoothed Particle Hydrodynamics

The numerical method called Smoothed Particle Hydrodynamics (SPH) is used along the thesis.The method has been introduced about three decades ago in astrophysics by Lucy 1977 and Gingold and Monaghan 1977. It dealt with simulation of interacting boundless fluid masses in vacuum. The SPH basics were inherited from statistical theories and Monte Carlo integrations.

More than 10 years after the SPH invention, the application of the method diversifies. For more than ten years it was solely used for astronomical problems. Then, its applications spread to in several physics and engineering problems, ranging from solid mechanics to multiphase flows. In Monaghan 1985 the method is applied for simulating free-surface inviscid flows. It was found to be more suitable to handle breaking and fragmentation than the existing method. The reason for this are its Lagrangian nature and the fact that the free-surface boundary condition is automatically verified.

SPH has experienced a large growth over the years and can now be considered, even if for not all the typology of application, as a reliable alternative to the mesh solvers. For a recent review see Monaghan 2012. A certain number of research groups are active in the SPH context. Probably the SPH code most used (and open source) over the world is SPHysics Gomez-Gesteira et al. 2012.

1.1.4 Theoretical aspects

For a general problem of interaction between a fluid and a body, there is the need of motion equations for the fluid, and motion equations for the body, both mainly issued from Newton's 2nd law. In addition to such a set of equations, some boundary conditions are needed to define the mathematical representation of the physical problem. A huge number of theorical and numerical

models exists for the three aspects. Some relevant elements and consequences of the hypotheses used in the present thesis are recalled below.

Viscous Newtonian fluid

The common theory used to model the viscous stresses for liquids like water or oil is as newtonian fluids. For these fluids the viscous stresses are then assumed to be linearly proportional to the local strain rate. Using this modelling together with Euler equation gives raise to the Navier Stokes equations, that are widely used in fluid dynamics. About the boundary conditions, the contact surface between a viscous fluid and a solid body is treated through an adherence "no-slip" condition, mathematically a Dirichlet boundary condition since it sets the value of the velocity field at the boundary. Except in most simple cases, the Navier-Stokes equations do not have an analytic solution. They have to be solved numerically after being discretised in time and space.

This leads to two types of difficulties: the calculation of spatial and time derivatives, that have been tackled using various techniques. The discretization needs to be done with very small elements in order to be representative of the real physical condition. Therefore, due to the available computational power at the time that this thesis is written, only moderate Reynolds numbers can be studied with a no slip boundary condition without any numerical "tricks".

For some realistic applications presented in the document like the sloshing and the TLD where a higher Reynolds number is mandatory, the problem has been simulated with a free-slip boundary condition, since the boundary layer dynamics is not the lead actor of the flow.

The complete problem studied in this document involves a viscous fluid but also a free surface. A method has to be found in order to define a multifluid interface and its dynamics.

Free Surface

In order to keep the scope of the document within reasonable limits, the cases of liquid-liquid interfaces will not be treated in this thesis.

In most situations there isn't just one or several liquids, but also gases, and the interface between liquids and gases is also a very complex phenomenon and has been the subject of many studies over the past centuries. This interaction itself is very complicated: there can be instabilities on the interface, and there can be mixing. The simple notion of interface between a fluid and a gas is not straightforward.

A first assumption that can be done to simplify the study of gas-liquid problems is to consider that the gas specific weight is smaller than the one of the liquid phase and therefore the interface could be treated as a free surface. In this way, no mixing is permitted, but the dynamics of the interface is then

easier to treat from a physical point of view. This assumption allows for the propagation of gravity waves, and large deformations of the free surface can be studied.

This thesis deals essentially with problems in which the presence of gas is simplified with one liquid phase and a free surface. The numerical method SPH used for this research is particularly adapted in order to work considering this hypothesis.

From a mathematical and a numerical point of view, modelling the dynamics of a patch of fluid with free surface is an arduous task, incorporating the difficulties of having a free-boundary problem and a viscous fluid.

Fluid/body coupling

In the present study even if the deformations of the solid bodies are not treated and therefore the full motion of the body may be treated using Newton's 2nd law to represent the rigid body dynamics, some coupling with the fluid has to be thoroughly taken into consideration. The fluid is affecting the body, and the body is affecting the fluid, and when the problem is discretised in time this coupling has to be accounted for. The effect of the body on the fluid is given by a boundary condition on the fluid patch. The effect of the fluid on the body is given by the forces and moment resulting from the stress integration over the boundaries.

Energy conservation and dissipation

The importance of modelling the fluid with its viscosity is related to the energy dissipation. Without viscosity, the flow can be usally modelled as irrotational and therefore the velocity field can be derived from a potential. As a consequence, no energy is lost in a fluid domain except for wave radiation out of the fluid domain.

Other typical effects involving fluid and body, as for example vortex induced vibrations, can not exist without viscosity. If the dissipation is well modelled, the result will likely be more accurate, and therefore more applications could be found. In order to be correctly modelled, it is important that the dissipation comes from the equations and the physical modelling and not from a bad discretization in time or in space. For this reason, the convergence properties of a model can be tested also looking at the conservation of energy. When the discretization is sufficient, the viscous dissipation will correspond to the one of the viscous stress tensor. This is a key point, since the lower the viscosity is, the more difficult the modelling, due to the very fine discretization that will be needed to correctly model the physics.

As a matter of fact, it may be important to stress that a correct modelling of viscosity effects is not guaranteed by the stability of a computation. Generally, the more dissipation we have in a computation, the more stable it will

be. However, for example using a finite volume discretization of a mesh, stability is commonly achieved for a mesh that is coarser than the one needed to obtain a full convergence on the dissipation term. This is due to the fact that numerical (and therefore unphysical viscosity) will help in improving the scheme stability.

With other methods, like the SPH widely used in the present thesis, the problem is slightly different. SPH method is conservative, and therefore the energy balance can be in principle always verified. If the resolution is not sufficient, spurious flow behaviour can happen. Therefore, similarly as what can be done with a mesh method, the convergence on the various terms of the energy balance will be a great indicator of the correct modelling of the flow. This theme is reccurent in this thesis. The focus is more on the study of the potential accuracy of the method than on the capability to provide solutions to complex problems with direct application. Consequently, the problems are often simplified.

In addition to the dissipation due to vortex generation, the presence of a free surface on a viscous fluid is linked itself to dissipation. This is also a point of study on the present thesis. The convergence properties of the dissipation in case of free-surface fragmentation are studied in some simplified cases. An interesting review of the studies of the breaking surface waves in deep and intermediate water depths is found in Perlin et al. 2013. A certain amount of work has been dedicated to the role of air in the dissipation mechanism, (see also the reviews Melville 1996 and Kiger and Duncan 2012). It is worth to note the following works: Iafrati 2009 and Iafrati 2011, focusing on the energy dissipation, and the recent paper Marrone et al. 2015.

Sloshing

A typical application where free-surface fragmentation matters is Sloshing.

Sloshing flows are those occurring when free-surface waves are generated inside tanks. Slosh refers to the movement of liquid inside another object (which is, typically, also undergoing motion) usually creating significant global and local loads on the tank due to the impact of travelling waves.

The highly non-linear features of this problem make difficult to model correctly the slosh dynamics using analytical or empirical models. The capability to properly predict the dynamic local and global loads acting on tanks for any filling condition is a challenge for any numerical algorithm.

An abundant literature on sloshing can be found, reviewed in the book of Prof. Ibrahim (Ibrahim 2005), and in the more recent book of Prof. Faltinsen and Prof. Timokha (Faltinsen and Timokha 2009).

This phenomenon is of interest for several branches of engineering including marine, aerospace and civil engineering. Important examples include propellant slosh in spacecraft tanks and rockets (especially upper stages). Nowadays,

the sloshing phenomenon is particularly important for Liquefied Natural Gas (LNG hereinafter) carriers. During LNG carriers operative life, sloshing may impede the operation in some particular filling conditions.

Specifically, when the frequency spectrum of the ship motion is focused on the region close to the lowest natural tank mode, violent free-surface flows may appear, inducing large local loads (see Faltinsen et al. 2004) and increasing the risk for the integrity of the structure.

Among the sloshing flows, low filling depth conditions are attractive due to the wave systems that are generated under these depth conditions, as example travelling waves and bores (*i.e.* hydraulic jump), see Olsen and Johnsen 1975.

Motion and vibration control - Anti Roll tank, TLD

The large loads induced by the motion of a fluid into a container may have a large effect on the motion of the container itself. Various systems use this property in order to control motions using antiresonance. Two examples are anti-roll tanks in ships and Tuned liquid dampers used to damp the motion of civil structures.

Passive anti-roll tanks are successfully used in fishing and cable-laying vessels to dampen their rolling movement. Since all ships are inherently stable, any device fitted to a ship to reduce its roll should be called a roll damper. The rolling movement of ships can be modeled as a one degree harmonic movement. These tanks contain water that follows the ship's rolling and acquires a phase lag with respect to the ship movement. If correctly designed, this lag is approximately 90 degrees for the most dangerous sea wave frequency, the natural frequency of the ship itself. In this condition, the generated moment is at its maximum and so we speak of resonance condition and natural frequency of the fluid mass. Therefore, the moment generated partially counteracts the sea wave moment.

In 1911, Frahm introduced a roll-damping tank that consisted essentially of a U-tube in which a moment counteracting the rolling motion was created by the oscillating water Van Den Bosch and Vugts 1966. Although a number of ships were provided with this type of tank, it never succeeded in becoming popular. This could partly be due to the difficulty to tune the tank for different conditions but there also appeared to exist, as in the days of Watts, a lack of confidence in a device incorporating large quantities of free-moving water.

In the last 40 years, in many countries, these devices have been installed, mainly in fishing vessels. Theoretical Goodrich 1968 and experimental work has been done (Bass 1998) but not many studies have been carried out on trying to perform numerical simulations of these devices. A specific numerical study using a 2D finite element method for U-tube passive anti-rolling tanks was done by Zhong et al. 1998 and Popov et al. 1993 who reported numerical

analysis of sloshing in a road container with a MAC type method for tracing the free-surface evolution.

It has long been appreciated that a ship rolling in waves can be represented by an equivalent mechanical vibratory system (Goodrich 1968). The mechanical equivalent to an anti-rolling tank is a damped vibration absorber.

In other types of structures, these damped vibration absorbers are being substituted by other types of liquid tuned absorbers (Anderson et al. 2000 and Ikeda and Nakagawa 1997) that are usually called as tuned sloshing dampers (TSD) or tuned liquid dampers (TLD). A tuned liquid damper, also known as a harmonic absorber, is a device mounted in structures to reduce the amplitude of mechanical vibrations. Their application can prevent discomfort, damage, or outright structural failure. They are frequently used in power transmission, automobiles, and buildings.

Additionally, many papers have reported on the sloshing phenomenon in a rigid rectangular tank and theoretical and experimental research has been carried out by means of the shallow-water wave theory (Verhagen and Van Wijngaarden 1965, Sun and Fujino 1994, Armenio and Rocca 1996, Modi and Seto 1997,and Ikeda and Nakagawa 1997), VOF method (Celebi and Akyildiz 2002), etc. Extensive comparative study on sloshing loads has been made (Cariou and Casella 1999 and Sames et al. 2002). Most of the methods reported were based upon finite difference, finite volume approaches or even shallow water equation solvers.

1.1.5 Numerical models for fluid/body interaction

As previously expressed, one main aim of the present study is to model the behaviour of a moving body in a certain fluid domain bounded in some parts by a free surface. Using a body with a fixed position in a mesh is therefore not an option.

Historically, the Numerical Wave Tanks (NWTs) used for modelling the interaction between fluid and rigid bodies have been developed in the framework of potential flow theory by using the Mixed Eulerian-Lagrangian Boundary Element Method (BEM-MEL) introduced by Longuet-Higgins and Cokelet 1976 and followed by Faltinsen 1977 and Vinje and Brevig 1981. Non-linear potential flow solvers allow long-time simulations with moderate computational effort and, consequently, are very useful for engineering applications related to safety of ships and offshore platforms in severe sea-state conditions (see *e.g.* Ferrant 2000 and Greco 2001). The main drawback of these numerical models is the inability to describe viscous flows, wave breaking and fragmentation of the air-water surface.

The need to go beyond such limitations encouraged the development of mesh-based Navier-Stokes models for solving free-surface flows. The most popular techniques used to treat the free surface are the Level Set function

(LS), the Volume Of Fluid (VOF) and the Constrained Interpolation Profile (CIP) (see respectively *e.g.* Sethian 1999, Hirt and Nichols 1981, Yabe et al. 2001). However, the simulation of a fully non-linear interaction between waves and floating bodies presents a number of difficult numerical issues, and is still considered a challenging problem. The full coupling between the fluid and rigid body requires some specific considerations. The floating body dynamics involves a relatively large time scale and acts around the equilibrium state, that is a very critical condition for the stability of any fluid solid interaction (FSI) code. Other difficulties are related to the motion of floating bodies inside the fluid domain. This is generally modelled by using sliding/deforming meshes (see *e.g.* Hadžić et al. 2005), dynamic overlapping grids (see *e.g.* Di Mascio et al. 2008 and Broglia et al. 2009) or by representing the body through an immersed boundary technique (first defined in Peskin 1977 and further developed in Hu and Kashiwagi 2009 and Yang and Stern 2012).

Indeed, the mainstream paradigm used for solving Navier-Stokes equations in the context of Hydrodynamics has been to use a Eulerian representation for the fluid. This allows to have great accuracy for the calculation of the spatial derivatives. But even if a large number of attempts have been done, some of them resulting quite successful, the interface treatment results tricky, and energy conservation is not easy to achieve.

In this thesis the Navier-Stokes equations are solved using a Lagrangian representation for the fluids. The computational nodes are not fixed but move with the flow. Recently particle methods, such as the Smoothed Particle Hydrodynamics (hereinafter SPH) or the Moving Particles Semi-implicit methods (hereinafter MPS) - see comparison between the methods in Souto-Iglesias et al. 2013 and Souto-Iglesias et al. 2014, have shown promising results in this context. In particular, in the present work the δ-SPH variation, defined in Antuono et al. 2010 and validated for NWT application in Antuono et al. 2011, is used. In principle, the meshless character of the SPH/MPS methods permits to treat the free motions of a body inside the fluid domain in an easier way compared to mesh-based solvers. Koshizuka et al. 1998 were the first to simulate a small body interacting with a breaking wave using the MPS particle method (see also Naito and Sueyoshi 2002). Concerning the SPH method, the first simulation of a solid body interacting with fluid was done by Monaghan and Kos 2000. Fluid body coupling with SPH was also performed in May and Monhagan 2003, Monaghan et al. 2003, Shao and Gotoh 2004, Oger et al. 2006 and Delorme et al. 2006. In Oger et al. 2006, an extensive validation was performed on a test involving the water entry of a wedge. Recently, in Ulrich and Rung 2012 the case of a water entry of a cube is discussed and the numerical evolution is qualitatively validated through comparison with snapshots from experiments. In Kajtar and Monaghan 2008 and Hashemi et al. 2012, some novel algorithms for the coupling between fluid and rigid/flexible bodies are proposed.

The Lagrangian representation of the fluid has some drawbacks for what concerns the spatial derivatives, but results in advantages in order to calculate the dynamic of the interface. In this thesis, much effort is dedicated in order to check convergence and energy conservation over a relative large time frame. Since the timeframe is wide, all cases are chosen so that they can be described with 2D modelling. The computations are done verifying as much as possible the conservation properties, and also avoiding as much as possible numerical errors associated to the method that could create unphysical dissipation. In order to assert in this two aims, that are central in this research, the choice has been not to use any turbulence model and nor any methods to adapt the particles' size.

The interface between the fluid and bodies is mainly treated in this thesis with a no-slip boundary condition. Consequently, the Reynolds numbers have been chosen relatively low since otherwise the computational effort would be out of our capabilities. This does not imply that the computations shown in the document are performed with a coarse representation of the geometry or the fluid domain, indeed some of them are relatively high demanding in terms of computational power.

1.1.6 Open problems

When looking at the accuracy in regards to the modelling of the viscous dissipation and complex free surface behaviour, the highly nonlinear interaction between gravity waves and floating bodies for NWT applications has still not been sufficiently addressed in the particle method literature. To this purpose, in the present work an extensive study of the interaction between fluid and floating bodies is proposed, providing accurate formulae for the evaluation of forces and torques and comparisons with experiments available in the literature. The correct simulation of this kind of problems requires an accurate development of some specific features of the SPH. A crucial point is the attainment of the correct stable equilibrium for a floating body which is not subjected to external excitations. In this regard, the definition of accurate formulae for the evaluation of the forces and torques on the body is of fundamental importance. In the present work, the theoretical derivation of these expressions and subsequent checking of the momenta and energy exchanges between fluid and moving bodies are paid much attention. A further fundamental aspect for a sound and reliable numerical description of floating bodies is the modeling of the intersection between the bodies and the free surface.

1.2 STRUCTURE OF THE THESIS

This thesis is divided in several parts: first, the general problem of a solid interacting with a viscous fluid in the presence of a free surface is formulated. The equations are written focusing on energy conservation. This part aims also at clarifying how the energy is dissipated.

Secondly, the corresponding numerical SPH model is written. The way to impose the boundary conditions is detailed for the case of a 2D moving body and a viscous fluid. Analogously to what is done in the theoretical part, energy conservation for the discrete particle system equations is also investigated, in order to be able to later monitor the sources of dissipation.

Thirdly, the numerical model is therefore tested and discussed on various validation cases. This dynamics includes different aspects but focused on: energy dissipation, and motion of a body in a fluid. Some simple test cases without body motion are also considered in order to analyse the energy dissipated by the numerical model. The computed values are then compared with the theoretical ones. Floating bodies are simulated checking that the correct equilibrium condition is obtained, and that the motions in waves reproduce the experimental values available in literature.

After these preliminary chapters stating different aspects of the problem and the numerical method used to solve it, three different topics are investigated in order to increase the knowledge about them. The flow around a cylinder interesecting or under the free surface is treated first. The investigation focuses on varying the cylinder submergence and the non-dimensional flow velocity. A limited number of studies is present in literature for this specific topic. The use of SPH allows for increasing the flow velocity and larger deformations of the free surface than previously described can be computed.

As a second topic to be thoroughly investigated, sloshing with horizontal excitation in shallow water condition has been chosen. The study is quite extensive on the subject in the sense that a lot of different conditions of Amplitude/Water height are investigated, both numerically and experimentally, and for a large range of frequencies. A certain number of typical wave systems are identified, and a map of occurrence is drawn. A particular case, in which no steady state condition is achieved, is identified possibly for the first time.

A final investigation is performed on a TLD problem. This topic involves almost all the aspects mentioned in the thesis. The interaction between the fluid and the solid makes the system move and the dissipation of energy by the fluid is also extremely important in the phenomenon. The study is performed in order to understand how non-linear aspects could influence the efficiency of this kind of system and what kind of misleading conclusions may result from linearizations.

Part I

THEORETICAL MODEL

2 PHYSICAL PROBLEM AND GOVERNING EQUATIONS

2.1 PHYSICAL PROBLEM

In engineering applications the fluid domain can be limited by several kinds of boundaries (see figure 2.1): solid boundaries, free surface, inflow and outflow.

If an interface between a liquid and a gaseous phase occurs, such that the latter does not influence the evolution of the former, this interface can be considered as a free surface. Free-surface flows can be solved by modelling only the liquid phase, provided that suitable boundary conditions are enforced on it. Denoting by $\partial\Omega_F$ the free-surface boundary (see Figure 2.1), a kinematic and a dynamic condition have to be imposed on $\partial\Omega_F$. The dynamic boundary condition requires the continuity of stress across the free surface. If there is a single phase, this implies stresses have to be null at the free surface.

About the body, the boundary condition can be Dirichlet, as it is imposing the adherence of the liquid to the solid, or Neumann, as it is imposing a non-penetration condition of the body.

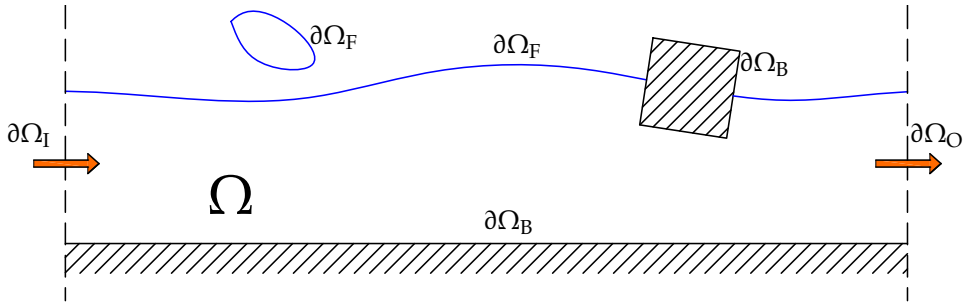

Figure 2.1.: Sketch of the fluid domain with solid boundaries, free surface, inflow and outflow.

2.2 NAVIER STOKES EQUATIONS

A two-dimensional fluid domain Ω is considered whose boundary, $\partial\Omega$, consists of a free surface, $\partial\Omega_F$, and of a solid boundary $\partial\Omega_B$. For the fluid the following set of compressible Navier Stokes equations is considered:

$$\begin{cases} \dfrac{D\rho}{Dt} = -\rho \operatorname{div}(\mathbf{u}), \\ \dfrac{D\mathbf{u}}{Dt} = \mathbf{f} + \dfrac{\operatorname{div}(\mathbb{T})}{\rho}, \\ \dfrac{D\mathbf{x}}{Dt} = \mathbf{u}, \end{cases} \tag{2.1}$$

where D/Dt represents the Lagrangian derivative, $\mathbf{u}$ the flow velocity, ρ is the fluid density, $\mathbb{T}$ the stress tensor, and $\mathbf{f}$ is a generic specific body force, usually the gravity $\mathbf{g}$. Thermal conductivity effects are here neglected. The pressure p is linked to density and internal energy through a state equation which changes depending on the nature of the fluid (gaseous or liquid). For example, in the weakly-compressible regime, for a liquid, a simple linear state equation can be used to match the pressure and density field:

$$p = p_0 + c_0^2 (\rho - \rho_0) \tag{2.2}$$

where, c_0 is the speed of sound assumed constant, and ρ_0 and p_0 are respectively the density and the pressure of the fluid at rest. The weakly-compressible regime (density variation smaller than $0.01\rho_0$) is guaranteed if the Mach number of the flow remains small enough during the time evolution (see *e.g.* Madsen and Schaffer 2006).

The fluid is assumed to be Newtonian, whose stress tensor is:

$$\mathbb{T} = (-p + \lambda \operatorname{tr}\mathbb{D})\,\mathbb{1} + 2\mu\,\mathbb{D}, \tag{2.3}$$

where $\mathbb{D}$ is the rate of strain tensor, i.e. $\mathbb{D} = (\nabla\mathbf{u} + \nabla\mathbf{u}^T)/2$. Finally, μ and λ are the viscosity coefficients.

The divergence $\operatorname{div}(\mathbb{T})$ can be expressed as:

$$\operatorname{div}(\mathbb{T}) = -\nabla p + \mu\nabla^2\mathbf{u} + (\lambda + \mu)\nabla(\nabla \cdot \mathbf{u}) \tag{2.4}$$

which reduces to

$$\operatorname{div}(\mathbb{T}) = -\nabla p + \mu\nabla^2\mathbf{u}. \tag{2.5}$$

for incompressible flow.

2.3 BOUNDARY CONDITIONS (BCS)

2.3.1 Velocity

A no-slip boundary condition (BC) is imposed along the bottom, $\partial\Omega_B$. Such a condition is expressed as:

$$\mathbf{u} = \mathbf{V}_{\partial\Omega_B}, \qquad \forall \mathbf{x} \in \partial\Omega_B, \tag{2.6}$$

where $\mathbf{V}_{\partial\Omega_B}$ is the solid boundary velocity.

Along the free surface, both kinematic and dynamic BCs should be fulfilled. As discussed, the kinematic free-surface BC implies that while evolving with the fluid flow, the material points initially on $\partial\Omega_F$ remain on $\partial\Omega_F$. Denoting by $\mathbf{n}$ the unit vector normal to the free surface and pointing out of the fluid, the kinematic free-surface condition is formalised by projecting the particle speed $\mathbf{u}$ and the boundary speed $\mathbf{V}_{\partial\Omega_F}$ in the direction of $\mathbf{n}$:

$$\mathbf{u} \cdot \mathbf{n} = \mathbf{V}_{\partial\Omega_F} \cdot \mathbf{n}, \qquad \forall \mathbf{x} \in \partial\Omega_F. \tag{2.7}$$

In other words, the kinematic free-surface BC implies that while evolving with the fluid flow, the material points initially on $\partial\Omega_F$ remain on it (in case of singular event like fluid-fluid and/or fluid-solid impacts this condition needs to be generalised).

2.3.2 Stress

The stress on the fluid domain boundaries $\partial\Omega$ is:

$$\mathbb{T}\mathbf{n} = [-p + \lambda \operatorname{div}(\mathbf{u})]\,\mathbf{n} + \mu(\mathbf{n} \times \boldsymbol{\omega}) + 2\mu \nabla\mathbf{u}\,\mathbf{n}. \tag{2.8}$$

On $\partial\Omega_B$ the term $\nabla\mathbf{u}\mathbf{n}_B$ can be substituted with $\partial\mathbf{u}/\partial n_B$ due to the impermeability of the solid boundary, leading to :

$$\mathbb{T}\mathbf{n}_B = [-p + \lambda \operatorname{div}(\mathbf{u})]\mathbf{n}_B + \mu(\mathbf{n}_B \times \boldsymbol{\omega}) + 2\mu \frac{\partial \mathbf{u}}{\partial n_B} \tag{2.9}$$

Therefore the stress on the body is composed by three terms, the first one is the normal pressure term (with a compressible component), the second one is a friction stress term on the body surface, the third one is different from zero only if the body surface is deforming or rotating (however for a rigid body the integral of this term on $\partial\Omega_B$ is null).

In this work, the surface tension is considered negligible, therefore, null stresses on free surface are enforced. This means that on $\partial\Omega_F$ the stress is zero and therefore the following equality holds:

$$2\mu \frac{\partial \mathbf{u}}{\partial n_F} = [p - \lambda \operatorname{div}(\mathbf{u})]\mathbf{n}_F + \mu(\boldsymbol{\omega} \times \mathbf{n}_F), \tag{2.10}$$

where the pressure and the friction stress components balance the stress term due to the deformation of the free surface.

Eq. (2.10) can be split in the normal and tangential components and rearranged as:

$$\begin{cases} p = \lambda \operatorname{div}(\mathbf{u}) + 2\mu \frac{\partial \mathbf{u}}{\partial n_F} \cdot \mathbf{n}_F, \\ \boldsymbol{\omega} \cdot (\mathbf{n}_F \times \boldsymbol{\tau}_F) = 2 \frac{\partial \mathbf{u}}{\partial n_F} \cdot \boldsymbol{\tau}_F, \end{cases} \qquad \forall \mathbf{r} \in \partial\Omega_F. \tag{2.11}$$

These are the two dynamic free-surface boundary conditions and imply that the pressure and the vorticity on the free surface are linked by its geometrical configuration and its normal fluid velocity gradients (Lundgren and Koumoutsakos 1999).

Considering that the stress on the free surface is zero, together with eq. (2.3) we get that $\boldsymbol{\tau} \cdot \mathbb{D}\,\mathbf{n} = 0$, which implies:

$$\frac{\partial \mathbf{u}}{\partial \tau} \cdot \mathbf{n}_F + \frac{\partial \mathbf{u}}{\partial n} \cdot \boldsymbol{\tau}_F = 0, \tag{2.12}$$

which allows to change the normal derivatives in the second eq. of (2.11) in tangential derivatives.

The second equation of (2.11) becomes then in 2D:

$$\omega \overset{2D}{=} 2 \frac{\partial \mathbf{u}}{\partial \tau} \cdot \mathbf{n}_F = 2 \frac{\partial u_n}{\partial \tau} - 2\mathbf{u} \cdot \frac{\partial \mathbf{n}_F}{\partial \tau} \tag{2.13}$$

In (Lundgren and Koumoutsakos 1999):

$$\frac{\partial \mathbf{n}_F}{\partial \tau} = \kappa \tau$$

being κ the curvature of the free surface in the considered point. Using this relation the BC becomes:

$$\omega \overset{2D}{=} 2 \frac{\partial \mathbf{u}}{\partial \tau} \cdot \mathbf{n}_F = 2 \frac{\partial u_n}{\partial \tau} - 2 u_\tau \kappa \tag{2.14}$$

where $[u_\tau, u_n]$ are the tangential and normal components of the velocity field.

3 ENERGY EQUATIONS

3.1 INTRODUCTION

This chapter aims at obtaining a detailed decomposition of the terms present in the equation of the energy conservation in the case of a Newtonian and weakly-compressible fluid applied to a finite control volume. The decomposition is used in chapter 5 where the terms are adapted to the SPH formalism. The definitions are used later in the thesis (chapter 6 and 7) in order to monitor the behaviour of the numerical method used during the research.

3.2 ENERGY CONSERVATION

A fluid domain is considered with a free surface and a solid body. The power that the fluid exerts on the solid boundary $\partial\Omega_B$ is given by integrating the elementary power acting on each point of $\partial\Omega_B$ by the stress forces, denoting by $\mathbf{n}$ the unit vector normal pointing out of the fluid domain.

$$\mathcal{P}_{\mathtt{fluid/body}} = -\int_{\partial\Omega_B} \mathbb{T}\mathbf{n}\cdot\mathbf{u_B}\,dS \tag{3.1}$$

The power $-\mathcal{P}_{\mathtt{fluid/body}} = \mathcal{P}_{\mathtt{body/fluid}} := \mathcal{P}_{ext}$ has to be converted into the total energy of the fluid. The integral can be extended to the whole boundary $\partial\Omega$ since no power is exerted on the fluid by the free surface. An equivalent way to define the power using the divergence theorem gives therefore:

$$\mathcal{P}_{ext} = \int_\Omega \mathrm{div}\,(\mathbb{T}\mathbf{u})dV \tag{3.2}$$

Using the divergence theorem eq. 3.2 becomes:

$$\int_\Omega (\mathrm{div}\,\mathbb{T})\cdot\mathbf{u}dV \;=\; -\int_\Omega \mathbb{T}:\mathbb{D}\,dV + \mathcal{P}_{ext} \tag{3.3}$$

The external power is therefore split in two different parts. The first (in the left hand side of equation 3.3) represents the mechanical power, and the second (right hand side of the same equation) represents the dissipation and the compressibility. The two integrals are treated in the next two subsections.

3.2.1 Mechanical power

Using momentum conservation (second equation of 2.1):

$$\rho \frac{D\mathbf{u}}{Dt} = \operatorname{div} \mathbb{T} + \rho \mathbf{f} \tag{3.4}$$

$$\int_\Omega \operatorname{div}(\mathbb{T}) \cdot \mathbf{u} \, dV = \int_\Omega \left(\rho \frac{D\mathbf{u}}{Dt} - \rho \mathbf{f} \right) \cdot \mathbf{u} \, dV \tag{3.5}$$

The body force can be seen as the sum of conservative and non-conservative body forces:

$$\mathbf{f} = \mathbf{g} + \mathbf{f}_{NC} \, . \tag{3.6}$$

The conservative body force admits a potential field G so that $\nabla G = \mathbf{g}$. In the case of the usual gravity force field $G = -gz$, where z is the vertical coordinate. The previous equation becomes:

$$\int_\Omega \operatorname{div}(\mathbb{T}) \cdot \mathbf{u} \, dV = \frac{D}{Dt} \int_\Omega \rho \left(\frac{\mathbf{u}^2}{2} - G \right) dV - \int_\Omega \rho \mathbf{f}_{NC} \cdot \mathbf{u} \, dV \tag{3.7}$$

The following definitions can be introduced:

$$\mathcal{E}_K := \int_\Omega \frac{\mathbf{u}^2}{2} \rho dV \, , \qquad \mathcal{E}_P := \int_\Omega -G \, \rho dV \, , \tag{3.8}$$

where E_k is the kinetic energy and E_p the potential energy and their sum gives the mechanical energy:

$$\mathcal{E}_M := \mathcal{E}_P + \mathcal{E}_K \, . \tag{3.9}$$

The power due to the non-conservative force is defined with:

$$\mathcal{P}_{NC} := \int_\Omega \rho \, \mathbf{f}_{NC} \cdot \mathbf{u} \, dV \tag{3.10}$$

therefore

$$\int_\Omega \operatorname{div}(\mathbb{T}) \cdot \mathbf{u} \, dV = \mathcal{P}_M - \mathcal{P}_{NC} \, . \tag{3.11}$$

The non conservative power $\mathcal{P}_{NC}$ is omitted for the rest of the thesis.

3.2.2 Compressibility and energy dissipation

The second term of the rhs of (3.3) is the internal energy time derivative $\dot{\mathcal{E}}_I$. It can be expressed as:

$$\dot{\mathcal{E}}_I = \int_\Omega \mathbb{T} : \mathbb{D} \, dV = \mathcal{P}_C - \mathcal{P}_D - \mathcal{P}_B^\lambda, \tag{3.12}$$

where the three terms in the rhs are:

$$\begin{cases} \mathcal{P}_D := -2\,\mu \int_\Omega \mathbb{D} : \mathbb{D}\, dV \\ \mathcal{P}_C := -\int_\Omega p\, \mathrm{div}(\mathbf{u})\, dV \\ \mathcal{P}_B^\lambda := -\lambda \int_\Omega [\mathrm{div}(\mathbf{u})]^2\, dV \end{cases} \tag{3.13}$$

$\mathcal{P}_D$ is the classical viscous dissipation term for a Newtonian fluid. $\mathcal{P}_B^\lambda$ is the dissipative power caused by the fluid compressibility (usally negligible with the weakly compressible approach). The time variations of these two components are always negative.

The third term, the power $\mathcal{P}_C$ is associated with the fluid compressibility. $\mathcal{E}_C$ obtained by integration of $\mathcal{P}_C$ can be reshaped as a potential energy using the equation of state and the continuity equation. In the case where a simple linear state equation is used, this term becomes:

$$\mathcal{E}_C = \mathcal{E}_C(\rho_0) + c_0^2 \int_\Omega \left[\log\left(\frac{\rho}{\rho_0}\right) + \frac{\rho_0}{\rho} - 1 \right] \rho\, dV, \tag{3.14}$$

where $\mathcal{E}_C(\rho_0)$ is the internal energy value set for the fluid at rest condition. The contribution $\mathcal{P}_C$ to the evolution of the flow does not introduce irreversibility.

3.2.3 Global balance

Eq. (3.3) can be written, using the previous definitions, as:

$$\boxed{-\mathcal{P}_{ext} + \mathcal{P}_M + \mathcal{P}_C = \mathcal{P}_D + \mathcal{P}_B^\lambda,} \tag{3.15}$$

i.e., the sum of the power due to the external forces, the power associated to the reversible compressibility and the power of the inertial force is balanced by the power dissipated by the fluid.

3.3 DETAILED DECOMPOSITION OF THE VISCOUS DISSIPATION TERM

This section aims at obtaining a detailed decomposition of the viscous dissipation term $\mathcal{P}_D$ into volume and surface integrals. Using the definition of $\mathcal{P}_D$ (equation 3.13) and adding and subtracting the enstrophy, $\mathcal{P}_D$ can be written:

$$\mathcal{P}_D = -2\mu \int_\Omega (\nabla\mathbf{u} : \nabla^T\mathbf{u})\, dV - 2\mu \int_\Omega \boldsymbol{\omega}^2/2\, dV. \tag{3.16}$$

To proceed in the analysis it is useful to consider the relation:

$$\nabla \mathbf{u} : \nabla^{T} \mathbf{u} = \nabla \cdot (\nabla \mathbf{u} \mathbf{u}) - \nabla(\mathrm{div}\mathbf{u}) \cdot \mathbf{u} . \tag{3.17}$$

Using equation (3.17) the divergence theorem can be applied to the first term of (3.16) getting:

$$\mathcal{P}_D = -2\mu \int_{\partial\Omega} (\nabla \mathbf{u}\, \mathbf{u}) \cdot \mathbf{n}\, dS - \mu \int_{\Omega} \boldsymbol{\omega}^2\, dV + 2\mu \int_{\Omega} \nabla(\mathrm{div}\mathbf{u}) \cdot \mathbf{u} dV . \tag{3.18}$$

Using some definitions:

$$\mathcal{P}_D = \mathcal{P}^{Deform} + \mathcal{P}_\omega - \mathcal{P}_F , \tag{3.19}$$

where the three terms in the rhs are:

$$\begin{aligned} \mathcal{P}^{Deform} &= -2\mu \int_{\partial\Omega} (\nabla \mathbf{u}\, \mathbf{u}) \cdot \mathbf{n}\, dS , \\ \mathcal{P}_\omega &:= -\mu \int_{\Omega} \boldsymbol{\omega}^2\, dV , \\ \mathcal{P}_F &:= -2\mu \int_{\Omega} \nabla(\mathrm{div}\mathbf{u}) \cdot \mathbf{u} dV . \end{aligned} \tag{3.20}$$

Decomposition of the compressible term

The previous balance 3.17 consists of one boundary integral and two volume integrals. It can be further decomposed. The divergence theorem can be applied on the last term (defined as $\mathcal{P}_F$), which is null in an incompressible fluid.

Considering that:

$$\nabla(\mathrm{div}\mathbf{u}) \cdot \mathbf{u} = \mathrm{div}[\mathrm{div}(\mathbf{u})\, \mathbf{u}] - \mathrm{div}^2(\mathbf{u}) , \tag{3.21}$$

$\mathcal{P}_F$ can be decomposed in:

$$\mathcal{P}_F = -2\mu \int_{\partial\Omega} \mathrm{div}(\mathbf{u})(\mathbf{u} \cdot \mathbf{n}) dS + 2\mu \int_{\Omega} \mathrm{div}^2(\mathbf{u})\, dV , \tag{3.22}$$

where the two terms in the rhs are:

$$\begin{aligned} \mathcal{P}_E^{2\mu} &:= (2\mu) \int_{\partial\Omega} \mathrm{div}(\mathbf{u})\, \mathbf{u} \cdot \mathbf{n}\, dS , \\ \mathcal{P}_B^{2\mu} &:= -2\mu \int_{\Omega} [\mathrm{div}(\mathbf{u})]^2\, dV . \end{aligned} \tag{3.23}$$

Note the following expression which will be used for numerical purposes:

$$\mathcal{P}_F = -\mathcal{P}_E^{2\mu} - \mathcal{P}_B^{2\mu} . \tag{3.24}$$

3.3.1 Complete expression of the dissipation term

Considering eq. 3.24, the dissipative term $\mathcal{P}_D$ of eq. 3.19 can be reshaped as:

$$\boxed{\mathcal{P}_D = \mathcal{P}^{Deform} + \mathcal{P}_E^{2\mu} + \mathcal{P}_\omega + \mathcal{P}_B^{2\mu}.} \tag{3.25}$$

Since $\mathcal{P}^{Deform}$ and $\mathcal{P}_E^{2\mu}$ are obtained through surface integrals, their sum can be written splitting them between the wall and the free-surface:

$$\mathcal{P}^{Deform} + \mathcal{P}_E^{2\mu} = \mathcal{P}_{FS} + \mathcal{P}_{wall}, \tag{3.26}$$

leading to this expression for $\mathcal{P}_D$:

$$\boxed{\mathcal{P}_D = \mathcal{P}_{FS} + \mathcal{P}_{wall} + \mathcal{P}_\omega + \mathcal{P}_B^{2\mu},} \tag{3.27}$$

where the four terms in the rhs are:

$$\begin{aligned}
\mathcal{P}_{FS} &:= 2\mu \int_{\partial\Omega_F} [-(\nabla \mathbf{u}\, \mathbf{u}) \cdot \mathbf{n} + \operatorname{div}(\mathbf{u})(\mathbf{u} \cdot \mathbf{n})]\, dS \\
\mathcal{P}_{wall} &:= 2\mu \int_{\partial\Omega_B} [-(\nabla \mathbf{u}\, \mathbf{u}_B) \cdot \mathbf{n} + \operatorname{div}(\mathbf{u})(\mathbf{u_B} \cdot \mathbf{n})]\, dS \\
\mathcal{P}_\omega &:= -\mu \int_\Omega \boldsymbol{\omega}^2\, dV \\
\mathcal{P}_B^{2\mu} &:= -2\mu \int_\Omega [\operatorname{div}(\mathbf{u})]^2\, dV,
\end{aligned} \tag{3.28}$$

where the physical meaning of these terms are respectively: the power dissipated on the free surface $\mathcal{P}_{FS}$; on the wall $\mathcal{P}_{wall}$; the enstrophy $\mathcal{P}_\omega$; and finally an additional dissipation contribution linked to compressibility.

3.3.2 Note on the free-surface term

The dissipative power acting on the free surface is defined in equation 3.28 as $\mathcal{P}_{FS}$. It becomes:

$$\boxed{\mathcal{P}_{FS} = \mathcal{P}_{FS}^{Deform} + \mathcal{P}_{FS}^{(2\mu)E};} \tag{3.29}$$

being the two terms adapted from the previous definitions:

$$\begin{aligned}
\mathcal{P}_{FS}^{(2\mu)E} &:= (2\mu) \int_{\partial\Omega_F} \operatorname{div}(\mathbf{u})\, \mathbf{u} \cdot \mathbf{n}\, dS \\
\mathcal{P}_{FS}^{Deform} &:= -2\mu \int_{\partial\Omega_F} [(\nabla \mathbf{u}\, \mathbf{u}) \cdot \mathbf{n}]\, dS
\end{aligned} \tag{3.30}$$

Other definition of $\mathcal{P}_{FS}$ could be (the demonstration is given in Appendix C):

$$\mathcal{P}_{FS} = \int_{\partial\Omega_F} (-p\mathbf{u}\cdot\mathbf{n} + \lambda \mathrm{div}(\mathbf{u})\,\mathbf{u}\cdot\mathbf{n} + \mu(\boldsymbol{\omega}\times\mathbf{n})\cdot\mathbf{u})\ dS \tag{3.31}$$

The following terms can be then defined on the free surface:

$$\begin{aligned}
\mathcal{P}_{FS}^{Pres} &:= -\int_{\partial\Omega_F} p\,\mathbf{u}\cdot\mathbf{n}\,dS\,,\\
\mathcal{P}_{FS}^{(\lambda)E} &:= (\lambda)\int_{\partial\Omega_F} \mathrm{div}(\mathbf{u})\,\mathbf{u}\cdot\mathbf{n}\,dS\,,\\
\mathcal{P}_{FS}^{Visc} &:= \mu\int_{\partial\Omega_F} (\boldsymbol{\omega}\times\mathbf{n})\cdot\mathbf{u}\,dS.
\end{aligned} \tag{3.32}$$

The free surface term formulated in equation 3.31 is therefore, using these definitions:

$$\boxed{\mathcal{P}_{FS} = \mathcal{P}_{FS}^{Pres} + \mathcal{P}_{FS}^{(\lambda E)} + \mathcal{P}_{FS}^{Visc}\,.} \tag{3.33}$$

3.3.3 Detailed balance of the conservation of energy

Once the dissipative term $\mathcal{P}_D$ is fully decomposed, it is possible to use it in the expression of the conservation of energy equation (3.15), recalled below:

$$-\mathcal{P}_{ext} + \mathcal{P}_M + \mathcal{P}_C = \mathcal{P}_D + \mathcal{P}_B^{\lambda}\,, \tag{3.34}$$

The equation (3.28) can be rearranged with equation (3.15). Using the following simplifications: $\mathcal{P}_B^{(\lambda+2\mu)} := \mathcal{P}_B^{\lambda} + \mathcal{P}_B^{2\mu}$, and $\mathcal{P}_{Body} := \mathcal{P}_{ext} + \mathcal{P}_{wall}$

The term $\mathcal{P}_{Body}$ defined in this way can be rewritten in a similar form as $\mathcal{P}_{FS}$ (details are in Appendix C):

$$\boxed{\mathcal{P}_{Body} = \mathcal{P}_{body}^{Pres} + \mathcal{P}_{body}^{(\lambda+2\mu)E} + \mathcal{P}_{body}^{Visc}\,,} \tag{3.35}$$

where the three terms in the rhs are:

$$\begin{aligned}
\mathcal{P}_{body}^{Pres} &:= -\int_{\partial\Omega_B} p\,\mathbf{u}_B\cdot\mathbf{n}\,dS\\
\mathcal{P}_{body}^{(\lambda+2\mu)E} &:= (\lambda+2\mu)\int_{\partial\Omega_B} \mathrm{div}(\mathbf{u})\,\mathbf{u}_B\cdot\mathbf{n}\,dS\\
\mathcal{P}_{body}^{Visc} &:= \mu\int_{\partial\Omega_B} (\boldsymbol{\omega}\times\mathbf{n})\cdot\mathbf{u}_B\,dS
\end{aligned} \tag{3.36}$$

The conservation of energy can be finally expressed as:

$$\boxed{\mathcal{P}_M + \mathcal{P}_C - \mathcal{P}_B^{\lambda+2\mu} = \mathcal{P}_{Body} + \mathcal{P}_{FS} + \mathcal{P}_\omega\,.} \tag{3.37}$$

In the case when there is no moving body, the dissipation is expressed through one volume integral connected to the enstrophy and one surface integral on the free surface. This expression will be tested numerically using the SPH methods in chapters 6 and 7.

3.4 RIGID BODY CASE

If the body can be considered as rigid body, whose center of gravity moves with a velocity $\mathbf{V}_O$, the velocity u_B of a point belonging to the body can be expressed as:

$$\mathbf{u}_B(\mathbf{r}) = \mathbf{V}_O + \boldsymbol{\omega}_B \times (\mathbf{r} - \mathbf{r}_O)\,. \tag{3.38}$$

Under this assumption, the terms defined in equation (3.36) become:

$$\begin{aligned}
\mathcal{P}^{Pres}_{body} &= V_0 \cdot \int_{\partial\Omega_B} -p\,\mathbf{n}\,dS + \int_{\partial\Omega_B} \boldsymbol{\omega}_B \times (\mathbf{r}-\mathbf{r}_0)\cdot(-p\mathbf{n})\,dS = \\
&\quad V_0 \cdot \mathbf{F}^{Pres}_{body/fluid} + \boldsymbol{\omega}_B \cdot \mathbf{T}^{Pres}_{body/fluid}\,, \\
\mathcal{P}^{\lambda B}_{body} &= V_0 \cdot \lambda \int_{\partial\Omega_B} \mathrm{div}(\mathbf{u})\,\mathbf{n}\,dS + \lambda \int_{\partial\Omega_B} \boldsymbol{\omega}_B \times (\mathbf{r}-\mathbf{r}_0)\cdot[\mathrm{div}(\mathbf{u})\mathbf{n}]\,dS = \\
&\quad V_0 \cdot \mathbf{F}^{B}_{body/fluid} + \boldsymbol{\omega}_B \cdot \mathbf{T}^{B}_{body/fluid}\,, \\
\mathcal{P}^{Visc}_{body} &= -\mu \int_{\partial\Omega_B} \boldsymbol{\omega} \times [\mathbf{V}_0 + \boldsymbol{\omega}_B \times (\mathbf{r}-\mathbf{r}_0)]\cdot\mathbf{n}\,dS = \\
&\quad V_0 \cdot \mu \int_{\partial\Omega_B} (\boldsymbol{\omega}\times\mathbf{n})\,dS + \boldsymbol{\omega}_B \cdot \mu \int_{\partial\Omega_B} (\mathbf{r}-\mathbf{r}_0)\times(\boldsymbol{\omega}\times\mathbf{n})\,dS = \\
&\quad V_0 \cdot \mathbf{F}^{viscous}_{body/fluid} + \boldsymbol{\omega}_B \cdot \mathbf{T}^{viscous}_{body/fluid}\,,
\end{aligned} \tag{3.39}$$

where the identity (A.1 in appendix) has been used.

Part II

NUMERICAL MODEL

4 THE SPH MODEL FOR THE NAVIER-STOKES EQUATIONS

4.1 DELTA-SPH EQUATIONS

The δ-SPH scheme proposed by Antuono et al. (Antuono et al. 2010, Antuono et al. 2012a) is adopted. The fluid is assumed to be barotropic and weakly-compressible and the reference equations are the Navier-Stokes equations.

The δ-SPH scheme reads:

$$\begin{cases} \dfrac{D\rho_i}{Dt} = -\rho_i \displaystyle\sum_j (\mathbf{u}_j - \mathbf{u}_i)\cdot\nabla_i W_{ij}\, V_j + \delta\, h\, c_0 \sum_j \psi_{ij}\, \dfrac{(\mathbf{r}_j - \mathbf{r}_i)\cdot\nabla_i W_{ij}}{\|\mathbf{r}_j - \mathbf{r}_i\|^2}\, V_j\,, \\ \dfrac{D\mathbf{u}_i}{Dt} = -\dfrac{1}{\rho_i}\displaystyle\sum_j (p_j + p_i)\,\nabla_i W_{ij}\, V_j \;+\; \mathbf{f}_i \;+\; \nu\,\dfrac{\rho_0}{\rho_i}\sum_j \pi_{ij}\,\nabla_i W_{ij}\, V_j\,, \\ \dfrac{De_i}{Dt} = -\dfrac{p_i}{\rho_i}\displaystyle\sum_j (\mathbf{u}_j - \mathbf{u}_i)\cdot\nabla_i W_{ij}\, V_j \;+\; \nu\,\dfrac{\rho_0}{\rho_i}\sum_j \dfrac{\pi_{ij}}{2}\,(\mathbf{u}_j - \mathbf{u}_i)\cdot\nabla_i W_{ij}\, V_j\,, \\ \dfrac{D\mathbf{r}_i}{Dt} = \mathbf{u}_i\,, \\ p_i = c_0^2\,(\rho_i - \rho_0)\,, \end{cases} \tag{4.1}$$

where ρ_i, p_i, $\mathbf{u}_i$, V_i and e_i are respectively the density, the pressure, the velocity, the volume and the internal energy of the i-th particle. The speed of sound c_0 is set in order to guarantee density variation smaller than $0.01\rho_0$. Symbol ∇_i indicates the differentiation with respect to the position of the i-th particle while $\mathbf{f}_i$ denotes the body force acting on it. Finally, W_{ij} is the kernel function. In this work, unless specified differently, a Renormalised Gaussian kernel (see *e.g.* Molteni and Colagrossi 2009) has been used. W has a compact support of radius $3h$, where h is the *smoothing length*. For $h \to 0$ and $\Delta X/h \to 0$ (ΔX being the particle mean spacing, the system (4.1) converges to the Navier-Stokes equations (see *e.g.* Colagrossi et al. 2011).

The main feature of the δ-SPH scheme relies in the use of a proper artificial diffusive term into the continuity equation in order to remove the spurious

numerical high-frequency oscillations in the pressure field. The arguments of the diffusive and viscous terms are respectively:

$$\psi_{ij} = 2\,(\rho_j - \rho_i) - \left(\langle\nabla\rho\rangle_i^L + \langle\nabla\rho\rangle_j^L\right)\cdot(\mathbf{r}_j - \mathbf{r}_i) \qquad ,$$

$$\pi_{ij} = K\,\frac{(\mathbf{u}_j - \mathbf{u}_i)\cdot(\mathbf{r}_j - \mathbf{r}_i)}{\|\mathbf{r}_j - \mathbf{r}_i\|^2}\,,$$

where $K = 2(n+2)$ and n is the spatial dimension of the problem at hand. Symbol $\langle\nabla\rho\rangle_i^L$ indicates the renormalised density gradient -see (Randles and Libersky 1996) for more details. The (dimensionless) parameter δ is set equal to 0.1 when used in the simulations.

The viscous forces are modelled through the viscous formula of Monaghan & Gingold (Monaghan and Gingold 1983) that preserves both linear and angular momenta. In system (4.1) the energy equation is uncoupled with the momentum one and it is just used to check the conservation of the total energy of the particles system. Indeed, in absence of solid walls and external forces system (4.1) conserves the total energy exactly (see *e.g.* Benz 1989). Generally, this is no longer true in presence of solid walls because of the numerical enforcement of the boundary conditions. Then, a check on the energy conservation is made *a posteriori* (see chapter 8).

4.2 INITIAL PARTICLE DISTRIBUTION

The fluid particles are initially positioned using a "packing" algorithm described in Colagrossi et al. 2012. Thanks to this procedure, at the initial instant all particles have approximately the same volume, namely V_0, which is equal to the fluid domain volume divided by the number of fluid particles. Consistently, the particle mean spacing is denoted by $\Delta x = V_0^{1/n}$. The average number of particles in the kernel support is set by choosing the ratio $h/\Delta x$. In the present work $h/\Delta x$ is set equal to 1.33 which in two dimensions corresponds to about 50 interacting particles.

Along with the volume distribution, the initial pressure and the velocity fields are prescribed as well. The initial density distribution $\rho_i(t_0)$ is evaluated by means of the state equation and the particle masses are computed through the equation $m_i = V_0\,\rho_i(t_0)$. The mass of the i-th particle remains constant during the time evolution ensuring the total mass conservation of the particles system. The volume distribution is updated in time using the density field, *i.e.* $V_i(t) = m_i/\rho_i(t)$.

4.3 PRESENCE OF A BODY AND ENFORCEMENT OF THE SOLID-BOUNDARY CONDITION THROUGH A GHOST-FLUID METHOD

At continuum, the presence of a body surrounded by a fluid is given by a boundary condition on the fluid patch. When the fluid is discretised, several options are possible in order to impose the boundary condition, but all of them can be expressed as a force term F_i^{body} in equation (4.1). Several methods are used to evaluate this term: repulsive forces (Monaghan 1994), boundary integral (De Leffe et al. 2011; Ferrand et al. 2013; Macià et al. 2012), and ghost techniques (Colagrossi and Landrini 2003; Macià et al. 2011; Marrone et al. 2011a).

The ghost-fluid technique is used to enforce proper boundary conditions on the body surface. Specifically, the solid domain is modelled through a set of "imaginary particles" (hereinafter denoted as "ghost particles" and labelled with the subscript "s") and all the fluid fields (that is, velocity, pressure and internal energy) are extended on these fictitious particles through proper mirroring techniques. The latter is used as a reference in the following and the expression of F_i^{body} is given by:

$$F_i^{body} = \sum_{j \in solid} \left[-(p_j + p_i) + \rho_0 \nu \pi_{ij} \right] \nabla_i W_{ij} V_i V_j \,, \tag{4.2}$$

in which the first term on the right-hand side represents the pressure component and the second acts as the viscous component of the stress tensor:

$$\begin{aligned} F_i^{body} &= F_i^p + F_i^\nu \,, \\ F_i^p &= \sum_{j \in solid} -(p_j + p_i) \nabla_i W_{ij} V_i V_j \,, \\ F_i^\nu &= \sum_{j \in solid} \rho_0 \nu \pi_{ij} \nabla_i W_{ij} V_i V_j \,. \end{aligned} \tag{4.3}$$

Different mirroring techniques are adopted to enforce different boundary conditions (e.g., Dirichlet or Neumann conditions). To this end, the solid surface is discretised in equispaced body nodes and layers of ghost particles are disposed in the solid region. The ghost particle positions have been obtained by using the technique described in (Marrone et al. 2011a) (see the sketch in the left plot of figure 4.1). The pressure, velocity and internal energy assigned to the fixed ghost particles, namely $(\mathbf{u}_s, p_s, e_s)$, are computed by using the values obtained at specific interpolation nodes internal to the fluid and uniquely

associated with the fixed ghost particles. Hereinafter, the interpolated values are indicated through $(\mathbf{u}^*, p^*, e^*)$.

The internal energy is mirrored on the fixed ghost particles to enforce the Neumann condition $\partial e/\partial \mathbf{n} = 0$, where $\mathbf{n}$ is the normal unit vector to the solid profile. This means that no heat flux is allowed across the solid boundary. Similarly, the pressure field p_s is mirrored on the fixed ghost particles to enforce the following Neumann condition:

$$\frac{\partial p}{\partial \mathbf{n}} = \rho \left[\mathbf{f} \cdot \mathbf{n} - \frac{D\mathbf{u_b}}{Dt} \cdot \mathbf{n} + \nu \nabla^2 \mathbf{u} \cdot \mathbf{n} \right], \tag{4.4}$$

where $\mathbf{f}$ is a generic body force and $\mathbf{u_b}$ is the velocity of the solid boundary (for details see (Marrone et al. 2011a)). This leads to:

$$p_s = p^* + \frac{\partial p}{\partial \mathbf{n}} \cdot (\mathbf{r}^* - \mathbf{r}_s) \tag{4.5}$$

The velocity field is subject of a specific treatment. As sketched in the right plot of figure 4.1, the ghost velocity $\mathbf{u}_s$ depends on both $\mathbf{u}^*$ and $\mathbf{u}_b$, the latter being the velocity of the nearest body node. De Leffe et al. (De Leffe et al. 2011) found that, in order to avoid inconsistencies and loss of accuracy, different mirroring techniques have to be used to evaluate $\langle \nabla \cdot \mathbf{u} \rangle$ and $\langle \nabla^2 \mathbf{u} \rangle$. The specific mirroring techniques treat differently the components of $\mathbf{u}^*$ in the normal and tangential direction to the solid surface (right plot of figure 4.1).

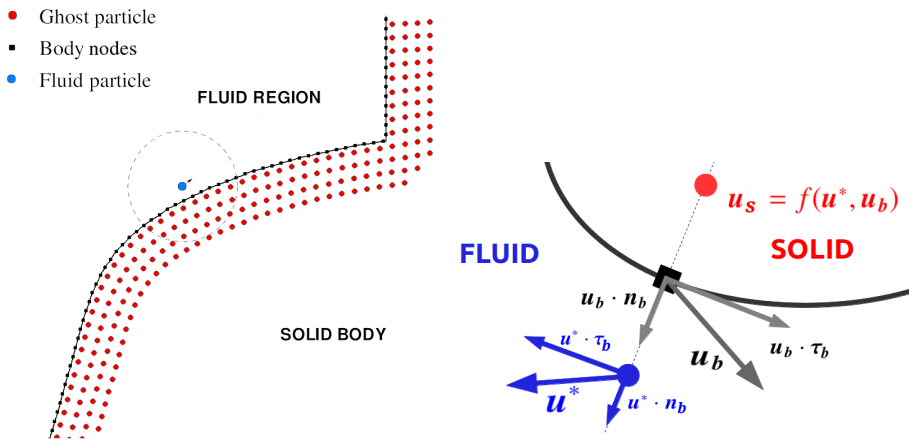

Figure 4.1.: Sketch of the ghost-fluid approach. Left: Discretization of the ghost-fluid through ghost particles. Right: Mirroring of the velocity.

De Leffe et al. (De Leffe et al. 2011) proved that the velocity-divergence operator is convergent and consistent if the normal component of $\mathbf{u}^*$ is mirrored

in the frame of reference of the solid profile, leaving the tangential component unaltered:

$$\langle \nabla \cdot \mathbf{u} \rangle \qquad \begin{cases} \mathbf{u}_s \cdot \mathbf{n} = 2\,\mathbf{u}_b \cdot \mathbf{n} - \mathbf{u}^* \cdot \mathbf{n}\,, \\ \mathbf{u}_s \cdot \boldsymbol{\tau} = \mathbf{u}^* \cdot \boldsymbol{\tau}\,. \end{cases} \tag{4.6}$$

Conversely, to evaluate $\langle \nabla^2 \mathbf{u} \rangle$, the velocity field has to be mirrored to approximate no-slip conditions along the solid bodies. A common way (adopted in this work) is to reverse the tangential component, leaving the normal one unaltered:

$$\langle \nabla^2 \mathbf{u} \rangle \qquad \begin{cases} \mathbf{u}_s \cdot \mathbf{n} = \mathbf{u}^* \cdot \mathbf{n}\,, \\ \mathbf{u}_s \cdot \boldsymbol{\tau} = 2\,\mathbf{u}_b \cdot \boldsymbol{\tau} - \mathbf{u}^* \cdot \boldsymbol{\tau}\,. \end{cases} \tag{4.7}$$

4.3.1 Numerical treatment of the intersection between the free surface and the body

In order to correctly treat the intersection between the free surface and solid boundaries, it is necessary to implement an algorithm able to determine when a portion of the ghost-fluid region is immersed or not. To this purpose, the condition immersed/not immersed of a ghost particle is defined by the state of the associated interpolation node. The position of the interpolation node with respect to the free surface is evaluated through a Level-Set function ϕ. The absolute value of ϕ represents the distance of the interpolation node from the free surface, namely $d = |\phi|$ (see the left plot of figure 4.2). When $\phi \leqslant 0$, the node is immersed in the fluid domain and the physical quantities on the ghost particle are obtained by using equations (4.4), (4.6) and (4.7). When $\phi > 0$, the interpolation node is out of the fluid domain and it is necessary to switch off the interpolation node and the associated ghost particle.

In the case $\phi > 3h$, the distance of the interpolation node from the free surface is greater than the (adopted) kernel support and, consequently, all the interpolated values are naturally zero since there are no neighbour fluid particles. In the case $0 < \phi < 3h$, part of the kernel support is covered by the fluid domain and non-physical values of $p, \mathbf{u}$ and e are interpolated on the node. To identify the nodes falling within the latter case, the function $\xi(\mathbf{x})$ is introduced:

$$\xi(\mathbf{x}) = \frac{h}{2} \frac{\sum_i \nabla W_i(\mathbf{x})\, V_i}{\sum_j W_j(\mathbf{x})\, V_j}\,. \tag{4.8}$$

This function is evaluated at the node position and its value is used to decide when an interpolation node has to be switched off. When the node is inside the fluid and $\phi \leqslant -3h$, $\xi(\mathbf{x})$ is close to zero, since in equation (4.8) the numerator is approximately null and the denominator is close to 1. Now, let us

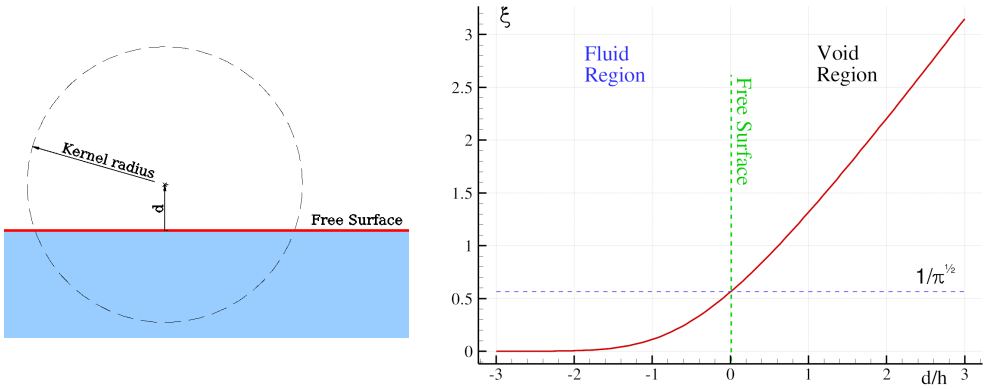

Figure 4.2.: Sketch of the procedure to identify nodes inside/outside the fluid domain. Left: sketch of an interpolation node outside the fluid domain at distance d from the free surface. Right: behaviour of the function $\xi(\mathbf{x})$ (see eq. (4.8)) by varying ϕ.

consider the case of a node on the free surface, *i.e.* $d = 0$. If the free surface is regular and h is small enough, the free surface in the neighbourhood of the node can be approximated with a straight line and the function $\xi(\mathbf{x})$ is almost equal to $1/\sqrt{\pi}$ (using a renormalised Gaussian kernel). Note that, in the neighbourhood of the free surface, $\xi(\mathbf{x})$ increases almost linearly with ϕ (see the right plot of figure 4.2). Then, the simplest choice would be to switch off the nodes where $\xi(\mathbf{x}) \geqslant 1/\sqrt{\pi}$. Unfortunately, the free surface is generally not very regular and cannot be approximated through a straight line. Then, a conservative threshold for ξ has been chosen. Specifically, a node at the position $\mathbf{x_N}$ for which $\xi(\mathbf{x_N}) = 0.8$ is still considered inside the fluid. This threshold is in agreement with the values given by Marrone et al. (Marrone et al. 2010) who proposed a definition of the free surface in the SPH context.

Figure 4.3 displays a sketch of the whole procedure described above. The ghost particles that have the corresponding interpolation node inside the fluid domain are active (coloured in red in the sketch) and their physical quantities are obtained according to equations (4.4), (4.6) and (4.7). The ghost particles associated to nodes which are outside the fluid domain are inactive, that is, they are not visible to the fluid particles.

4.3.2 In/outflow conditions

In free-surface continuous flows, such as open channel flows can occur, a general boundary treatment has to be used to impose suitable in/out-flow boundary conditions. In the present work the algorithm proposed by Federico et al. 2012 is adopted. The modelling permits to investigate a wide range of flow phenomena in water streams through the initial imposition of flow characteristics such as surface elevation, velocity and pressure at in/out-flow boundaries.

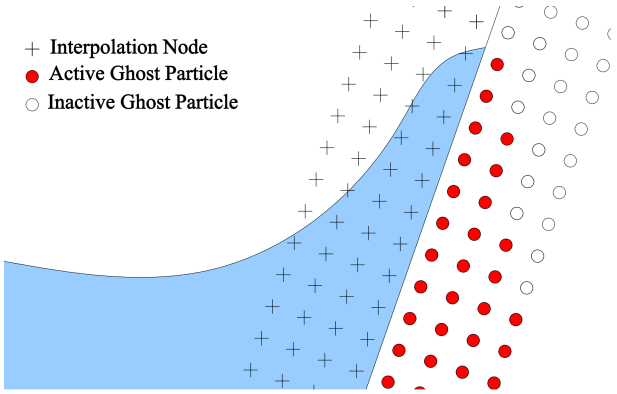

Figure 4.3.: Sketch of the activated ghost particles at the intersection between the free surface and the body surface.

It allows also the enforcement of different conditions between upstream and downstream.

In order to assign different upstream and downstream flow conditions, two new sets of boundary particles are defined. In all, four sets of particles are used: fluid (f), fixed ghost (s), inflow (i) and outflow (o) particles. Similarly to the fixed ghost particles, the in/out-flow particles affect the fluid particles but not vice versa. The region covered by these particles is at least as wide as the kernel radius.

Fig. 4.4 shows the initial sketch of the computational domain: different colours are associated to different sets of particles. The flow extends along the x-axis and is limited by an *inlet* and an *outlet* boundary. An *inflow* and an *outflow* threshold are defined, the particles that cross these thresholds change the set they belong to.

The use of in/out-flow particles allows the imposition of different velocity and pressure fields both upstream and downstream in the computational domain. A constant or time variation of the water level can be assigned at upstream boundary, while the downstream condition is determined by the flow evolution. Note that the use of in/out-flow particles avoids the generation of unphysical weakly-compressibility related pressure shock waves due to the direct creation/removal of fluid particles.

4.3.3 Evaluation of Forces and Torques using the ghost-fluid technique

To find out the formulation for global loads exerted by the fluid on solid structures, it is convenient to develop the analysis at the continuum level. The fluid and solid domains are denoted by Ω_f and Ω_s respectively. The forces on solid bodies can be evaluated by using two main approaches: the evaluation of the forces integrating the stresses along the body surface and the technique here proposed where, similarly to Doring et al. 2004, a volume integral over the

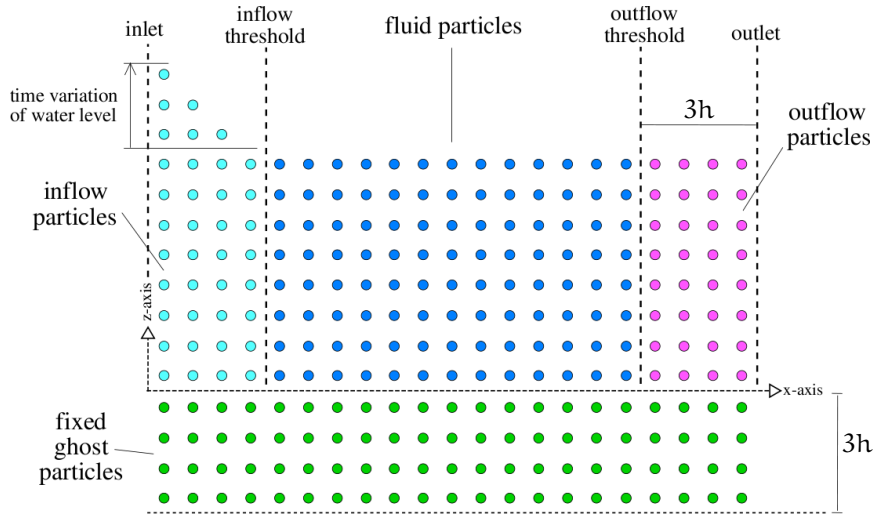

Figure 4.4.: Initial sketch of the computational domain: different colours are associated to different sets of particles.

ghost particle domain is used. In the following the equivalence of these two approaches is given.

Denoting by $\langle \mathbb{T} \rangle$ the smoothed stress tensor, the global force on the body is:

$$\mathbf{F}_{\text{fluid-solid}} = \int_{\partial \Omega_s} \langle \mathbb{T} \rangle \cdot \mathbf{n} \, dS \,, \tag{4.9}$$

where $\mathbf{n}$ is the unit outward normal to the solid profile. Assuming the flow field to be mirrored on the solid body through a proper ghost-fluid technique, the stress tensor can be decomposed in:

$$\langle \mathbb{T} \rangle(\mathbf{r}) = \int_{\Omega_f} \mathbb{T}' \, W(\mathbf{r}' - \mathbf{r}) \, dV' + \int_{\Omega_s} \mathbb{T}^* \, W(\mathbf{r}^* - \mathbf{r}) \, dV^* \,, \tag{4.10}$$

where the starred variables indicate quantities mirrored over the solid domain Ω_s. Substituting (4.10) into (4.9) and using the divergence theorem and the symmetry properties of the kernel function, we obtain the following equality:

$$\mathbf{F}_{\text{fluid-solid}} = \int_{\Omega_f} dV \int_{\Omega_s} (\mathbb{T}^* + \mathbb{T}) \cdot \nabla W(\mathbf{r}^* - \mathbf{r}) \, dV^* + \mathcal{O}(h) \,, \tag{4.11}$$

where ∇ indicates the differentiation with respect to the position $\mathbf{r}$. The terms of order $\mathcal{O}(h)$ indicate the contributions due to the presence of the free surface. These terms are small since, by definition, the tension along the free surface is zero.

When equation (4.11) is discretised, we get:

$$\mathbf{F}_{\text{fluid-solid}} = \sum_{i \in \text{fluid}} \sum_{j \in \text{solid}} \left(\mathbb{T}_j + \mathbb{T}_i\right) \cdot \nabla_i W_{ij} \, V_i \, V_j \,, \tag{4.12}$$

where i and j denote quantities associated with the fluid particles and the ghost particles respectively. One of the advantages of equation (4.12) is that it does not require interpolation on body nodes. For this reason, it is simpler and faster to use in practical applications. Since the inner summation of (4.12) approximates the divergence of the stress tensor, in practical simulations it is sufficient to substitute the corresponding operator of the SPH scheme at hand. In the present case, this leads to:

$$\mathbf{F}_{\text{fluid-solid}} = \sum_{i \in \text{fluid}} \sum_{j \in \text{solid}} \left[- \left(p_j + p_i\right) + \rho_0 \, \nu \, \pi_{ij} \right] \nabla_i W_{ij} \, V_i \, V_j \,, \tag{4.13}$$

in which the first term on the right-hand side represents the pressure component and the second acts as the viscous component of the stress tensor.

The evaluation of the torque $\mathbf{T}_{\text{fluid-solid}}$ acting on the solid body can be derived by using the same approach shown above. Let us consider a fixed point $\mathbf{r}_0$. Then, the torque with respect to it is:

$$\mathbf{T}_{\text{fluid-solid}} = \int_{\partial\Omega_s} (\mathbf{r} - \mathbf{r}_0) \times \langle \mathbb{T} \rangle \cdot \mathbf{n} \, dS \,, \tag{4.14}$$

and, following the procedure used for the evaluation of the force, it is possible to rearrange the above expression as follows:

$$\begin{aligned} \mathbf{T}_{\text{fluid-solid}} = \int_{\Omega_f} dV \int_{\Omega_s} \Big\{ & \quad (\mathbf{r}^* - \mathbf{r}_0) \times \Big[\mathbb{T} \cdot \nabla W(\mathbf{r}^* - \mathbf{r}) \Big] + \\ & + \quad (\mathbf{r} - \mathbf{r}_0) \times \Big[\mathbb{T}^* \cdot \nabla W(\mathbf{r}^* - \mathbf{r}) \Big] \Big\} \, dV^* + \mathcal{O}(h) \,. \end{aligned} \tag{4.15}$$

By analogy with formula (4.2), the above equation is discretised as follows:

$$\begin{aligned} \mathbf{T}_{\text{fluid-solid}} = \sum_{i \in \text{fluid}} \sum_{j \in \text{solid}} \Big\{ & \quad (\mathbf{r}_j - \mathbf{r}_0) \times \Big[(-p_i + \rho_0 \, \nu \, \pi_{ij}/2) \, \nabla_i W_{ij} \Big] + \\ & + \quad (\mathbf{r}_i - \mathbf{r}_0) \times \Big[(-p_j + \rho_0 \, \nu \, \pi_{ij}/2) \, \nabla_i W_{ij} \Big] \Big\} \, V_i \, V_j \,. \end{aligned} \tag{4.16}$$

The expressions derived above for the force and torque remind somehow the technique proposed in (Monaghan et al. 2003) and (Kajtar and Monaghan 2008). However, it is important to underline that, apart from the different enforcement of solid boundary conditions, in those cases the formulation is directly obtained from a momentum balance between the fluid and the repulsive

body particles. Conversely, in the present case, the global loads are derived from the evaluation of the stress tensor on the body surface by means of a proper ghost-fluid extension in the solid region.

4.4 ALGORITHM FOR HANDLING FLUID–BODY COUPLING

The solid dynamics is modelled by the Newton's law of motion. Linear and Angular momentum equation are given in a simple 2D framework by:

$$\begin{cases} M\dfrac{d\mathbf{V}_G}{dt} = M\mathbf{g} + \mathbf{F}_{\text{fluid-solid}}\,, \\ I_G\dfrac{d\Omega_G}{dt} = T_{\text{fluid-solid}}\,, \end{cases} \tag{4.17}$$

where $\mathbf{V}_G$ and Ω_G are the velocity of the centre of gravity and the angular velocity of the body, M and I_G are the mass and the moment of inertia of the body around the centre of gravity and, finally, $\mathbf{F}_{fluid-solid}$ is the hydrodynamic force acting on the body. Here, $T_{fluid-solid}$ is the projection of the hydrodynamic torque along the unit vector $\mathbf{k}$ normal to the plane, that is $T_{fluid-solid} = \mathbf{T}_{\text{fluid-solid}} \cdot \mathbf{k}$.

The dynamical state of the fluid particles, ghost particles and body nodes can be expressed through the vectors y_f, y_s and y_b respectively:

$$\begin{aligned} y_f &= (\ldots, \rho_i, \mathbf{u}_i, \mathbf{r}_i, \ldots) && i \in \text{Fluid} \\ y_s &= (\ldots, \rho_j, \mathbf{u}_j, \mathbf{r}_j, \ldots) && j \in \text{Solid} \\ y_b &= (\ldots, \mathbf{r}_k, \mathbf{u}_k, \mathbf{a}_k, \mathbf{n}_k, \ldots) && k \in \text{Body Surface} \end{aligned} \tag{4.18}$$

Further, the dynamical state of the rigid body is expressed by:

$$y_g = (\mathbf{r}_G, \mathbf{V}_G, \theta_G, \Omega_G) \tag{4.19}$$

where $\mathbf{r}_G$ and θ_G are respectively the position vector of the centre of gravity and the related angle of rotation.

The coupling between the two systems from equations (4.1) and (4.17) can be represented by:

$$\begin{cases} \dot{y_f} &= F_f(y_f, y_s, t)\,, & y_f(t_0) = y_{f0}\,, \\ \dot{y_g} &= F_g(y_g, y_f, y_s, t)\,, & y_g(t_0) = y_{g0}\,, \\ y_s &= F_s(y_b, y_f, t)\,, & \\ y_b &= F_b(y_g, \dot{y_g}, y_{b0})\,, & y_{b0} = y_b(t_0)\,, \end{cases} \tag{4.20}$$

where the last two equations represent, respectively, the dependence of the ghost state (equations 4.5, 4.6 and 4.7) and of the body nodes state from the rigid motion equations.

The weakly-compressible SPH equations march in time using an explicit scheme. Then, for the sake of simplicity, the whole system (4.20) follows the same time integration scheme. The 4^{th} order Runge Kutta algorithm offers a good balance between velocity and stability and has been used for integrating the system of equations (4.20). In the latter, the acceleration of the body appears on both sides of the equations. This is common in explicit schemes for fluid-body coupling. In potential flow solvers the body acceleration is generally taken into account through the added mass term (see e.g. Vinje and Brevig 1981), enabling to move the body acceleration term from the right-hand side to the left-hand side. The added mass approach is also applied in other numerical solvers as an under-relaxation correction in the body motion (see *e.g.* Hadžić et al. 2005). Differently, in the present scheme the acceleration of the body on the right-hand side is taken from the previous Runge-Kutta substep. This procedure is justified by the use of a very small time-step required by the weakly-compressible assumption, as briefly recalled below.

At the generic time instant t^n, the state vector y_b is determined through $\dot{y_g}$ (predicted at the previous Runge-Kutta substep) and y_g. Then, the ghost fluid state y_s is obtained through the interpolation on the fluid particles, y_f, and the mirroring procedure (which requires y_b, as discussed in 4.3). The global loads $(\mathbf{F}, \mathbf{T})_{\text{fluid-solid}}$ are evaluated though equations (4.12) and (4.16) and $\dot{y_g}$ is obtained by (4.17). Finally, the interaction between fluid and ghost particles gives $\dot{y_f}$ through equation (4.1). The iteration substep ends with the integration of $\dot{y_g}$ and $\dot{y_f}$ to obtain respectively y_g and y_f at the time instant t^{n+1}.

As far as the time integration of system (4.20) is concerned, the time step has to account for the maximum acceleration (both body nodes and fluid particles) $|\mathbf{a}| = \max(\|\mathbf{a}_f\|_\infty, \|\mathbf{a}_b\|_\infty)$, the viscous diffusion and the sound speed. The time-step bounds deriving from the first two terms have been obtained following (Morris et al. 1997):

$$\Delta t_1 \leqslant 0.25 \sqrt{\frac{h}{|\mathbf{a}|}} \tag{4.21}$$

$$\Delta t_2 \leqslant 0.125 \frac{h^2}{\nu} \tag{4.22}$$

while the third limit is derived following Monaghan and Kos 1999:

$$\Delta t \leqslant \text{CFL}_3 \min_i \left[\frac{h}{c_0 + \epsilon \max_j \pi_{ij}} \right] \tag{4.23}$$

For a fourth-order Runge-Kutta scheme and for the renormalised gaussian kernel, $\text{CFL}_3 \leqslant 2.0$ is found heuristically to ensure the stability of system (4.20).

5 ENERGY CONSERVATION IN THE SPH MODEL

5.1 INTRODUCTION

In this chapter, the equations of chapter 3 are written in the discrete SPH formalism. This aims at evaluating numerically some relevant terms present in the energy conservation equation and particularly those relative to the dissipation. The differences between the form of the conservation of energy at continuum level and at discrete level can be understood from this chapter. The analysis presented in this section is used in chapters 6 and 7. Some important power balances of chapter 3 are recalled below.

The conservation of energy at the continuum level, for the fluid/body problem was defined in equation 3.15 as:

$$-\mathcal{P}_{ext} + \mathcal{P}_M + \mathcal{P}_C = \mathcal{P}_D + \mathcal{P}_B^{\lambda}, \tag{5.1}$$

i.e., the sum of the power due to the external forces, the power associated to the reversible compressibility and the mechanical power are balanced by the power dissipated by the fluid.

The dissipation term $\mathcal{P}_D$ was also decomposed at the continuum level in equation 3.28:

$$\mathcal{P}_D = \mathcal{P}_{wall} + \mathcal{P}_{FS} + \mathcal{P}_\omega + \mathcal{P}_B^{2\mu}, \tag{5.2}$$

such as $\mathcal{P}_D$ is the sum respectively of the power dissipated on the wall, on the free surface, the enstrophy, and finally some small dissipation linked to the compressibility.

The first definition of the term linked to the dissipation on the free surface was written in equation 3.29:

$$\mathcal{P}_{FS} = 2\mu \int_{\partial\Omega_F} [-(\nabla \mathbf{u}\,\mathbf{u}) \cdot \mathbf{n} + \mathrm{div}(\mathbf{u})(\mathbf{u} \cdot \mathbf{n})]\, dS \tag{5.3}$$

equivalent to equation 3.29 recalled below:

$$\mathcal{P}_{FS} = \mathcal{P}_{FS}^{Deform} + \mathcal{P}_{FS}^{(2\mu)E}. \tag{5.4}$$

In this chapter, and in the applications where the decomposition of the various power terms is attempted numerically, the delta-SPH scheme is not considered. Further details about the implications of the delta scheme in the energy balance can be found in Antuono et al. 2015.

5.2 SPH DISCRETIZATION OF THE ENERGY EQUATION

Considering the particle system on the SPH model, the related mechanical and internal energies are given as:

$$\begin{aligned} \mathcal{E}_M^{SPH} &= \sum_i \left(m_i \frac{\mathbf{u}_i^2}{2} + m_i\, g\, z_i \right), \\ \mathcal{E}_I^{SPH} &= \sum_i m_i\, e_i, \end{aligned} \tag{5.5}$$

where the time derivative of the specific internal energy of the i-th particle is given in equation (4.1). Therefore:

$$\begin{aligned} \frac{d\mathcal{E}_I^{SPH}}{dt} &= -\sum_i \sum_j \frac{m_i\, m_j}{\rho_i\, \rho_j} p_i (\mathbf{u}_j - \mathbf{u}_i) \cdot \nabla_i W_{ij} + \\ &+ \mu \sum_i \sum_j \frac{m_i\, m_j}{\rho_i\, \rho_j} \frac{\pi_{ij}}{2} (\mathbf{u}_j - \mathbf{u}_i) \cdot \nabla_i W_{ij}. \end{aligned} \tag{5.6}$$

Following the definition given in chapter 3 at continuum and recalled in the introduction, it is possible to define from equation 5.6 the two power components:

$$\begin{cases} \mathcal{P}_C^{SPH} = -\sum_i \sum_j \frac{m_i\, m_j}{\rho_i\, \rho_j} p_i\, (\mathbf{u}_j - \mathbf{u}_i) \cdot \nabla_i W_{ij}, \\ \mathcal{P}_{D+B}^{SPH} = -\mu \sum_i \sum_j \frac{m_i\, m_j}{\rho_i\, \rho_j} \frac{\pi_{ij}}{2} (\mathbf{u}_j - \mathbf{u}_i) \cdot \nabla_i W_{ij}. \end{cases} \tag{5.7}$$

The first term in the right-hand side of equation 5.6 is linked to the power component $\mathcal{P}_C$, due to the compressibility, and the second is connected to viscous components $\mathcal{P}_D$ and $\mathcal{P}_B$.

As shown in Colagrossi et al. 2011, it is not possible to separate the two components $\mathcal{P}_D$ and $\mathcal{P}_{\lambda B}$ in the SPH viscous operator and for this reason the notation $\mathcal{P}_{D+B}^{SPH}$ is kept in the following. Furthermore, in Colagrossi et al. 2011 it is demonstrated that the SPH viscous operator adopted in the present scheme forces the constrain $\lambda = \mu$. Therefore, the limit for the convergency of $\mathcal{P}_{D+B}^{SPH}$ is

$$\lim_{h \to 0; N \to \infty} \mathcal{P}_{D+B}^{SPH} = \mathcal{P}_D + \mathcal{P}_B^{\mu}. \tag{5.8}$$

Substituting the linearised equation of state used in this work and the SPH continuity equation in $\mathcal{P}_C^{SPH}$, after some maths it is possible to recover the the following expression:

$$\mathcal{E}_C^{SPH} = \mathcal{E}_C^{SPH}(\rho_0) + c_0^2 \sum_i m_i \left[\log\left(\frac{\rho_i}{\rho_0}\right) + \frac{\rho_0}{\rho_i} - 1 \right]. \tag{5.9}$$

Equation (5.6) can be rewritten in a compact way as:

$$\frac{d\mathcal{E}_I^{SPH}}{dt} = \frac{d\mathcal{E}_C^{SPH}}{dt} - \mathcal{P}_{D+B}^{SPH}\,. \tag{5.10}$$

Thanks to the symmetry property of the kernel function it is possible to demonstrate that the system of equations (4.1) conserves exactly the energy of the particle system (see *e.g.* Colagrossi et al. 2014):

$$\frac{d\mathcal{E}_M^{SPH}}{dt} + \frac{d\mathcal{E}_I^{SPH}}{dt} = 0 \tag{5.11}$$

Considering that the viscous operator used in the present SPH model is a pure dissipative term (see *e.g* Violeau 2009) , it follows that:

$$\frac{d\mathcal{E}_M^{SPH}}{dt} + \frac{d\mathcal{E}_C^{SPH}}{dt} = \mathcal{P}_{D+B}^{SPH} \leqslant 0 \tag{5.12}$$

therefore, the second law of thermodynamic is respected at discrete level.

Definition

With the exception of kinetic energy, potential energy and compressible energy, the terms are defined as a power in this sections. The power terms are directly derived from the numerical equations or from interpolations on the data (see section 5.3). In order to quantify the dissipation of energy connected to the different effects along a simulation, it is useful to integrate the power terms in time. In the following $\Delta\mathcal{E}_X^Y$ is a notation referred to the definition:

$$\Delta\mathcal{E}_X^Y(t) = \int_{t0}^{t} \mathcal{P}_X^Y \, dt\,. \tag{5.13}$$

In the next chapters, some simulations are performed to illustrate these terms, the energy dissipated by the particle system is made non dimensional using the mechanical energy corresponding to the initial condition, $\mathcal{E}_{M0}$. At the end of each simulation, the ratio $\Delta\mathcal{E}_{D+B}^{SPH}(t_f)/\mathcal{E}_{M0}$ provides in this way a clear indication of the dissipation taking place during such simulation, when no external power is given to the system.

5.2.1 Ghost fluid treatment in the conservation of energy

In the sums in previous equations, the j index runs on all particles, fluid and ghost.

$$
\begin{aligned}
\mathcal{P}_C^{solid} &:= - \sum_{i\in fluid} \sum_{j\in solid} \frac{m_i\, m_j}{\rho_i\, \rho_j}\, p_i\, (\mathbf{u}_j - \mathbf{u}_i)\cdot \nabla_i W_{ij},\\
\mathcal{P}_C^{fluid} &:= - \sum_{i\in fluid} \sum_{j\in fluid} \frac{m_i\, m_j}{\rho_i\, \rho_j}\, p_i\, (\mathbf{u}_j - \mathbf{u}_i)\cdot \nabla_i W_{ij},\\
\mathcal{P}_V^{solid} &:= -\mu \sum_{i\in fluid} \sum_{j\in solid} \frac{m_i\, m_j}{\rho_i\, \rho_j}\, \frac{\pi_{ij}}{2}\, (\mathbf{u}_j - \mathbf{u}_i)\cdot \nabla_i W_{ij},\\
\mathcal{P}_V^{fluid} &:= -\mu \sum_{i\in fluid} \sum_{j\in fluid} \frac{m_i\, m_j}{\rho_i\, \rho_j}\, \frac{\pi_{ij}}{2}\, (\mathbf{u}_j - \mathbf{u}_i)\cdot \nabla_i W_{ij}.
\end{aligned}
\tag{5.14}
$$

With these definitions, the following relations are verified:

$$
\mathcal{P}_C^{SPH} = \mathcal{P}_C^{fluid} + \mathcal{P}_C^{solid}, \tag{5.15}
$$

$$
\mathcal{P}_{D+B}^{SPH} = \mathcal{P}_V^{fluid} + \mathcal{P}_V^{solid}. \tag{5.16}
$$

5.3 ENERGY COMPONENTS THROUGH MOVING LEAST SQUARE INTERPOLATION ON SCATTERED DATA

In the previous section it has been shown that the main energy components appear naturally when the continuum equations are written in the SPH formalism. A further decomposition can be attempted using using the Moving Least Square (MLS) interpolation formula on the scattered particle data at each time step. In the following, first order MLS formulae are used (see *e.g.* Fries and Matthies 2004,Colagrossi 2005) in order to attempt to set similar balances to the ones set, in chapter 3 observed at the continuum level. Through these MLS formulae the velocity gradient, $\langle \nabla \mathbf{u} \rangle^{MLS}$, divergence and vorticity fields, $\langle \mathrm{div}\mathbf{u} \rangle^{MLS}$, $\langle \omega \rangle^{MLS}$ can be retrieved form the SPH outputs (*i.e.* from the particle positions, velocities and volumes):

$$
\begin{cases}
\langle \nabla \mathbf{u} \rangle^{MLS}(\mathbf{r}_i) &= \displaystyle\sum_{j\in Fluid} \mathbf{u}_j \otimes \nabla W_{ij}^{MLS}\, V_j\,,\\
\langle \omega \rangle^{MLS}(\mathbf{r}_i) &= \displaystyle\sum_{j\in Fluid} \mathbf{u}_j \times \nabla W_{ij}^{MLS}\, V_j\,,\\
\langle \mathrm{div}\mathbf{u} \rangle^{MLS}(\mathbf{r}_i) &= \displaystyle\sum_{j\in Fluid} \mathbf{u}_j \cdot \nabla W_{ij}^{MLS}\, V_j\,,
\end{cases}
\tag{5.17}
$$

where the Moving Least-Squares gradient $\nabla W^{MLS} = [\partial_x W^{MLS}, \partial_y W^{MLS}]$ is given by:

$$\begin{cases} \partial_x W_{ij}^{MLS} = \mathbf{M}_i^{-1}\, \boldsymbol{e}_2 \cdot \mathbf{b}_{ij}\, W_{ij}\,, & \partial_y W_{ij}^{MLS} = \mathbf{M}_i^{-1}\, \boldsymbol{e}_3 \cdot \mathbf{b}_{ij}\, W_{ij}\,, \\ \mathbf{b}_{ij}^T := [1\,, (x_j - x_i)\,, (y_j - y_i)]\,, & \boldsymbol{e}_2^T := [0,1,0]\,,\ \boldsymbol{e}_3^T := [0,0,1]\,, \\ \mathbf{M}_i := \sum_j \left[\mathbf{b}_{ij} \otimes \mathbf{b}_{ij}\right] W_{ij}\, V_j\,. \end{cases} \tag{5.18}$$

In equation (5.18) the indices i and j refer to the particle indices and not to the spatial components.

From eq. (5.17), it is possible to evaluate the power component due to the enstrophy, $\mathcal{P}_\omega^{MLS}$ and the dissipation components $\mathcal{P}_D^{MLS}$, $\mathcal{P}_{\mu B}^{MLS}$. The MLS formulae are also used for the calculation of other components, like $\mathcal{P}_F^{MLS}$, defined in equation 3.22.

The power terms are evaluated with MLS using only the fluid particles. Indeed, it is not straightforward to use the ghost particles since different "ghost-velocity" fields need to be defined for different differential operators (see chapter 4). Therefore the sum of the components $\mathcal{P}_D^{MLS}$ and $\mathcal{P}_{\mu B}^{MLS}$ is much closer to $\mathcal{P}_V^{fluid}$ than to the total viscous term $\mathcal{P}_{D+B}^{SPH}$:

$$\mathcal{P}_D^{MLS} + \mathcal{P}_{\mu B}^{MLS} \approx \mathcal{P}_V^{fluid}\,. \tag{5.19}$$

Indeed, the limit of these components gives:

$$\begin{cases} \lim\limits_{h\to 0;\mathcal{N}\to\infty} (\mathcal{P}_D^{MLS} + \mathcal{P}_{\mu B}^{MLS}) = \lim\limits_{h\to 0;\mathcal{N}\to\infty} \mathcal{P}_V^{fluid} = (\mathcal{P}_D + \mathcal{P}_{\mu B})\,, \\ \lim\limits_{h\to 0;\mathcal{N}\to\infty} \mathcal{P}_V^{solid} = 0\,. \end{cases} \tag{5.20}$$

In practice, in the next section, it is shown that the convergence of $\mathcal{P}_V^{solid}$ to zero is very slow and therefore it is convenient to take $\mathcal{P}_V^{solid}$ into account in the following decomposition (see eq. (5.16)):

$$\mathcal{P}_{D+B}^{SPH} \approx \mathcal{P}_D^{MLS} + \mathcal{P}_{\mu B}^{MLS} + \mathcal{P}_V^{solid}\,. \tag{5.21}$$

Integrating in time the following relation up to final time of the simulation, t_f, holds:

$$\Delta\mathcal{E}_{D+B}^{SPH}(t_f) \approx \Delta\mathcal{E}_D^{MLS}(t_f) + \Delta\mathcal{E}_{\mu B}^{MLS}(t_f) + \Delta\mathcal{E}_V^{solid}(t_f)\,. \tag{5.22}$$

If the spatial resolutions adopted in the SPH simulations are not fine enough, the relation (5.22) cannot be satisfied mainly due to the numerical errors on the MLS interpolation. Conversely when the error:

$$E_1 := \frac{\left[\Delta\mathcal{E}^{SPH}_{D+B} - \Delta\mathcal{E}^{MLS}_{D} - \Delta\mathcal{E}^{MLS}_{\mu B} - \Delta\mathcal{E}^{solid}_{V}\right](t_f)}{\mathcal{E}_{M0}} \tag{5.23}$$

is small, this is an indication that the numerical solution starts to be good enough and close to a convergent limit.

It is important to underline that not all the terms converge with the same rate, for example the sum:

$$\boxed{\mathcal{P}_{\omega *} := \mathcal{P}^{MLS}_{\omega} + \mathcal{P}^{solid}_{V}.} \tag{5.24}$$

converges much faster than $\mathcal{P}^{MLS}_{\omega}$ and $\mathcal{P}^{solid}_{V}$. The same holds for $\mathcal{P}^{SPH}_{D+B}$ with respect to $(\mathcal{P}^{MLS}_{D} + \mathcal{P}^{MLS}_{\mu B})$ and $\mathcal{P}^{solid}_{V}$.

5.3.1 Free-surface terms

In section (3.3.2), it was shown how the viscous dissipation can be decomposed in components which are volume integrals $\mathcal{P}^{MLS}_{\omega}$, $\mathcal{P}^{MLS}_{\mu B}$ and boundary integrals like $\mathcal{P}_{FS}$ on the free surface.

Considering the case where the body does not move, the dissipation $\mathcal{P}_D$ expressed in equation 3.28 simplifies in:

$$\mathcal{P}_D = \mathcal{P}_{FS} + \mathcal{P}_{\omega} + \mathcal{P}^{2\mu}_{B}, \tag{5.25}$$

$\mathcal{P}_D$, $\mathcal{P}_{\omega}$ and $\mathcal{P}^{2\mu}_{B}$ can be evaluated using the MLS interpolation. For $\mathcal{P}_{FS}$, the discrete and Lagrangian nature of SPH makes unclear the definition of a discrete free-surface integral and its evaluation is not straightforward for the following reasons:

1. particles belonging to the free-surface need to be detected and, as shown in Marrone et al. 2010, this identification is not unique but depends on the specific algorithm and from the parameters connected with it.
2. once the particles on the free surface have been collected it is necessary to calculate the normal vector to this surface
3. if the free surface is highly fragmented, it can be difficult to perform geometrical connections needed for the surface integration (see *e.g.* Antuono et al. 2013)

Using the algorithm proposed in Marrone et al. 2010, a subset of particles FS belonging to the free surface can be defined. The algorithm gives also the evaluation of the normal vector field, and the surface integral $\mathcal{P}_{FS}$ defined by eq. 3.29 expressed at continuum level:

$$\mathcal{P}_{FS} = \mathcal{P}^{Deform}_{FS} + \mathcal{P}^{(2\mu)E}_{FS}; \tag{5.26}$$

can be approximated as:

$$\mathcal{P}_{FS}^{MLS} := 2\mu \sum_{k \in FS} \left[\langle \mathrm{div}(\mathbf{u}) \rangle_k^{MLS} \mathbf{u}_k - \langle \nabla \mathbf{u} \rangle_k^{MLS} \mathbf{u}_k \right] \cdot \mathbf{n}_k \, \Delta S_k \tag{5.27}$$

where the length of the surface elements is simply approximated as $\Delta S_k = (V_k)^{1/n_{Dim}}$.

In this expression, the MLS interpolation is still needed to evaluate the velocity gradient in Eq. (5.27). Then, the free-surface terms defined in (5.27) can be inaccurate when the free surface is highly fragmented. In such condition, the the surface integral $\mathcal{P}_{FS}$ can be evaluated by subtraction using the energy balance (3.30) and the relations (5.21), (5.24) :

$$\boxed{\mathcal{P}_{FS}^{sub} := \mathcal{P}_{D+B}^{SPH} - \mathcal{P}_{\omega^*}^{MLS} - 3\,\mathcal{P}_{\mu B}^{MLS},} \tag{5.28}$$

where the superscript *sub* is used to differentiate this term to the one calculated through (5.27). The accuracy of (5.28) is directly connected to the one of the MLS interpolation and monitored through the relation:

$$E_2 := \frac{\left[\Delta\mathcal{E}_{FS}^{sub} - \Delta\mathcal{E}_{FS}^{MLS}\right](t_f)}{\mathcal{E}_{M0}} = \frac{\left[\Delta\mathcal{E}_{D+B}^{SPH} - \Delta\mathcal{E}_{\omega^*}^{MLS} - 3\Delta\mathcal{E}_{\mu B}^{MLS} - \Delta\mathcal{E}_{FS}^{MLS}\right](t_f)}{\mathcal{E}_{M0}}. \tag{5.29}$$

To give an idea, for complex cases the two monitor parameters E_1, eq. 5.23, and E_2, eq. 5.29 are less than 0.10 when the numerical solutions obtained can be considered accurate enough. In the next chapters, simple viscous cases are used to study the behaviour of different terms. In particular, the study aims at separating the dissipation in enstrophy from the dissipation linked with the free surface.

Part III

NUMERICAL TESTS AND VALIDATION

6 ATTENUATION OF A VISCOUS STANDING WAVE

6.1 DEFINITION OF THE PROBLEM

The problem investigated in this section is the viscous attenuation of a standing wave in deep water condition. Periodic conditions are used for the vertical boundaries while the sea bottom is modelled through a solid flat surface where no-slip condition is enforced (see Fig. 6.1). The formalism used in this chapter has been established mainly in chapters 3 and 5. Because of the deep water condition, the bottom solid boundary has a negligible role and therefore the vorticity field is mainly concentrated near the free surface.

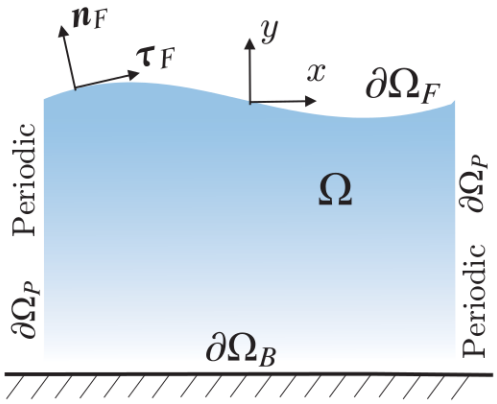

Figure 6.1.: Sketch of the problem of the viscous standing wave.

The damping of viscous gravity waves has been recently studied in Antuono and Colagrossi 2012 where an analytical solution of the linearised Navier-Stokes equation was derived for a wide range of Reynolds numbers and water depths. In Colagrossi et al. 2013 the same problem was considered in the framework of the SPH model where it is shown that, using proper spatial resolutions and a proper number of interacting neighbours, a good agreement between SPH and the analytical solution can be obtained. In the present work this previous analysis is extended varying the Reynolds number and the wave amplitude. In particular the maximum wave steepness considered in this work is larger than the breaking limit $kA = 0.68$ (see *e.g.* Dean and Dalrymple 1991), being A the wave amplitude and k the wave number. In this way, the effect of breaking waves on the viscous dissipation can be also discussed for this scenario.

The analysis conducted in this chapter focuses mainly on quantifying the terms $\mathcal{P}_{FS}$ (associated with the free-surface deformation) and $\mathcal{P}_{\omega}$ (associated with enstrophy) during the time evolution. Various combinations of the viscosity $Re \in [125 - 2000]$ and the amplitude A of the standing wave are tested. The amplitude of the standing wave is set through the parameter $\epsilon = 2A/L$, $\epsilon \in [0.1 - 0.4]$. The Reynolds number for this problem is defined as $Re = H\sqrt{gH}/\nu$ to avoid dependencies of ϵ on this parameter. When increasing the amplitude and the Reynolds number, the free surface starts to break inducing large effects on the components $\mathcal{P}_{FS}$ and $\mathcal{P}_{\omega}$. For this first test-case, and for all the investigated combinations (A,Re), the term $\mathcal{P}_{FS}$ remains always dominant with respect to $\mathcal{P}_{\omega}$.

In this chapter, an analysis is conducted to evaluate the importance of the compressibility: on the global balance, and the contribution to the free surface term $\mathcal{P}_{FS}$.

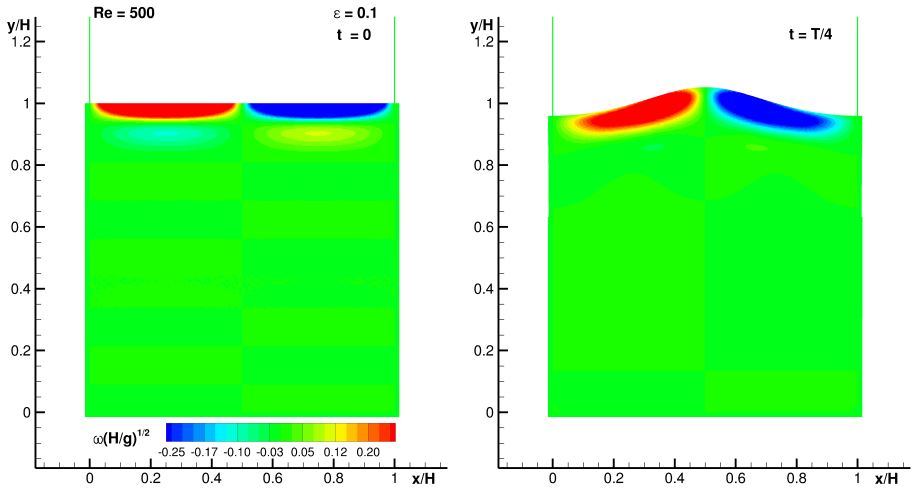

Figure 6.2.: Vorticity field for the standing wave problem for two time instants $t = 0$ and $t = T/4$, T being the linear theory period of oscillation Dean and Dalrymple 1991.

Figure 6.2 describes the initial configuration of the problem. Here, L is the wave length and $H = L$ is the still water depth, the dimensionless wave number kH is therefore equal to 2π. Note that the latter value means that the analysis is performed in a deep water regime (*i.e.* $kH \geqslant \pi$). The boundary layer of the free surface is well visible from the vorticity fields plotted in Fig. 6.2 while the bottom boundary layer is not visible in the range of values used because of the deep water regime. As a consequence, the effect of the bottom boundary layer can be neglected, hence simplifying the analysis.

The free surface is initially flat in order to simplify particle positioning. The initial pressure and velocity fields were evaluated using the analytical solution of Antuono and Colagrossi 2012. The initial value of the mechanical energy is

computed and denoted as $\mathcal{E}_{M0}$. The potential energy is set equal to zero at the initial time (*i.e.* $\mathcal{E}_{M0} = \mathcal{E}_{K0}$).

Five Reynolds numbers and four wave amplitudes are investigated to describe different dissipation laminar regimes. The period of oscillation, T, depends on the two parameters Re and ϵ. For high Re and small ϵ, T is close to the one predicted by linear theory (Dean and Dalrymple 1991), $T_{lin} = 2\pi/\sqrt{gk}$. Since $kH = 2\pi$ in present example, $T_{lin} = \sqrt{2\pi}\sqrt{H/g}$. Taking advantage of this, $\sqrt{H/g}$ will be used to make time non-dimensional in some graphs.

For the SPH simulations presented in this subsection the maximum spatial resolution adopted is $H/\Delta x = 800$ (corresponding to a total number of particles equal to 640000) and the smoothing length is $h/\Delta x = 2.8$ (Wendland C2 kernel is used for all the simulations in this chapter). Indeed, using these parameters the results presented in Colagrossi et al. 2013 are close to a convergence limit.

The final time of the simulations, hereinafter t_f, has been chosen (see Table 6.1) large enough so that mechanical energy is dissipated until its value is approximately 1% of its initial value, $\mathcal{E}_{M0}$.

	t_f/T_{lin}	ϵ = 0.1	0.2	0.3	0.4
Re = 125	2.4	1E-04	1.2E-03	3.2E-03	6.4E-03
Re = 250	4.0	1.9E-03	3.0E-03	5.2E-03	8.1E-03
Re = 500	6.4	7.2E-03	7.8E-03	1.1E-02	1.7E-02
Re = 1000	12	5.6E-03	6.3E-03	7.6E-03	1.1E-02
Re = 2000	20	6.4E-03	1.1E-02	1.1E-02	7.1E-03

Table 6.1.: Energy dissipated at the end of the simulation with respect to the initial value $\mathcal{E}_{M0}$: *i.e.* $[\mathcal{E}_{M0} - \Delta\mathcal{E}^{SPH}_{D+B}(t_f)]/\mathcal{E}_{M0}$.

When a low viscosity liquid like water is considered, the velocity field associated with a gravity wave can be considered practically irrotational and divergence free. Therefore, such velocity field can be expressed through a potential velocity, *i.e.*, $\mathbf{u} = \nabla\Phi$. Under these conditions, $\mathcal{P}_\omega$ is negligible and the viscous dissipation can be expressed using only the component $\mathcal{P}_{FS}$ which becomes:

$$\mathcal{P}_D \simeq \mathcal{P}_{FS} \simeq -2\mu \int_{\partial\Omega_F} \nabla\nabla\Phi\,\nabla\Phi\cdot\mathbf{n}\,dS \simeq -2\mu\int_0^L (\Phi_{xy}\,\Phi_x + \Phi_{yy}\,\Phi_y)\,dx \qquad (6.1)$$

where the right hand side, is a linearised approximation valid for small ϵ. This is the relation used in Lighthill 2001 (see page 234) to estimate the viscous damping of water waves. This consideration highlights that, for gravity wave dynamics, $\mathcal{P}_{FS}$ is generally dominant with respect to $\mathcal{P}_\omega$. In the next subsections we show how those two contributions change with the viscosity of the flow and the intensity of the velocity field given in the initial condition.

6.2 EFFECTS OF THE WEAKLY COMPRESSIBILITY ON TIME EVOLUTION OF THE ENERGY COMPONENTS

Following Colagrossi et al. 2013 the speed of sound, c_0, adopted in the SPH scheme has been set large enough to ensure the weakly compressible regime. In particular, for the standing wave test case, c_0 is set 10 times larger than the velocity $\sqrt{gH}$. Figure 6.3 shows the kinetic energy decay for Re=500 and $\epsilon = 0.1$. The spatial resolution adopted is $H/\Delta x = 800$ and the speed of sound is $c_{01} = 10\sqrt{gH}$. With these parameters the SPH solution is practically superimposed with the analytical solution from Antuono and Colagrossi 2012 which was derived assuming the fluid as incompressible. The increase of the speed of sound to a value $c_{02} = 100\sqrt{gH}$ has therefore negligible influence on $\mathcal{E}_k$. However, the CPU cost increases of a factor 10.

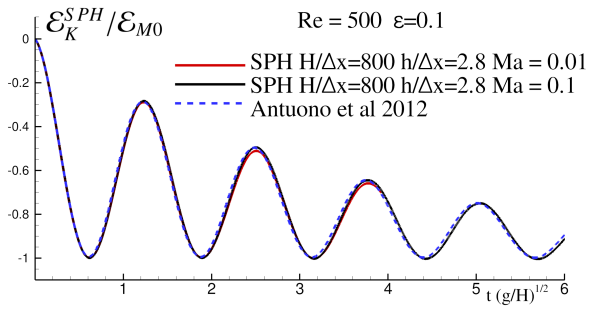

Figure 6.3.: SPH kinetic energy, $\mathcal{E}_K^{SPH}$, as a function of time, for Re=500 and ϵ=0.1. The SPH solution is compared with the analytical one (dashed line).

Differently from the kinetic energy $\mathcal{E}_K$, the potential energy, $\mathcal{E}_P$, is a quantity more sensitive to the fluid compressibility. In the left plot of figure 6.4, the time evolution of the SPH potential energy is depicted using the speed of sound c_{01}; $\mathcal{E}_P^{SPH}$ clearly shows fluctuations due to the acoustic waves propagation. This induces a non negligible change in the particle positions and therefore the gravitational potential. When increasing the speed of sound to c_{02}, these effects are drastically reduced (see the right plot of figure 6.4). The time evolutions of the sum of the gravitational and compressible potential, $(\mathcal{E}_P^{SPH} + \mathcal{E}_C^{SPH})$, present a behaviour very similar to the behaviour of the kinetic energy $\mathcal{E}_K^{SPH}$. This indicates that, in the weakly compressible regime, gravitational and compressible potentials can exchange energy among each other without affecting the global inertial evolution of the flow.

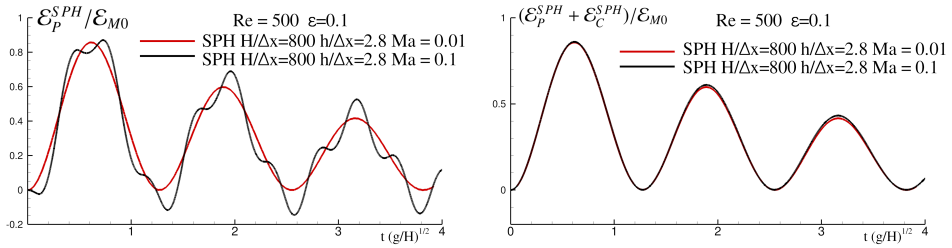

Figure 6.4.: Left: SPH potential energy, $\mathcal{E}_P^{SPH}$, as a function of time for Re=500 and ϵ=0.1 using two different speed of sounds $c_{01} = 10\sqrt{gH}$ and $c_{02} = 100\sqrt{gH}$. Right: time evolutions of the sum $(\mathcal{E}_P^{SPH} + \mathcal{E}_C^{SPH})$ for c_{01} and c_{02}.

6.3 HIGH VISCOSITY & SMALL AMPLITUDE: RE=125, $\epsilon = 0.1$

For this case, the initial energy $\mathcal{E}_{M0}$ is almost dissipated (about 80%), by the viscous effects, in just one oscillation cycle.

Figure 6.5 displays the evolution in time of the kinetic energy $\mathcal{E}_K$ and the dissipation caused by enstrophy $\Delta\mathcal{E}_\omega$. From the analytic solution of Antuono and Colagrossi 2012, in addtion to $\mathcal{E}_K(t)$, the enstrophy term $\Delta\mathcal{E}_\omega(t)$ value is also given. The SPH predictions are in good agreement with the analytical ones. For this case, at the end of the simulation, the dissipation associated with enstrophy amounts to 40% of the total dissipation. It is remarkable that, with a so high viscosity fluid, the free-surface term is still the dominant one.

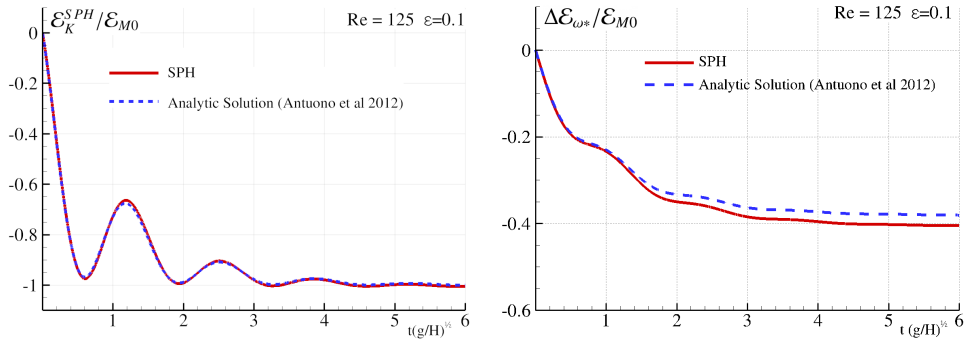

Figure 6.5.: Left: Kinetic energy, $\mathcal{E}_K(t)$ as a function of time for Re=125 ϵ=0.1. Right: Dissipation linked to enstrophy $\Delta\mathcal{E}_\omega(t)$ as a function of time.

6.4 HIGH VISCOSITY & LARGE AMPLITUDE: RE=125, $\epsilon = 0.4$

Snapshots of the vorticity field are pictured in Figure 6.6. Because of the high viscosity, the breaking of the free surface is however inhibited.

The vorticity is generated at the free surface. Indeed, the boundary condition (2.13) requires $\omega = 2\,\partial u_n/\partial \tau$, which remains confined on the free-surface boundary layer and is partially diffused in the interior of the fluid domain during the wave oscillations. During each period, the vorticity intensity decreases due to the mechanical energy dissipation.

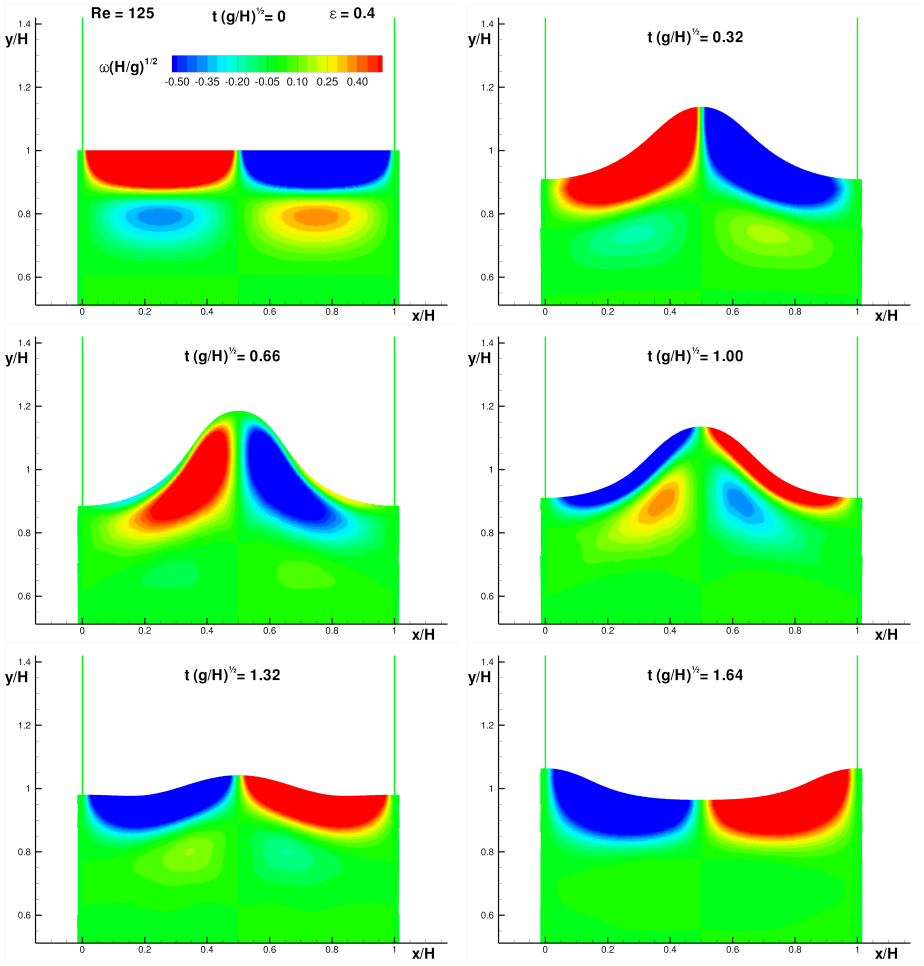

Figure 6.6.: Vorticity field, Re=125, ϵ=0.4.

Compared to the previous low amplitude case, the kinetic energy ratio $\Delta\mathcal{E}_k/\mathcal{E}_{M0}$ presents a slightly less sudden decrease as well as a larger increase in the period of oscillation (left plot of Figure 6.7). Nevertheless, also in this case the initial energy is, to a high extent, dissipated in the first wave oscilla-

tion. The component due to the enstrophy $\Delta\mathcal{E}_\omega/\mathcal{E}_{M0}$ behaves similarly, being slightly larger just during the first cycle (right plot of figure 6.7). These results show that the change in the amplitude, ϵ, has a limited effect on the behaviour of the energy decay. The final value of $\Delta\mathcal{E}_\omega$ is close to 40% of the initial energy $\mathcal{E}_{M0}$ for both amplitude ratios, ϵ, analysed. In next section, it is shown that this is not the case when increasing the Reynolds number because of the breaking wave events.

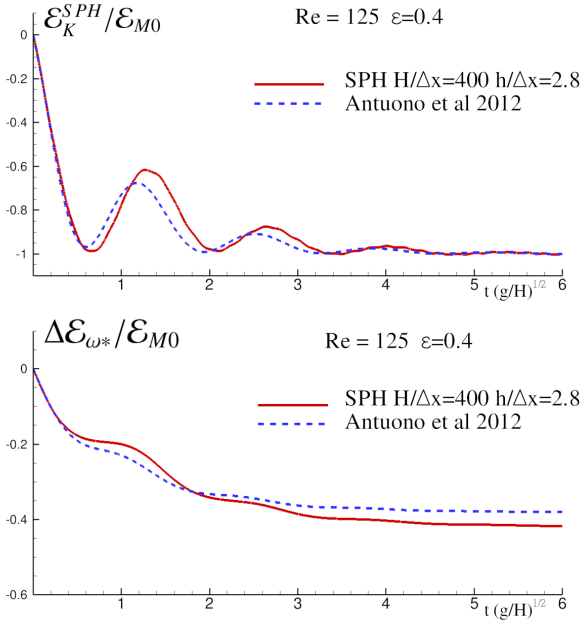

Figure 6.7.: Kinetic energy $\Delta\mathcal{E}_k$ (top) and dissipation term $\Delta\mathcal{E}_\omega$ as a function of time, Re=125, ϵ= 0.4.

The energy term $\Delta\mathcal{E}_{FS}$, evaluated through $\Delta\mathcal{E}_{FS}^{MLS}$, eq. (5.27), and through $\Delta\mathcal{E}_{FS}^{sub}$, eq. (5.28) , is plotted in time in Figure 6.8. The difference between the two plots is around 0.2% in relative terms, which means that the parameters used for the numerical simulations allow to solve in a good way the present test-case.

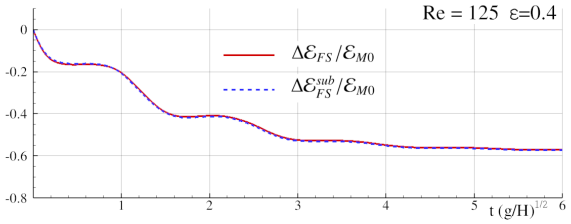

Figure 6.8.: Dissipation through the free surface term, $\Delta\mathcal{E}_{FS}$ as a function of time, Re=125, ϵ=0.4. Direct computation, eq. (5.27), and subtraction, eq. (5.28).

6.5 LOW VISCOSITY & LARGE AMPLITUDE: RE=2000, $\epsilon = 0.4$

For this case, large deformations of the free surface occur. They induce in the first cycle the formation of an overturning wave and a subsequent plunging breaking event. Some snapshots during the time evolution are reported in figure 6.10.

The dissipative enstrophy $\mathcal{P}_{\omega *}$ and free-surface power terms $\mathcal{P}_{FS*}$ are plotted in time on figure 6.9. The time istances of each frame of the figure 6.10 are marked by a vertical dashed line on the lower plot. During the first part of the evolution, the dissipation is maximum at $t(g/H)^{1/2}$ =1.83 and 2.89 when the velocity of the flow is higher, and minimum at $t(g/H)^{1/2}$ =2.22 and 3.72 when the velocity of the flow is the lower. When the plunging jet of the overturning wave reaches the free surface, the free-surface power term $\mathcal{P}_{FS*}$ suddenly increases and shows a peak when the cavity collapses ($t(g/H)^{1/2}$ =4.3). This phenomenon of cavity creation and collapsing is linked with an enstrophy creation and therefore the value of $\mathcal{P}_{\omega *}$ increases.

As a consequence of the change of the dynamic behaviour, the kinetic energy and the enstrophy are not following the solution of Antuono and Colagrossi 2012 any longer as it can be observed in figure 6.11. The dissipation though the free-surface term is not exactly the same following the two methods of calculation, but the time histories are still comparable.

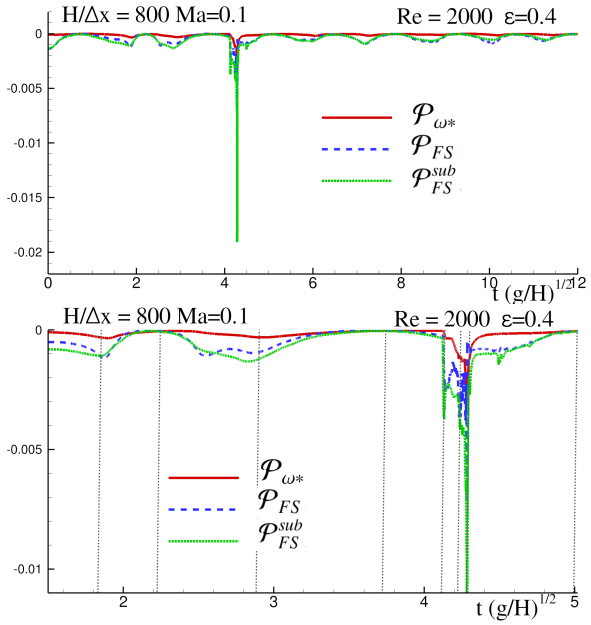

Figure 6.9.: Power relative to dissipation in enstrophy and in the free surface, Re=2000, ϵ=0.4. Vertical dashed lines indicate the time instants of each evolution picture in figure 6.10

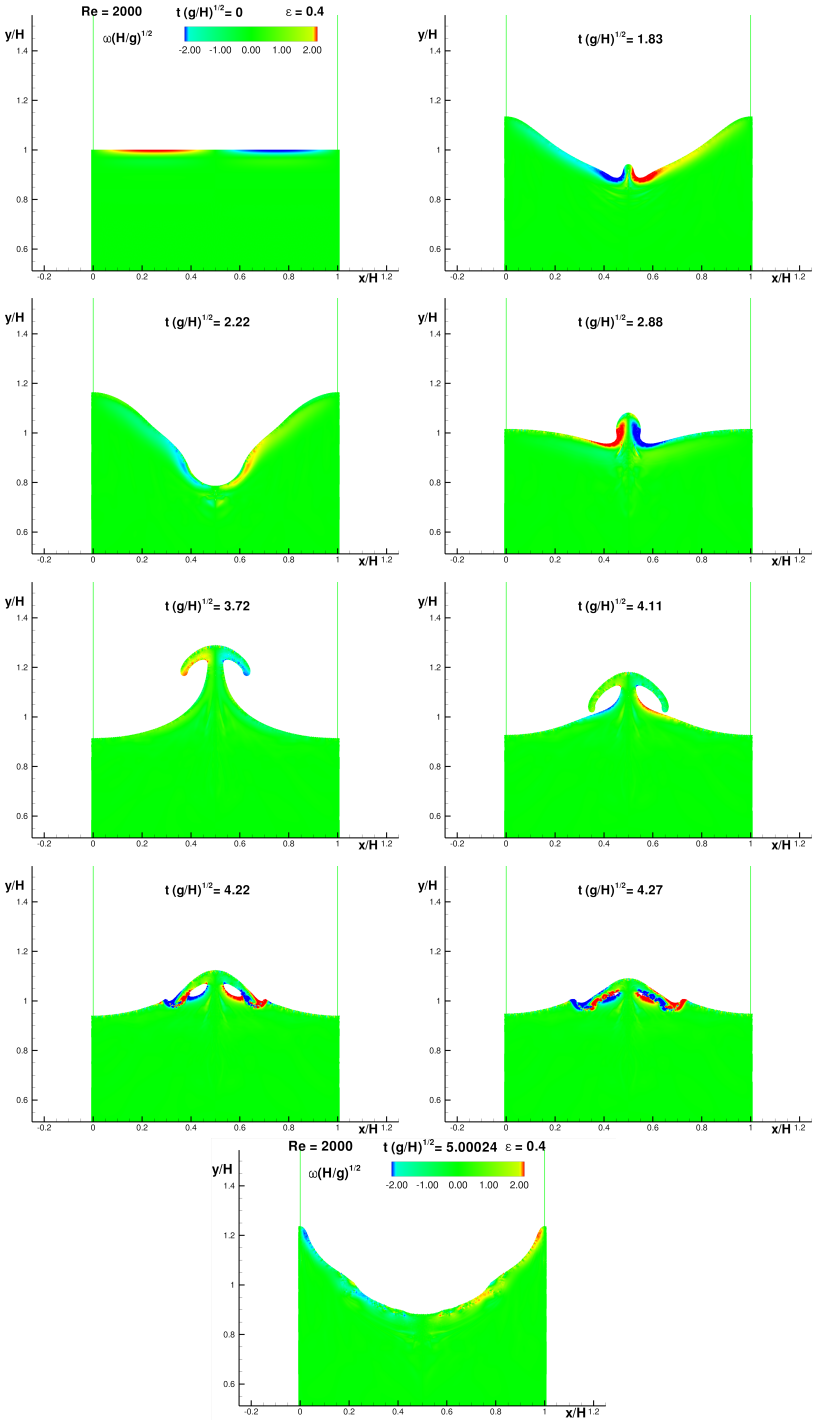

Figure 6.10.: Vorticity field, Re=2000, ϵ=0.4, H/Δx = 800

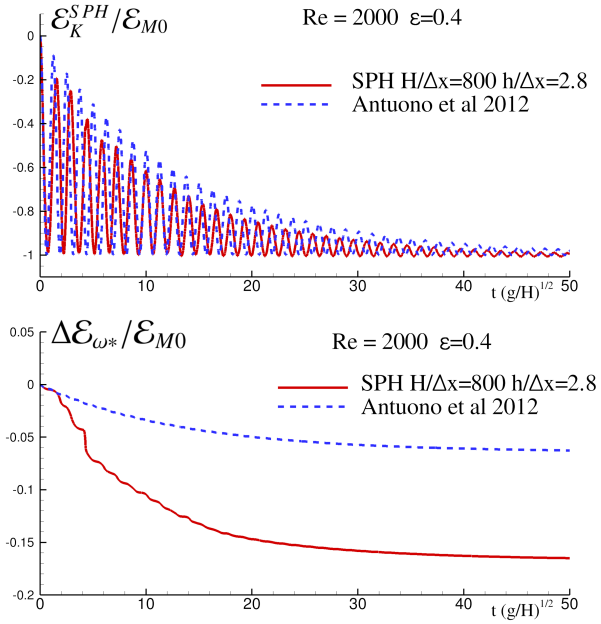

Figure 6.11.: Kinetic energy as a function of time, Re=2000, ϵ=0.4.

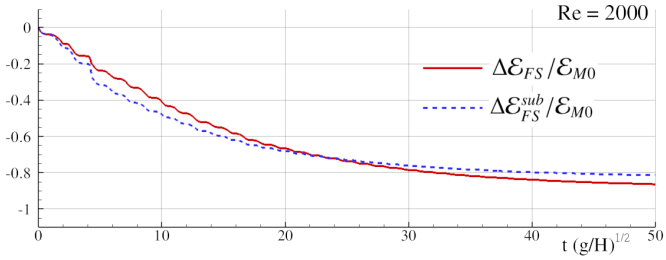

Figure 6.12.: Dissipation through the free-surface term as a function of time, Re=2000, ϵ=0.4.

6.6 SUMMARY OF THE INFLUENCE OF THE REYNOLDS NUMBER AND THE WAVE AMPLITUDE ON THE VISCOUS DISSIPATION

In previous sections, four cases of the test matrix shown in table 6.1 have been discussed in detail, showing how the viscous dissipation distributes between the components $\Delta\mathcal{E}_\omega$ and $\Delta\mathcal{E}_{FS}$. The results of all 20 cases of that matrix are summarised in Figure 6.13, in which $\Delta\mathcal{E}_\omega$, measured at the end of the simulations, is plotted as a function of Reynolds number and wave amplitude. As the wave amplitude is set larger, the enstrophy component of dissipation, in modulus, tends to grow for all Reynolds numbers. However, this increase sees a drastic change for the highest Reynolds, for which large breaking takes place in the first period of oscillation. In this case, the vorticity generated by the cavities collapse induces a large increase of $|\Delta\mathcal{E}_\omega|$.

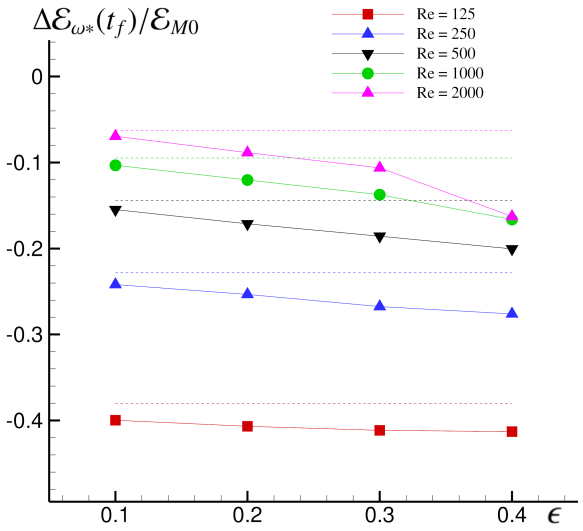

Figure 6.13.: Energy dissipation through enstrophy component $\Delta\mathcal{E}_\omega$ at the end of simulations, varying Re and ϵ. Dashed lines are analytical results from Antuono and Colagrossi 2012.

6.7 DETAILS OF THE FREE-SURFACE TERMS

It has been seen in chapter 3, that $\mathcal{P}_{FS}$ is composed from two distinct terms (see equation 3.29). The equation can be approximated in equation 5.27 of chapter 5 using the MLS interpolation as:

$$\mathcal{P}_{FS}^{MLS} = \mathcal{P}_{Deform\,FS}^{MLS} + \mathcal{P}_{FS\,2\mu E}^{MLS}; \tag{6.2}$$

being the two terms an SPH formulation of their expression at the continuum level:

$$\begin{aligned}\mathcal{P}^{MLS}_{FS\,2\mu E} &:= 2\mu \sum_{k\in FS} \langle \mathrm{div}(\mathbf{u})\rangle^{MLS}_k \mathbf{u}_k \cdot \mathbf{n}_k \Delta S_k\,,\\ \mathcal{P}^{MLS}_{Deform\,FS} &:= -2\mu \sum_{k\in FS} \langle \nabla \mathbf{u}\rangle^{MLS}_k \mathbf{u}_k \cdot \mathbf{n}_k \Delta S_k\,.\end{aligned} \tag{6.3}$$

The first term is null in an incompressible flow and should be retrieved also using the relation 3.24.

$$\mathcal{P}^{MLS}_{F} \approx -\mathcal{P}^{MLS}_{FS\,2\mu E} \tag{6.4}$$

The two terms of the previous expression (one volume integral and one boundary integral) compare well in figure 6.14, for the case Re=500 and ϵ=0.1. This gives an indication that the computation of the compressible term $\mathcal{P}^{(2\mu)E}_{FS}$ is accurate.

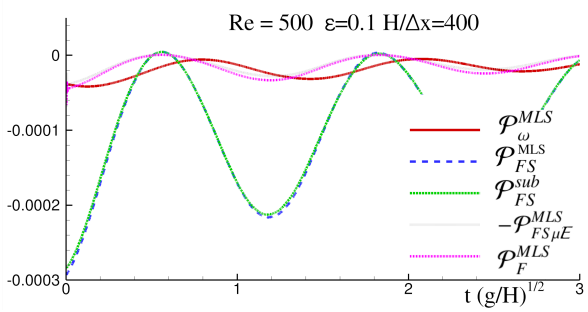

Figure 6.14.: Decomposition of the free surface term relative to dissipation, Re=500, ϵ=0.1. H/Δx=400.

It is interesting to note that the compressible part of the free surface term is smaller than the other term, but its quantity is similar to the enstrophy in this case. The next subsection aims at investigating whether this contribution is lower when increasing the particle resolution and decreasing the Mach number.

6.7.1 Convergence and Mach effect on the compressible dissipative term in the case without breaking

Figure 6.15 shows the differences of both $\mathcal{P}^{MLS}_{FS}$ and $\mathcal{P}_{\omega *}$ when the spatial resolution is varied between $H/\Delta x = 400$ and 800 and $Ma = 0.1$ and 0.01. It appears that the two varying factors induced a very limited effect on the plotted values. The computation seems to be suffienctly resolved. As it can be seen in the third plot of figure 6.15, when the mach number is lower, some unphysical effects are noticed on the enstrophy.

It can be further noticed that the pure compressible part of $\mathcal{P}_{FS}$, plotted on Figure 6.16 using its two equivalent definitions, is not more influenced by

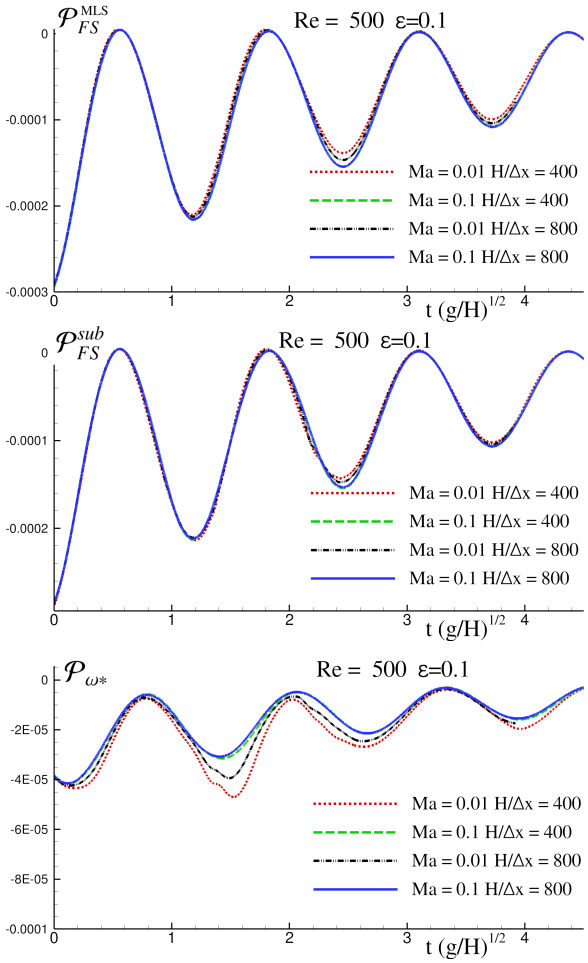

Figure 6.15.: Power relative to dissipation in enstrophy and in the Free Surface, Re=500, ϵ=0.1.

decreasing the Mach number. Indeed, the free-surface compressible term $\mathcal{P}_{2\mu E}^{MLS}$ seems to have reached a convergence value. This aspect would need further investigation.

6.7.2 Convergence and Mach effect on the compressible dissipative term in the case with the overturning wave

Figure 6.17 shows the differences of both $\mathcal{P}_{FS}$ and $\mathcal{P}_{\omega*}$ when the spatial resolution is varied between $H/\Delta x = 400$ and 800 and $Ma = 0.1$ and 0.01. The cavity closure of the overturning wave is shifted in time when the parameters are changed but the free-surface terms do not change its time history features, except that the peak is larger when the Mach number is higher (see the zoom on the right panels of figure 6.17).

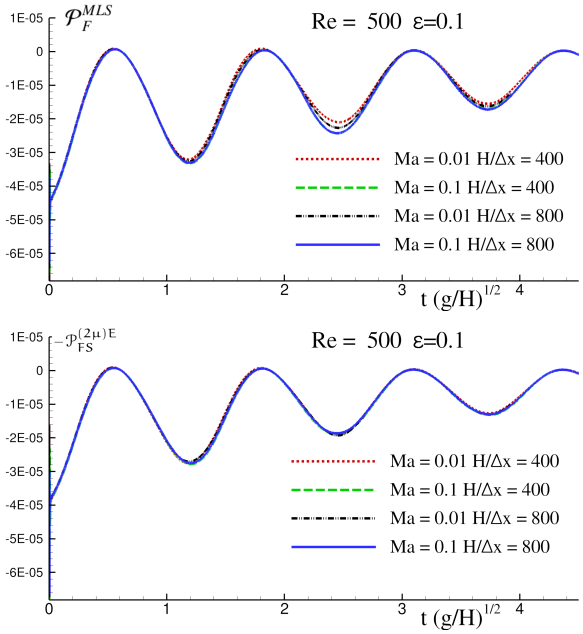

Figure 6.16.: Power relative to Free Surface terms decomposition, Re=500, ϵ=0.1.

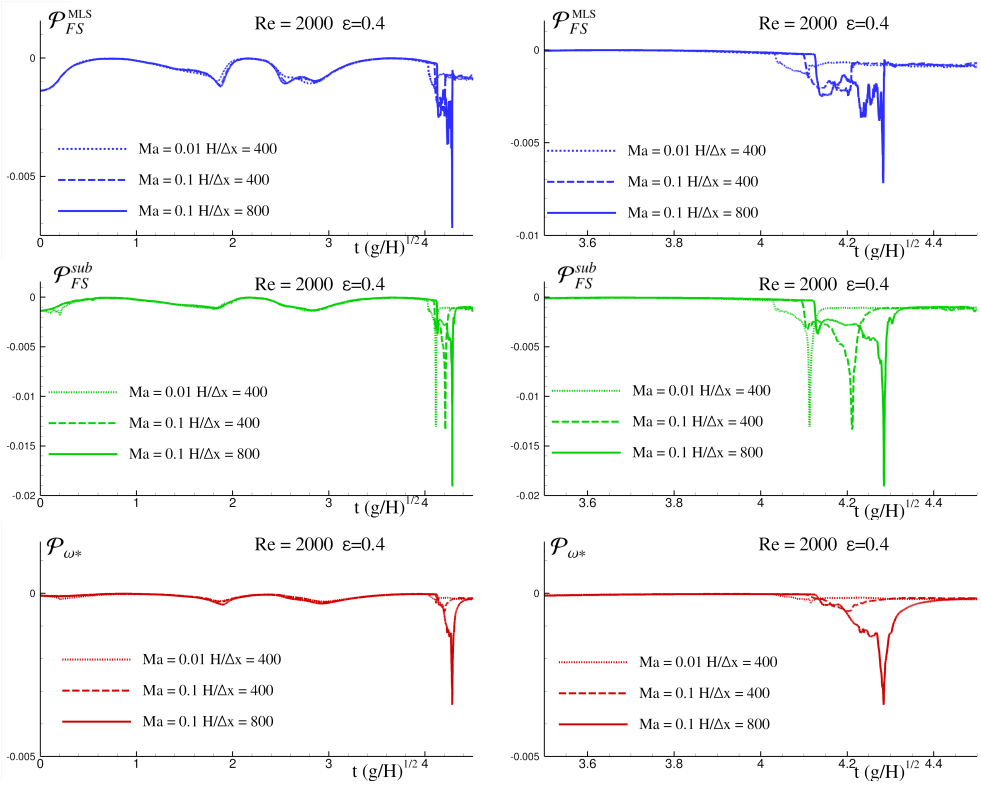

Figure 6.17.: Power relative to dissipation in enstrophy and in the Free Surface, Re=2000, ϵ=0.4.

6.7.3 Check of the balance involving MLS interpolation

As mentioned in section 5.3, some power terms obtained directly from the numerical scheme are expected to differ slightly from the ones obtained with MLS interpolation. The balance shown in equation (5.23) is exposed in table 6.2 for the different conditions. They express how the energy conservation is closed if looking at the terms similarly to what could be done at the continuum level. The SPH method is conservative by itself, but some unphysical behaviour could lead to a misbalance using equations like (5.23).

	Re = 125	250	500	1000	2000
ϵ = 0.1	2.0E-02	1.9E-02	1.4E-02	3.0E-03	-1.8E-02
ϵ = 0.2	1.7E-02	1.2E-02	-1.8E-03	-2.6E-02	-5.4E-02
ϵ = 0.3	1.6E-02	5.8E-03	-1.2E-02	-3.4E-02	-6.3E-02
ϵ = 0.4	1.4E-02	3.9E-03	-1.2E-02	-4.3E-02	-1.3E-01

Table 6.2.: Ratio E_1 obtained with the equation (5.23). ($H/\Delta x$ = 400)

The same balance can be estimated for different particle resolutions for the case with small amplitude ϵ=0.1. As expected the error decreases when the number of particle increases, as it is seen in table 6.3.

$H/\Delta x$	100	200	400	800
E_1	-0.098	-0.064	0.0144	0.0137

Table 6.3.: Ratio E_1 obtained by with the equation (5.23) varying spatial resolution for the case Re=500, ϵ=0.1

For the more energetic case ϵ = 0.4, Re=2000, the balance differs for more than 10%. A higher spatial resolution is necessary (see 6.4). For this condition the results for the spatial discretization $H/\Delta x = 800$ are shown in the next subsections.

$H/\Delta x$	100	200	400	800
E_1	X	X	-1.3E-01	-7.1E-02

Table 6.4.: Ratio E_1 obtained by with the equation (5.23) varying spatial resolution for the case Re=2000, ϵ=0.4

6.7.4 Check of the balance involving free-surface terms

Following the analysis and considerations of section 5.3, the free-surface term $\mathcal{P}_{FS*}$ can be retrieved by a boundary integral with equation (5.27) and by substraction with equation (5.28). The objective of this section is to check the correctness of the two techniques.

The comparison is done using the balance expressed in equation (5.29). The differences are exposed in table 6.5. Globally, the more energetic the flow is, with breakings and high deformation, the less similar the two terms obtained by the two definitions of the free-surface term are.

	Re = 125	250	500	1000	2000
ϵ = 0.1	2.6E-02	1.9E-02	1.1E-02	-1.5E-03	-2.5E-02
ϵ = 0.2	1.8E-02	8.1E-03	-2.9E-03	-1.7E-02	-3.3E-02
ϵ = 0.3	9.8E-03	-5.5E-03	-2.3E-02	-2.9E-04	-1.0E-02
ϵ = 0.4	-2.0E-03	-2.3E-02	-3.0E-02	-2.5E-02	-8.8E-02

Table 6.5.: Difference E_2 between the dissipation given by integration on the boundary and the same value obtained by substraction of volume terms.

The influence of the spatial resolution is presented in table 6.6 and 6.7. For the less energetic case, the accuracy improves largely until $H/\Delta x$=400, until it seems to reach a plateau where the balance is almost achieved. In the most energetic case, the comparaison is more difficult and also the most resoluted case close the balance at 5%. This result is useful to understand the difficulty in correctly evaluating the different dissipative terms in case of a breaking wave.

$H/\Delta x$	100	200	400	800
E_2	-0.14	-0.07	0.011	0.013

Table 6.6.: Ratio E_2 obtained by with the equation (5.29) for the case Re=500, ϵ=0.1. Difference between the dissipation obtained by boundary integration in the free-surface term and by substraction.

$H/\Delta x$	100	200	400	800
E_2	X	X	-8.8E-02	4.9E-02

Table 6.7.: Ratio E_2 obtained by with the equation (5.29) for the case Re=2000, ϵ=0.4. Difference between the dissipation obtained by boundary integration in the free-surface term and by substraction.

7 DAM BREAK FLOWS IN A CONFINED DOMAIN

7.1 DEFINITION OF THE PROBLEM

In this section, a confined Dam Break flow is considered. The problem is a 2D version of the experiment made by Buchner 2002 and recently the same problem has been experimentally studied in Lobovský et al. 2014. This test-case has been extensively used for validations in literature (see *e.g.* Zhou et al. 1999, Colagrossi and Landrini 2003, Ferrari et al. 2009, Marrone et al. 2012). The interested readers may refer to Marrone et al. 2015 for a detailed analysis of the same problem which focus on the physics and consider several numerical methods.

Due to the high Reynolds number of the experiments, a simple free-slip boundary condition - only tangential velocity at the boundary - is usually used to avoid the direct simulation of the boundary layer. Three dimensional effects are not negligible during the splashing stage, so the comparisons are also limited in time when a 2D framework is used.

The sketch of the problem is depicted in Figure 7.1.

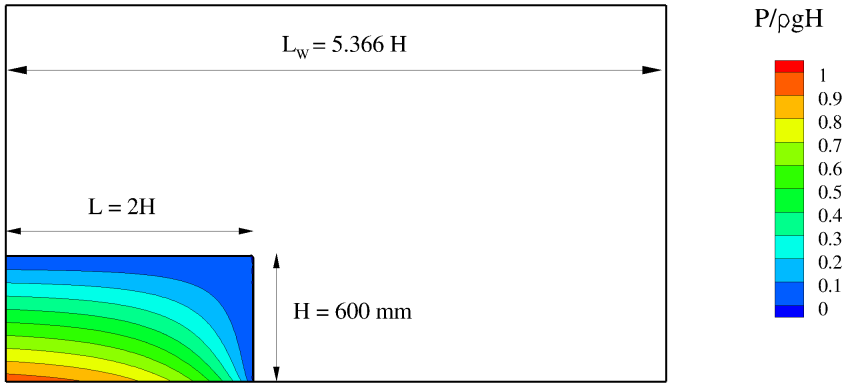

Figure 7.1.: Sketch of the dam-break flow against a vertical wall.

For this dam break case, two Reynolds numbers Re= $\frac{\sqrt{gH}H}{\nu}$ (100,1000) are investigated (with H the initial water height and g the acceleration of gravity).

In this work a no-slip boundary condition - fluid with zero velocity relative to the boundary is imposed on the solid walls to study the effects on the viscous dissipation. A boundary layer is expected to develop along the walls. The

results of a dam break simulation start to be close of the experimental evolution only when using the highest Re and a free-slip condition. It is expected therefore that the simulations performed in this chapter are not similar to the experiments.

7.2 HIGH VISCOSITY, RE=100

The evolution of the case run with Re=100 is pictured in figure 7.2. The larger part of the vorticity is generated on the thick boundary layer. After the fluid patch impacts on the vertical wall, the liquid rises but the viscosity is sufficiently large to impede the creation of an overturning wave. A travelling wave is therefore generated. The end of the simulation is similar to a standard highly viscous shallow water sloshing.

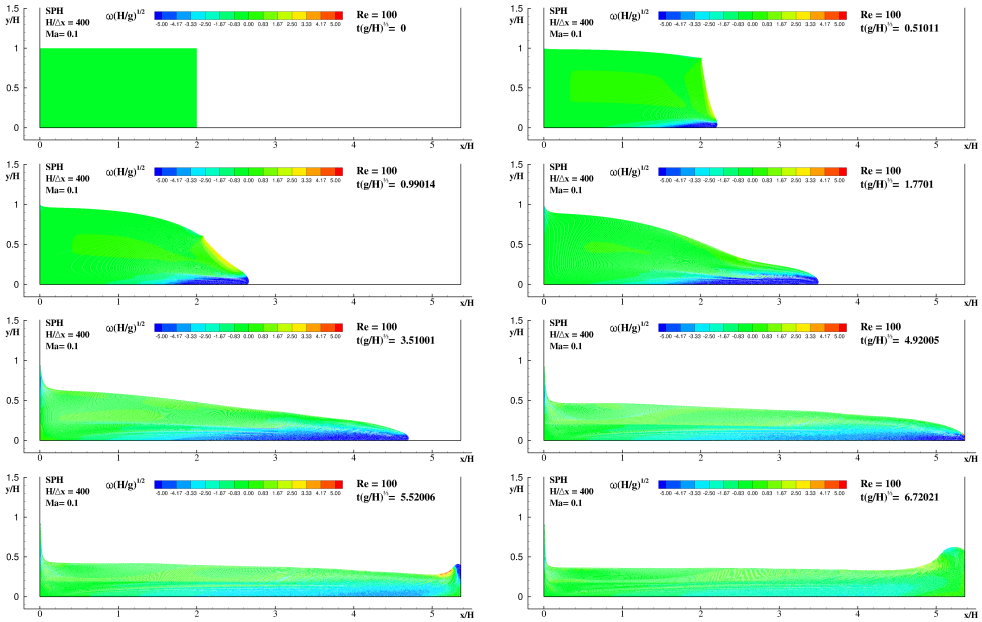

Figure 7.2.: Vorticity field, Re=100, H/Δx = 400

7.2.1 Re=100, Convergence properties of the conservation of energy

A series of simulation is performed increasing the spatial resolution. The convergence properties are monitored for the mechanical energy $\mathcal{E}_M^{SPH}/\mathcal{E}_{M0}$ and the mechanical power in figure 7.3. The differences between the results are easier to notice looking at the results in power. The two cases with the higher spatial resolution are very similar, therefore the convergence is achieved for this case.

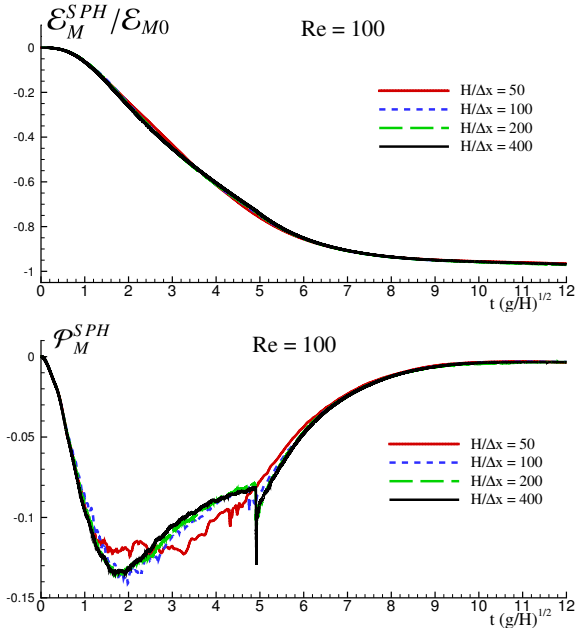

Figure 7.3.: Evolution of the time history of the mechanical energy (left plot), mechanical power (right plot). Re=100. Influence of the spatial resolution

The global balance of the SPH system is shown in figure 7.4, where the mechanical, compressible and dissipative power terms are shown. The sum of the three contributions is null because of the SPH properties (see balance in equation 5.12). As expected, the reversible power term connected to the weakly compressibility is limited.

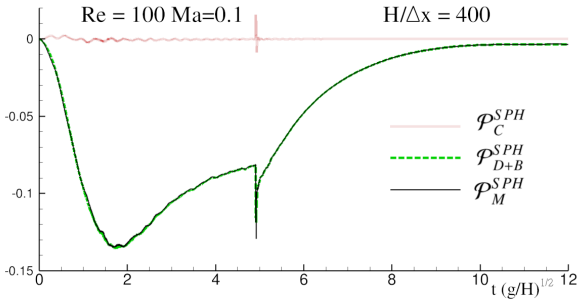

Figure 7.4.: Evolution of the time history of the mechanical power, the compressible power and the total dissipative power. H/Δx = 400, Re=100, Ma=0.1

The balance check is computed using SPH operators. No data MLS interpolation has been necessary. In the follow the dissipative term will be further decomposed.

7.2.2 Convergence of the total dissipation, effect of the ghost fluid, free-surface term

From the energy decomposition of the SPH system, it appeared that the ghost-fluid effect could be separated from the other components. This conducted to express the hypotheses of equation 5.21, which is verified in figure 7.5. The total dissipation of the SPH scheme can be divided in the dissipation $\mathcal{P}_D^{MLS}$ given by the kinematic properties of the solution and $\mathcal{P}_V^{solid}$ that is the effect of the viscous forces from the ghost fluid.

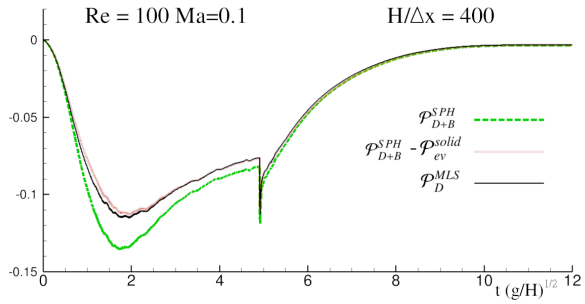

Figure 7.5.: Evolution of the dissipative power terms. $H/\Delta x = 400$, Re=100, Ma=0.1

The term linked to the ghost-fluid $\mathcal{P}_V^{solid}$ is directly linked to the fact that the Dirichlet boundary condition is smoothed close to the wall by the use of the ghost-fluid technique. Its value decreases when the resolution is increased. Figure 7.6 shows that the rate of decreasing is slow. But an interesting feature is given by the bottom plot. The sum of the enstrophy power term and the viscous power given by the ghost fluids $\mathcal{P}_{\omega*}$ converges faster. This means that in a certain sense the dissipative power given by the viscous "ghost" forces is equivalent to the enstrophy that would be originated by the boundary layer.

Relative importance between the dissipation in enstrophy and in the free surface term

Energy balances and convergence properties have been checked, the dissipation is decomposed in enstrophy and Free surface in figure 7.7. Almost all the initial mechanical energy is dissipated in enstrophy. The dissipation linked to the free-surface term is limited proportionaly to the one obtained integrating $\mathcal{P}_{\omega*}$.

7.3 LOW VISCOSITY, RE=1000

When the viscosity is lower, the water goes faster, the impact on the vertical wall is stronger and the water column on the right of the tank evolves in

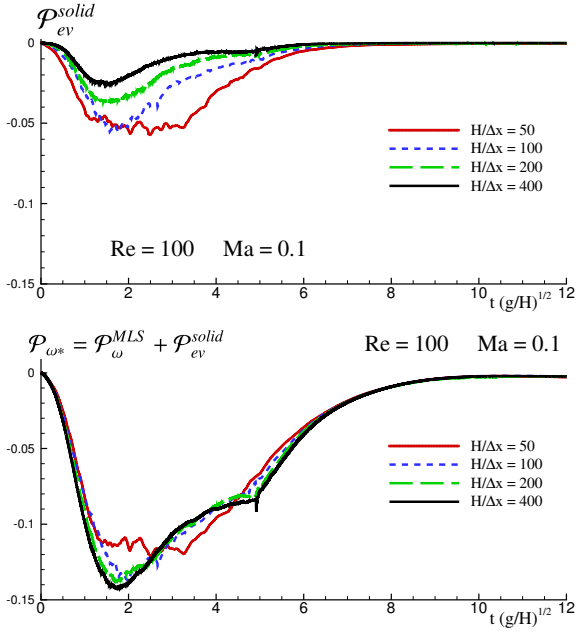

Figure 7.6.: Evolution of the time history of the power from the viscous boundary forces (top) and the viscous boundary forces plus the enstrophy (bottom), increasing the resolution, Re=100.

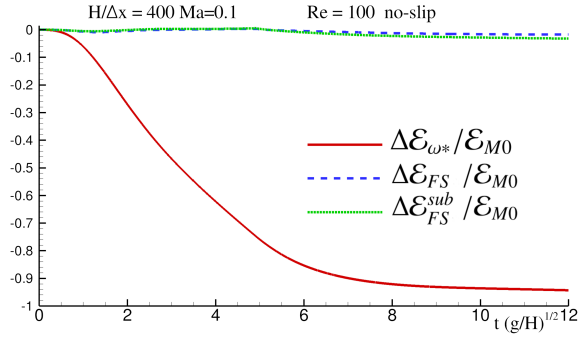

Figure 7.7.: Energy dissipated in enstrophy and by the free-surface deformation, Re=100.

breaking wave with high fragmentation of the free surface. The evolution is plotted in figure 7.8.

The convergence properties of the SPH dissipative term $\mathcal{P}_{D+B}^{SPH}$ are shown in the left plot of figure 7.9. The discussion has to be separated for two phases of the simulation. The convergence of the solution is achieved in the initial part of the simulation and also during the impact on the wall. This property changes when the plunging jet of the overturning wave touches the free surface and creates a cavity ($t(g/H)^{1/2} \approx 6.25$). After this feature the evolution changes with the increasing resolution and it is not possible to achieve a convergence on

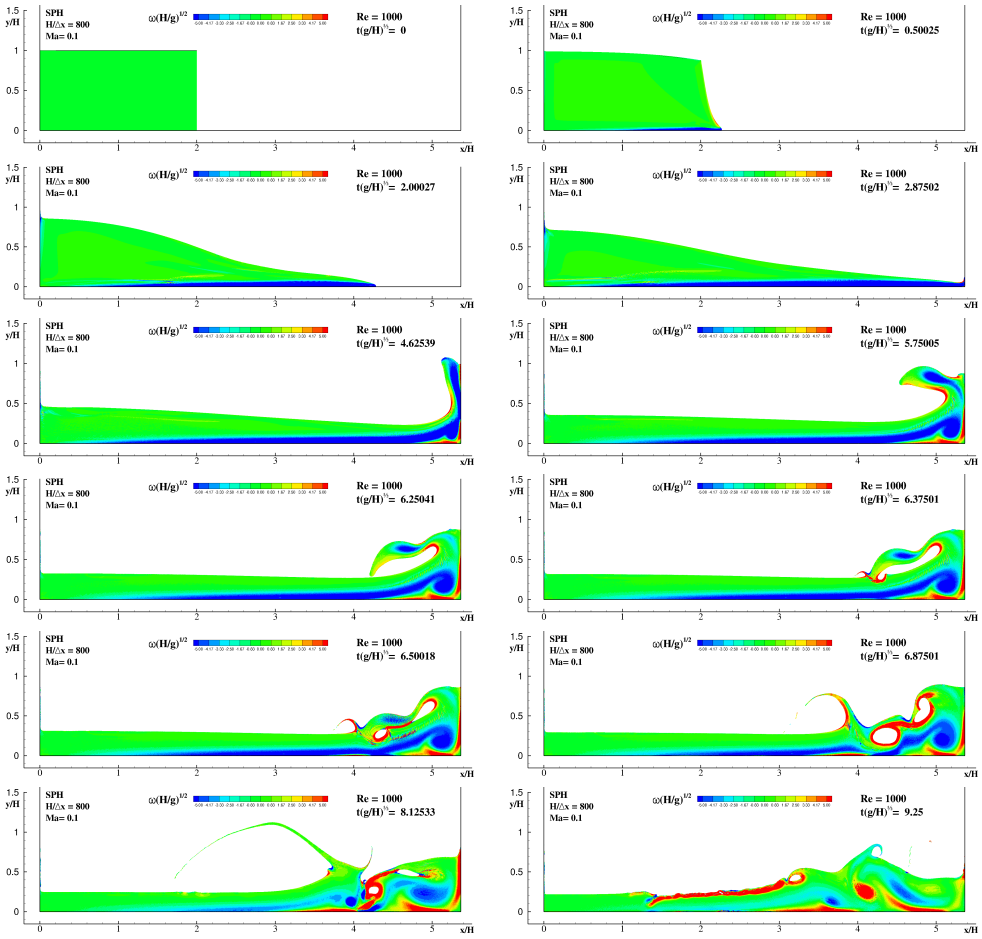

Figure 7.8.: Vorticity field, Re=1000, $H/\Delta x = 800$

the power term. The energy dissipated $\Delta\mathcal{E}^{SPH}_{D+B}/\mathcal{E}_{M0}$ is shown for the various spatial resolutions as shown in the left plot of figure 7.9. It can be observed that the energy dissipated at the end of the breaking stage is the same for all the spatial resolutions.

The convergence on the dissipative power from the boundary viscous forces: $\mathcal{P}_V^{solid}$ and the sum of the dissipative power from those effects and the dissipative power of enstrophy: $\mathcal{P}_{\omega*} = \mathcal{P}_\omega + \mathcal{P}_V^{solid}$ is detailed in figures 7.10.

Similar conclusions to those of the more viscous case can be drawn as for the initial part of the simulation. In this timeframe, the full contribution converges to the same solution. In the second phase, during the breaking events the the differences in the flow evolution induces differences between the various spatial resolutions.

The convergence of the energy dissipated in enstrophy, $\Delta\mathcal{E}_{\omega*}/\mathcal{E}_{M0}$ is shown in figure 7.11. At end of the breaking phase the energy dissipated in enstrophy is very similar for the two highest spatial resolutions.

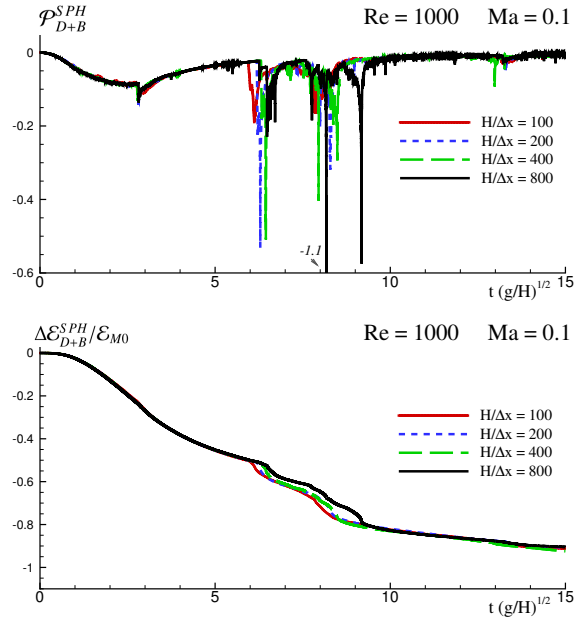

Figure 7.9.: Convergence on the SPH dissipation term, Re=1000.

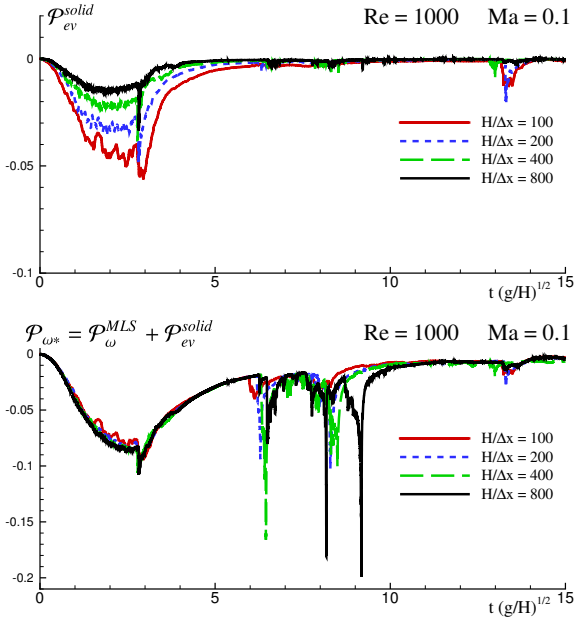

Figure 7.10.: Evolution of the time history of the power from the viscous boundary forces (top) and the viscous boundary forces plus the enstrophy (bottom), increasing the resolution. Re=1000.

Separation of the dissipative terms, free-surface terms

The decomposition in terms of power linked to the free-surface deformation and the enstrophy is shown in figure 7.12 for the higher spatial resolution simulated: $H/\Delta x = 800$. The simulation is still the one presented in figure 7.8.

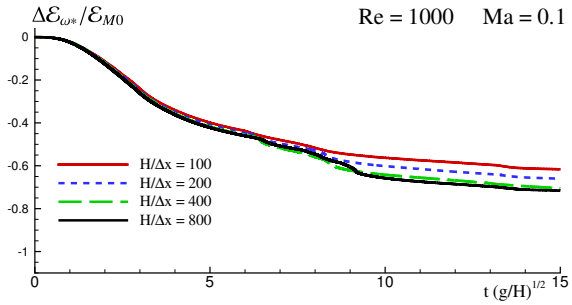

Figure 7.11.: Convergence on the SPH dissipation in enstrophy, Re=1000.

The free-surface role in the total dissipation is proportionaly higher than in the more viscous case Re=100. In the plot showing the dissipative power terms, the vertical lines indicates the time instants of each snapshot of the flow pictured in figure 7.8. The two methods of computing the free surface contribution are giving a very similar result, although the flow is rather complex.

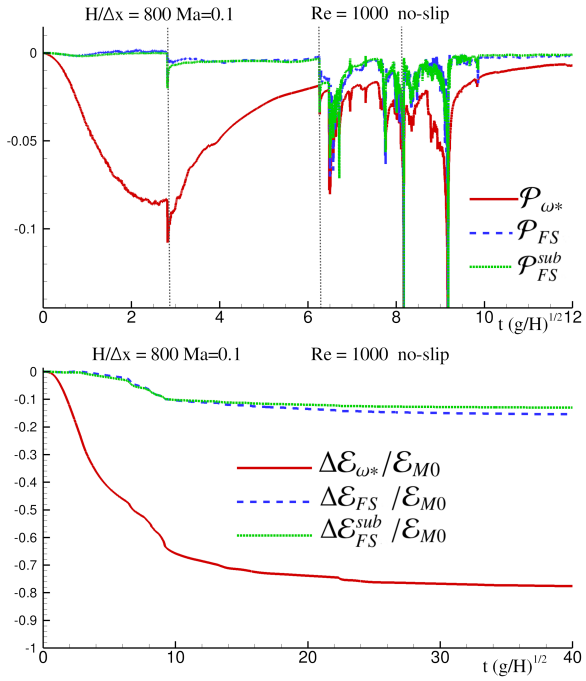

Figure 7.12.: Power and relative energy dissipated in enstrophy and by the free-surface deformation, Re=1000.

7.4 SUMMARY OF THE CHAPTER

The decomposition in energy terms done at continuum and adapted to the SPH model in the previous chapters has been tested on test cases. The results show that the numerical model reproduces accurately the physics if the parameters as the discretization and the Mach number are set to certain levels. The energy loss due to breaking has been divided into a enstrophy and free-surface term. The relative importance of the two contributions have been identified. Finally the effect of the presence of the ghost-fluid has been studied, showing interesting features.

8 NONLINEAR WATER WAVE INTERACTION WITH FLOATING BODIES IN SPH

8.1 INTRODUCTION

In this chapter five different test cases are discussed. The first one deals with a diffraction test in which a fixed body interacts with a regular wave system. For this problem experimental data for the forces and torque acting on the body are available and are used for the validation of the loads on bodies, crucial for the fluid-body coupling algorithm.

The second problem is dedicated to check the capability of the numerical model in maintaining in time the equilibrium of a simple floating body. In particular, it is shown that increasing the number of particles numerical errors on the body motions are reduced.

In the third test case, the robustness of the ghost-fluid technique discussed in section 4.3 is inspected by studying the time evolution of a complex floating body dropped in a water tank. It is also shown that the floating body reaches the correct static equilibrium at the end of the transient stage.

The fourth test deals with a simple floating box with a non uniform mass distribution. At the initial conditions the box is not in equilibrium and, consequently, it starts oscillating for several cycles around its equilibrium position. The convergence of the numerical scheme is measured heuristically and the mechanical energy exchange between the floating box and the fluid is analysed in detail.

In the final test case, the problem of a wave packet interacting with a floating box is studied. For this case the proposed ghost-fluid technique has been validated against experimental data available in the literature.

8.2 DIFFRACTION TEST ON A SEMI-IMMERSED TRIANGULAR BODY

Force and torque equations (4.12) and (4.16) are tested on a diffraction test case based on the experiments of Vugts 1968. The V-shape body is chosen for this test. The setup of the numerical test case is given in figure 8.1. The NWT has to be long enough in order to reach a steady-state oscillatory regime of the forces and moments acting on the shape and avoid spurious reflections at the

end of the tank. The depth has to be more than half wave length in order to simulate deep water waves.

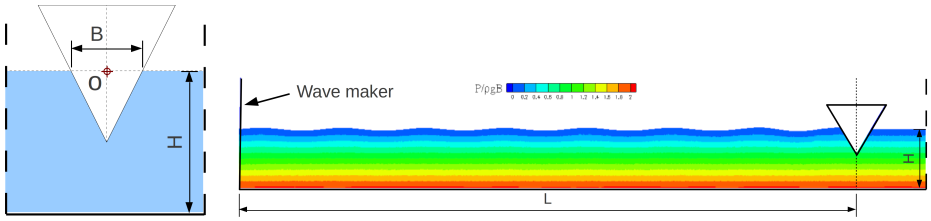

Figure 8.1.: Sketch of the 2D diffraction test case by Vugts 1968.

Seven tests have been done in a wide range of frequencies, namely $2.8 < \lambda < 17$, with $\lambda = 2\pi/k$ being the wave length. The steepness of the generated wave is fixed at $kA = 0.05$ (A being the wave amplitude) but, for the calculus of the non-dimensional results, the effective value of the amplitude/steepness is taken into account. The signals of the force and torque are characterised by quasi-harmonic oscillations over a mean value. Figure 8.2 displays the amplitude of these oscillations for the components of the force and the torque and the comparison with the experiments of Vugts 1968. For what concerns the torque, the V-Shaped body gives rise to an asymmetric oscillation at $kA = 0.05$. In this case, the value reported in figure 8.2 corresponds to the maximum displacement with respect to the mean value.

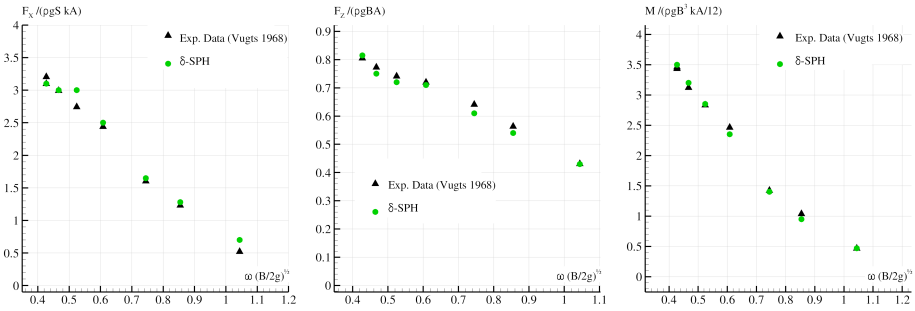

Figure 8.2.: Amplitude of the oscillations of the wave forces and torque for the diffraction test case: sway (left), heave (centre) and roll motion (right).

The overall agreement is fair though some discrepancies can be noticed. As a further check, an inspection of nonlinear effects on the V-shaped body would be necessary. However, in the experiments of Vugts 1968, the steepness of the incoming wave is not accurately documented.

8.3 FLOATING BODY IN REST CONDITION

The aim of this case is to check the stability of a 2D square initially floating in a tank in static equilibrium. The centre of gravity G of the body is the centre of the geometric figure. The body is a 2D box of breadth 0.8L and height 0.4L. The tank is large $L_{tank} = 5L$ and the filling height is fixed to $H_{tank} = 0.7L$. This trivial floating test is used to verify the stability of the algorithm, since the floating condition at rest generally spurs the development of instabilities, especially close to corners. Furthermore, it often represents the first part of a simulation involving water waves generated in a tank. Indeed, the box has to hold steady before the first wave comes.

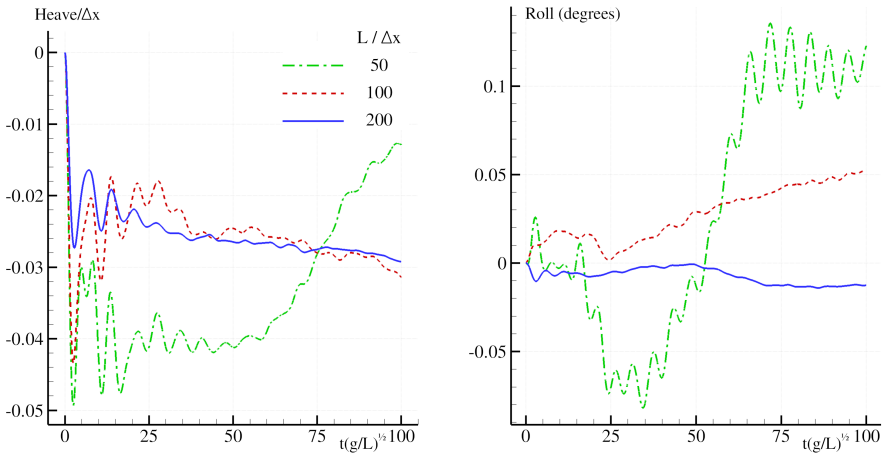

Figure 8.3.: Stability of 2D box at equilibrium in buoyancy condition: heave (left) and roll motion (right)

.

The results are shown in figure 8.3 for three discretizations. The vertical displacement shows a maximum of order $\mathcal{O}(\Delta x)$ (comparable with the spacing between particles) that is acceptable. For the roll motion, the spurious motion is of order 0.1 degrees for the coarser particles distribution and reduces by increasing the spatial resolution.

8.4 DROP OF A COMPLEX FLOATING BODY IN A WATER TANK

In this section, a floating body characterised by a complex 2D geometry is considered. The geometry, together with the axis and the origin are depicted in the left upper plot of figure 8.4 for the initial condition. The body surface presents no symmetry planes and is composed by different curved patches (both concave and convex) that connect twelve corners. The mass of the body

has been set equal to $M = 0.1483\rho L^2$ (where ρ is density of the fluid). The center of gravity, G, is positioned in the forward part of the body and its coordinates are $G = [0.2683L, 0.4352L]$ in the system indicated in figure 8.4. The moment of inertia with respect to G is $I_G = 0.01\rho L^4$. The Reynolds number (namely, $Re = L\sqrt{gL}/\nu$) is equal to 2000.

The chosen values of G and M ensure that only one stable equilibrium configuration exists. With respect to the initial configuration, this corresponds to a counter-clockwise rotation of 97.7 degrees around G and an immersion of the center of gravity equal to 0.5098L below the free surface.

Starting from the initial condition, the body is dropped with zero velocity. Under the action of the gravity a complex water entry stage occurs (see plot upper plots of figure 8.4). After that, the body quickly rotates and sinks. In

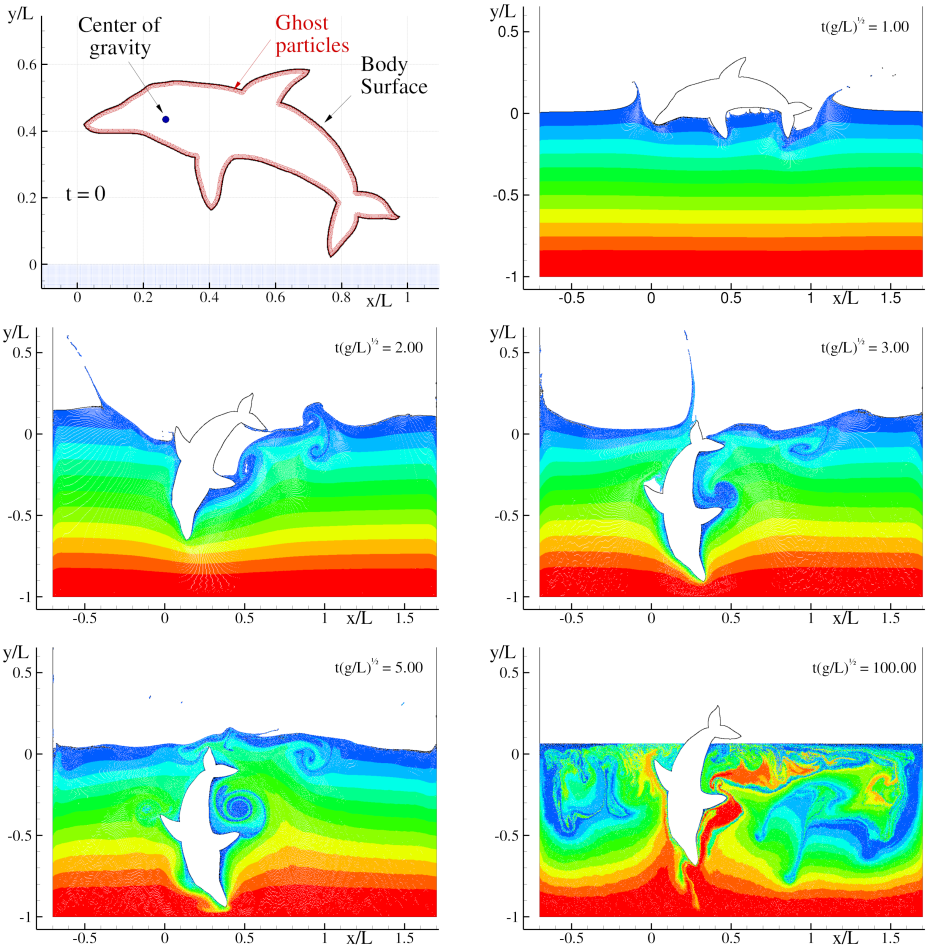

Figure 8.4.: Snapshots of the evolution of a complex floating body dropped in a water tank. The geometric details of the floating body are reported on the left upper plot. The particles are coloured according to their initial vertical positions.

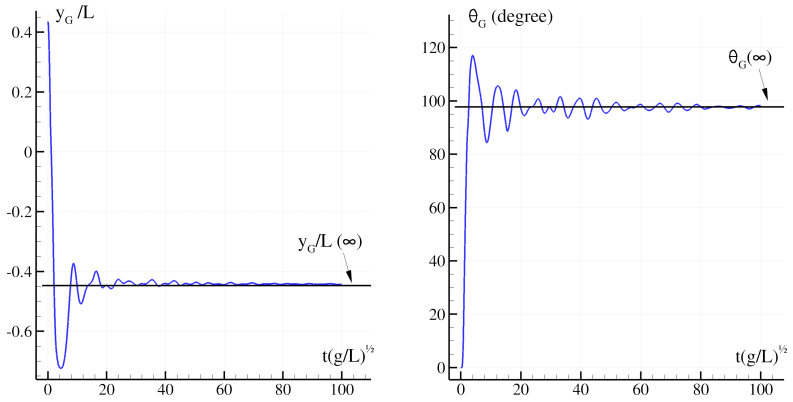

Figure 8.5.: complex floating body dropped in a water tank. Left: time history of the vertical position of the centre of gravity G (left) and of the rotation around it (right).

the meanwhile, an energetic wave motion takes place inside the tank (middle plots of figure 8.4). Due to the low viscosity adopted, the fluid motion is slowly damped in time (lower plots of of figure 8.4). At $t = 100\sqrt{L/g}$ the fluid and the body are almost at rest condition. The time histories of the vertical position of G, y_G, and of the angle of rotation, θ_b, are reported in figure 8.5. These plots show that the present numerical scheme is able to reach the correct equilibrium after a complex fluid-body interaction.

8.5 OSCILLATING FLOATING BOX: CONVERGENCE TESTS AND ENERGY CONSERVATION

In this section the long time evolution of a simple 2D floating box is studied in detail. The sketch of the problem is depicted in figure 8.6. The water tank

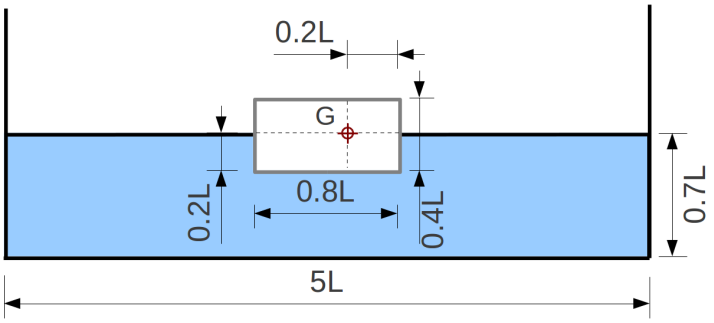

Figure 8.6.: Sketch of the 2D test case with a freely floating box with a non symmetric mass distribution.

has a total length of 5L while the box is $0.8L \times 0.4L$. The centre of gravity, G, is

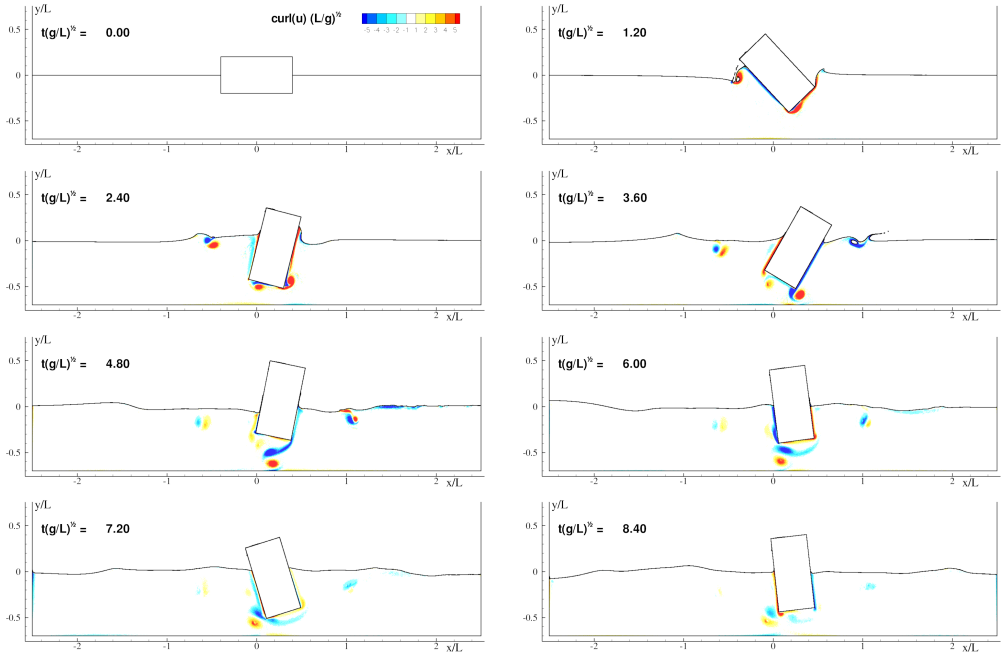

Figure 8.7.: Time evolution of the vorticity field for an oscillating floating box in a water tank ($L/\Delta x = 800$).

shifted horizontally by 0.2L and, therefore, the box is not in equilibrium in the initial condition. The filling height, H, is equal to 0.7L. Consequently, the tank bottom induces a relevant effect on the box motion, as well as on the wave radiated.

The mass of the box M is set equal to $M = 0.16\rho L^2$ (ρ is the fluid density), the momentum of inertia with respect G is $I_G = 0.01072\rho L^2$ and the Reynolds number is 5000. Because of the large value of Re, a very fine spatial resolution is needed to correctly capture the whole vortical structures developed during the evolution. Specifically, three spatial resolutions are adopted (namely, $L/\Delta x = 100, 200, 400$) to simulate a time evolution up to $t = 80\sqrt{L/g}$. A fourth test with $L/\Delta x = 800$ is performed but only for the first $20\sqrt{L/g}$ seconds. This fine spatial resolution requires 2 millions of particles and is used to show the evolution of the vorticity field in the first stage.

The whole time evolution is driven by the initial potential energy of the body and the box. During the motion this is dissipated and converted into internal energy by the viscous forces. After the fluid and the body motions are extinguished, the box reaches the unique stable configuration, that is the vertical position with centre of gravity immersed by 0.2L under the free surface. In such configuration the variation of the potential energy of the box and the fluid is respectively $\Delta E_p^{fluid} = 0.1MgL$ and $\Delta E_p^{solid} = -0.2MgL$. Then, the whole dynamical system (i.e. body and fluid) dissipates an energy equal to $0.1\,MgL$.

Figure 8.7 shows some snapshots of the time evolution with $L/\Delta x = 800$ (the colours indicate the intensity of the vorticity field). At the beginning of the simulation, the box starts rotating and, consequently, sheds vortexes from the corners and irradiates waves that propagate back and forth. The vortical structures interact with the bottom, with the free surface, and couple in dipole structures moving in the fluid domain.

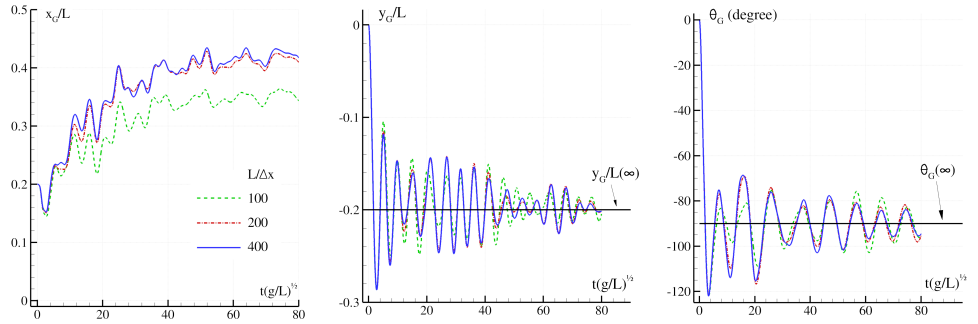

Figure 8.8.: Time evolution of a floating box in a water tank. Left: sway motion of the centre of gravity, x_G. Middle: heave motion, y_G. Right: roll angle around G, θ_b.

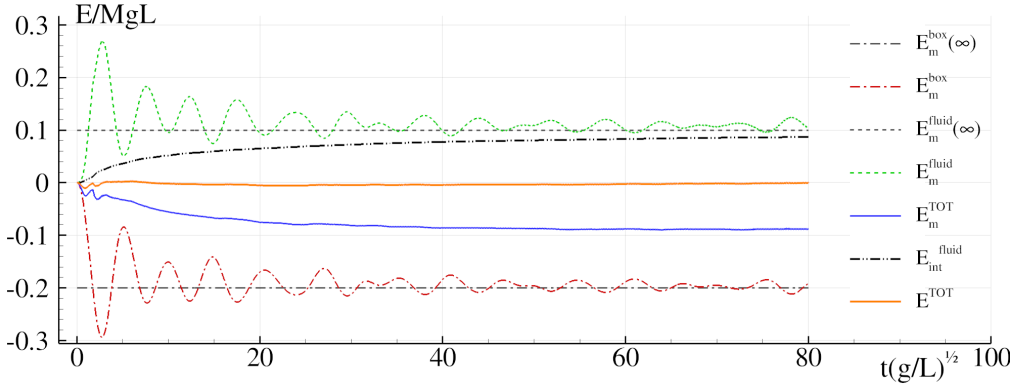

Figure 8.9.: Time evolution of a floating box in a water tank: mechanical energy of the fluid (E_m^{fluid}, dashed line), of the floating body (E_m^{box}, dash-dotted line) and of the internal energy of the fluid (E_{int}^{fluid}).

Figure 8.8 shows the time histories of the floating box motion in its three degrees of freedom. The results are obtained by using three different spatial resolutions, namely $L/\Delta x = 100, 200, 400$. The results of Figure 8.8 show that the data obtained with the highest resolution reach convergence. The time series $y_G(t)$ and $\theta_b(t)$ of figure 8.8 are used to evaluate, in L_2 norm, the distance between the results obtained with the different resolutions. The convergence rate lays between 1 and 2. This is the usual convergence rate for the δ-SPH model (see *e.g.* Antuono et al. 2010, Antuono et al. 2011, Marrone et al. 2011b) and shows that the coupling with a rigid body dynamics does not alter such a feature of the numerical scheme.

Finally, an analysis of the different energy contributions of the fluid-body system is performed. Figure 8.9 shows the time evolution of the mechanical energy of the body, E_m^{box}, and of the fluid, E_m^{fluid}. Part of E_m^{box} is initially transferred to the fluid, inducing an increase of E_m^{fluid}, while the total mechanical energy of the fluid-box system, that is $E_m^{TOT} = E_m^{box} + E_m^{fluid}$, decreasing under the action of the viscous forces. The total energy of the system, i.e. $E^{TOT} = E_{int}^{fluid} + E_m^{TOT}$, should be zero since no external force is doing work on the fluid-box system. Figure 8.9 shows that the total energy evaluated by the present model oscillates around zero but the amplitude of the oscillations is very small. This means that errors are generally very small and proves the accuracy of the body-fluid interaction model.

8.6 WAVE PACKET INTERACTING WITH A FLOATING BODY

In Hadžić et al. 2005 a detailed study of a floating body subjected to a wave packet was carried out. In particular, experimental data were obtained in a small towing tank of the Berlin University of Technology. The body was a rectangular prism 10cm wide, 5cm high and 29cm long, with density relative to water being 0.68. The body was located at $x = 2.11m$ away from the wavemaker, whose motion was controlled to produce a wave packet with a focusing point at the original location of the body. Because of the long transversal dimension of the prism, the experiments can be regarded as two-dimensional. The time history of the three degrees-of-freedom were recorded during the interactions with the wave packet. A sketch of the problem is depicted in figure 8.10. The mass of the body is 0.986Kg while the moment of inertia is $14\,Kg \cdot cm^2$ (the body is an aluminium box).

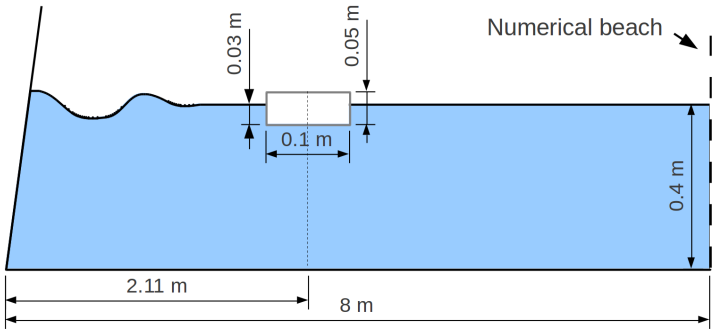

Figure 8.10.: 2D sketch of the freely floating box interacting with a wave packet).

Figure 8.11 shows the time history of the flap wavemaker angle used to generate the wave packet. This experimental condition is appropriate to validate the SPH capabilities in correctly reproducing the motion forced by the wave packet. At the focusing point the wave packet is quite steep and has a

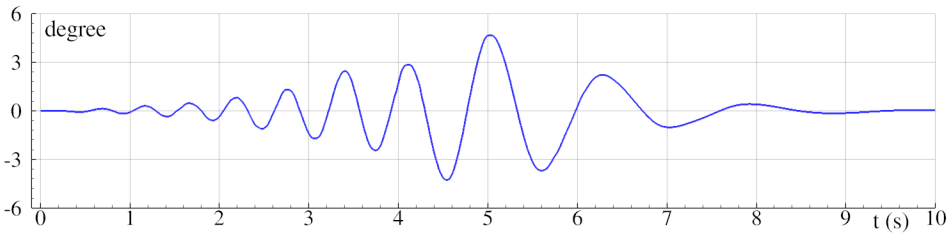

Figure 8.11.: Time history of the flap wavemaker angle used for the generation of a wave packet.

height equal to the body. Then, a nonlinear behaviour is observed in both the resulting wave evolution and the body motion.

In Antuono et al. 2011 the present δ-SPH scheme was already validated on the generation and propagation of wave packets. In that work, it was also pointed out that the ratio between the wave amplitude and the particle size, $A/\Delta x$, has to be of order of 10 to avoid overdamping. In the present test case the resolution adopted is $A/\Delta x = 40$, that is, sufficient to correctly model the wave packet in the numerical tank.

During the experiments the wave elevation was recorded by two fixed probes at $x = 1.65m$ and $x = 2.66m$ (see figure 8.13). Figure 8.12 shows the comparison between SPH and the time histories of the two wave elevations recorded, confirming the correct generation/propagation of the wave packet.

Two snapshots of the free-surface deformation and the position of the floating body at time $t = 7.2s$ and $t = 7.54s$ are depicted in figure 8.13. The comparison with the two experimental pictures shows a good matching between the SPH solution and the experiments during the interaction between the wave packet and the floating body. The comparison of the time histories of the floating motions is shown in figure 8.14.

8.7 SUMMARY OF THIS CHAPTER

A SPH solver has been developed for applications in the framework of NWT (Numerical Wave Tanks) and floating bodies. To this aim, a complete algorithm able to compute viscous and fully-coupled Fluid-Solid interactions has been described.

No-slip boundary conditions on the solid surface are enforced through a ghost-fluid technique. For the problems considered, the intersection between the free surface and the solid profile has to be carefully addressed. The assessment of loads acting on bodies is validated through a difficult diffraction test case with satisfactory results.

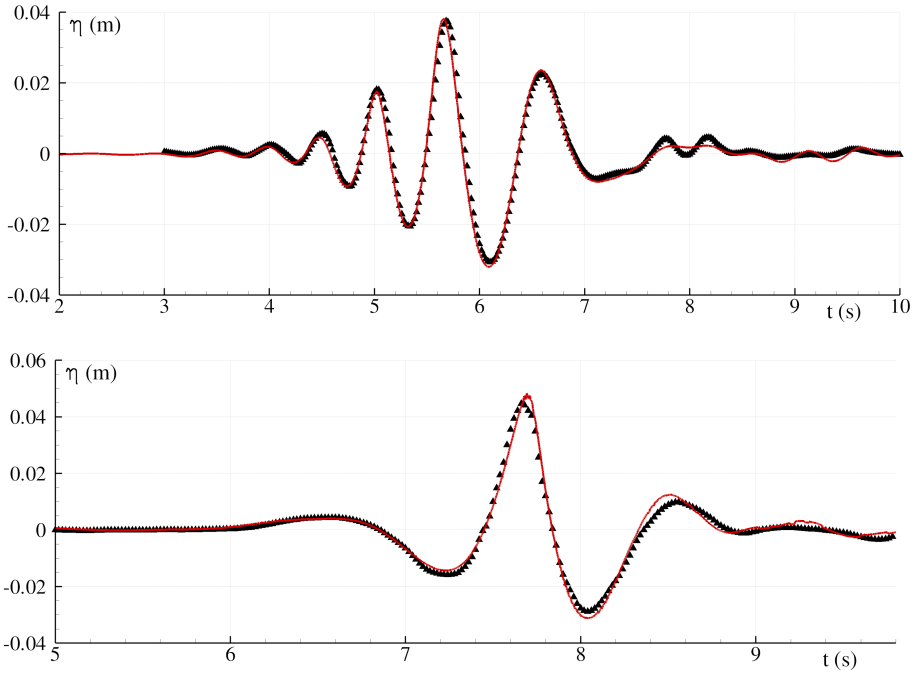

Figure 8.12.: Time histories of the wave elevation during the evolution of the wave packet (SPH, solid line; experimental data, ▲). Top: $x = 1.65m$. Bottom $x = 2.66m$.

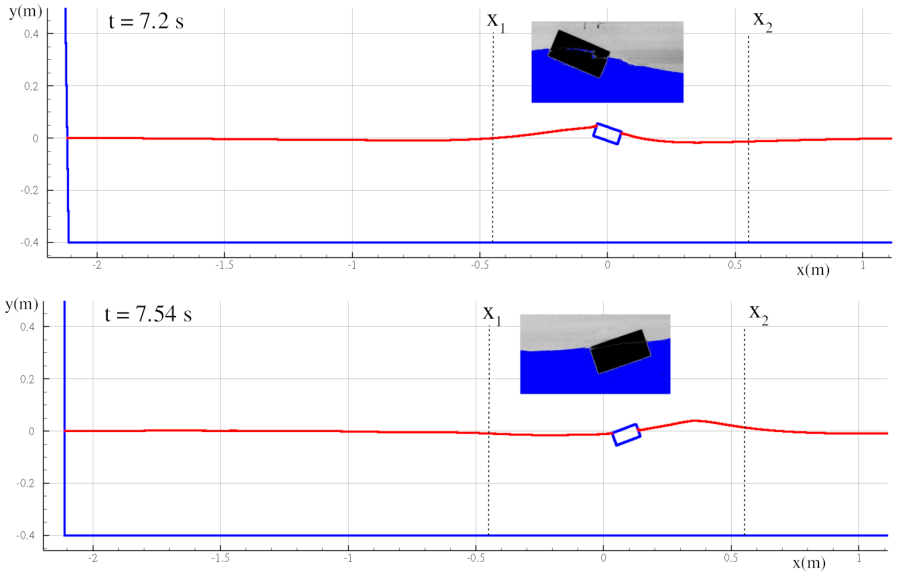

Figure 8.13.: Free-surface deformation and position the floating body at $t = 7.2s$ (top) and $t = 7.54s$ (bottom). Pictures of the experiments are reported on the top part of the plots. The wave probes positions x_1 and x_2 are also reported.

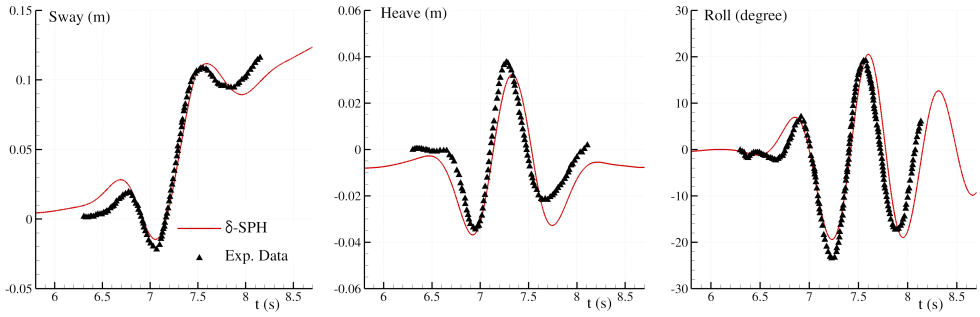

Figure 8.14.: Time histories of the floating body motions during the interaction with the wave packet (SPH, solid line; experimental data, ▲).

Stability, convergence and conservation properties of an explicit synchronous algorithm for the full coupling between fluid and rigid bodiesare tested on several freely-floating test cases and a final validation of the full algorithm is performed for the interaction between a 2D box and an incoming wave packet.

Part IV

PHYSICAL INVESTIGATIONS

9 FLOW PAST A CIRCULAR CYLINDER CLOSE TO A FREE SURFACE

9.1 INTRODUCTION

The flow past a submerged cylinder is an old challenge in hydrodynamics. First treated as an inviscid problem in the first part of the 20th century, Havelock was able, in a series of articles starting with Havelock 1927, to construct a complete formal solution to the linear problem and to find an expression for the lift and drag dependence on submergence and Froude number. The linear problem was later treated in a more satisfactory way by Wehausen and Laitone 1960. According to Tuck 1965, who presented a higher order solution, linearising the problem is acceptable only if the cylinder is at a deep submergence level compared with its own dimensions. Clearly in this case also the body will produce small waves merely because it is a relatively distant disturbance. There is a substantial body of work done on non-linear free-surface potential flows around a cylinder or an obstacle (see e.g. Vanden-Broeck 1987). In particular, Scullen and Tuck 1995; Scullen 1998 showed that they had convergence problems with their non-linear solver at certain Froude numbers (≈ 0.7) when the cylinder got close to the free surface.

In real engineering problems there is a prevalence of viscosity effects and wave-breaking. The potential flow assumption is not applicable. There are engineering problems of large interest in the offshore industry where the forces on cylinders are crucial, in particular those in which vortex-induced-vibrations (VIV) occur Williamson and Govardhan 2004. VIV can also be used for energy generation, with miniature and mid-size electric power generators currently under development Ding et al. 2013; Nguyen et al. 2013. The flow dynamics of horizontal cylinders in currents and waves is also relevant for the problem of oil spill containment with mechanical barriers (Amini et al. 2008; Wicks 1969).

Miyata et al. 1990 did seminal experimental and numerical work on the topic. They were able to measure how decreasing depth can induce a reduction in drag and an increase in lift forces acting on the cylinder. The Froude numbers (when not otherwise specified, the Froude number refers to the diameter) of their experiments (≈ 0.24) are lower than the ones considered in later literature, which makes their research more likely to be relevant for applications more focused on such low speed regimes. Carberry 2002 carried out experiments at fixed intermediate Froude (0.167) and moderate Reynolds (2100) numbers. The deformation of the free-surface is in this case very limited, and he could identify three flow modes depending on the cylinder submergence ratio. Each

mode is characterised by a certain combination of lift time history pattern and mean and instantaneous vorticity fields. Considering the range of Froude numbers treated in this research, it will be later seen that the flow taxonomy is going to be substantially more complex.

Sheridan et al. 1995, 1997 studied experimentally the vorticity patterns in the wake downstream cylinders close to a free surface at moderately large Reynolds numbers (6000-9000) and Froude numbers (0.47-0.72). They described the presence of what they called metastable modes, meaning that two states in the wake are possible: in the first state, a jet is generated on the free surface, above the cylinder, which remains parallel to the free surface. In the second state, the most frequent, the jet is projected downwards into the bulk of the cylinder rear flow, interacting with the negative vorticity later generated at the top of the cylinder. The transition between the two states occurs with characteristic times much longer than those associated with the von Kármán shedding.

Prof. Bernitsas and his group have been investigating the flow behind horizontally submerged cylinders with the aim, as mentioned earlier, of using it to generate electrical power. In Ding et al. 2013 they documented numerical work conducted in deep water conditions using a finite volume solver. However, the flow around the cylinder becomes a more challenging problem as the cylinder gets closer to the free surface.

Using the commercial package FLUENT, Reichl et al. 2005 computed the flow around submerged cylinders at low Reynolds number (180), with Froude numbers equal or smaller than 0.6, and with submergence ratios between 2.5 and 0.1. They compared their simulations with the experiments by Sheridan et al. 1995, 1997. Even with different Reynolds numbers, Reichl et al. 2005 found that the shedding patterns depended more on the submergence ratio and Froude number than on viscous effects. As a matter of fact, Reichl et al. 2001; Reichl et al. 2003 had previously found phenomena that strongly resembled Sheridan et al. 1995, 1997 metastable flows and which occurred, in their simulations, at Reynolds numbers around 40 times lower than in Sheridan et al. 1995, 1997 experiments.

FLUENT uses Volume of Fluid (VOF) technique to track the free surface. This interface capturing technique can exhibit excessive diffusion when the free surface becomes fragmented, as it is the case when the cylinder gets close to, or intersects, the free surface. In addition, with a Eulerian technique, such as Fluent's finite volume, the investigation of mixing and transport properties of the flow is not straightforward. Performing a numerical investigation with a less diffusive Lagrangian technique thus becomes interesting.

The Smoothed Particle Hydrodynamics method presented in the previous chapters is the numerical model that has been used to perform the simulations in the present research.

In all the cited literature, the cylinder is completely submerged. The dynamics of partially submerged cylinders is also interesting and was treated by Triantafyllou and Dimas 1989 who discussed the stabilising effect of the free surface on the wake of partially submerged cylinders. Due to the nature of their analysis they considered some restrictive assumptions, the main one being that the free surface remains flat during the evolution of the instabilities. They were able to predict that the von Kármán type vortex shedding, though blocked at intermediate Froude numbers, is again the prevalent instability above a certain Froude number. The numerical technique used in the present work allows to verify their prediction without such a restrictive assumption on the free surface. Dimas 1998; Dimas and Triantafyllou 1994 also investigated more general cases, introducing a given initial shear flow and following its evolution over time with Euler equations and a with single-valued free surface model.

Considering this literature analysis, the following questions will be investigated in the present chapter:

(1) Extend existing knowledge by computing and analyzing larger Froude numbers and lower and negative submergences cases.

(2) Investigate the mixing and transport processes in the cylinder wake when close to a free surface, including the influence of breaking.

(3) Investigate the existence of specific instabilities.

(4) Discuss Triantafyllou and Dimas 1989 predictions regarding stability modes at the free surface.

(5) Provide benchmark data that can be taken as a reference to be challenged by other researchers.

The chapter is organised as follows: the physical problem is first described by presenting the physical domain and the continuum equations. Next further details specific to this chapter are given about the computational model. Results are presented thereafter, comparing them withe the existing literature when possible. Finally, some conclusions are drawn.

9.2 PHYSICAL MODEL

9.2.1 Physical problem

Two-dimensional monophasic flow around a low submergence cylinder with diameter d, its axis parallel to the free surface and perpendicular to the incoming flow is considered in this work. A sketch of the problem is depicted in Fig.

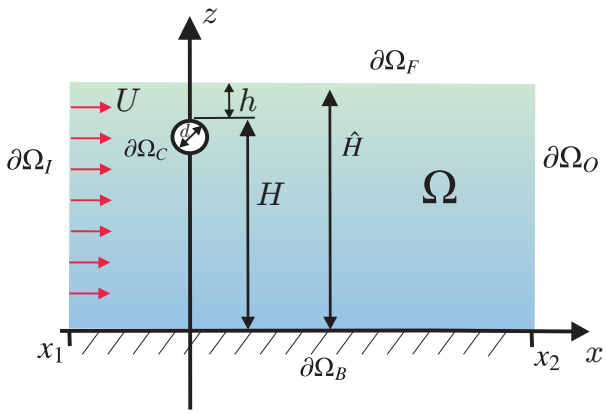

Figure 9.1.: Case setup notation and system of reference. Reichl et al. 2005 notation is used.

9.1 in order to introduce the notation and problem setup. Reichl et al. 2005 convention for the notation has been used. The gap h between the cylinder top and the undisturbed free surface is taken as the measure of the cylinder submergence. The cylinder is fixed with its center at coordinates $(0, H - d/2)$. Uniform inflow velocity U is imposed on $x = x_1$.

The flow is governed by a series of non-dimensional numbers: the gap (or submergence) ratio h/d, Reynolds number and a set of Froude numbers.

Reynolds number is defined as:

$$Re = \frac{U\, d}{\nu}, \tag{9.1}$$

with ν being is the liquid kinematic viscosity.

Following Sheridan et al. 1997, three different Froude numbers are defined, depending on whether $\hat{H}$, d, or h is chosen as characteristic length:

$$Fr_{\hat{H}} = \frac{U}{\sqrt{g\hat{H}}}, \qquad Fr_d = \frac{U}{\sqrt{gd}}, \qquad Fr_h = \frac{U}{\sqrt{gh}}, \tag{9.2}$$

where g is the gravity acceleration. Unless otherwise specified, when referring to the Froude number in the text, it is assumed that we refer to the Froude number based on the diameter.

9.2.2 Boundary conditions (BCs)

A no-slip BC is imposed on the cylinder surface, $\partial\Omega_C$, while a free-slip BC is imposed along the bottom, $\partial\Omega_B$. Along the free surface, both kinematic and dynamic BCs should be fulfilled. The kinematic free-surface BC implies that

while evolving with the fluid flow, the material points initially on $\partial\Omega_F$ remain on $\partial\Omega_F$. This condition fails to hold when two fronts merge during impact events (e.g., plunging breaking wave).

At the inlet $\partial\Omega_I$, a constant velocity inlet boundary condition is imposed and pressure is set as hydrostatic in that boundary. At the outlet downstream boundary $\partial\Omega_O$, zero-gradient boundary conditions for pressure and velocity fields are imposed.

9.3 COMPUTATIONAL MODEL

9.3.1 Field equations

For of the problem proposed in section 9.2, the fluid domain is assumed to be discretised with N fluid particles. The δ-SPH scheme presented in chapter 4 is adopted to compute the numerical solution.

All the simulations to be discussed in this work have been run on a desktop PC equipped with six-core Xeon 2.33 GHz processors. The present SPH algorithm, which has been parallelised with a simple OpenMP programming strategy, requires a time cost of 25 µs per particle, per iteration and per core.

9.3.2 Enforcement of the boundary conditions

The ghost-fluid technique is used to enforce the boundary conditions on the body surface. Specifically, the solid domain is modelled through a set of "imaginary particles" and the velocity-pressure fields are extended on these fictitious particles through a mirroring technique (for details see *e.g.* Macià et al. 2012). Different mirroring techniques can be adopted to enforce different boundary conditions (i.e. free-slip on the bottom and no-slip on the cylinder). The details of the mirroring procedure adopted in this work are described in chapter 4.

Regarding the free-surface boundary conditions, the kinematic one is identically fulfilled as a consequence of the particle Lagrangian formalism. Regarding the dynamic boundary condition, in the weakly compressible SPH formalism, such condition is implicitly satisfied in a weak sense, as demonstrated in Colagrossi et al. 2009 for inviscid fluid and in Colagrossi et al. 2011 for viscous flow.

Inflow and outflow boundary conditions are set as in Federico et al. 2012 where suitable sets of inflow and outflow particles are defined to enforce upstream and downstream conditions. In the inflow boundary, pressure and velocity are imposed on the particles. When fluid particles cross the outflow they

keep their velocity and pressure until they leave the area where interactions with other fluid particles are still possible.

9.4 NUMERICAL INVESTIGATION

9.4.1 General

Due to the scope and objectives of the present research, in which very high Froude number flows are dealt with, the size of the physical and computational domain can play a significant role in the flow physics. For this reason, the inflow, outflow and bottom positions used in the simulations have been thoroughly documented.

In addition, in order to get accurate results, suitable spatial resolutions have to be set with the aim of resolving all the main vorticity scales for the selected Reynolds number, 180. In other words, the numerical resolutions adopted must be sufficient to achieve, within reasonable bounds, convergent results. As high-quality variable resolution SPH formulations are not available yet for this type of problem, the same particle size applies over all the whole domain.

Considering these two aspects, analyses have been performed in order to: firstly; find a compromise on the domain size so that the computational effort is kept under control and, secondly; checking convergence by increasing the number of particles for two representative cases.

The techniques used to assess the influence of the computational domain dimensions and the number of particles on the results were to examine vorticity fields, the streamlines and the lift and drag coefficients time histories.

Since the focus of the present work is on the physics of flow and not on numerical aspects of the simulations, these analyses are documented in appendix 9.9.

In the plots, lift and drag forces have been made non dimensional using the relations:

$$C_L(t) = \frac{L(t) - B}{0.5\,\rho\,d\,U^2}, \qquad C_D(t) = \frac{D(t)}{0.5\,\rho\,d\,U^2}, \tag{9.3}$$

where $L(t)$ and $D(t)$ are the instantaneous lift and drag values, computed as described in Bouscasse et al. 2013a; Marrone et al. 2013. As can be appreciated in equation (9.3), in order to evaluate the lift coefficient, a constant hydrostatic vertical force, B, (corresponding to undisturbed free-surface condition buoyancy) has been subtracted from the computed lift time history. Note that for the half-submerged cases, this buoyancy B is set to half the one corresponding to submerged cases. Time histories of forces have been treated by a low-pass filter in order to remove oscillations given by the weakly compressible approach.

9.4.2 List of case studies

As mentioned in the introduction, a renowned work on the numerical analysis of the flow around a cylinder beneath a free surface is the one carried out during Reichl 2001 PhD thesis, which led to influential publications such as Reichl et al. 2005; Reichl et al. 2001; Reichl et al. 2003. Test conditions considered in this thesis and related publications, all with $Re = 180$, have been collected and are summarised in Fig. 9.2. The conditions have been assigned a different marker depending on the type of flow. On one side, for large gap ratios, vortex shedding was observed by Reichl and colleagues, suggesting that the flow has strong similarities with unbounded cylinder flow. The shedding was shown to be blocked as the cylinder approaches the free surface. It must be highlighted that, in order to block the shedding for low Froude number, it is necessary to get closer to the free surface than is the case when higher Froude numbers are considered. For some intermediate Froude number cases, metastable states (as described in the Introduction) were observed.

In the same Fig. 9.2, the cases considered in the present research have been added. As it can be appreciated, these cases extend the research of Dr. Reichl and colleagues to larger Froude numbers and to negative submergences (half-submerged cases) keeping the Reynolds number as 180. The motivation for the Reynolds number choice is threefold:

1. For $Re = 180$, no significant 3D effects in the flow are expected (Barkley and Henderson 1996), which allows us to state that 2D simulations can capture the dynamics. Since the analysis is wide, keeping computational effort within reasonable limits is paramount and 2D simulations are a major advantage in these regards.

2. The aim is to resolve all the vorticity scales (to conduct a DNS) in the flow. This would be extremely difficult (maybe impossible at this stage) if a larger Reynolds number had been chosen. It has to be accounted that a free-surface flow with no surface tension is resolved, for which the suitability of turbulence models is questionable.

3. And last but not least, there is a substantial body of literature on this problem, led by Reichl and colleagues, which can serve as a reference for present work.

The cases are organised around the following main four sequences:

1. The first sequence looks at the effect of submergence on the flow characteristics for $Fr_d = 1$, higher than the range considered by Reichl and colleagues (see Fig. 9.2). Since the numerical technique used, SPH, is capable of modelling more complex free-surface dynamics (strong breaking and fragmentation) when compared to FLUENT VOF technique used

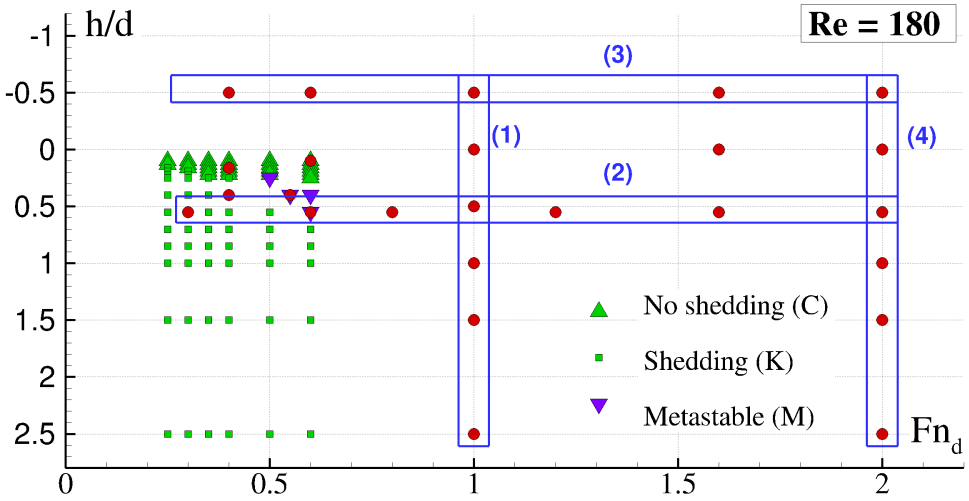

Figure 9.2.: Summary of the cases simulated classified by Fr_d and h/d. $Re = 180$. Green (and blue) are conditions presented in Reichl 2001; Reichl et al. 2005; Reichl et al. 2001; Reichl et al. 2003. Red points are the conditions tested in the present work.

by Dr. Reichl and colleagues, gap ratios equal to zero or even negative values (tangent and intersecting the undisturbed free surface) have been investigated.

2. The second sequence looks at the impact that Froude number has on the cylinder wake and downstream free surface shape for a fixed submergence. Froude numbers as high as 2.0 are investigated, extending the previously existing literature. A submergence ratio of $h/d = 0.55$ was chosen for this sequence based on the fact that Reichl and colleagues discussed some cases with this submergence in detail.

3. It is advanced now that interesting flow types have been found when investigating sequence number 2. The natural follow-up is therefore to assess to what extent these flows occur when the cylinder is half-submerged, thus motivating this third sequence, which mimics the previous one but setting $h/d = -0.5$.

4. Again, based on what has been found in previous sequences, it was decided that it would be relevant for the research to investigate the flow dependence on the cylinder submergence, like in sequence 1, but at the highest Froude number $Fr_d = 2.0$.

5. Finally, some isolated points have been chosen in order to revisit some of the cases for which the metastable regime was found by Reichl et al. 2005.

The analysis to be conducted hereinafter follows the order in which these sequences have been introduced. It has to be stressed that although the emphasis will be on the flow characteristics, drag and lift coefficient time histories will be also provided. The aim is that this study will serve as reference data so that other solvers can either better confirm or challenge the present results.

Different types of flows will be identified later in the chapter. In order to name them in a compact way they will be labeled with 3 letters: the first letter will refer to the type of flow around the cylinder: K (von Kármán), C (coanda), M(metastable) and B (cylinder surface acting as a barrier for the free-surface streak lines). A second letter will be used for designating the free-surface pattern: F (Flat) S(Spilling) P(Plunging). Finally, a third letter will be used for describing the interaction between vorticity from cylinder and from FS: I(Interaction) R(Recirculation zone under FS) V(large vortex). More details on these flow types will be given, and the labeling will be used in the summary of all cases.

Fr_d	h/d	$\hat{H}/d$	$Fr_{\hat{H}}$
1	2.5	6	0.41
1	2.0	6	0.41
1	1.5	6	0.41
1	1.0	6	0.41
1	0.5	6	0.41
1	0.0	6	0.41
1	-0.5	6	0.41

Table 9.1.: Sequence 1: influence of submergence on flow characteristics: numerical test matrix. $Re = 180$ in all cases. Particle resolution: $\Delta x/d = 0.01$. Domain horizontal limit: $x_1/d = -11$ and $x_2/d = 26$

9.5 SEQUENCE 1: INFLUENCE OF SUBMERGENCE ON FLOW CHARACTERISTICS AT INTERMEDIATE-HIGH FROUDE NUMBER $Fr_d = 1$

Case studies have been considered setting $Fr_d = 1.0$ and looking at several gap ratios, h/d, from deep submergence cases to free surface piercing ones. A list of these cases, using the notation of Fig. 9.1, is presented in Table 9.1. The most representative of these cases are discussed in detail in the following sections.

9.5.1 Large gap ratio (deep submergence), $h/d = 2.5$ (KSN)

The analysis starts with the case with the deepest cylinder position. Looking at the flow features, a clear von Kármán vortex shedding pattern is observed (Fig. 9.3) with a Strouhal number, St=0.21, slightly larger than the unbounded flow reference, $St_\infty = 0.191$, obtained using a particle vortex method (see Rossi et al. 2015 for details). The cylinder wake induces the formation of a small spilling breaker at the free surface. The vorticity generated with that breaking is diffused in a narrow region close to the free surface, which prevents it from interacting with the cylinder wake. Such small-scale breaking events resemble those, induced by a free-surface drift layer, studied by Dimas 2007.

Due to the vortex shedding the mixing is intense and similar to that observed in cylinder unbounded flows (see Fig. 17 in Marrone et al. 2013). However, the transversal expansion of the detached vortices does not occur due to their confinement between the free surface and the channel bottom. Even though the mixing is intense, the upper layers of water (coloured in blue) remain close to the free surface, consistently with the aforementioned absence of interaction between free-surface and cylinder wake vorticity fields.

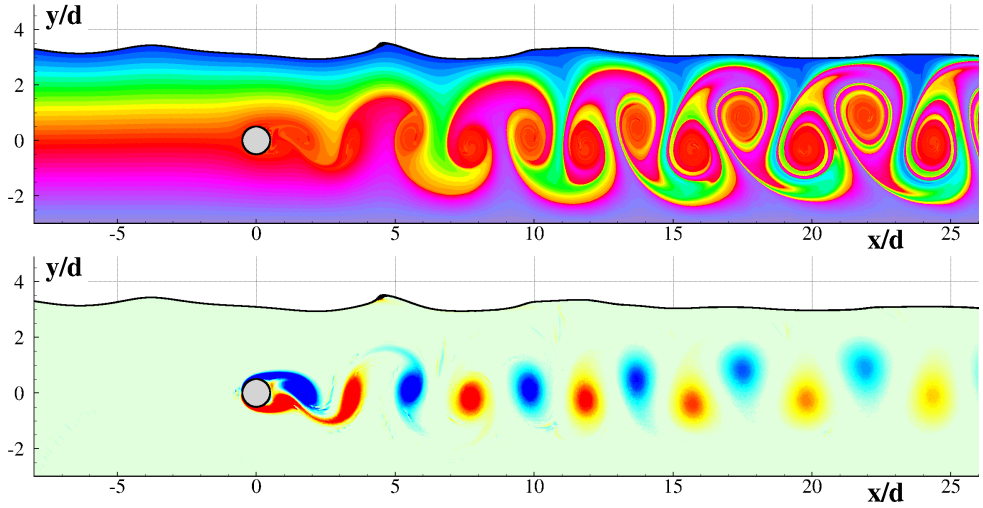

Figure 9.3.: Influence of submergence on flow characteristics: $h/d = 2.5$, $Fr_d = 1$. (Flow label KSN) Streaklines (top) and vorticity field (bottom) plots, $t(g/d)^{0.5} = 68$. Dimensionless vorticity curl($\mathbf{u}$) $\sqrt{d/g}$ scales from -2 (blue) to 2 (red).

The drag coefficient is reasonably stable (Fig. 9.4), with a value, 1.58, which is higher than the reference one for unbounded flow domain, 1.28 ± 0.036 Rossi et al. 2015. This value, 1.28, is labeled as C_{D_∞} to be used, hereinafter, to normalise the drag coefficient. As later discussed in appendix 9.9, the presence of the free surface and the bottom modifies the forces around the cylinder and justifies the divergence between the value obtained in this case and the reference unbounded domain solution.

The net lift value is zero (Fig. 9.4), as is to be expected considering the large distance between the cylinder and the free surface. The lift coefficient oscillations rms is approximately 0.66, reasonably close to the value 0.59 obtained in the unbounded condition.

9.5.2 Moderate gap ratio (intermediate submergence), $h/d = 1.5$ (KSI)

As for $h/d = 2.5$, a clear vortex shedding pattern originating from the cylinder is observed (Fig. 9.5) and the Strouhal number grows very slightly (0.23 compared to 0.21 for $h/d = 2.5$). The breaking intensity at the free surface is larger, compared to $h/d = 2.5$, and cyclical plunging breaking events take place (similarly to the ones observed by Landrini et al. 2007) (see movie provided as supplementary material). It is relevant to mention that these breaking events are an important additional vorticity generation mechanism, as can be appreciated in the bottom panel of Fig. 9.5.

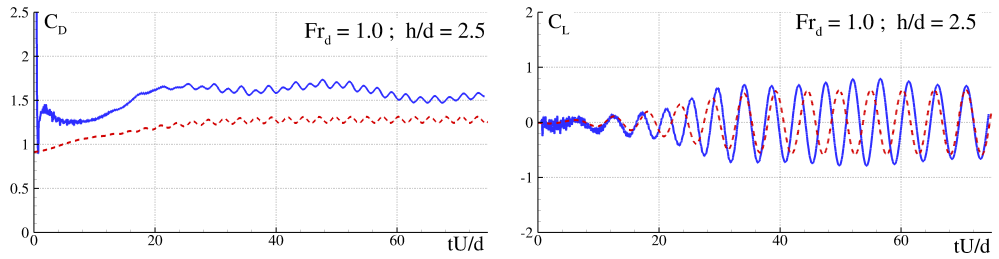

Figure 9.4.: Influence of submergence on flow characteristics: drag and lift coefficient time histories, $h/d = 2.5$, $Fr_d = 1$, $Re = 180$ (solid line) compared to unbounded domain reference solution (dashed line), obtained with the DVH method described in Rossi et al. 2015.

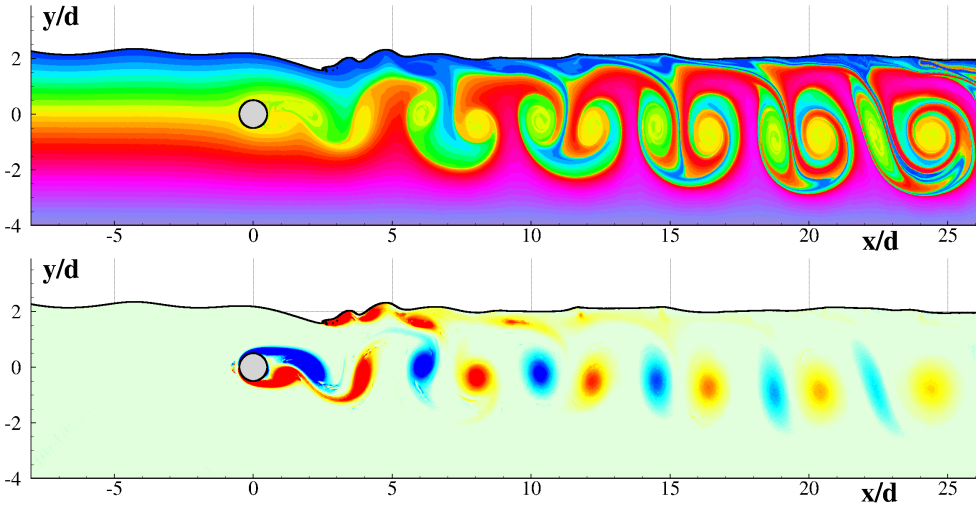

Figure 9.5.: Influence of submergence on flow characteristics: $h/d = 1.5$, $Fr_d = 1$. (Flow label KSI) Streaklines (top) and vorticity field (bottom) plots, $t(g/d)^{0.5} = 75$. Dimensionless vorticity $\mathrm{curl}(\mathbf{u})\sqrt{d/g}$ scales from -2 (blue) to 2 (red).

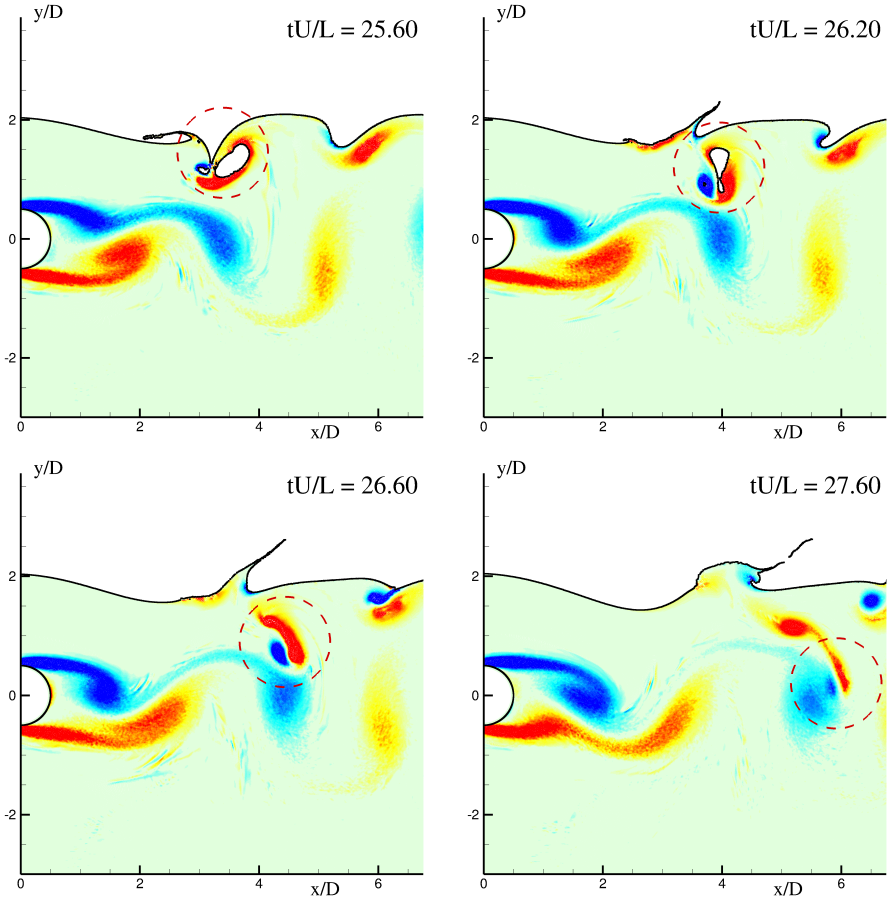

Figure 9.6.: Influence of submergence on flow characteristics: $h/d = 1.5$. Enlarged view of the vorticity field behind the cylinder, $t(g/d)^{0.5} = 25.6; 26.2; 26.6; 27.6$. Dimensionless vorticity $\mathrm{curl}(\mathbf{u})\sqrt{d/g}$ scales from -4 (blue) to 4 (red).

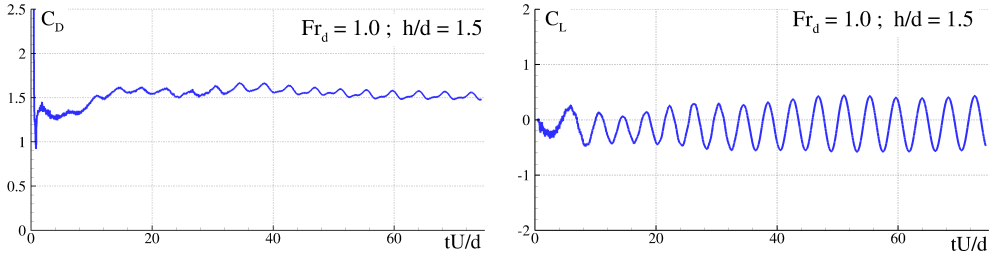

Figure 9.7.: Influence of submergence on flow characteristics: drag and lift coefficient time histories. $h/d = 1.5$, $Fr_d = 1$.

It is notable that the vorticity originated by the breaking interacts in a complex way with the cylinder wake, something that does not happen for the previous deeper case. This can be appreciated in the zoomed view of Fig. 9.6 in which, in order to better appreciate the vorticity flow details, its color range has been doubled. As a consequence of this vorticity interaction, the mixing is intense, with substantial entrapping of the free-surface layers in the bulk of the domain (see top part of Fig. 9.5). It is important, at this point, to bring forward the groundbreaking linear stability analysis of Triantafyllou and Dimas 1989, in which, the role of the free surface was included. Due to the limitations of their model, however, they wer not able to capture the instabilities arising from breaking and could not explain these strong interactions between breaking waves and cylinder wake vorticity fields.

Regarding forces, mean drag remains at the same value of the previous case, even if its time behaviour is not sinusoidal (left panel of Fig. 9.7). Lift periodic oscillations are reduced in amplitude (right panel of Fig. 9.7), but are still present, consistent with the still prevailing alternate vorticity shedding regime.

9.5.3 Small gap ratio (low submergence), $h/d = 0.5$ (CSV)

The von Kármán vortex shedding from the cylinder surface is blocked as h/d is reduced from 1.5 to 0.5 and a Coanda-like flow develops (Fig. 9.8). Moreover, the cylinder wake is deflected downwards "attracting" a jet of material from the free surface, projecting it into the bulk of the fluid. The cylinder wake is almost steady. A similar behaviour for smaller gap ratio (0.25) and Froude number (0.6) is documented by Reichl et al. 2005 (§3.7.3).

In this particular case, the free surface shows unsteady behaviour due to the cyclical onset of breaking waves which gives rise to vorticity of both signs. The vortices combine with each other resulting in a complex wake behind the cylinder. In particular, large positive vortices develop on the far wake region (see upper part of Fig. 9.8) by merging approximately 3 consecutive vortices originating from the free surface. This successive merging induces an accumulation of vorticity which continues until this vortical structure reaches a certain size and magnitude, being then advected downstream and downwards (see detailed description in Fig. 9.9). This phenomenon will be referred to as a "meta-vortex".

A sequence of frames corresponding to instants whose difference is the unbounded flow vortex shedding period (i.e. St_∞^{-1}) is presented in Fig. 9.10. It cannot be inferred from this short sequence that the shedding of these meta-vortices occurs with full periodicity. If that were the case, and based on the present simulation, its Strouhal number would be around 3 times smaller (around 0.08) than the individual vortex generation in the free surface. Due to

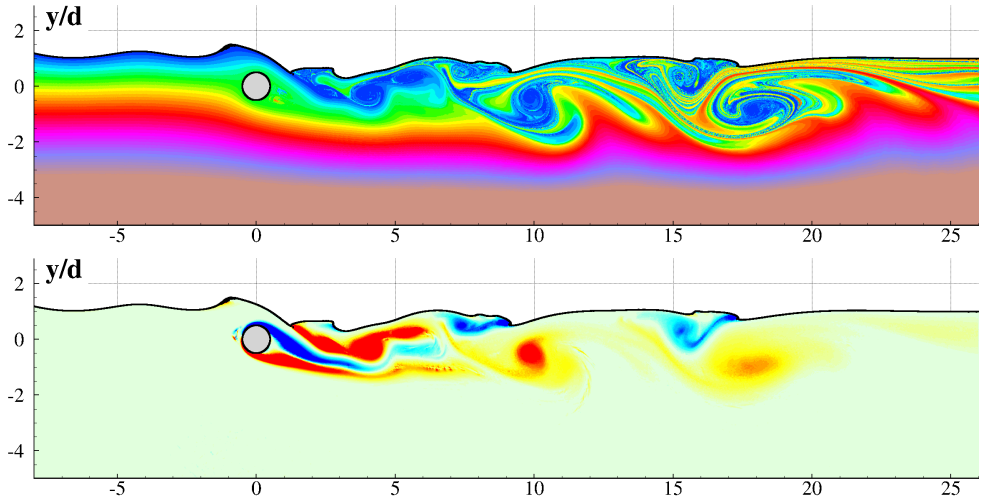

Figure 9.8.: Influence of submergence on flow characteristics: $h/d = 0.5$, $Fr_d = 1$. (Flow label CSV) Streaklines (top) and vorticity field (bottom) plots, $t(g/d)^{0.5} = 50$. Dimensionless vorticity curl($\mathbf{u}$) $\sqrt{d/g}$ scales from -2 (blue) to 2 (red).

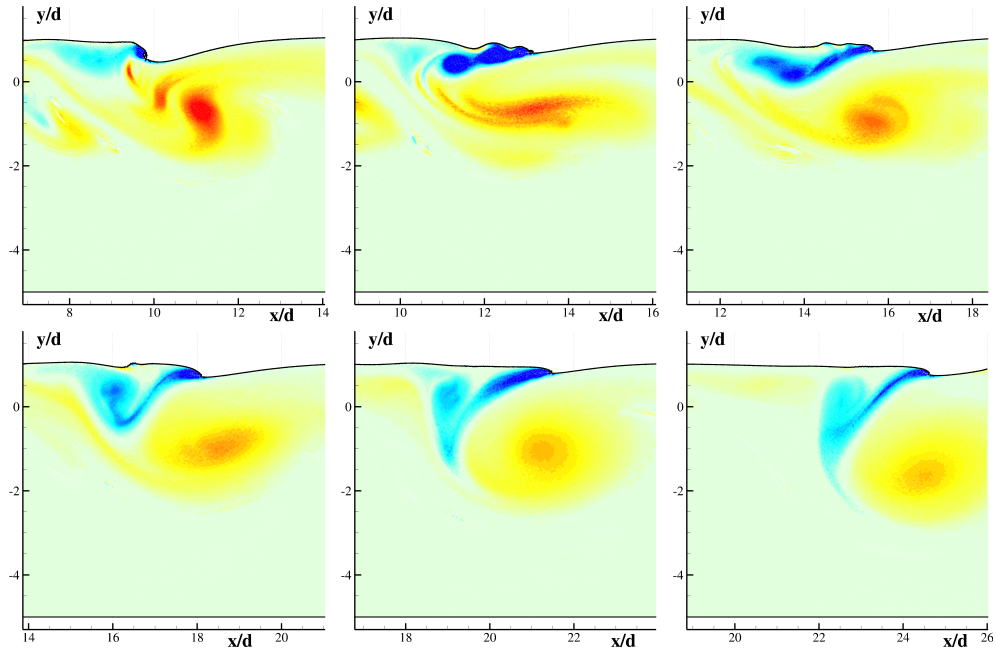

Figure 9.9.: Meta-vortex formation: $h/d = 0.50$, $Fr_d = 1.0$, $t(g/d)^{0.5} = 39, 43, 47, 51, 55, 59$ (from left to right and top to bottom). Dimensionless vorticity curl($\mathbf{u}$) $\sqrt{d/g}$ scales from -4 (blue) to 4 (red).

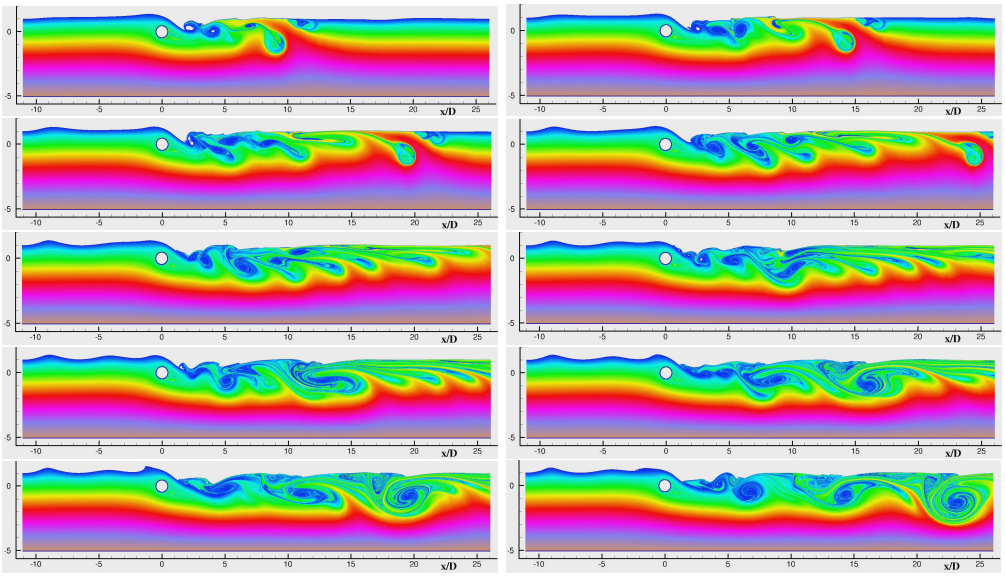

Figure 9.10.: Meta-vortices, $Fr_d = 1\text{-}h/d = 0.5$, from top to bottom: $t(g/d)^{0.5} = 12.4 + 5 + 5 + ...$

the demanding computational effort to confirm this, it is left for future work to conduct longer simulations.

It is interesting to think of this process of merging vortices as resembling the cyclone formation process, something **Ritchie˙Holland˙MWR˙2014˙cyclogenesis** investigated, discussing how vorticity produced by different sources accumulates to form larger structures leading to tropical cyclones in the north western Pacific.

To our knowledge, this form of instability has not been previously reported in the literature. It must be said that since the cylinder wake is almost steady, and the unsteadiness of the far-wake region is induced by the breaking, this case cannot be considered as a metastable configuration. However, these large downstream meta-vortices share some similarities with the far wake patterns in metastable states briefly described by Reichl et al. 2003.

Regarding forces, periodic lift oscillations disappear, consistent with the fact that alternate vorticity shedding is blocked, and a substantial net negative lift appears (see Fig. 9.11). Drag seems to oscillate in the last part of the simulation with a period similar to the large meta-vortices. The drag coefficient mean value is 1.52, slightly lower than the previous cases.

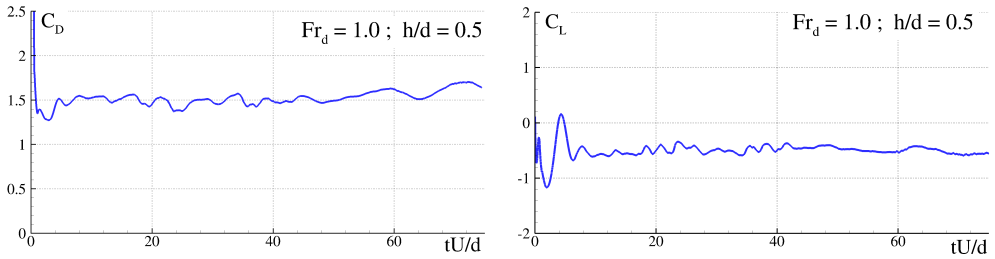

Figure 9.11.: Influence of submergence on flow characteristics: drag and lift coefficient time histories. $h/d = 0.5$, $Fr_d = 1$.

9.5.4 Null gap ratio (tangency), $h/d = 0$ (CFR)

This is a quite challenging case from the computational point of view since the cylinder top is in contact with (tangent to) the undisturbed free surface. It was not treated by Reichl et al. 2005.

A Coanda-like flow is established in this case, with the cylinder bottom wake being significantly deflected (Fig. 9.12) and a layer of fluid getting attached to the top part of the cylinder to be projected downwards at the rear of the cylinder. However, this jet does not reach great depths, remaining close to the free surface. Due to this, the large recirculation area that is formed downstream remains close to the free surface, gets stretched, and is slowly advected downstream without mixing with the bulk of the fluid. A typical length of around 15 diameters can be assigned to this area, which is of the same order as the length of the steady unstable recirculation bubble, obtained for this Reynolds number for unbounded cylinder flows by Fornberg 1985.

The vorticity generation is quite stationary (bottom panel of Fig.9.12) leading to basically constant drag and lift time histories. Compared to all previous submergences, drag drops and the net negative lift is larger and quite constant, as can be seen in Fig. 9.13.

9.5.5 Negative gap ratio (half-submerged cylinder), $h/d = -0.5$ (BSI)

This is a difficult case, not treated by Reichl et al. 2005. The first distinct flow feature that can be appreciated (Fig. 9.14) is that the cylinder acts as a barrier for the free-surface particle trajectories and the fluid does not flow over the obstacle, whose top part remains dry. This behaviour resembles that of mechanical containment systems for oil spills, as those discussed by, e.g. Amini et al. 2008; Wicks 1969. Regarding the wake, very small vortices are generated which are convected downstream, leaving a quite stable stretched recirculation area.

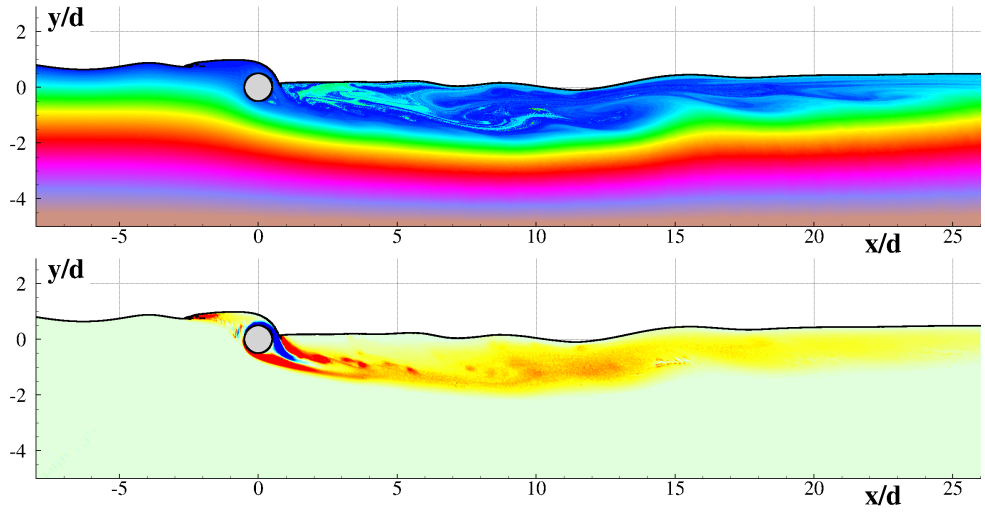

Figure 9.12.: Influence of submergence on flow characteristics: $h/d = 0$, $Fr_d = 1$. (Flow label CFR) Streaklines (top) and vorticity field (bottom) plots, $t(g/d)^{0.5} = 75$. Dimensionless vorticity $\mathrm{curl}(\mathbf{u})\sqrt{d/g}$ scales from -2 (blue) to 2 (red).

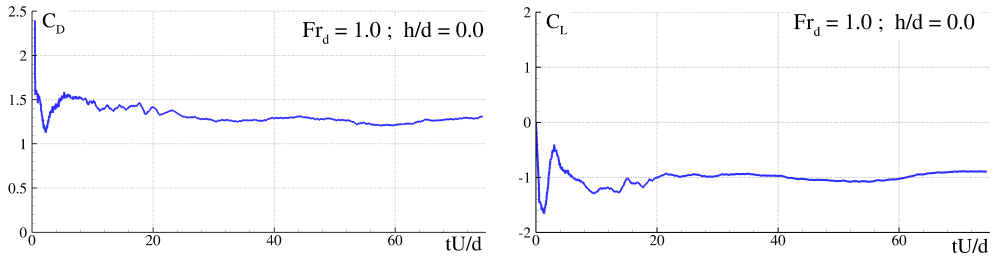

Figure 9.13.: Influence of submergence on flow characteristics: drag and lift coefficient time histories. $h/d = 0$, $Fr_d = 1$.

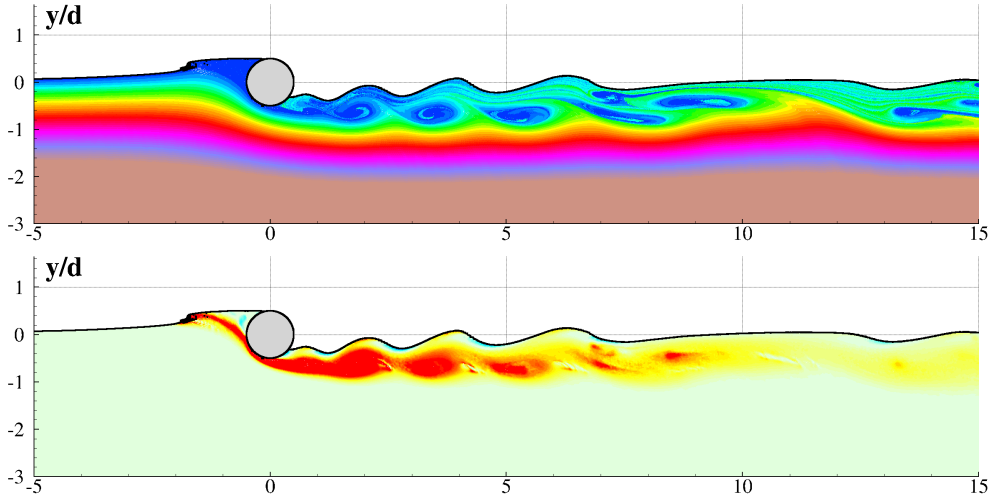

Figure 9.14.: Influence of submergence on flow characteristics: $h/d = -0.5$, $Fr_d = 1$. (Flow label BSI) Streaklines (top) and vorticity field (bottom) plots, $t(g/d)^{0.5} = 75$. Dimensionless vorticity $\mathrm{curl}(\mathbf{u})\sqrt{d/g}$ scales from -2 (blue) to 2 (red).

This stabilizing effect of the free surface on the wake of partially submerged cylinders has been discussed in detail by Triantafyllou and Dimas 1989. They extended linear stability analysis to problems with a free surface. They explained that the presence of the free surface may help to stabilize the wake of a half submerged cylinder, transforming (at certain Froude numbers) the unbounded flow von Kármán vortex shedding absolute instability into a convective instability. According to Triantafyllou and Dimas 1989, above a certain threshold, $Fr_d = 1.77$, this effect would not take place and the absolute instability of staggered von Kármán type vortex shedding would be recovered. It must be borne in mind that Fr_d is 1.0 in this case, well below the referred threshold.

It is also notable that small amplitude propagating waves are generated downstream of the cylinder, travelling a short distance downstream before getting quickly damped. They can be appreciated in the top panel of Fig. 9.14.

As for $h/d = 0$, the vorticity generation is again quite stationary (bottom panel of Fig.9.14) leading to basically constant drag and lift time histories. Drag drops again, compared to all previous submergences, and a large net negative lift is generated, as can be seen in Fig. 9.15.

9.5.6 Influence of submergence on flow characteristics: summary

The free-surface elevation mean and root-mean-square (rms) bars (computed in all instances for this paper after subtracting the mean), for the considered

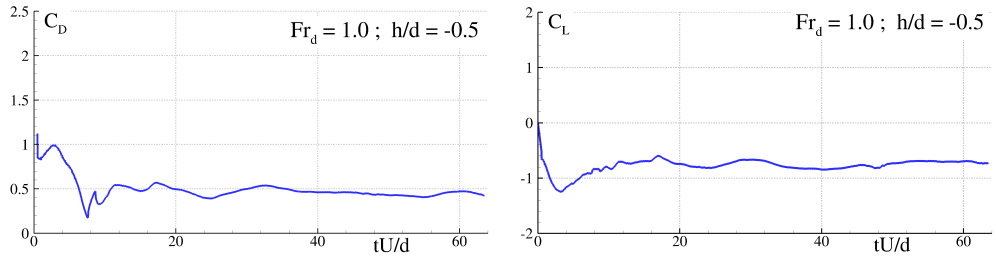

Figure 9.15.: Influence of submergence on flow characteristics: drag and lift coefficient time histories. $h/d = -0.5$, $Fr_d = 1$.

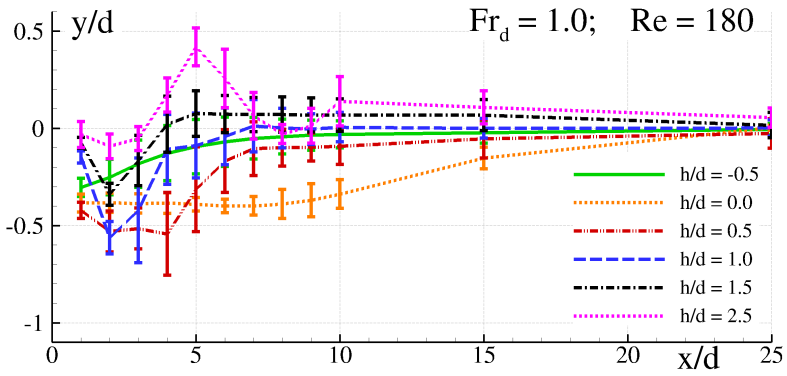

Figure 9.16.: Variation of the free-surface profile with submergence: $Fr_d = 1.0$.

cases, are displayed in Fig. 9.16. When observed together, it is interesting that the largest downstream free -surface positive elevation occurs for the deepest submergence. Regarding the wave trough, its depth grows as the submergence is reduced. This fact is qualitatively in agreement with the observations by Duncan 1983 for a submerged hydrofoil (see Fig. 3 in such reference).

Coming back to Fig. 9.16, the largest volume of displaced liquid corresponds to $h/d = 0$, indicating that a significant amount of kinetic energy from the incoming flow is transformed into potential energy through the creation of the recirculation area (see again Fig. 9.12).

A summary of computed forces can be seen in Table 9.2 and graphically in Fig. 9.17, including rms bars. The drag coefficient tends to stabilise as submergence increases, laying above the deep water conditions reference value 1.28 ± 0.036 Rossi et al. 2015, a fact that is explained on the basis of the presence of the bottom and the free surface. The drag coefficient drops monotonically as submergence gets smaller, reaching a minimum of 0.45 for $h/d = -0.5$. This tendency is qualitatively in agreement with low Froude number flows observations by Miyata et al. 1990.

h/d	Re	Fr_d	C_D	C_D/C_{D_∞}	C_L	$C_{L_{rms}}$	St	St/St_∞
-0.5	180	1.0	0.45	0.35	-0.74	0.06	-	-
0.0	180	1.0	1.26	0.99	-1.00	0.06	-	-
0.5	180	1.0	1.52	1.19	-0.48	0.06	-	-
1.0	180	1.0	1.46	1.14	-0.17	0.12	0.30	1.55
1.5	180	1.0	1.54	1.21	-0.08	0.38	0.23	1.22
2.5	181	1.0	1.58	1.24	-0.02	0.57	0.21	1.10

Table 9.2.: Sequence 1: results summary for submergence dependence analysis at fixed $Fr_d = 1.0$. Mean values of C_D and C_L reported. All cases $Re = 180$

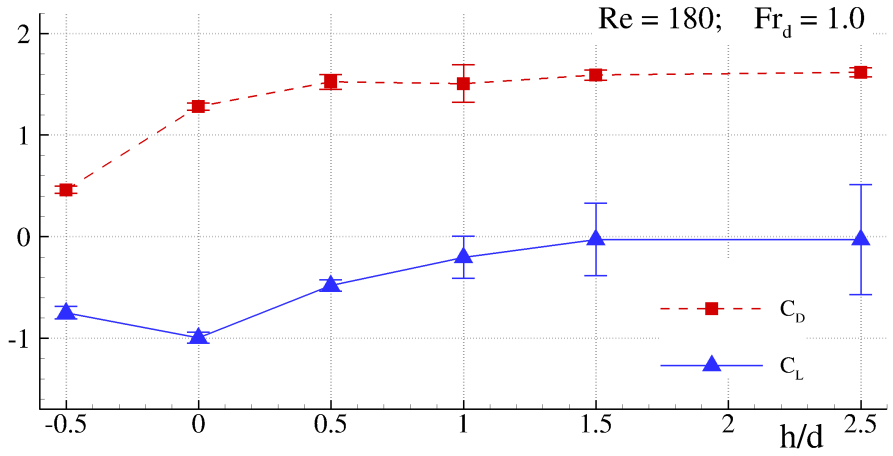

Figure 9.17.: Variation of horizontal and vertical force coefficients with submergence: $Fr_d = 1$.

Such qualitative agreement with Miyata et al. 1990 also holds for the lift coefficient, whose net value is negligible for large submergences and negative as the cylinder approaches the free surface. The rms of the lift coefficient is also presented in Table 9.2. The value, 0.57, obtained at $h/d = 2.5$, compares reasonably well with value of 0.59 of Rossi et al. 2015, corresponding to unbounded flow conditions.

Regarding the Strouhal number, it is slightly larger than the unbounded flow reference value of 0.191 obtained with the DVH method described in Rossi et al. 2015. The normalised Strouhal, based on that value, presents a maximum of 1.55 at $h/d = 1.0$ and shedding stops for lower submergences. These results are coherent with those found by Reichl et al. (see Reichl et al. 2005 Fig. 8) for lower Froude numbers (between 0.25 and 0.40, compared to 1.0 in the present study).

9.6 SEQUENCE 2: INFLUENCE OF FROUDE NUMBER ON FLOW CHARACTERISTICS AT MODERATE SUBMERGENCE: $h/d = 0.55$

A set of tests has been carried out varying Fr_d, from 0.3 to 2.0, setting the submergence ratio $h/d = 0.55$. This gap ratio was given substantial attention by Reichl et al. 2005, since for this and lower ratios, metastable states were described.

The channel depth has been varied in order to keep $Fr_{\hat{H}}$ not larger than 0.5. The computational domain has been made longer for high Froude number cases in order obtain enough information to properly analyze the wake. A summary of the cases analysed is presented in Table 9.3. Specific discussion of selected cases, among these, follows, starting with the lowest Froude number one.

Fr_d	h/d	$\hat{H}/d$	$Fr_{\hat{H}}$	x_1/d	x_2/d
0.3	0.55	7	0.11	-8	26
0.6	0.55	7	0.23	-8	26
0.8	0.55	9	0.27	-10	26
1.0	0.55	11	0.30	-10	26
1.2	0.55	11	0.36	-10	26
1.6	0.55	11	0.48	-18	36
2.0	0.55	16	0.50	-18	36

Table 9.3.: Sequence 2: case studies with varying Fr_d and $h/d = 0.55$. In all the simulations $\Delta x/d = 0.02$.

9.6.1 Low Froude number: $Fr_d = 0.3$ (KFI)

Streaklines and vorticity fields for one arbitrary instant in the simulation are presented in Fig. 9.18. As can be appreciated, the free surface hardly gets deformed, with the flow resembling that of a cylinder close to a no slip wall, something discussed in detail by Reichl et al. 2005. This case, $h/d = 0.55$, $Fr_d = 0.3$ was actually considered by Reichl et al. 2005 (see Fig. 3(b) in their paper). They did not provide a scale for their vorticity field but, from observation of the figures, the qualitative agreement can be deemed good. It can be inferred that this Froude number was chosen by Reichl et al. 2005 because they indicate it approximately marks the boundary between low- and high-Froude number cases. It has to be borne in mind that their Froude number range went up to 0.6. Since that range is extended to 2.0 in the present analysis, more nuances can be introduced regarding the characterization of Froude number regimes: low

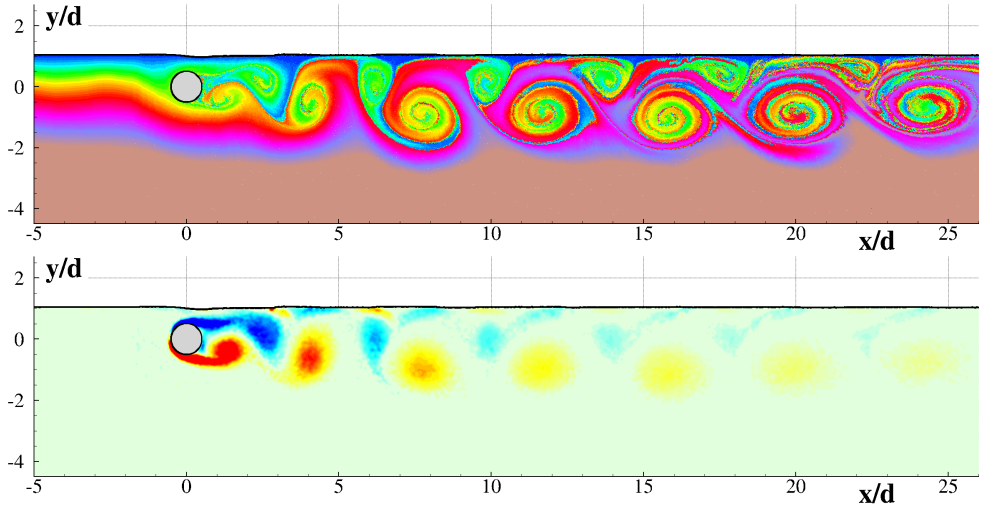

Figure 9.18.: Influence of Froude number on flow characteristics: $h/d = 0.55$, $Fr_d = 0.3$. (Flow label KFI) Streaklines (top) and vorticity field (bottom) plots, $t(g/d)^{0.5} = 149.6$. Dimensionless vorticity curl$(\mathbf{u})\sqrt{d/g}$ scales from -0.8 (blue) to 0.8 (red).

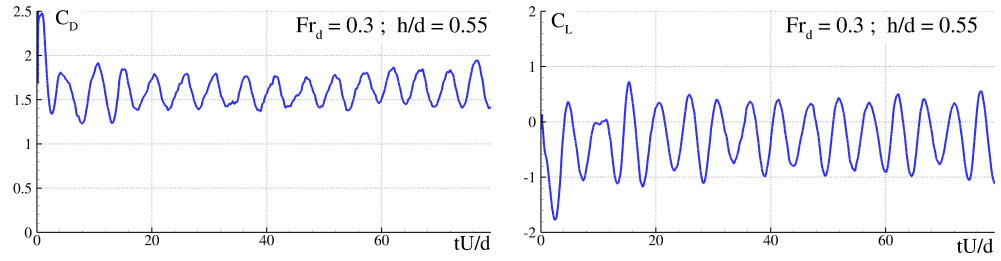

Figure 9.19.: Influence of Froude number on flow characteristics: drag and lift coefficient time histories. $h/d = 0.55$, $Fr_d = 0.3$.

($Fr_d = 0.3$), intermediate ($0.3 < Fr_d \leqslant 0.6$), intermediate-high ($0.6 < Fr_d \leqslant 1.2$), high ($1.2 < Fr_d \leqslant 1.6$), and very high ($Fr_d > 1.6$).

Drag and lift coefficients time histories are shown in Fig. 9.19. The alternate shedding is responsible for the periodic behaviour of these coefficients that show a Strouhal number very similar to the unbounded reference value. The normalised mean value of the drag coefficient is 1.26. A slightly net negative lift value of -0.26 is obtained, which presents oscillations with an rms of 0.6, similar to the unbounded flow reference value of Rossi et al. 2015.

9.6.2 Intermediate Froude number: $Fr_d = 0.6$ (CFR)

As the Froude number moves from 0.3 to 0.6, the physics changes dramatically. The free surface remains almost flat, as for $Fr_d = 0.3$, but the von Kármán vortex street onset is completely blocked (see Fig. 9.20). A recirculation area is formed just behind the cylinder and close to the free surface. This circulating fluid is slowly advected and diffused downstream close to the free surface, without getting mixed with the bulk of the fluid.

As can be appreciated in Fig. 9.20, layers of positive vorticity are generated at the free surface and at the bottom of the cylinder, enclosing a layer of negative vorticity originating from the top part of the cylinder. The layer of negative vorticity is weakened through its interaction with the positive vorticity generated at the free surface. This kind of dynamics is described in detail by Brøns et al. 2014 for a case with the same Froude number and slightly smaller submergence ratio.

The cross annihilation between the negative vorticity originating from the cylinder boundary and the positive one from the free surface results in a distinct wake, which, according to Reichl et al. 2005, can be associated to the existence of metastable states. Actually, Sheridan et al. 1997 found metastable states for the same Froude number $Fr_d = 0.6$ and for submergence ratios $0.75 \geqslant h/d \geqslant 0.24$, within which, the present case, $h/d = 0.55$, falls.

This case, $h/d = 0.55$, $Fr_d = 0.6$, was considered by Reichl et al. 2005 (see vorticity field in Fig. 3(d) in their paper). As for $Fr_d = 0.3$, they did not provide a scale for their vorticity field. However, comparing their results and the bottom panel of Fig. 9.20, the qualitative agreement can be deemed good.

A similar vorticity flow structure to the one corresponding to this case was described in section 9.5.4, for the case with $Fr_d = 1$, and similar submergence $h/d = 0.5$. In that case, large meta-vortices were generated, something which suggests that some relationship between the metastable states and the large meta-vortices could exist. This aspect deserves further investigation.

Drag and lift coefficients time histories are shown in Fig. 9.21. Since the shedding has been blocked, the periodic behaviour in the coefficients has vanished. There are however some low frequency oscillations of the drag coefficient (normalized Strouhal of 0.14) that could be related to an underlaying connection with the metastable states. In contrast, the lift coefficient becomes approximately constant after an initial transient. The normalised mean value of the drag coefficient is 1.12 and the lift coefficient is -0.3.

9.6.3 Intermediate-high Froude number: $Fr_d = 1.2$ (CPV)

A different dynamics emerges as Fr_d grows from 0.6 to 1.2, keeping h/d fixed at 0.55 (see Fig. 9.22). Although no vortices are shed from the cylinder, the positive vorticity generated by the spilling breaker, at the free surface, builds

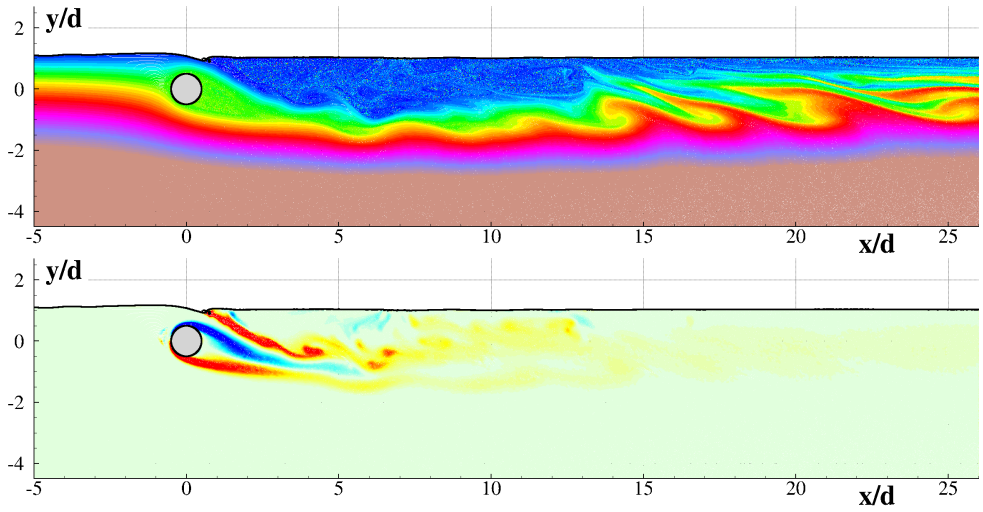

Figure 9.20.: Influence of Froude number on flow characteristics: $h/d = 0.55$, $Fr_d = 0.6$. (Flow label CFR) Streaklines (top) and vorticity field (bottom) plots, $t(g/d)^{0.5} = 300.0$. Dimensionless vorticity $\mathrm{curl}(\mathbf{u})\sqrt{d/g}$ scales from -2 (blue) to 2 (red).

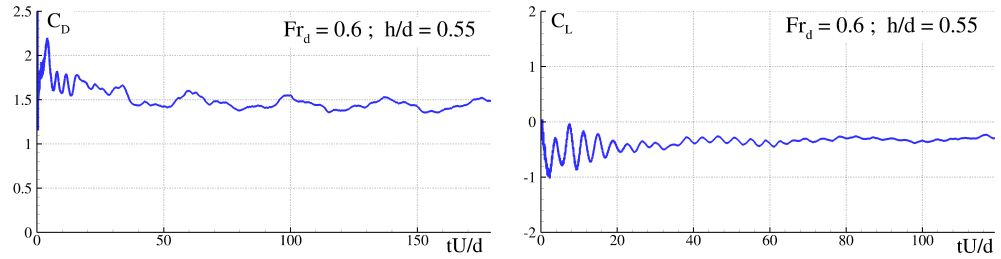

Figure 9.21.: Influence of Froude number on flow characteristics: drag and lift coefficient time histories. $h/d = 0.55$, $Fr_d = 0.6$.

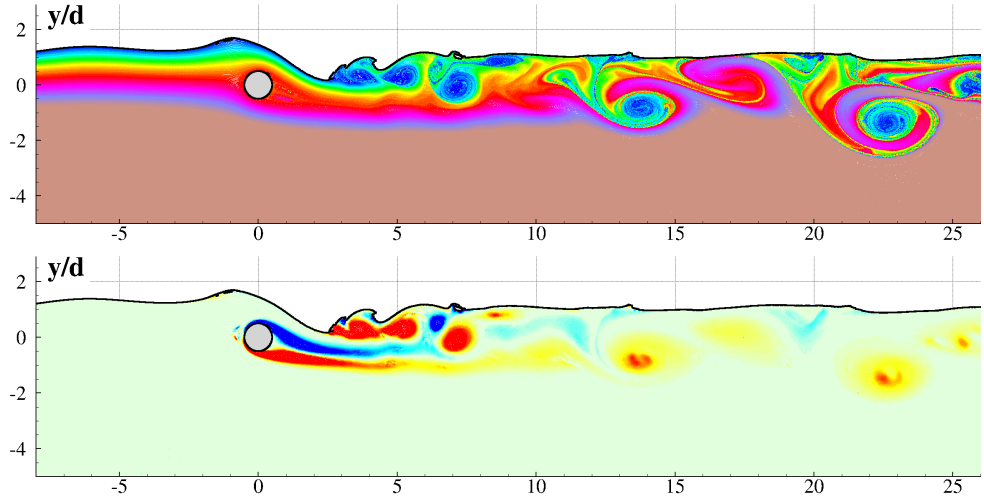

Figure 9.22.: Influence of Froude number on flow characteristics: $h/d = 0.55$, $Fr_d = 1.2$. (Flow label CPV) Streaklines (top) and vorticity field (bottom) plots, $t(g/d)^{0.5} = 150$. Dimensionless vorticity $\mathrm{curl}(\mathbf{u})\sqrt{d/g}$ scales from -2 (blue) to 2 (red).

up a large positive meta-vortex behind the cylinder which is then advected downstream. A similar dynamics was also identified in sequence one, for $Fr_d = 1.0$ and $h/d = 0.5$ (see section 9.5.3), which approximately falls between these two cases ($Fr_d = 0.6 - 1.2$, $h/d = 0.55$). Although these meta-vortices are not strictly periodic, its approximate Strouhal number is around 0.05 (see videos provided as supplementary materials), which is around 4 times smaller than St_∞.

It is notable that vorticity generated by the breaking processes is not accounted for in Triantafyllou and Dimas 1989 free-surface flows linear stability analysis. However, as previously discussed, such vorticity plays a key role in the development of this meta-vortex instability type.

Drag and lift coefficients time histories are shown in Fig. 9.23. Both coefficients display a quite stable behaviour. However, some low amplitude subharmonics can be appreciated in the drag, possibly related to the meta-vortices dynamics. The normalised mean value of the drag coefficient is 0.98 with a net negative lift of -0.18.

9.6.4 High Froude number: $Fr_d = 1.6$ (CPI)

Moving to even a higher Froude number, the unsteadiness of the problem grows and the large meta-vortices dynamics is less noticeable since the downstream convection is too fast for the vortices to merge from one breaking event to the next. For this reason, the prevalent regime consists of vortex pairs gener-

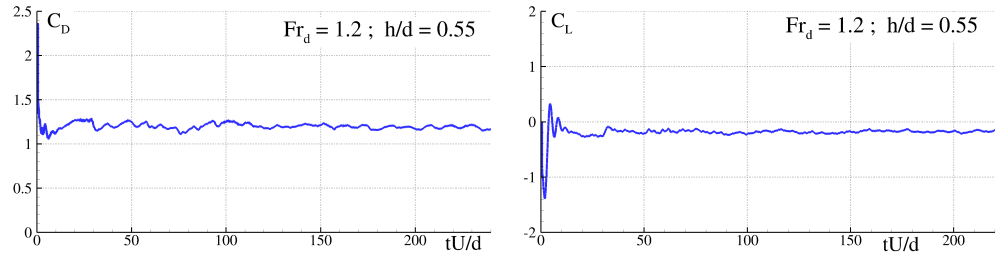

Figure 9.23.: Influence of Froude number on flow characteristics: drag and lift coefficient time histories. $h/d = 0.55$, $Fr_d = 1.2$.

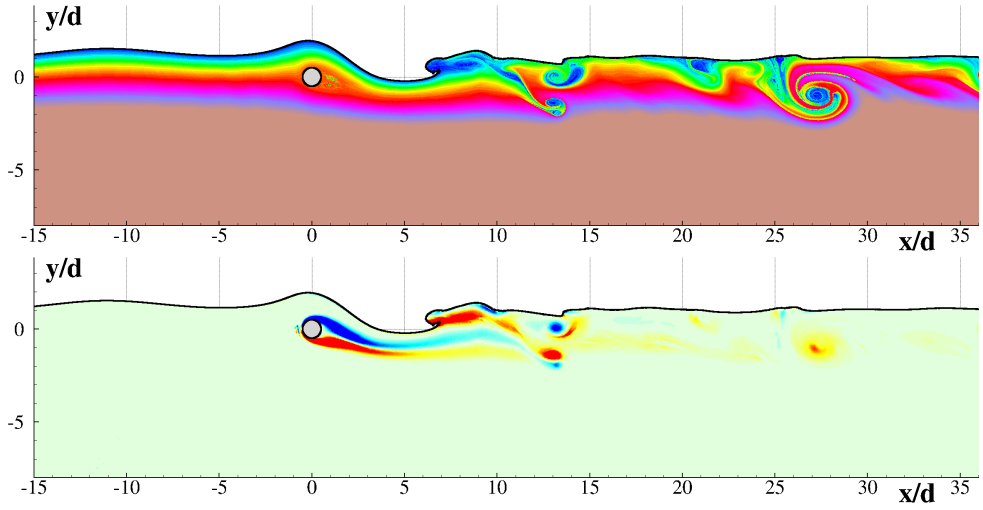

Figure 9.24.: Influence of Froude number on flow characteristics: $h/d = 0.55$, $Fr_d = 1.6$, $t(g/d)^{0.5} = 108$. (Flow label CPI) Streaklines (top) and vorticity field (bottom) plots. Dimensionless vorticity $\mathrm{curl}(\mathbf{u})\sqrt{d/g}$ scales from -2 (blue) to 2 (red).

ated through breaking being advected downstream, with moderate transport of mass from the free surface to the bulk of the fluid (Fig. 9.24).

Drag and lift coefficients time histories are shown in Fig. 9.25. Their values are essentially constant after a short initial transient. The normalised mean value of the drag coefficient is 0.81 while net lift is close to zero.

9.6.5 Very high Froude number: $Fr_d = 2.0$ (KPI)

This is the case with the strongest dynamics. Interestingly, a von Kármán street vortex type instability is recovered, which increases the unsteadiness and complexity of the flow (Fig. 9.26). Positive vortices detaching from the bottom of the cylinder merge with same sign vortices originating at the free

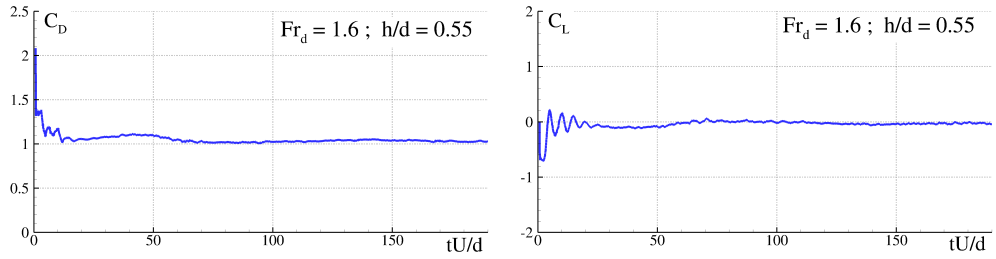

Figure 9.25.: Influence of Froude number on flow characteristics: drag and lift coefficient time histories. $h/d = 0.55$, $Fr_d = 1.6$.

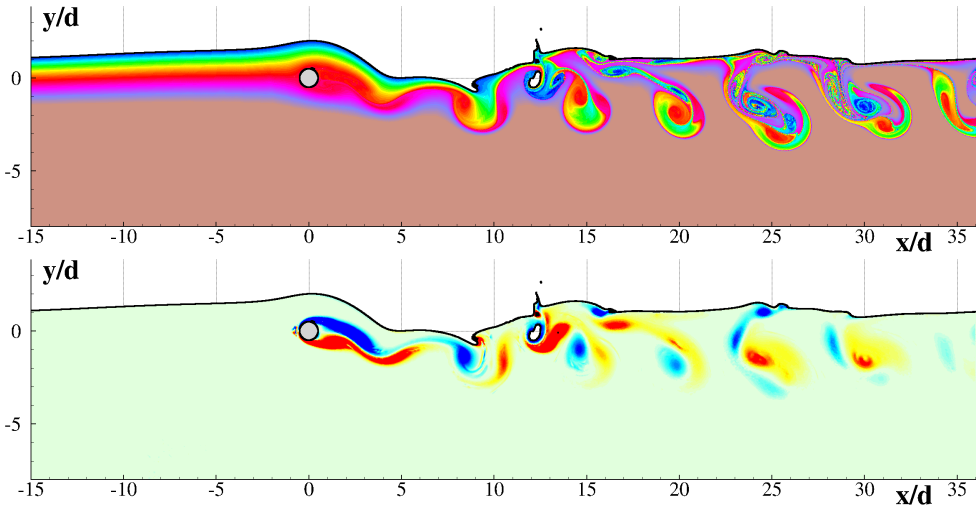

Figure 9.26.: Influence of Froude number on flow characteristics: $h/d = 0.55$, $Fr_d = 2.0$, $t(g/d)^{0.5} = 80$. (Flow label KPI) Streaklines (top) and vorticity field (bottom) plots. Dimensionless vorticity $\mathrm{curl}(\mathbf{u})\sqrt{d/g}$ scales from -2 (blue) to 2 (red).

surface. This merging projects material from the bottom parts of the fluid domain towards the free surface, creating complex mixing patterns.

As discussed in section 9.5.5, Triantafyllou and Dimas 1989 explained that for a half-submerged cylinder, above a certain threshold, $Fr_d = 1.77$ ($Fr_{d/2} = 2.5$ if the Froude number is based on the cylinder radius, as it is Triantafyllou and Dimas 1989 case), the von Kármán street vortex is again the prevalent instability type. This transition seems to happen, with the present case submergence, $h/d = 0.55$, also in the range of Fr_d between 1.6 and 2.0. This statement is supported by the fact that the von Kármán instability is prevalent for $Fr_d = 2.0$ while that is not the case for previous example, $Fr_d = 1.6$, which is below Triantafyllou and Dimas 1989 threshold. Considering that Triantafyllou and Dimas 1989 linear stability analysis refers to a half submerged cylinder, it becomes relevant to investigate whether the transition found for

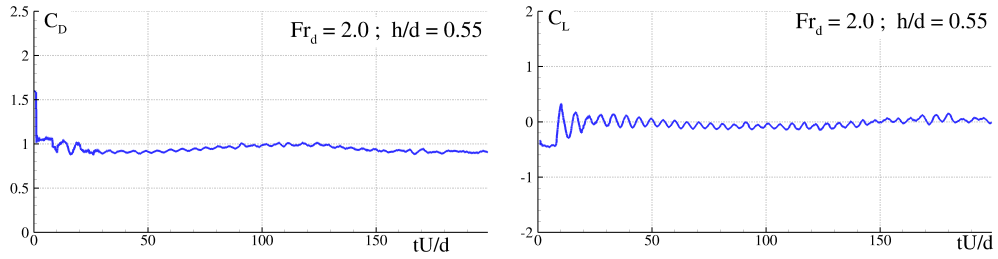

Figure 9.27.: Influence of Froude number on flow characteristics: drag and lift coefficient time histories. $h/d = 0.55$, $Fr_d = 2.0$.

$h/d = 0.55$ also takes place for the half submerged case ($h/d = -0.5$). A section treating this matter is included later.

Drag and lift coefficient time histories are shown in Fig. 9.27. The fact that the vortex shedding is recovered has a noticeable effect in these coefficients, with low amplitude high frequency oscillations and a normalised Strouhal of 0.98. The mean value of the drag coefficient is 0.92 and the lift coefficient presents small amplitude oscillations whose rms is approximately 0.07.

9.6.6 Froude number flow dependence summary

Regarding the wake structure, the von Kármán vortex shedding that has been found to occur for low Froude numbers ($Fr_d \approx 0.3$), is blocked for intermediate and high Froude numbers ($0.6 \leqslant Fr_d \leqslant 1.6$) and is recovered for very high Froude numbers ($Fr_d \approx 2$). A similar behaviour, in a different context, occurs for tilted cylinders piercing a free-surface Meunier 2012.

The free-surface elevation mean and rms intervals for the considered cases are displayed in Fig. 9.28. As can be seen, the amplitude and wave-length of the free-surface deformation grow with the Froude number. These are facts qualitatively consistent with the increase, for displacement hulls, of wave-making resistance with Froude number (see e.g. Lewis 1989).

A summary of computed forces can be seen in Fig. 9.29. The drag coefficient slightly diminishes as Froude number increases. Lift coefficient follows the opposite trend, with even weaker variations. A global explanation for these trends is, at this stage, not available. Working on it is left for future study.

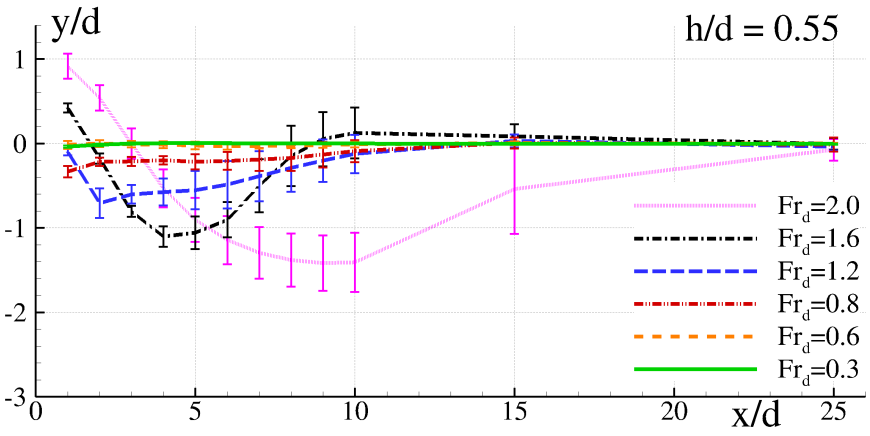

Figure 9.28.: Variation of the free surface profile with Froude number. $h/d = 0.55$

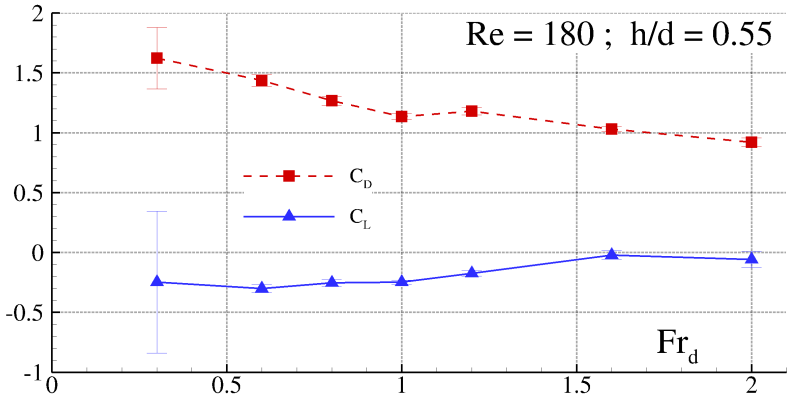

Figure 9.29.: Variation of horizontal and vertical force coefficients with Froude number for fixed $h/d = 0.55$.

h/d	Re	Fr_d	C_D	C_D/C_{D_∞}	C_L	$C_{L_{rms}}$	St	St/St_∞
0.55	180	0.3	1.61	1.26	-0.26	0.60	0.20	1.03
0.55	180	0.6	1.44	1.12	-0.30	0.03	-	-
0.55	180	0.8	1.26	0.98	-0.25	0.03	-	-
0.55	180	1.0	1.13	0.89	-0.25	0.01	-	-
0.55	180	1.2	1.19	0.93	-0.18	0.03	-	-
0.55	180	1.6	1.03	0.81	-0.02	0.03	-	-
0.55	180	2.0	0.92	0.72	-0.06	0.07	0.19	0.98

Table 9.4.: Sequence 2: Froude number flow dependence summary: $h/d = 0.55$. Mean values of C_D and C_L reported.

Fr_d	h/d	$\hat{H}/d$	$Fr_{\hat{H}}$	x_1/d	x_2/d
2.0	-0.50	14	0.53	-18	36
1.6	-0.50	9	0.53	-18	36
1.0	-0.50	6	0.41	-11	26
0.6	-0.50	6	0.24	-8	26
0.4	-0.50	6	0.16	-8	26

Table 9.5.: Sequence 3: case studies with half-submerged cylinder and varying Fr_d. $\Delta x/d = 0.02$ in all cases.

9.7 SEQUENCE 3: INFLUENCE OF FROUDE NUMBER ON FLOW CHARACTERISTICS FOR THE HALF-SUBMERGENCE CONDITION

As discussed in section 9.6.5 a transition in the kind of shedding occurs between $Fr_d = 1.6$ and $Fr_d = 2.0$ for $h/d = 0.55$, with the von Kármán street vortex being recovered in the latter, as predicted by Triantafyllou and Dimas 1989 linear free-surface stability analysis for a half-submerged cylinder. This fact has motivated the inclusion of a sequence with $h/d = -0.5$ and some cases with $h/d = 0$. The ones corresponding to $h/d = -0.5$ are specifically discussed in this section while those corresponding to $h/d = 0$ are just labeled when results are globally taxonomised later. In order to improve the readability it has been found convenient to start the discussion of this sequence by the highest Froude number case, moving down to smaller Fr_d cases.

9.7.1 Very high Froude number: $Fr_d = 2.0$ ((C/K)PI)

Coming to the case with $Fr_d = 2.0$, the fluid flows on top of the cylinder and a jet is formed. Although some flapping in the vorticity layers detaching from the cylinder can be appreciated (see Fig. 9.30), the von Kármán street vortex does not take place and most of the vorticity that is advected downstream is generated by consecutive plunging breakers.

Regarding drag and lift, the coefficients are quite stable, with a drag coefficient around 0.5 and a zero lift coefficient (see Fig. 9.31). The reduction in drag coefficient, from around 1.0 for $h/d = 0.55$ to $C_D = 0.5$ for $h/d = -0.5$, can be partially attributed to the fact that a significant part of the flow detaches from the cylinder surface, as can be appreciated in Fig. 9.30. As a final comment for this case, the very short duration of the initial transient is a distinct feature to be highlighted when comparing this case to the rest in the test matrix.

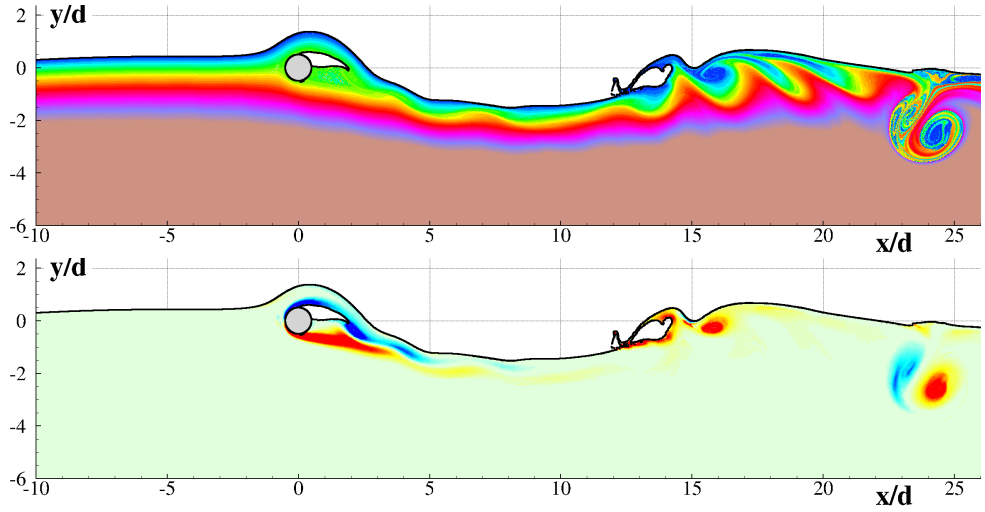

Figure 9.30.: Influence of Froude number on flow characteristics: $h/d = -0.5$, $Fr_d = 2.0$, $t(g/d)^{0.5} = 142.40$. (Flow label [C/K]PI) Vorticity field (bottom) plots. Dimensionless vorticity $\mathrm{curl}(\mathbf{u})\sqrt{d/g}$ scales from -3 (blue) to 3 (red).

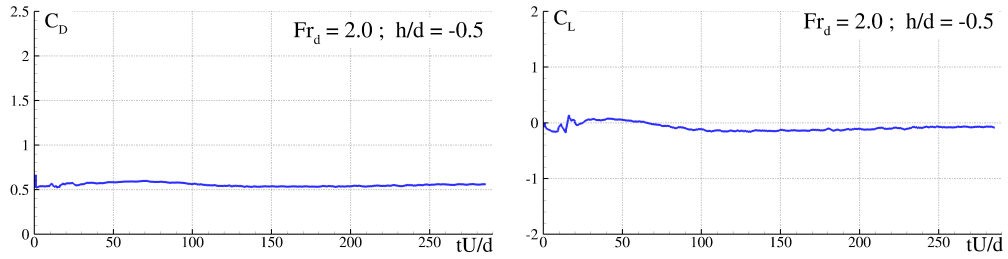

Figure 9.31.: Influence of Froude number on flow characteristics: drag and lift coefficient time histories. $h/d = -0.5$, $Fr_d = 2.0$.

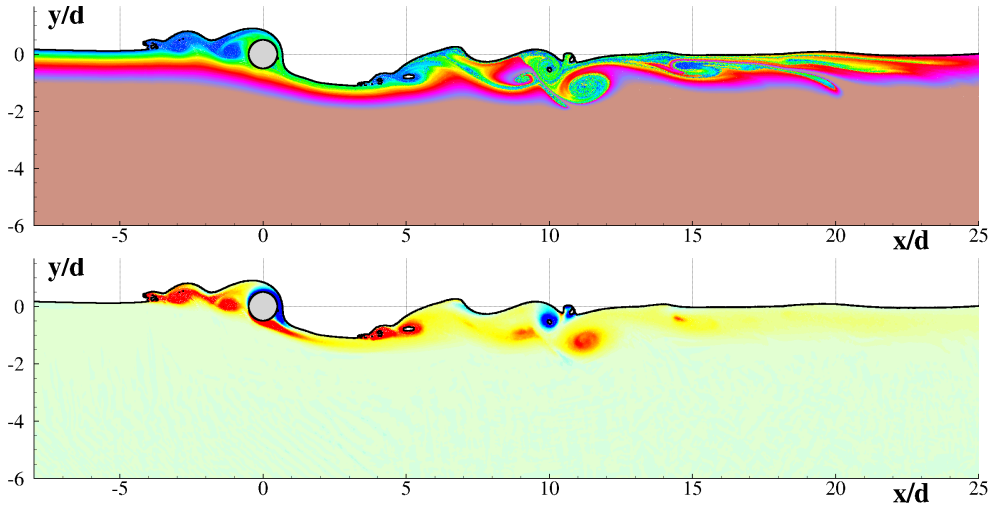

Figure 9.32.: Influence of Froude number on flow characteristics: $h/d = -0.5$, $Fr_d = 1.6$, $t(g/d)^{0.5} = 150$. (Flow label [B/C]PI) Streaklines (top) and vorticity field (bottom) plots. Dimensionless vorticity curl($\mathbf{u}$) $\sqrt{d/g}$ scales from -3 (blue) to 3 (red).

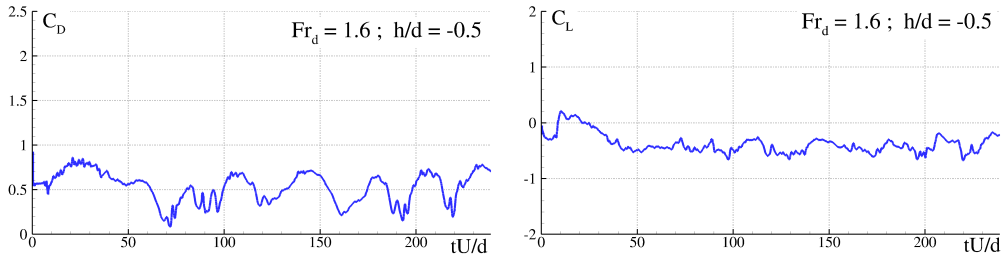

Figure 9.33.: Influence of Froude number on flow characteristics: drag and lift coefficient time histories. $h/d = -0.5$, $Fr_d = 1.6$.

9.7.2 High Froude number: $Fr_d = 1.6$ ((B/C)PI)

For $Fr_d = 1.6$, the flow is non-periodic. A layer of positive vorticity is generated at the bottom part of the cylinder, interacting downstream with the free surface breaking structures (see bottom panel of Fig. 9.32). The right-top part of the cylinder presents an intermittency phenomenon and becomes dry in some stages of the process (see top panel of Fig. 9.32 and video provided as supplementary material). This intermittency is reflected in both the lift and drag curves, which present significant oscillations lacking a periodic pattern (see Fig. 9.33). If a Fourier analysis is performed on the drag coefficient time history, the typical normalised Strouhal number of these oscillations is 0.13.

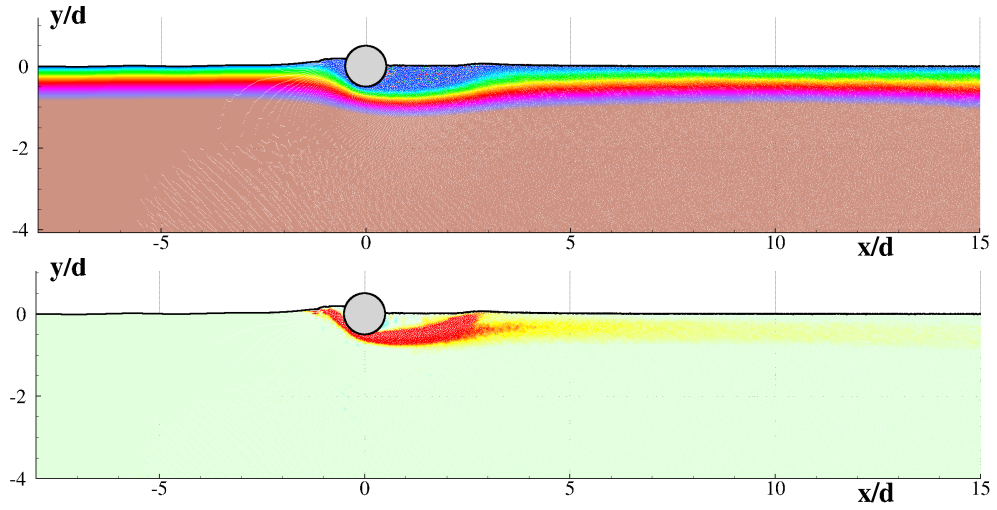

Figure 9.34.: Influence of Froude number on flow characteristics: $h/d = -0.5$, $Fr_d = 0.6$. (Flow label BFR) Streaklines (top) and vorticity field (bottom) plots, $t(g/d)^{0.5} = 200$. Dimensionless vorticity $\mathrm{curl}(\mathbf{u})\sqrt{d/g}$ scales from -1 (blue) to 1 (red).

9.7.3 Moderate Froude number: $Fr_d = 0.6$ (BFR)

The case with $Fr_d = 1.0$ was already discussed as part of sequence number one in section 9.5.5. This is the reason for the jump between $Fr_d = 1.6$ and the present section $Fr_d = 0.6$.

The streaklines and vorticity graphs are shown in Fig. 9.34. A small recirculation area is formed behind the cylinder, bounded by a thick layer of positive vorticity. The cylinder resembles a flow barrier that, unlike for $Fr_d = 1$, does not efficiently work as such. Actually, the particles at the free-surface just flow under the cylinder and form the recirculation area. The subsequent particles do not stay in that recirculation area but are advected downstream and come back to the free surface without being mixed with the bulk of the fluid, nor transported to low depth zones (see movie provided as supplementary material).

The positive vorticity layer creates a significant suction on the cylinder, leading to a negative lift coefficient of approximately -0.58. Lift presents slight oscillations, which can be related to the ones observable in the vorticity layer (see again movie).

The flow is overall radically different to the one corresponding to the same Froude number but with a submergence ratio $h/d = 0.55$, discussed in section 9.6.2, in which a jet of surface particles was projected into the cylinder wake. In that case, the drag coefficient reached a value of 1.5, while in this case it falls to around a value of 0.25, the lowest amongst all the analyzed cases.

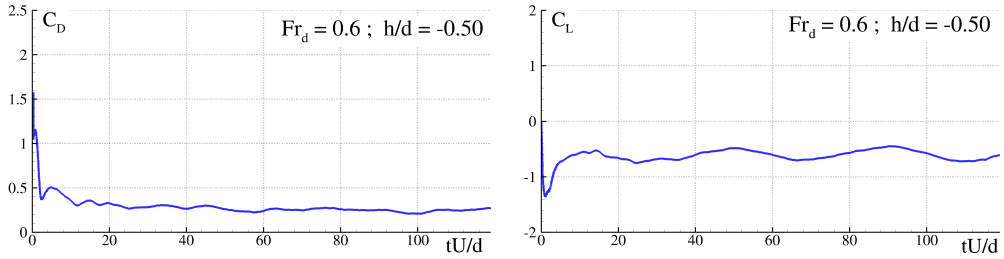

Figure 9.35.: Influence of Froude number on flow characteristics: drag and lift coefficient time histories. $h/d = -0.5$, $Fr_d = 0.6$.

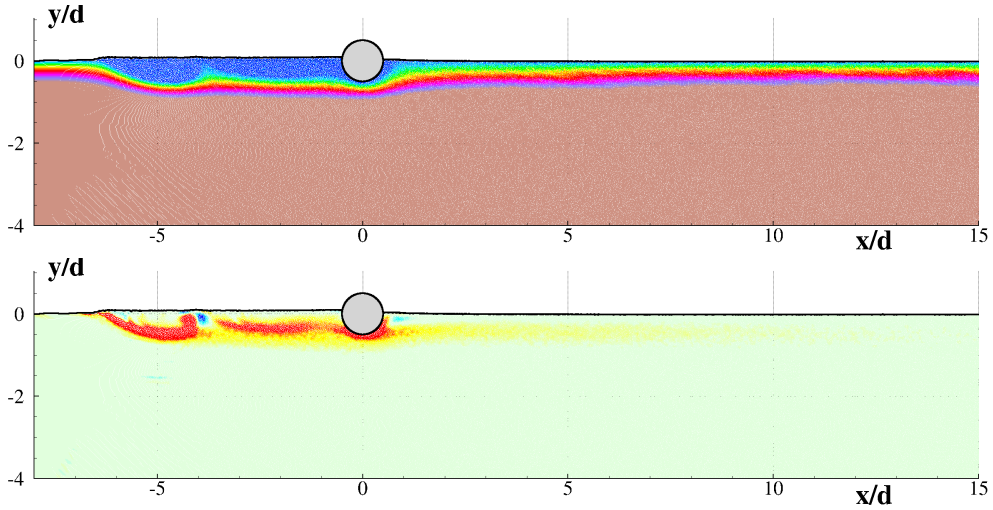

Figure 9.36.: Influence of Froude number on flow characteristics: $h/d = -0.5$, $Fr_d = 0.4$. (Flow label BFI) Streaklines (top) and vorticity field (bottom) plots, $t(g/d)^{0.5} = 600$. Dimensionless vorticity $\mathrm{curl}(\mathbf{u})\sqrt{d/g}$ scales from -1 (blue) to 1 (red).

9.7.4 Low Froude number: $Fr_d = 0.4$ (BFI)

The last case discussed in this half-submerged configuration sequence corresponds to a Froude number $Fr_d = 0.4$. A change in the flow pattern from 0.6 to 0.4 is noticeable in Fig. 9.36. In the latter, the cylinder quite effectively acts as a barrier for the transport downstream of the free surface fluid particles. The recirculation area is now formed upstream of the cylinder and positive vorticity is generated in this recirculation area.

Regarding force coefficients, the transient period is long for this case (see supplementary material movies). Drag coefficient tends to a value around 0.35 while lift coefficient reflects the mild suction generated by the positive vorticity layer below the cylinder, oscillating around a value of -0.25.

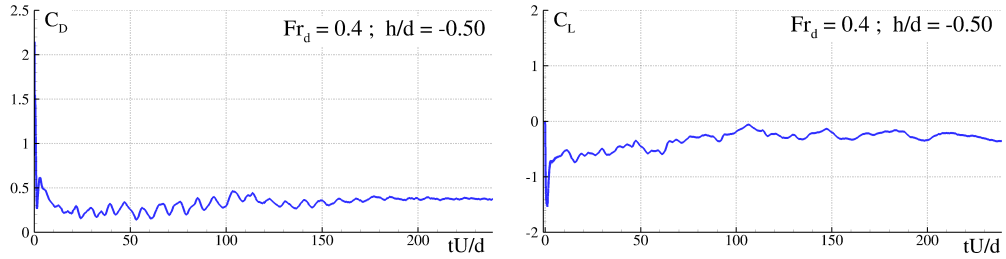

Figure 9.37.: Influence of Froude number on flow characteristics: drag and lift coefficient time histories. $h/d = -0.5$, $Fr_d = 0.4$.

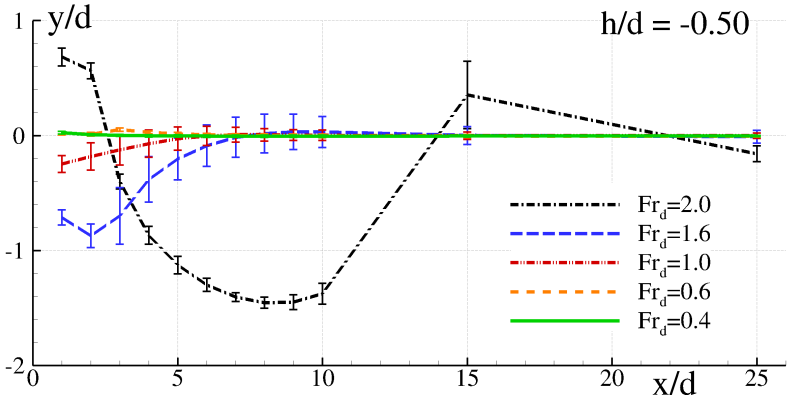

Figure 9.38.: Variation of the free surface profile with Froude number. $h/d = -0.5$

9.7.5 Influence of Froude number on flow characteristics for the half-submergence condition: summary

The free-surface elevation mean and rms intervals for the considered cases are displayed in Fig. 9.38. A downstream shift, with growing Fr_d, of the minimum, is visible, as was the case for the sister sequence 2 (see Fig. 9.28). Although, overall, the tendencies observed for $h/d = 0.55$ have survived when moving to the half-submerged condition, the difference between 1.6 and 2.0 profiles is now larger.

Force coefficients have been plotted in Fig. 9.39. The tendencies observed for $h/d = 0.55$ of decaying C_D with Fr_d do not hold for the half-submerged case, in which the drag coefficient experiences moderately low variations, with values much lower than those of $h/d = 0.55$. Lift coefficient is significantly different too, with significant negative values due to the suction of the positive vorticity generated below the cylinder and discussed when presenting the individual cases.

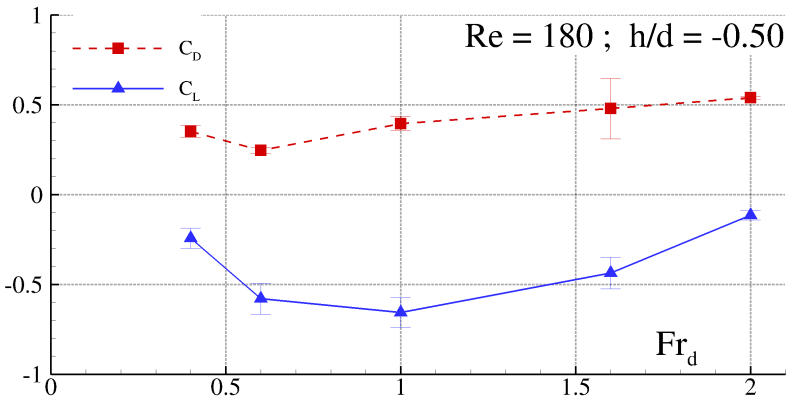

Figure 9.39.: Variation of horizontal and vertical force coefficients with Froude number for fixed $h/d = -0.5$.

h/d	Re	Fr_d	C_D	C_D/C_{D_∞}	C_L	$C_{L_{rms}}$	St	St/St_∞
-0.5	180	0.4	0.35	0.27	-0.24	0.06	-	-
-0.5	180	0.6	0.25	0.19	-0.58	0.09	-	-
-0.5	180	1.0	0.40	0.31	-0.66	0.08	-	-
-0.5	180	1.6	0.48	0.37	-0.44	0.09	0.03	0.13
-0.5	180	2.0	0.54	0.42	-0.11	0.03	-	-

Table 9.6.: Sequence 3: Froude number flow dependence summary: $h/d = -0.5$. Mean values of C_D and C_L reported.

Fr_d	h/d	$\hat{H}/d$	$Fr_{\hat{H}}$	x_1/d	x_2/d
2	1.0	16	0.50	-18	36
2	1.5	16	0.50	-18	36
2	2.5	16	0.50	-18	36

Table 9.7.: Sequence 4: influence, at very high Froude number, of submergence on flow characteristics: test matrix. $\Delta x/d = 0.02$ in all cases.

9.8 SEQUENCE 4: INFLUENCE OF SUBMERGENCE ON FLOW CHARACTERISTICS AT VERY HIGH FROUDE NUMBER, $Fr_d = 2$.

This is the fourth and last sequence considered in the present work (see Fig. 9.2). It replicates the initial sequence of section 9.5 but doubles the Froude number, from 1.0 to 2.0. The motivation for this sequence is to understand how this increase in the Froude number affects the dynamics across different submergences. Some of these very high Froude number cases, namely those corresponding to the sequences 2 and 3, have been discussed in those sequences and therefore, only the ones not considered there are treated in this section. A list of these new cases, using the notation of Fig. 9.1, is presented in Table 9.7. Those with the same submergence of the cases discussed in detail in sequence one, are treated next.

9.8.1 Large gap ratio (deep submergence), $h/d = 2.5$ (KSN)

A very noticeable von Kármán street vortices wake has been found for this case (see Fig. 9.40), analogous to the one discussed for the same submergence case with $Fr_d = 1$ in section 9.5.1. The periodicity of the wake is reflected in the force coefficients: the normalised drag coefficient is 0.82 compared to 1.24 for $Fr_d = 1.0$. The rms of the lift also drops, from 0.57 to 0.18. By contrast, the Strouhal number remains similar, very close to the reference unbounded conditions value. (see Fig. 9.41).

Regarding the free surface shape, while it remains almost flat for $Fr_d = 1$, a long and large amplitude wave is found for $Fr_d = 2.0$, whose length is in agreement with potential flow theory for deep condition water waves obtained from linear dispersion relation (see e.g. Dean and Dalrymple 1991).

9.8.2 Moderate gap ratio (intermediate submergence), $h/d = 1.5$ (KSI)

The von Kármán street vortices wake occurring for the deepest submergence case persists as we move to a smaller submergence, $h/d = 1.5$ (see Fig. 9.42).

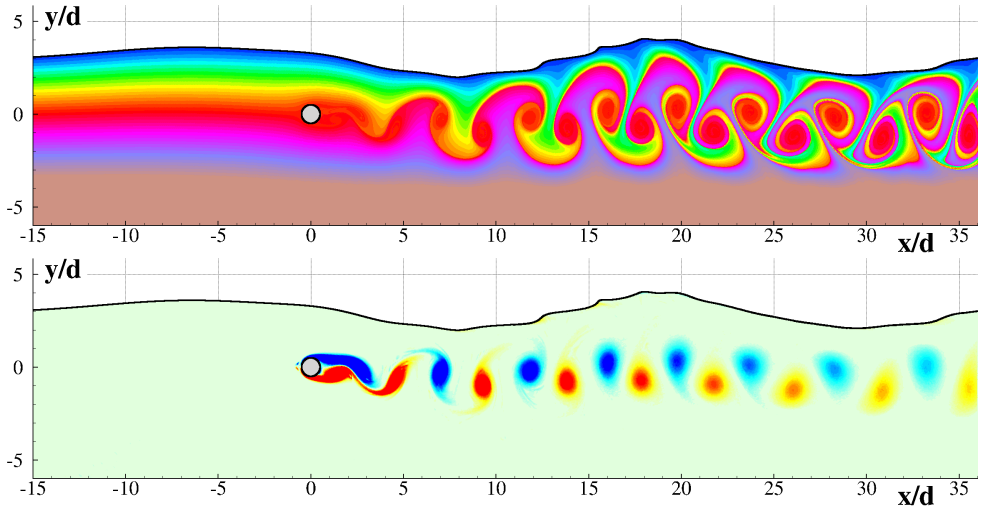

Figure 9.40.: Influence of Froude number on flow characteristics: $h/d = 2.5$, $Fr_d = 2.0$. (Flow label KSN) Streaklines (top) and vorticity field (bottom) plots, $t(g/d)^{0.5} = 100.0$. Dimensionless vorticity $\mathrm{curl}(\mathbf{u})\sqrt{d/g}$ scales from -2 (blue) to 2 (red).

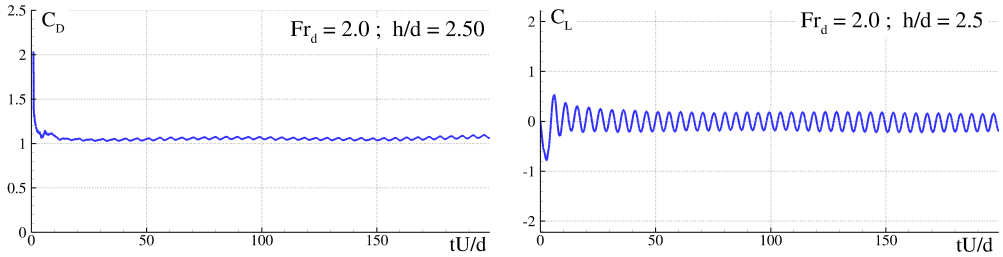

Figure 9.41.: Influence of submergence on flow characteristics: drag and lift coefficient time histories. $h/d = 2.5$, $Fr_d = 2$.

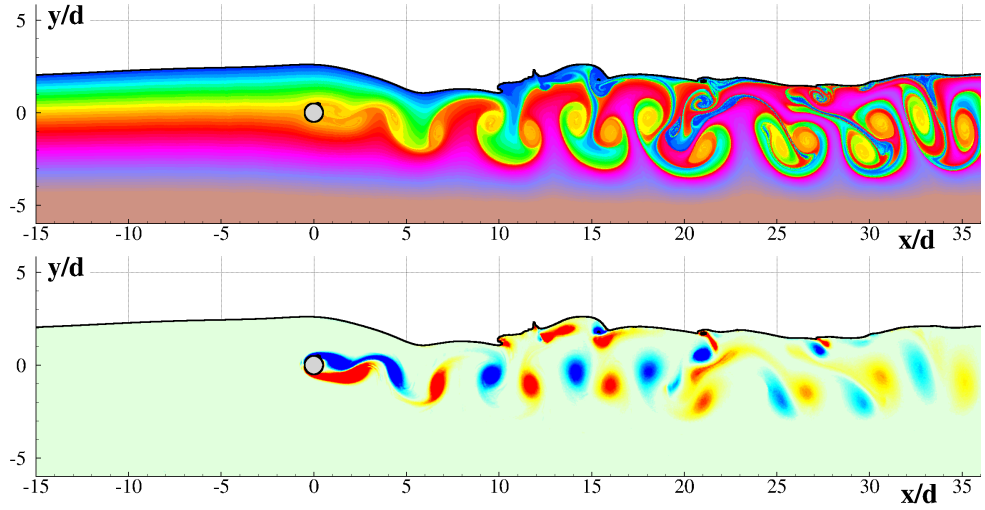

Figure 9.42.: Influence of Froude number on flow characteristics: $h/d = 1.5$, $Fr_d = 2.0$. (Flow label KSI) Streaklines (top) and vorticity field (bottom) plots, $t(g/d)^{0.5} = 70.0$. Dimensionless vorticity $\mathrm{curl}(\mathbf{u})\sqrt{d/g}$ scales from -2 (blue) to 2 (red).

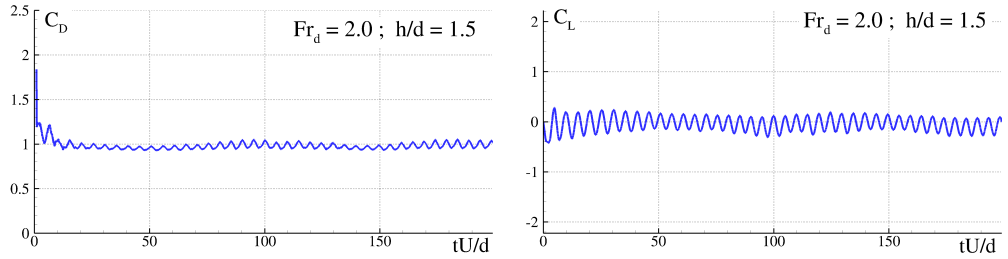

Figure 9.43.: Influence of submergence on flow characteristics: drag and lift coefficient time histories. $h/d = 1.5$, $Fr_d = 2$.

They were also present for the same submergence case with $Fr_d = 1$. Similar tendencies for the force coefficients and shedding frequency found for $h/d = 2.5$ are also present in this submergence (Fig. 9.43).

Regarding the free surface shape, a significant amplitude trough is noticeable just downstream from the cylinder, larger than the one found for $Fr_d = 1.0$, with a more intense breaking taking place at the free surface.

9.8.3 Influence of submergence at very high Froude number $Fr_d = 2$ on flow characteristics: summary

The free-surface elevation mean and rms intervals for the cases corresponding to sequence 4 in Fig. 9.2 are displayed in Fig. 9.44. It comprises not only

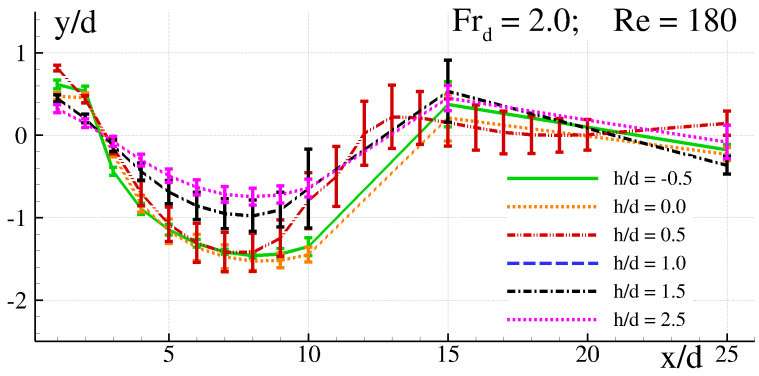

Figure 9.44.: Variation of the free-surface profile with submergence: $Fr_d = 2.0$.

the data of the two cases that have been presented but those which belonged to the intersection between sequences 2-3 and 4. A very consistent trough, of around one diameter amplitude downstream from the cylinder, is noticeable across all submergences considered. According to the variability interval, the unsteadiness is at it maximum for the case with $h/d = 0.5$. The free-surface profiles were radically different for the sister sequence number 1 presenting then a much larger variability across the range of considered submergences, as can be appreciated looking at Fig. 9.16.

Regarding the forces, a summary of computed forces can be seen in Table 9.8 and graphically in Fig. 9.45, including bars for the oscillation amplitudes. The drag coefficient increases slightly with submergence, from 0.5 for $h/d = -0.5$ to approximately $C_D = 1.0$ for $h/d = 0.5$, remaining basically constant for larger submergences. The behaviour was similar for $Fr_d = 1$ (see Fig. 9.17) but the value found there for the larger submergences was approximately 1.5, equally closer, but above the unbounded cylinder case. This difference suggests that we may have to go to much larger submergences for $Fr_d = 2.0$ to approach the unbounded domain limit.

The lift coefficient is slightly negative for $h/d \leqslant 0$ and close to zero for the rest of submergences. This value presented a more complex behaviour for $Fr_d = 1$, consistent with the fact that the flow presented a larger variability.

Regarding the Strouhal number, while slightly larger values than the unbounded flow condition reference values were found at $Fr_d = 1.0$ in the previous case, here they are very similar and stable across the different submergences.

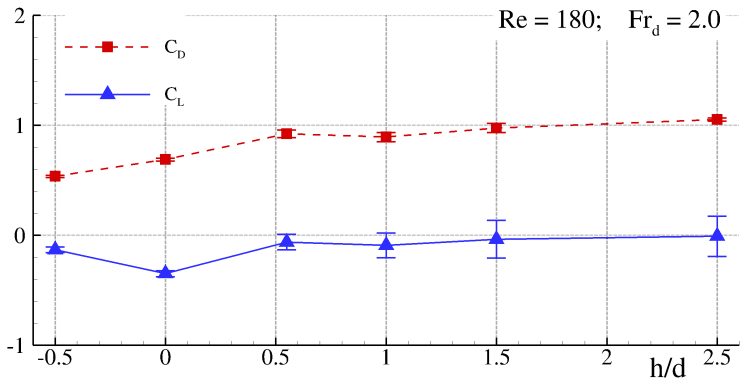

Figure 9.45.: Variation of horizontal and vertical force coefficients with submergence: $Fr_d = 2$.

h/d	Re	Fr_d	C_D	C_D/C_{D_∞}	C_L	$C_{L_{rms}}$	St	St/St_∞
-0.5	180	2.0	0.54	0.42	-0.13	0.03	-	-
0.0	180	2.0	0.69	0.54	-0.35	0.03	-	-
0.6	180	2.0	0.92	0.72	-0.06	0.07	0.19	0.98
1.0	180	2.0	0.89	0.70	-0.09	0.11	0.20	1.03
1.5	180	2.0	0.98	0.76	-0.04	0.17	0.20	1.04
2.5	181	2.0	1.05	0.82	-0.01	0.18	0.20	1.07

Table 9.8.: Sequence 4: results summary on flow dependence on submergence at very high $Fr_d = 2.0$. Mean values of C_D and C_L reported.

9.9 INFLUENCE OF THE COMPUTATIONAL DOMAIN SIZE AND RESOLUTION ON THE RESULTS

9.9.1 Channel depth

A first set of tests with varying channel depth, aimed at evaluating the influence of the bottom position on the dynamics, is considered. A representative intermediate, $Fr_d = 1.0$, as well as the maximum Froude number considered, $Fr_d = 2.0$, have been chosen, with $h/d = 0$. A summary of channel depths analysed, assuming the notation of Fig. 9.1, is presented in Table 9.9.

$\hat{H}/d$	h/d	Re	$Fr_{\hat{H}}$	Fr_d	x_1/d	x_2/d	$\Delta x/d$
4	0	180	0.50	1	-11	26	0.04
6	0	180	0.41	1	-11	26	0.04
11	0	180	0.30	1	-11	26	0.04
20	0	180	0.22	1	-11	26	0.04
44.5	0	180	0.30	2	-18	36	0.04
22.5	0	180	0.42	2	-18	36	0.04
15.5	0	180	0.51	2	-18	36	0.04
9	0	180	0.67	2	-18	36	0.04

Table 9.9.: Dimensions of the computational domain: influence of the channel depth, $\hat{H}$. Numerical tests matrix with fixed $Fr_d = 1$.

For cases with $Fr_d = 1$, the results for drag and lift curves are shown in Figure 9.46 where it can be appreciated that drag coefficient curves are similar in shape but their values present significant variations if $Fr_{\hat{H}}$ is larger than 0.3. These differences are explained on the basis of the influence that the presence of the bottom has on the flow, deforming the streamlines (see Fig. 9.47). However, looking at that same figure, such influence can be considered not so significant in regards to the type of flow that appears in the wake.

Regarding cases with $Fr_d = 2.0$, drag coefficient shows little dependence with $Fr_{\hat{H}}$ and if $Fr_{\hat{H}} \leqslant 0.5$ the channel depth does not seem to influence the value of the lift coefficient (see Fig. 9.48). Considering this brief analysis, simulations have been conducted with a maximum value of $Fr_{\hat{H}} = 0.42$ for low and moderate Fr_d cases and with a maximum value of $Fr_{\hat{H}} = 0.5$ for high Fr_d cases.

9.9.2 Inflow and outflow boundaries

Regarding the positions of the inflow and outflow boundaries, the presence of the cylinder in the flow creates waves that propagate downstream and up-

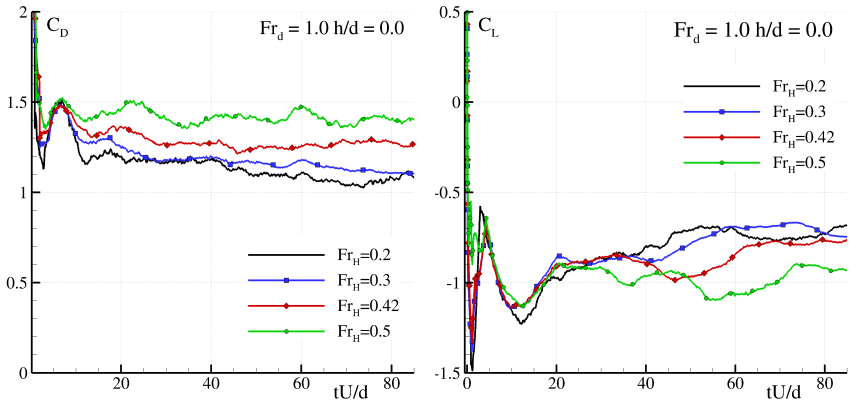

Figure 9.46.: Dimensions of the computational domain: influence of the channel depth, $\hat{H}$. Drag and lift coefficient time histories (Froude number Fr_d=1.0).

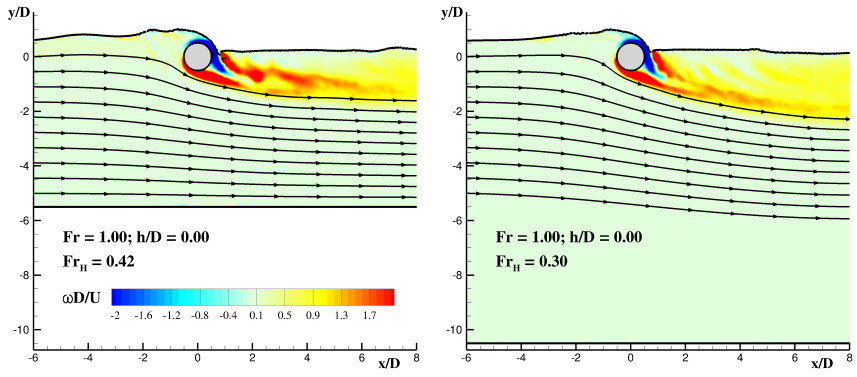

Figure 9.47.: Dimensions of the computational domain: influence of the channel depth, $\hat{H}$. Enlarged view of the vorticity field and streamlines around the cylinder at $Fr_d = 1.0$ and $h/d = 0$: Left $Fr_H = 0.42$, right $Fr_H = 0.30$.

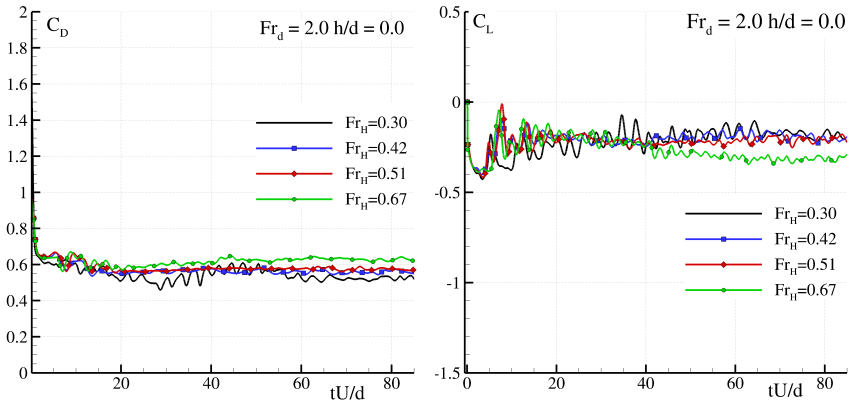

Figure 9.48.: Dimensions of the computational domain: influence of the channel depth, $\hat{H}$. Drag and lift coefficient time histories (Froude number Fr_d=2.0).

$\hat{H}/d$	h/d	Re	$Fr_{\hat{H}}$	Fr_d	x_1/d	x_2/d	$\Delta x/d$
6	0	180	0.41	1	-11	26	0.04
6	0	180	0.41	1	-16	26	0.04
6	0	180	0.41	1	-8	34	0.04

Table 9.10.: Influcence of the inflow and outflow position, $Fr_d = 1$: test matrix.

stream. The position of the boundaries must be such that, on one hand, the homogeneity of the inflow velocity is guaranteed and, on the other, the wake and downstream free surface shape are not affected by the outflow boundary position.

In order to verify such matters, a set of numerical tests has been considered, with $Fr_d = 1$ and $h/d = 0$ and 0.4. The channel depth is also fixed, $H/d = 6$. A summary of the cases analyzed is presented in Table 9.10.

The Drag and Lift obtained are plotted in Fig. 9.49. The position of the outflow modifies the time history but has only a small effect on the mean value.

The influence of the inflow and outflow boundary position has also been analyzed in another condition, namely for $Fr_d = 0.55$ and $h/d = 0.4$. This condition is quite significant since it was the focus of a dedicated analysis by Reichl et al. 2005. The tests are summarised in Table 9.11.

The drag and lift coefficients obtained are plotted in Fig. 9.50. Again, the position of the outflow boundary modifies the time history but has only a minor effect on the mean value. Considering both analyses, the simulations have been conducted with inlet boundaries verifying that $x_1/d \leqslant -8$ and outlet ones with $x_2/d \geqslant 26$.

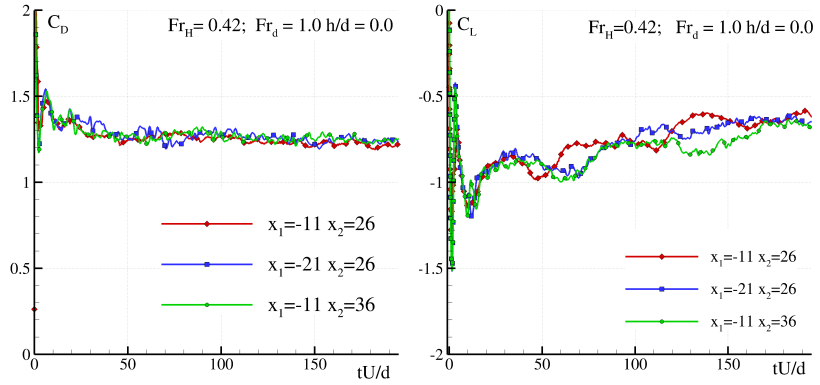

Figure 9.49.: Influence of the position of inflow and outflow: close up view of the drag and lift coefficient time history.

$\hat{H}/d$	h/d	Re	$Fr_{\hat{H}}$	Fr_d	x_1/d	x_2/d	$\Delta x/d$
6.9	0.4	180	0.21	0.55	-8	26	0.04
6.9	0.4	180	0.21	0.55	-21	26	0.04
6.9	0.4	180	0.21	0.55	-11	36	0.04

Table 9.11.: Influence of the inflow and outflow position, $Fr_d = 0.55$: test matrix

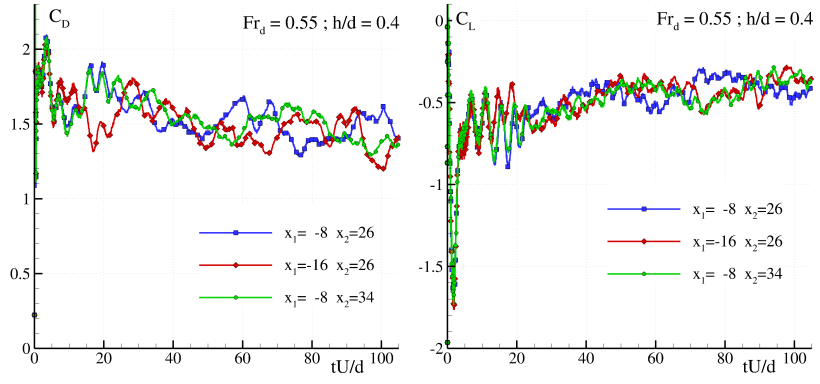

Figure 9.50.: Drag and lift coefficient time histories. Influence of the inflow/outflow boundaries position.

9.9.3 Numerical resolution

It could be argued that the previous sections discussion on influence of the domain size could be affected by the particle resolution. This question is closely related to the convergence of the numerical scheme. A set of checks have been devised with the following characteristics:

1. $Fr_d = 1.0$, $h/d = 0$, fixed channel depth $\hat{H}/d = 6$, inlet/oulet boundaries at $x_1/d = -11$, $x_2/d = 26$, respectively, and two different particle resolutions: $\Delta x/d = 0.01, 0, 02, 0.04$.

   In Fig. 9.51 the time histories of the drag & lift coefficient for these cases are plotted. Both coefficients appear to have converged, with negligible differences between $\Delta x/d = 0.01$ and $\Delta x/d = 0.02$ curves. From this, it can be deemed that $\Delta x/d = 0.02$ could be enough to perform the simulations. Since the increase in computational cost, due to using a larger number of particles, is, in some cases, admissible, full computations discussed have been carried out with either $\Delta x/d = 0.02$ or with the finest resolution, $\Delta x/d = 0.01$.

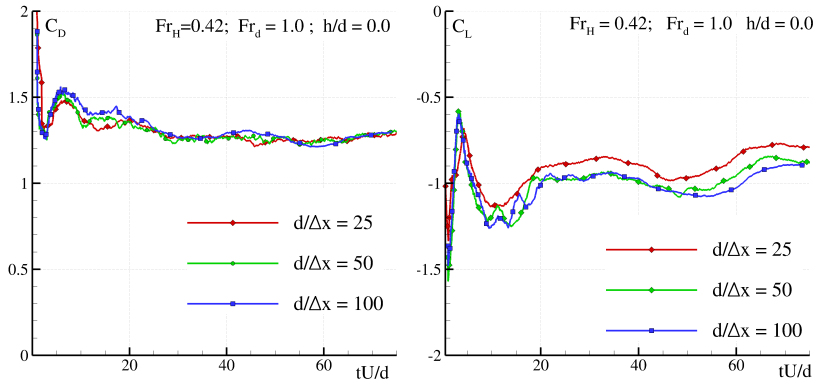

Figure 9.51.: Drag and lift coefficient time histories. Influence of the spatial resolution (Froude number Fr_d=1.0).

2. $Fr_d = 2.0$, $h/d = 0$, fixed channel depth $\hat{H}/d = 9$, inlet/oulet boundaries at $x_1/d = -18$, $x_2/d = 36$, respectively, and two different particle resolutions: $\Delta x/d = 0.02, 0.04$.

   In Fig. 9.52 the time histories of the drag & lift coefficients for $Fr_d = 2.0$ cases are plotted. There is some difference in the drag coefficient while the lift coefficient for both resolutions fits within a narrow band. The results can be considered close enough to justify the use of a resolution of $\Delta x/d = 0.02$ for high Froude number cases. This means it is not necessary

to resort to $\Delta x/d = 0.01$, which would be too computationally demanding due to the domain sizes required for these high Froude number cases.

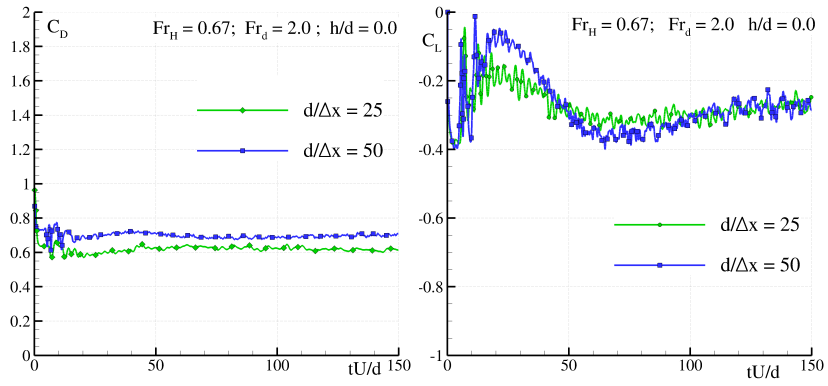

Figure 9.52.: Drag and lift coefficient time histories. Influence of the spatial resolution (Froude number Fr_d=2.0).

9.10 SUMMARY OF THE CHAPTER

This study has examined two-dimensional monophasic flow past a horizontal circular cylinder intersecting, or close to, a free surface at low Reynolds number, 180. It has looked at low, moderate and large Froude number (between 0.3 and 2.0), based on the cylinder diameter. The numerical technique used has been the meshless method Smoothed Particle Hydrodynamics. The detached flow pattern dependence on the submergence of the cylinder and on the Froude number has been investigated. Vorticity, mixing processes, vortex generation patterns, free-surface breaking, and drag/lift coefficient behaviour have been discussed. Taking advantage of the Lagrangian nature of the solver, mixing processes have been documented with more detail than previous studies.

An analysis based on varying the cylinder submergence has been carried out fixing the Froude number to a value of one. For large submergences the flow has been found to behave similarly to unbounded flows, with von Kármán street of vortices developing at a frequency comparable to classic unbounded flows literature. As the submergence is reduced, certain mixing with the free surface occurs and substantial breaking takes place. Moreover, it has been found that below a certain distance from the free surface, the classical von Kármán street of shedding vortices does not take place, while moderate vortex shedding departs from vorticity generated at the free surface. In some of these cases, consecutive vortices may merge, leading to the formation of a large

meta-vortex which is advected downstream, a previously unreported form of wake instability to the authors' knowledge.

Within the submergence dependence analysis, computations have been carried out for a cylinder in contact with the undisturbed free surface as well as a half submerged cylinder. In both cases the Froude number was equal to one. For these configurations, the vorticity layer remains fixed between the cylinder and the free surface, and a recirculating area at the wake develops.

Regarding the dependence of the flow on Froude number, an analysis has been carried out for a submergence ratio of 0.55, which had been given some attention in previous literature at low and moderate Froude numbers. That range has been extended here reaching up to a value of 2. For this submergence, up to Froude number 1.6, the von Kármán vortex shedding is blocked, but that is not the case when the Froude number reaches a value of 2. This transitional effect is in agreement with the stability analyses of half submerged cylinders in the existing literature.

In order to investigate whether this transition occurred for the half submerged condition, a dedicated sequence was set up. For the high Froude number cases, the incoming fluid flows over the cylinder and the von Kármán street vortex does not take place. For lower Froude number cases, the cylinder acts as a barrier to the incoming flow.

Finally the dependence of the flow on submergence for the highest Froude number, 2.0, was investigated. The free surface shows less variability when compared to the sequence with $Fr_d = 1.0$. In the deepest submergence case, the flow physics has some resemblances with potential flow water waves.

Drag and lift coefficients have not been the main focus of the present work. They have however been investigated and found coherent with the physics described for each analyzed condition. In addition, these drag and lift coefficients have been found to compare reasonably with experimental results available in the literature for larger Reynolds number regimes.

Some questions have been, for different reasons, left open, and remain as future work goals:

1. The matrix of cases completed in the present work has significantly extended previously existing literature. However, in order to have a more detailed map of the flow dependence on Froude number and submergence ratio, a matrix with more test cases would be necessary.

2. An explanation of the drag and lift coefficient tendencies when varying the Froude number for a fixed submergence is left for future work.

3. In some of previous experimental and numerical works, the existence at low submergences of meta-stable states characterised by low frequency flapping of the jet projected from the free surface into the cylinder wake, had been described. Flow patterns that resemble such behaviour have

been found in the present research for low submergences and moderate Reynolds numbers. However, it remains as future research to conduct longer simulations under those conditions which may allow the detection of whether such distinct instability types are replicated.

4. The analysis conducted in some of the cases presented in this chapter suggests some relationship between the metastable states, and the large meta-vortices, could exist. This aspect also deserves further investigation.

5. A coupled model of the flow around the cylinder and corresponding forces with a dynamic model such as that used by Ding et al. 2013, overcoming its limitations when close to a free surface, is an interesting future research goal.

6. A final relevant future work line, related to the previous one, is the dynamics of a cylinder subjected to a uniform current, its own buoyancy and one, or several, mooring tethers, in the presence of a free surface. This dynamics shares similarities with that investigated by Fani and Gallaire 2015 in the case of a cylindrical pendulum subjected to its own weight, tether reaction and the fluid dynamic forces.

10 NUMERICAL AND EXPERIMENTAL INVESTIGATION OF NONLINEAR SHALLOW WATER SLOSHING

10.1 INTRODUCTION

Sloshing flows are those occurring when free-surface waves are generated inside tanks, usually creating significant global and local loads on the tank due to the impact of travelling waves. An abundant literature on sloshing can be found, reviewed in the book of Prof. Ibrahim (Ibrahim 2005), and in the more recent book of Prof. Faltinsen and Prof. Timokha (Faltinsen and Timokha 2009).

These phenomena are of interest for several branches of engineering including marine, aerospace and civil engineering. Nowadays, the sloshing phenomenon is particularly important for Liquefied Natural Gas carriers (LNG hereinafter). During LNG operative life, sloshing may prevent to operate in some particular filling conditions. The capability to properly predict the dynamic local and global loads acting on tanks for any filling condition is a challenge for any numerical algorithm. Specifically, when the frequency spectrum of the ship motion is focused on the region close to the lowest natural tank mode, violent free-surface flows may appear, inducing large local loads (see Faltinsen et al. 2004) and increasing the risk for the integrity of the structure.

Among the sloshing flows, low filling depth conditions are attractive due to the wave systems that are generated under these depth conditions, as example travelling waves and bores - *i.e.* hydraulic jump (Olsen and Johnsen 1975). A first attempt of classification of the different wave systems has been proposed by Olsen and Johnsen 1975 who, however, only focused their analysis on a single sloshing case (i.e., filling height and amplitude excitation) for the roll motion. In Bridges 1986, the transition from cnoidal waves to travelling hydraulic jump is discussed for larger wave amplitudes. Following the work of Olsen and Johnsen 1975, a wider analysis is tried in the present work. Specifically, we focus on the sway motion (horizontal amplitude excitation) and consider a broad range of frequencies, filling conditions and amplitude excitations. When possible, the sloshing motions are classified by following Olsen & Johnsen while a novel configuration is added for those wave systems that are not described in their work.

An extensive experimental campaign has been carried out at CNR-INSEAN in the shallow-water regime to investigate the sloshing response in a wide range of frequency and amplitude excitations. Specifically, moderate and large sway amplitudes have been tested for five filling heights and a narrow rectan-

gular tank has been used to limit the 3D effects. Regarding the small amplitudes regime, the experimental campaign of Lepelletier and Raichlen 1988 has been used.

The numerical simulations have been performed to cover the configurations where no experiments were available to provide an exhaustive description of the shallow-water sloshing motion. In order to have a complete understanding of such a phenomenon and to recover some information not available with the experiments (e.g., wave elevation on the whole tank), the numerical simulations have been performed on a set of cases overmatching the experimental tests. Because of the major role played by nonlinearities and of the complex free-surface evolution (e.g., fragmentation and wave breaking), the numerical simulation of violent sloshing flows is a very demanding problem. In this context, the SPH scheme has proved to be a reliable choice (see, for example Bouscasse et al. 2007; Bulian et al. 2010; Colagrossi et al. 2010; Souto-Iglesias et al. 2006), thanks to its Lagrangian structure and to the absence of any computational grid. In particular, here, the δ-SPH scheme is adopted.

In all the simulations/experiments, a rectangular tank is used and the frame of reference is set like in figure 10.1. Specifically, L and D indicate the tank length and breath respectively, h the filling height and $k = \pi/L$ the wave number.

10.2 CNR-INSEAN EXPERIMENTAL SET-UP

The tank used during the experimental campaign at CNR-INSEAN is $L = 1$ m long, $D = 0.1$ m wide and is filled with water up to a height h. To ensure a purely sinusoidal motion, $A\sin(2\pi t/T)$ along the longitudinal direction, an *ad hoc* mechanical system has been used. Here A is the displacement amplitude and T is the period of the prescribed motion. The geometry of the tank, *i.e.* $D/L = 0.1$, ensures an almost-2D flow in the main tank plane.

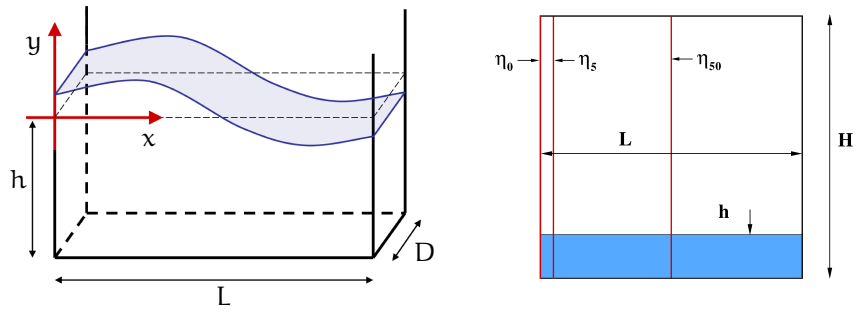

Figure 10.1.: Left: sketch of the tank and of the frame of reference. Right: sketch of the probes used during the experimental campaign at CNR-INSEAN.

Three capacitance wave probes are placed at the sides of the tank. The first one η_1 is positioned at a distance of 1 cm from one side, the second one η_5 at distance of 5 cm and the third one η_{50} at the middle of the tank. During the tests, flow visualisations have been performed through a digital video camera (JAI CV-M2). This camera has a spatial resolution of 1600x1200 pixels and frequency rate equal to 15 Hz. It has been placed in front of the tank and sufficiently far from it to record the global behaviour of the wave propagating. Finally, a wire potentiometer has been used for a direct measurement of the position of the tank. Particular care has been devoted to the synchronisation of the several acquisition systems with different sampling rates, used for the recording of the signals.

10.3 NUMERICAL SPH SIMULATION AND TUNING OF THE VISCOSITY

Simulations of sloshing problems generally require a huge computational time, even in a 2D framework. Indeed, it is necessary to overcome the transitory stage and reach a periodic state condition. The time needed for each run depends on the spatial resolution and the time step adopted. A large convergence study has been performed and the tests shown are simulated with a sufficient discretization.

Apart from these aspects, the average cost for each sloshing test case is of about 10 hours with an optimised parallel code running on 8 Xeon 2.33 GHz cores. To cover all the cases presented in this work, about 250 simulations have been run, simulating about ten hours of physical time.

The Reynolds number of the sloshing experiments considered in the present work is of the order $\mathcal{O}(10^5)$. In this context, the flow is turbulent and three-dimensional, therefore, an direct numerical simulation should model turbulence along with the viscous dissipations induced inside the fluid bulk and by the boundary layers. This would imply the modelling of small-scale phenomena which are very complex and that would lead to an enormous computational time.

In the sloshing literature these small-scale effects are generally approximated or neglected entirely, leading to simplified models (see, for example, Faltinsen and Timokha 2001, Hill 2003, Faltinsen et al. 2006). The validity of the approximations is checked "a posteriori" by comparison with experiments. This is also the procedure adopted in the present work.

In sloshing numerical simulations the turbulence is generally neglected while the viscous dissipations due to boundary layers is represented through approximated models. Under the hypothesis that the flow is laminar and using a

first-order solution, Keulegan 1959 obtained the following damping term for the kinetic energy of the sloshing motion:

$$\beta = 4\nu k^2 + \sqrt{\frac{kc\nu}{2}}\left(\frac{2h+D}{hD}\right), \tag{10.1}$$

where $k = \pi/L$ is the wave number, ν is the kinematic viscosity of the fluid and c is the shallow water celerity, that is, $c = \sqrt{gh}$. The above expression represents the mean dissipation rate during a period of the evolution and takes into account both the dissipation in the fluid bulk (first term in the right-hand side) and the dissipation due to the boundary layers at the tank walls (second term in the right-hand side). Conversely, for an SPH scheme with free-slip conditions along solid boundaries (that is, like the SPH scheme adopted here), the damping coefficient for gravity waves is $\beta_{SPH} = 4\nu_{SPH}k^2$ (see Antuono et al. 2012b for details).

Since the structure of the SPH damping coefficient is intrinsically different from (10.1), the SPH can only approximately model the dissipation due to boundary layer. However, a good approximation is to require that the order of magnitude of β_{SPH} is similar to that of β. After several tests, it is found that

$$\beta_{SPH} \simeq 0.2\,\beta \tag{10.2}$$

generally gives a good agreement between experiments and SPH results. This approximation allows choosing the value of the SPH viscosity. Using the celerity $\sqrt{gh}$ as a reference velocity and ν_{SPH}, it is possible to define a Reynolds number for the SPH scheme:

$$Re_{SPH} = \frac{h\sqrt{gh}}{\nu_{SPH}} = h\sqrt{gh}\,\frac{20}{\beta}\left(\frac{\pi}{L}\right)^2. \tag{10.3}$$

This is used in the following to express the SPH viscosity as a function of the damping coefficient β. It has been checked that limited variations of the coefficient 0.2 in (10.2) do not induce significant changes in the SPH simulations. This confirms that, notwithstanding the relation (10.2) is quite a rough approximation, what is really relevant for the SPH model is the order of magnitude of the numerical viscosity more than the choice of an hypothetical "exact" value for ν_{SPH}.

10.4 NONLINEAR SHALLOW WATER SLOSHING INSIDE A SWAYING TANK

The shallow water flows that occur in a sloshing tank either subjected to sway or roll motion are extremely dependent on the excitation frequency. Olsen

and Johnsen 1975 performed some systematic studies on the roll motion. They found that for very low excitation the sloshing is characterised by a standing wave (I in figure 10.2). For slightly higher excitation frequency, a set of small travelling waves appears (II in figure 10.2). With a small rise in frequency, the train of waves is suddenly transformed into a bore (*i.e.* hydraulic jump) that travels from mid section (III in figure 10.2). For even higher frequency, the bore travels from one side of the tank to the other (IV in figure 10.2). If the frequency keeps rising, the bore becomes a solitary wave (or more precisely a 1-mode cnoidal standing wave following Bridges 1986) (V in figure 10.2). The presence of these different propagation patterns highlights the complexity

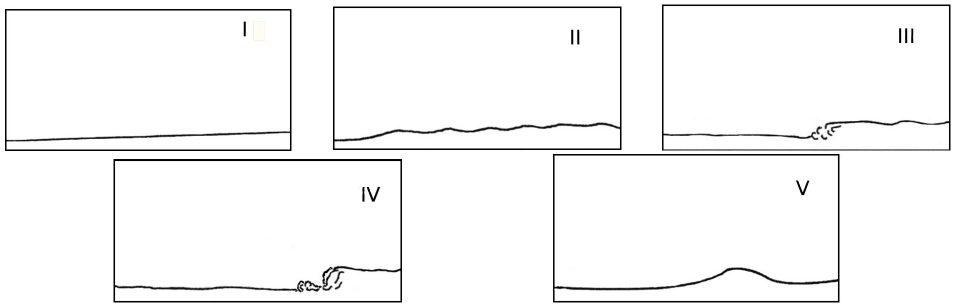

Figure 10.2.: Free-surface patterns described by Olsen and Johnsen 1975 for shallow-water roll motion.

and the non-linearities involved in the phenomena. These flow features are strongly dependent on the excitation amplitude A, the circular frequency of oscillation ω and the filling height h.

The sloshing phenomenon is characterised by natural frequencies of oscillations. These are derived using the linear theory as a first-order approximation and read:

$$\omega_r^{(n)} = \sqrt{g\,n\,k\tanh(n\,k\,h)} \qquad n = 1, 2, 3, \ldots \tag{10.4}$$

For the ease of the notation, the lowest natural frequency (that is, $n = 1$) it is simply denoted by ω_r. Violent surface-wave response may take place when the forcing frequency is close to ω_r, regardless of the forcing amplitude. This resonant excitation ceases at a critical frequency ω_f close to ω_r due to a bifurcation phenomenon explained in Faltinsen et al. 2000. Resonance arises also around higher natural frequencies (that is, $n > 1$) even if these generally induce a weaker wave response. In our particular case, the five scenarios described by Olsen and Johnsen 1975 are obtained by increasing the excitation frequencies from zero up to the first bifurcation.

Unfortunately, the study of Olsen and Johnsen is just limited to few cases of roll motion. Then, the aim of the present work is to perform a similar analysis for the sway motion covering a broad range of excitation amplitudes and fre-

	A/h	h/L	motion regime	Experimental campaign
Series 1	0.033	0.098	weak	Lepelletier and Raichlen 1988
Series 2	0.065	0.051	weak	Lepelletier and Raichlen 1988
Series 3	0.500	0.060	moderate	CNR-INSEAN (*see* section 10.2)
Series 4	0.800	0.125	strong	CNR-INSEAN
Series 5	2.333	0.030	strong	CNR-INSEAN

Table 10.1.: Experimental campaigns considered in the present work.

quencies. Following Olsen and Johnsen , a classification of the sway motions occurring for shallow depth is given. Remarkably, a new configuration has been added to those proposed by Olsen and Johnsen.

10.4.1 Present investigation

The parameters A, ω, h are chosen on a broad range of physical cases. Several series, each characterised by a couple (A, h) - amplitude of the horizontal excitation and the water depth - are investigated. For each of them, several runs have been performed varying the excitation frequency, ω, and detecting the value ω_f where the bifurcation occurs.

The water depth varies between $0.03L - 0.125L$ so that all the cases under consideration belong to the shallow water regime. Details of the adopted series are summarised in Table 10.1.

The analysis is focused on the steady-state conditions, in the sense given by Faltinsen et al. 2000, that is, as the periodic behaviour observed after the end of the transient. The steady state range can be identified as

$$T_S = [t_{end} - nT, t_{end}] \tag{10.5}$$

where t_{end} is the last time recorded and n the number of periods in the steady range regime. The latter number varies with ω since the duration of the transitory stage changes from one case to the other and is influenced by the occurrence of beating phenomena.

During the steady state, the wave elevation at fixed longitudinal positions of the tank has been recorded. The wave elevation is measured through capacitance wire probes whose signal is proportional to the whole wet surface. The same strategy has been used numerically, i.e. the wave elevation in a prescribed position is calculated as the integral along the vertical direction of the vertical coordinate occupied by the fluid particle. The average maximum wave height is simply denoted by η_a and the index a indicates the longitudi-

nal position of the numerical wave probe (as percentage of the tank length, i.e. $a = 100\,(x/L)$)

For small and moderate amplitude of the excitation, a periodical wave elevation (with the period of the excitation) is recorded at the regime state. In contrast, for large amplitude, the stochastic characteristics of the flow (with breaking waves, impacts, splashes and jet) may induce a sub-harmonic behaviour. Then, the mean of the maximum wave heights recorded at each cycle during the temporal range T_S is taken as significant parameter. The associated standard deviation σ, giving a measure of the stochastic behaviour, can be used as an indicator of the severity of the considered sloshing flow. Then, η_a (with the associated σ) as function of the excitation pulsation ω is used in the follow to define the global flow regimes characterizing the sloshing flow.

The excitation amplitude of the two first series in Table 10.1 is very small and waves are non-breaking: wave trains and solitary waves are observed. The low value of σ stresses the high repeatability which characterizes non-breaking sway motions. In the last two series the motion amplitude is very large, high breaking bores develop and, close to the bifurcation frequency, energetic roof impacts take place. For series 1, 2 and 3, the bifurcation is characterised by an abrupt jump of η_a at $\omega = \omega_f$ and is easily detectable. Conversely, the bifurcation seems to disappear for Series 4 and 5 (that is, for the most energetic sloshing cases) and η_a essentially behaves as a continuous function of ω. The local stochastic behaviours and, therefore, a low repeatability are characteristic of violent impacts (see, for example, Lugni et al. 2010a,b).

Among the large amount of data, some interesting cases reproducing the typical configuration of Olsen have been selected and studied in detail with photos and time-space data.

Small amplitude sway motion

Lepelletier and Raichlen 1988 performed a campaign for small amplitude motions and considered two different filling heights and geometries. In the present work, these configurations are denoted through Series 1 and 2 (see table 10.1). Series 1 is characterised by $h/L = 0.098$ and, therefore, is very close to the intermediate water regime. The tank dimensions are $L = 60.95\,cm$, $D = 23\,cm$ and the still water level is $h = 6\,cm$. The first resonant frequency predicted through the linear theory is $\omega_r = 3.89\,s^{-1}$, the horizontal forcing law is sinusoidal and its amplitude is $A = 0.196\,cm$.

The left plot of figure 10.3 displays the maximum wave height at $x/L = 0$ (that is, η_0) as obtained by the experimental measurements (triangles and thin solid line) and by the δ-SPH scheme (diamonds and thin solid line). In the same Figure 10.3 the standard deviation (namely, σ) of the numerical maximum wave height is also displayed. Note that σ is very small and the variations of η_0 are limited to few percentages. This is a consequence of the fact

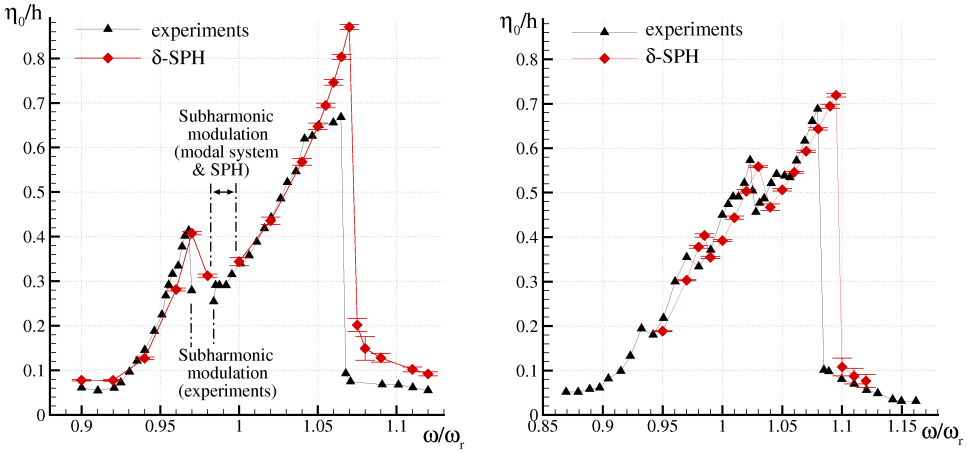

Figure 10.3.: Sway motion, response amplitude operator at $x/L = 0$ for the Lepelletier and Raichlen 1988 experiments. Left: $h/L = 0.098$, $A/h = 0.033$ (Series 1), Right: $h/L = 0.051$, $A/h = 0.065$ (Series 2).

that the sloshing motion presents an high repeatability during the steady state regime. A local maximum along the left branch of the response amplitude operator ($\omega/\omega_r \simeq 0.97$) separates two regimes of the sloshing motion: a two-wave regime (*Conf. II*) and a solitary-wave regime (*Conf. V*). Between these regimes a special region of motion was detected during the experimental campaign. In that region no steady state was attained and a nonlinear subharmonic modulation of 18 periods was observed (see Lepelletier and Raichlen 1988). Remarkably, the δ-SPH scheme predicts the same modulation in a region very close to that shown by the experiments (see the left plot of figure 10.3). Details on the nonlinear beating phenomenon are provided in figure 10.4 where the time history of the wave elevation recorded at $x/L = 0.05$ is plotted. In this case, very long simulations have been performed to ensure the attainment of a periodic asymptotic solution.

For the Series 2 (see table 10.1), the tank dimensions are $L = 117.5\,cm$, $D = 12\,cm$ and the still water level is $h = 6\,cm$, and $\omega_r = 2.04\,s^{-1}$. The horizontal forcing law is sinusoidal and its amplitude is $A = 0.39\,cm$.

The right plot of figure 10.3 displays the comparison between the experiments by Lepelletier & Raichlen (triangles and thin solid line) and the δ-SPH scheme (diamonds and thin solid line)for maximum wave height measured at the left wall of the tank ($x/L = 0$). The local maxima (sawtooth) that appear along the left branch of the response amplitude operator (see right plot of figure 10.3) correspond to the boundaries of different regimes of the sloshing evolution. Each regime is characterised by a specific number of waves and this number decreases as the peaks approach the bifurcation point. This particularity has been deeply investigated in Cox et al. Cox et al. 2005. For example, Figure 10.5 some snapshots of a two-wave regime (*Conf. II*) at the frequency

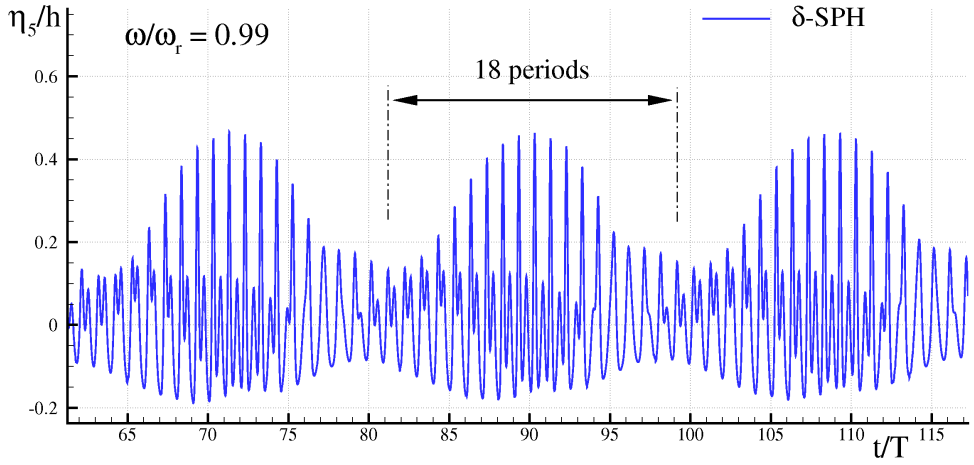

Figure 10.4.: Time history of the wave elevation measured at $x/L = 0.05$ (Series 1, $\omega/\omega_r = 0.99$) as predicted by the δ-SPH scheme.

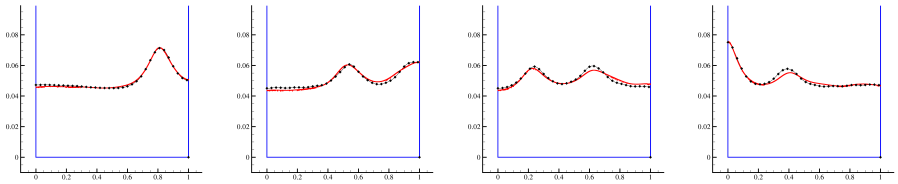

Figure 10.5.: Snapshots of the free-surface evolution for the Series 2 ($h/L = 0.051$, $A/h = 0.065$, $\omega/\omega_r = 1.02$). Black diamonds indicate the analytical solution obtained through the modal system described in Antuono et al. 2012b.

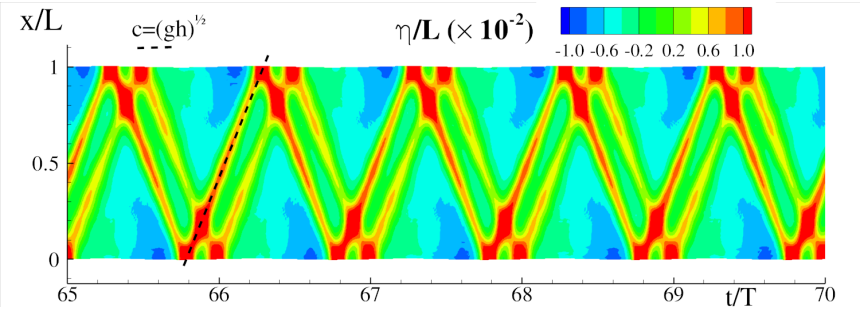

Figure 10.6.: Free-surface evolution in the time-space plane for Series 2 ($\omega/\omega_r = 1.02$).

$\omega/\omega_r = 1.02$. These SPH results have been compared with the modal system described in Antuono et al. 2012b, showing an excellent match. Figure 10.6 shows the contour plot of the wave elevation in a time-space plane for the same case. The two-wave system is clearly visible, its velocity of propagation is almost constant and very close to $c = \sqrt{gh}$ (dotted black line). This was ex-

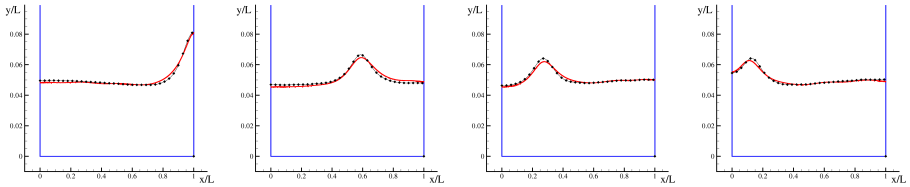

Figure 10.7.: Snapshots of the free-surface evolution for the Series 2 ($h/L = 0.051$, $A/h = 0.065$, $\omega/\omega_r = 1.08$). Black diamonds indicate the analytical solution obtained through the modal system described in Antuono et al. 2012b.

pectable since the sloshing dynamics is quite weak and, consequently, waves propagate in accordance with the shallow-water linear theory.

The last regime before the bifurcation is characterised by a solitary wave (*Conf. V*) that moves back and forth in the basin. Figure 10.7 displays some snapshots of the free surface for this case. As in the precedent case, figure 10.8 shows the contour plot of the wave elevation in a time-space plane. The propagation velocity of the solitary wave is again close to $c = \sqrt{gh}$.

After the bifurcation, only small-amplitude standing waves (*Conf. I*) of length 2L are observed for the range simulated (until $\omega_f < \omega < 1.15\,\omega_r$).

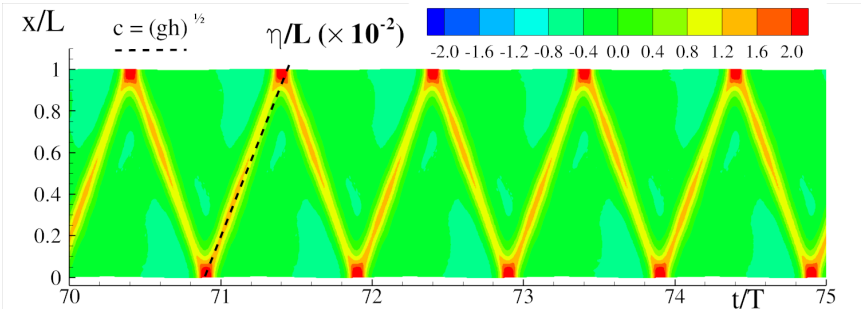

Figure 10.8.: Free surface evolution in the time-space plane for Series 2 ($\omega/\omega_r = 1.08$).

Moderate amplitude sway motion

Series 3 represents a typical sloshing case where non-linearities play a major role and wave breaking and jet run-ups/run-downs on vertical walls occur. In table 10.1, the sloshing motion of this series is classified as "moderate".

The maximum wave heights recorded at $x/L = 0.05$ and $x/L = 0.50$ are displayed in figure 10.9. The bifurcation occurs at $\omega/\omega_r = 1.35$, that is, at a higher frequency with respect to the Series 1 and 2. This behaviour is quite common in sloshing problems. Indeed, an increase of the motion amplitude (that is, A) generally corresponds to an increase of the bifurcation frequency ω_f with respect to the natural frequency ω_r. For this series the standard deviation on η_a largely spreads because of local phenomena (like run-up jets,

breaking waves, splash-ups, etc.) which induce a non-repeatability behaviour on the free-surface motion.

Figure 10.9 clearly shows that the wave height at $x/L = 0.05$ is larger than that recorded in the middle of the tank and this is induced by the run-ups against the vertical wall.

Similarly to the previous sloshing cases, the Series 3 shows interesting features as the frequency of the sway motion increases. For low frequencies, standing waves (*Conf. I*) modulated with a linear beating are observed and the wave elevation inside the tank is very small. Increasing the frequency up to $\omega/\omega_r \simeq 0.8$, the system reaches the stable branch of the bifurcation and undular bores (*Conf. II*) are observed. The steepness of the leading crest increases with the frequency until wave breaking occur at $\omega/\omega_r = 0.874$. This behaviour, shown in figure 10.10, is confirmed by both experiments and numerical results with an overall satisfactory agreement.

The top panel of figure 10.11 shows the contour plots of the wave elevation on the time-space plane. This allows a simple and clear tracking of the wave trains propagating inside the tank and of their self-interaction at the side walls. In this case, the velocity of propagation is generally smaller than $\sqrt{gh}$. The bottom panel of figure 10.11 displays the comparison between experiments and numerics for the wave elevation measured at $x/L = 0.05$. Increasing ω, the breaking wave (initially *Conf. III*) becomes more energetic and intense splash-up events are observed for $0.9\,\omega_r < \omega < \omega_f$ (*Conf. IV*). In this region the profile of the response amplitude operator (see figure 10.9) becomes flatter since part of the wave energy is dissipated during the breaking events. At $\omega/\omega_r = 1.192$ a single traveling wave appears (*Conf. V*). Close to the vertical walls, this overturns to form a plunging jet (see figure 10.12). This behaviour is predicted by both experiments and numerics.

The top panel of figure 10.13 displays the contour plots of the wave elevation in the time-space plane. Here, the path of a single traveling wave is clearly

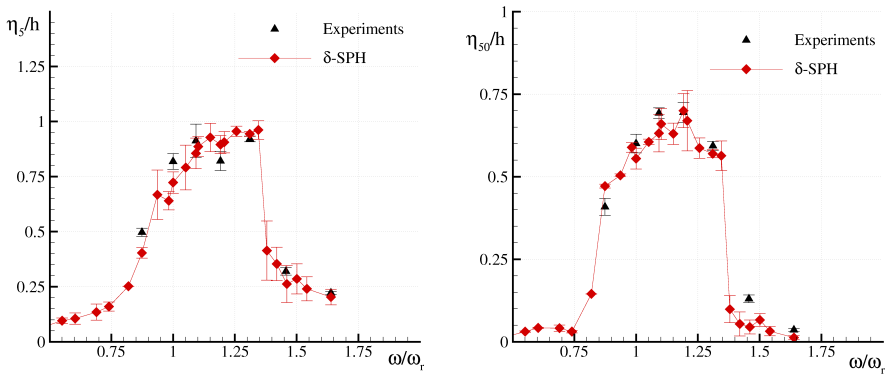

Figure 10.9.: Sway motion, response amplitude operator for the Series 3 described in table 10.1. Left: at $x/L = 0.05$, Right: at $x/L = 0.50$.

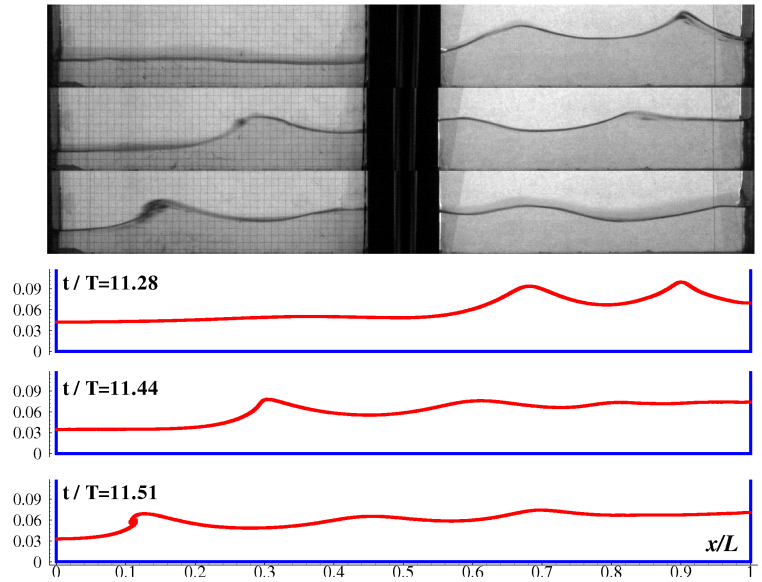

Figure 10.10.: Snapshots of the free-surface evolution for Series 3 ($\omega/\omega_r = 0.874$). Comparison between experimental data (top) and numerical simulations (bottom).

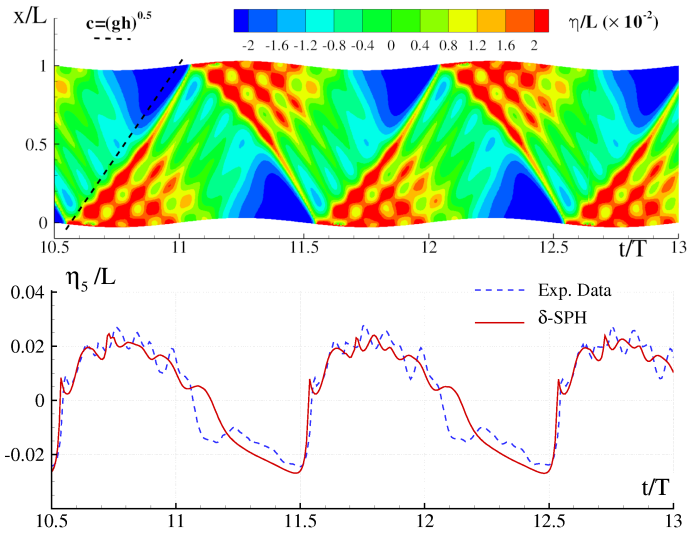

Figure 10.11.: Time history of the wave elevation for Series 3 ($\omega/\omega_r = 0.874$): evolution in the time-space plane (top panel, numerical solution) and comparison with experimental data at $x/L = 0.05$ (bottom).

visible. Differently from the previous case (top panel of figure 10.11), the velocity of propagation is close to $\sqrt{gh}$.

In the lower panel of figure 10.13, the time histories of the wave elevation measured at $x/L = 0.05$ wall are reported for both experiments and numerics. In this case, the non-repeatability of the sloshing evolution is quite evident.

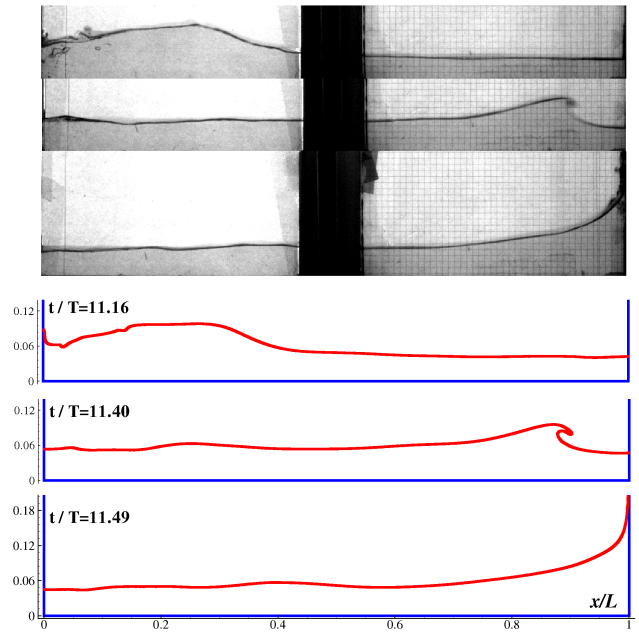

Figure 10.12.: Snapshots of the free-surface evolution for Series 3 ($\omega/\omega_r = 1.192$). Comparison between experimental data (top) and numerical simulations (bottom).

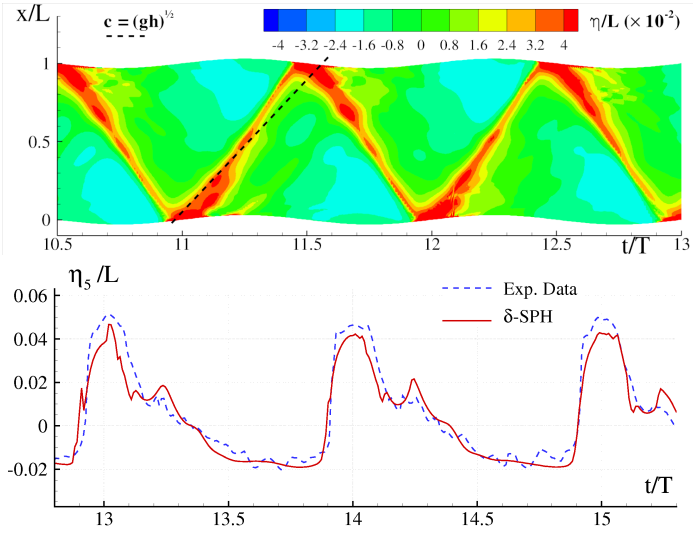

Figure 10.13.: Time history of the wave elevation for Series 3 ($\omega/\omega_r = 1.192$): evolution in the time-space plane (top panel, numerical solution) and comparison with experimental data at $x/L = 0.05$ (bottom).

After the bifurcation (specifically, for $\omega_f < \omega < 1.15\,\omega_r$), the wave amplitude strongly reduces. In any case, the flow evolution is still complex and, differently from the Series 1 and 2, it is not characterised by standing waves nor by other kind of flow shown by Olsen, but by a configuration here denoted as (*Conf. VI*), that we will describe in the following sections.

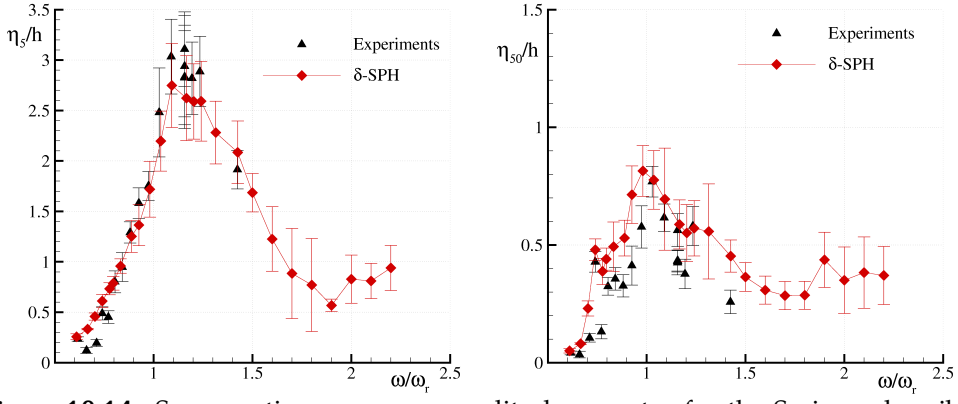

Figure 10.14.: Sway motion, response amplitude operator for the Series 4 described in table 10.1. Left: $x/L = 0.05$, Right: $x/L = 0.50$.

Large amplitude sway motion with a moderate water depth

The Series 4 is characterised by $h/L = 0.125$ and $A/h = 0.80$, that is, by a water depth at the higher limit of the shallow water regime and by a horizontal motion of amplitude comparable to the water depth. Under these conditions, breaking bores with intense splash-up events occur during the flow evolution and this series represents a very demanding test case for numerical schemes.

Figure 10.14 displays the maximum wave height recorded at $x/L = 0.05$ (η_5, left plot) and at $x/L = 0.5$ (η_{50}, right plot) for both experiments and numerics. With respect to the previous Series, the behaviour of η_5 is quite different since it increases for $0.6 < \omega/\omega_r < 1.15$ and decreases for $\omega/\omega_r > 1.5$ without showing any bifurcation phenomena. The standard deviation of η_5 largely increases in the range $1 < \omega/\omega_r < 1.9$ because of the occurrence of violent fluid dynamics. In particular, breaking bores develop at $\omega/\omega_r = 0.74$ (*Conf. III*). Wave breaking and splash-up events become stronger and stronger as the frequency increases (*Conf. IV* around $\omega/\omega_r = 0.84$) and, finally, impacts on the roof are observed for $\omega/\omega_r > 1$.

An example of the complex flow evolution which characterizes the Series 4 is given in figure 10.15. In this case, $\omega/\omega_r = 1$ and both numerical and experimental results display a violent breaking bore followed by strong splash-up events. The top panel of figure 10.16 displays the wave elevation contour in the time-space plane. The velocity of the bore seems initially smaller than $\sqrt{gh}$ but increases during the evolution. The good agreement between the experiments and the δ-SPH scheme is confirmed in the bottom panel of the same figure where the saw-tooth profile of the wave elevation is observed both experimentally and numerically.

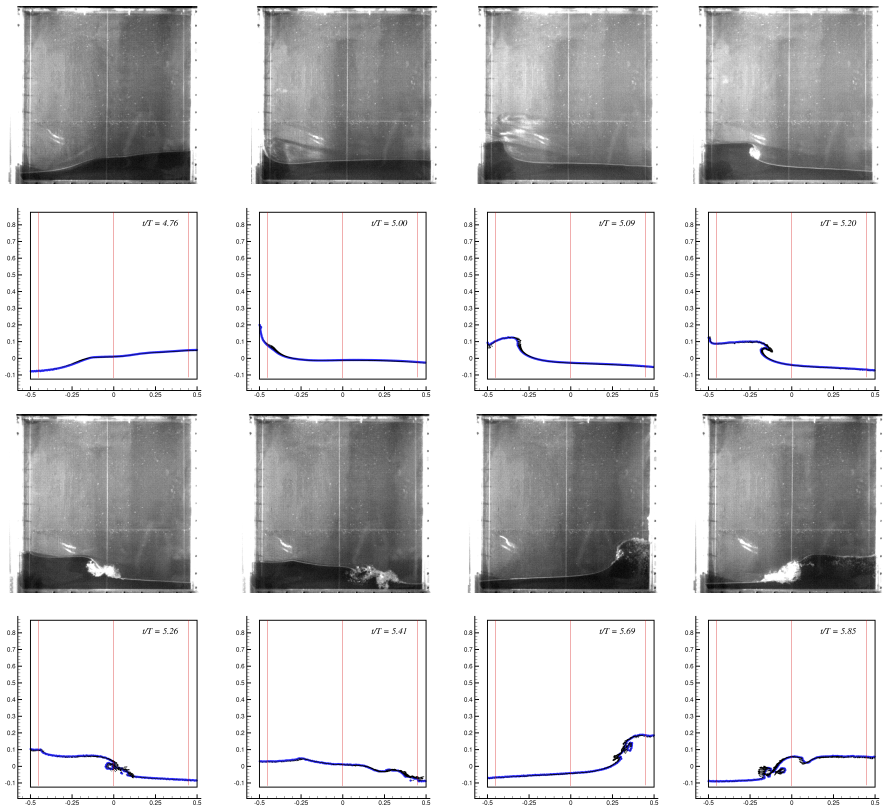

Figure 10.15.: Series 4: comparison between experimental and numerical results ($\omega/\omega_r = 1$).

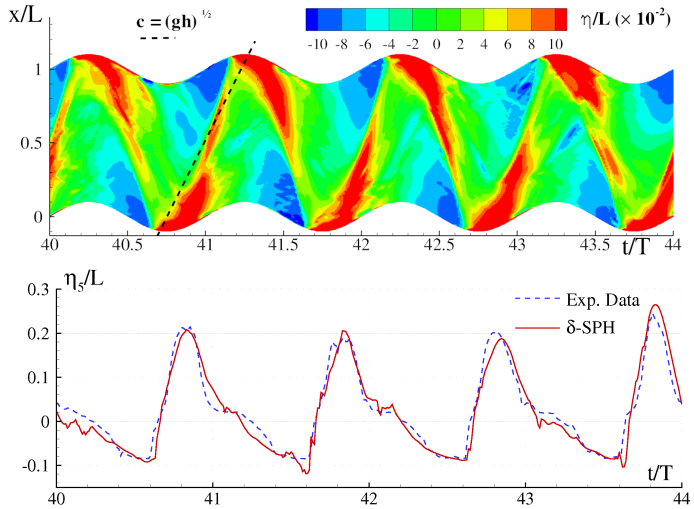

Figure 10.16.: Time history of the wave elevation for Series 4 ($\omega/\omega_r = 1$): evolution in the time-space plane (top panel, numerical solution) and comparison with experimental data at $x/L = 0.05$ (bottom).

Large amplitude sway motion with a small water depth

As a last example, the Series 5 (see table 10.1) is considered. This Series is characterised by $h/L = 0.03$ and $A/h = 2.33$, that is, by very shallow depth and by a large horizontal motion.

The maximum wave heights recorded at $x/L = 0.05$ and $x/L = 0.50$ are reported respectively in the left and right plot of figure 10.17. For this series, the experimental data are available only at six frequencies. The overall behaviour is somehow similar to that of Series 4. Specifically, no bifurcation is observed and the profile of η_5 (left plot of figure 10.17) appears even more rounded than that displayed for Series 4. This result clearly shows that the behaviour of the sloshing problems described in the present section is completely different by the hard-spring model discussed in Faltinsen et al. 2000. Indeed, the occurrence of breaking bores generated by large sway motions leads to large dissipations which affect the response of the fluid between the first and the second resonant natural frequencies.

For $\omega/\omega_r = 0.705$ standing waves without any beating phenomenon have been observed while, increasing the frequency, undular bores (*Conf. II*) develop. Because of the large amplitude of the excitation, the steepness of the leading crest is very high and breaking occur for $\omega/\omega_r > 0.85$.

Figure 10.18 shows the motion of a breaking bore for $\omega/\omega_r = 1.231$. The bore is quite energetic and, therefore, this case is classified as *Conf. IV*. For the same case, figure 10.19 (top panel) displays the contour levels of the wave elevation in the time-space plane. Here, the splash-up regions and the scar lines of the free surface are well visible. Because of the splash-up events, the velocity of propagation is much larger than $\sqrt{gh}$. Finally, the bottom panel of figure 10.19 shows the comparison between the experiments and the numerical solution for the wave elevation measured at $x/L = 0.05$.

Increasing the oscillation frequency up to $\omega = 2.31\omega_r$, the sloshing flow reduces its energy and the bore behaviour disappear. Two wave systems develop inside the tank, as clearly shown in the time-space plane obtained from the δ-SPH simulations (top plot of figure 10.20). The interactions between these waves lead to a strong increase of the wave elevation at a distance of about $0.2L$ from the vertical walls. As a consequence, the maximum of η is not attained at the vertical wall anymore. This sixth scenario has not been discussed in Olsen

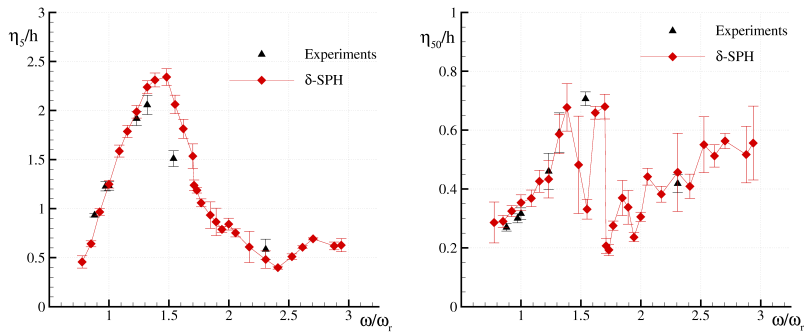

Figure 10.17.: Sway motion, response amplitude operator for the Series 5 described in table 10.1. Left: $x/L = 0.05$, Right: $x/L = 0.50$.

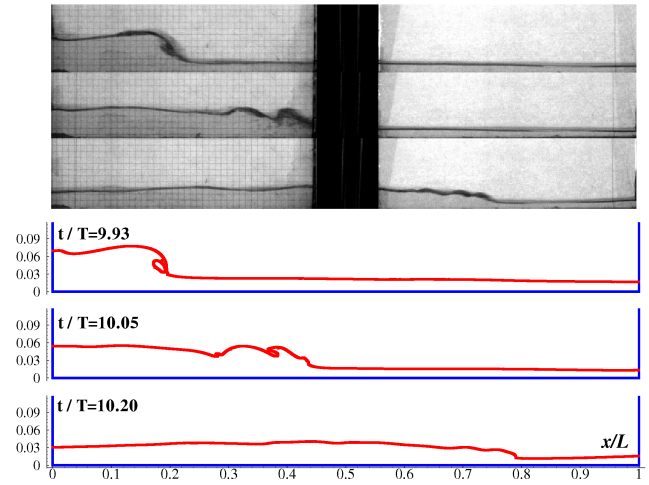

Figure 10.18.: Series 5: comparison between experimental data (top) and numerical results (bottom) for $\omega/\omega_r = 1.231$.

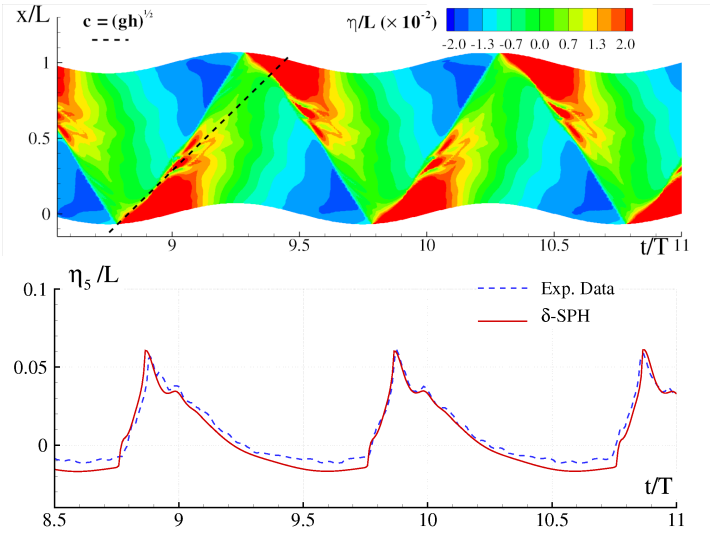

Figure 10.19.: Time history of the wave elevation for Series 5 ($\omega/\omega_r = 1.231$): evolution in the time-space plane (top panel, numerical solution) and comparison with experimental data at $x/L = 0.05$ (bottom).

and Johnsen 1975 and is, to our knowledge, completely new. Continuing their classification, this scenario has been labeled as *Conf. VI*.

When the sway amplitude is very large, as in the Series studied here, the nonlinearities induce a peculiar behaviour on *Conf. VI* which consists in a total asymmetry of the wave system. Indeed, the wave elevation measured at one side of the tank is not a simple half-period time shift of that recorded on the other side. This has been confirmed experimentally and numerically, as shown in the bottom plots of figure 10.20. On the top part of figure 10.21 three digital photos are reported showing three different time instants where the strong

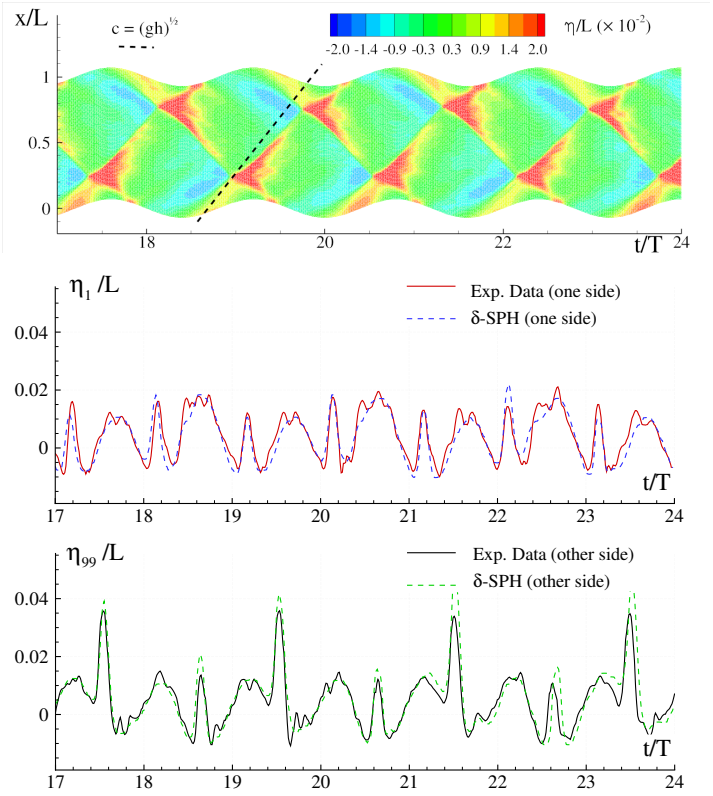

Figure 10.20.: Time history of the wave elevation for Series 5 ($\omega/\omega_r = 2.31$): evolution in the time-space plane (top panel, numerical solution) and comparison with experimental data at $x/L = 0.01$ (bottom).

nonlinear interaction between the two-wave systems can be appreciated. On the bottom part of the same figure the numerical evolution of the free surface has been extracted at the same time instants.

10.4.2 Summary of the sloshing scenarios

Following the approach of Olsen and Johnsen 1975, a classification of the different scenarios for sway motions in shallow depths is depicted. Such a classification has been performed for the lowest and the highest filling heights, i.e. $h/L = 0.03$, $h/L = 0.125$, using five sway amplitudes, namely: $A/L = 0.01, 0.03, 0.04, 0.05, 0.07, 0.10$.

Numerical simulations have been used for those configurations which are not covered by experiments. The good agreement between the δ-SPH and the experimental measurements provided in the previous sections confirms the reliability and accuracy of the δ-SPH scheme in the prediction of sloshing phenomena.

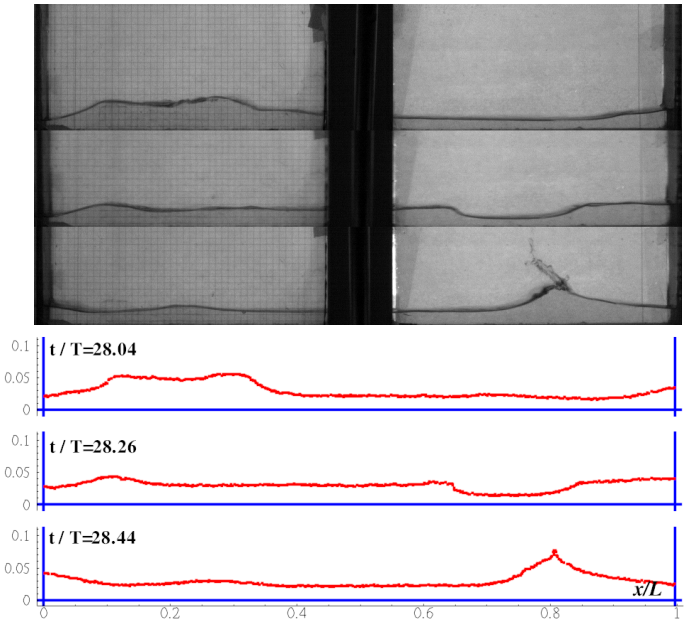

Figure 10.21.: Series 5: comparison between experimental data (top) and numerical results (bottom) for $\omega/\omega_r = 2.31$.

For $h/L = 0.03$, almost 180 simulations have been run, covering the frequencies range $[0.71\omega_r, 2.41\omega_r]$. The top plot of figure 10.22 displays the maximum wave elevation at 1cm from the vertical wall (*i.e.* η_1) as predicted by the δ-SPH scheme. The standard deviation has also been reported. The bifurcation phenomenon is well visible and the plot shows that the ω_f moves rightward when the sway amplitude increases. Remarkably, for the highest amplitude (that is, $A/L = 0.1$) the bifurcation is close to the second linear resonance.

All the cases shown in the top panel of figure 10.22 have been classified using the five configurations proposed by Olsen & Johnsen and the sixth sloshing scenario described in Section §10.4.1 (see the bottom panel of figure 10.22). On the same graph, the parabolic law of Verhagen and Van Wijngaarden 1965 has been reported (the derivation of this law for sway motion is described in Faltinsen and Timokha 2009). This law is obtained by using the two-dimensional shallow water theory and relies on the hypothesis that A/h is small. Specifically, it predicts that a propagating bore (namely, scenarios *Conf. III* and *Conf. IV*) may only occur when the couple $(A/h, \omega/\omega_r)$ is inside the parabola depicted in the bottom panel of figure 10.22. In the present experimental and numerical analysis, this forecast is verified when $A/h \leqslant 1.5$ while, for higher values, energetic bores (*Conf. IV*) may develop to the right of the parabola.

The above analysis has been repeated for the filling height $h/L = 0.125$, simulating more than 110 runs (among these, 80 have been performed in the same conditions of the experiments while the remaining runs have been simulated in order to complete the analysis). The top plot of figure 10.23 shows the maxi-

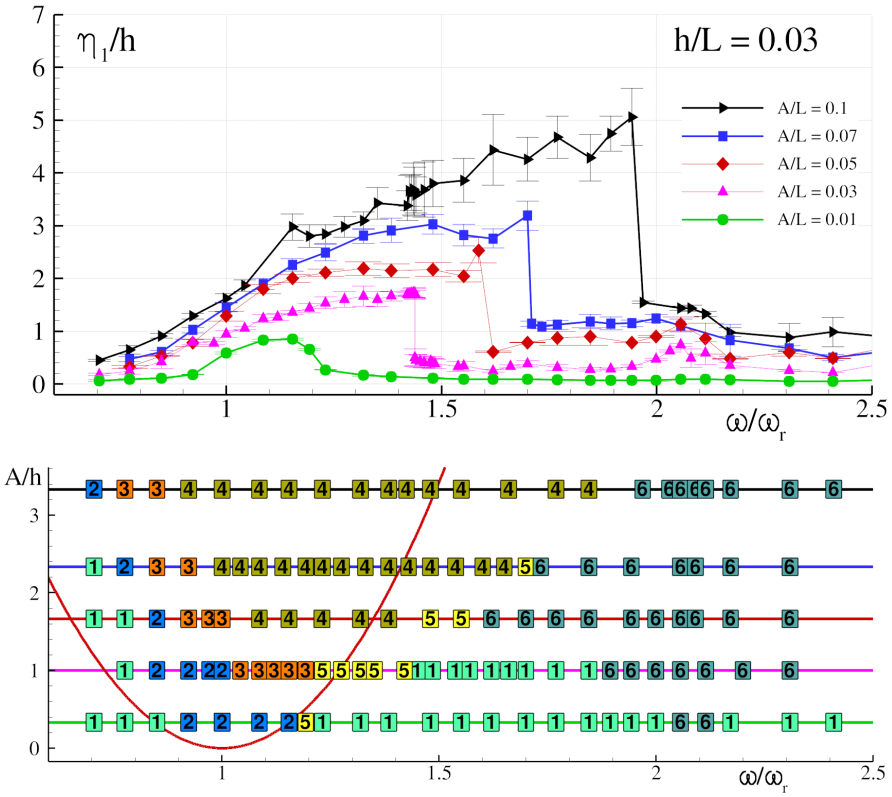

Figure 10.22.: The maximum wave elevation (top) and wave configurations (bottom) for several frequencies and sway amplitudes ($h/L = 0.03$).

mum wave elevation for η_1 as predicted by the δ-SPH scheme. Differently from the previous case, the bifurcation phenomenon disappears. The maximum wave height decreases continuously in the frequency interval $(1.2\omega_r, 2.0\omega_r)$ without any sharp discontinuity. For the largest values of the sway amplitude (that is, $A/L = 0.07$ and $A/L = 0.1$), the standard deviation associated with η_1 is very large because of the violent flow motion occurring inside the tank. The different sloshing cases have been classified in the bottom graph of figure 10.23. This time, the two-dimensional shallow water theory is in good agreement with the results and all the couples (A, ω) leading to *Conf. III* and *Conf. IV* occur inside the Verhagen & Van Wijngaarden parabola. This is likely due to the fact that the ratio A/h is always smaller than 1. It is worth mentioning that for the lowest sway amplitude (that is, $A/L = 0.03$) a subharmonic modulation may develop before the transition from *Conf. II* to *Conf. V*. This is caused by nonlinear beating phenomena and is somehow similar to what observed for the Series 1.

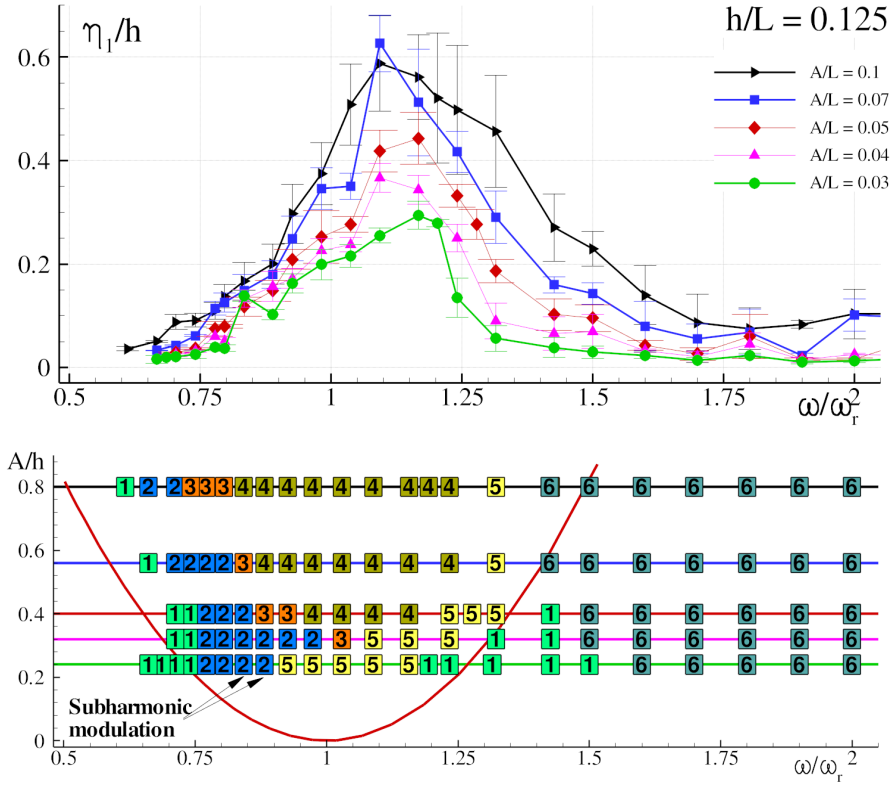

Figure 10.23.: The maximum wave elevation (top) and wave configurations (bottom) for several frequencies and sway amplitudes (h/L = 0.125).

10.5 SUMMARY OF THE CHAPTER

An extensive study of the shallow water sloshing problems has been done using both experimental and numerical data. Different configurations (Series) of sway motion have been considered in detail, spreading from small-amplitude excitations ($A/h = 0.033, 0.065$) to moderate ($A/h = 0.500$) and large excitations ($A/h = 0.800, 2.333$). For each Series, wave amplitude operators have been computed by varying the frequency of the excitation. Specific cases have been selected among the broad range of simulations to describe the main features of the sloshing motion (wave trains, wave breaking, jet run-up/run-down at the vertical walls, etc.). The results have been analyzed according to the classification proposed by Olsen and Johnsen 1975, proving the existence of a novel sloshing configuration, namely *Conf. VI*.

Finally, a summary has been done for two filling ratios, describing the wave scenarios and the wave amplitude operators for a large range of frequencies and inspecting the influence of the excitation amplitude.

11 MECHANICAL ENERGY DISSIPATION INDUCED BY SLOSHING AND WAVE BREAKING IN A FULLY COUPLED ANGULAR MOTION SYSTEM. I. THEORETICAL FORMULATION AND NUMERICAL INVESTIGATION

11.1 INTRODUCTION

In recent decades, a certain amount of studies have been dedicated to the damping/suppression of unwanted oscillations. This is especially true for civil infrastructures such as large buildings or bridges for which some mechanical damping systems for structural vibration control have also been devised (Kareem et al. 1999). Among them, Tuned Liquid Dampers (TLD) (see left sketch of Fig. 11.1) exploit the liquid sloshing motion in a tank in order to counteract the external forces and dissipate energy. These dampers can be used to control a building's motion during earthquakes and strong winds (Novo et al. 2014; Tamura et al. 1995), motion instabilities in spacecrafts (Abramson 1966; Graham and Rodriguez 1952) and the rolling motion in ships (Armenio et al. 1996a,b; Bass 1998).

The topic is receiving nowadays substantial attention in countries like Japan, where a campaign to install dampers in existing buildings is ongoing (Yamamoto and Sone 2014). The extra weight due to the damper, to be added to a building commonly on its top floors, often requires extremely expensive reinforcement of the building structure. For example, as reported in the media, adding mass dampers to the Shinjuku Mitsui Building in Tokyo has been budgeted in USD 51 million. Enhancing the effectiveness of dampers, while keeping their weight low, becomes thus extremely important from the economic point of view.

With all these motivations, and concentrating on the TLD concept, several investigations have been performed over the years in an attempt to reproduce sloshing flows. The first studies were performed using a potential flow linear or non-linear theory, but later studies were conducted using CFD. Abundant sources can be found in the books of Faltinsen and Timokha 2009 and Ibrahim 2005.

Modeling the energy dissipation in sloshing has always been a challenge. As an example, in order to take into account the viscosity effects and the boundary layers, some formulae for dissipation have to be added to potential flow based or shallow-water based models. In 1983, Demirbilek treated this problem of dissipation in sloshing waves both theoretically and numerically Demirbilek 1983a,b,c considering the full Navier Stokes equations. This allowed him to obtain some results regarding the influence of both Froude and Reynolds numbers on the dissipation values, but without any validation.

Sun and Fujino 1994 performed a numerical and experimental analysis of the problem in a tank without immersed screens or structures. They identified the breaking as an important source of dissipation and determined a semi-analytical procedure to take it into account. Reed et al. 1998 investigated in greater detail the effects of large amplitude sloshing on a TLD. Marsh et al. 2011 performed experimental and numerical works regarding the analysis of dissipation mechanisms in egg-shaped sloshing absorbers, focusing on sloshing and solid boundary layer effects. From a physical point of view, the study of the dissipation induced by a free-surface flow is arduous, especially in the presence of a wave breaking flow. Perlin et al. 2013 presented a review and analysis on works dedicated to dissipation under wave breaking.

Cooker 1994, 1996 performed elegant decay experiments with a free oscillating tank suspended as a bifilar pendulum in the shallow-water limit, suggesting that hydraulic jump theory can provide some insight into the dissipation mechanisms. The transfer of energy between a moving vessel and the contained fluid is studied in Turner and Bridges 2013.

The calculation of resonance properties for a coupled system is often difficult in the presence of a liquid. For that, different techniques have been developed in order to model the sloshing flow and solve the coupled problem, namely Yu et al. 1999 and Tait 2008 using a mass-spring subsystem, Frandsen 2005 using potential flow theory and Ardakani and Bridges 2010; Ardakani et al. 2012 using shallow water equations.

Recently, an alternative TLD configuration defined as a hybrid mass liquid damper (HMLD) (see Banerji and Samanta 2011 and Fig. 11.1, right) was introduced.

The idea is to tune the mass damper M_h to maximize the force counteraction between the primary and secondary structures and to attach a sloshing damper to the mass damper in order to dissipate large amounts of energy through violent sloshing. An optimally designed HMLD configuration is shown to be more effective as a control device than the standard TLD configuration since it maximises the force counteracting and dissipating effects.

In the present chapter, a specially devised fully coupled damper system first described in Bulian et al. 2010, called hereinafter Pendulum-TLD, is analysed. The mechanical system is essentially a non-linear driven pendulum, where the pendulum is a rectangular tank rotating around a fixed pivot. With the tank

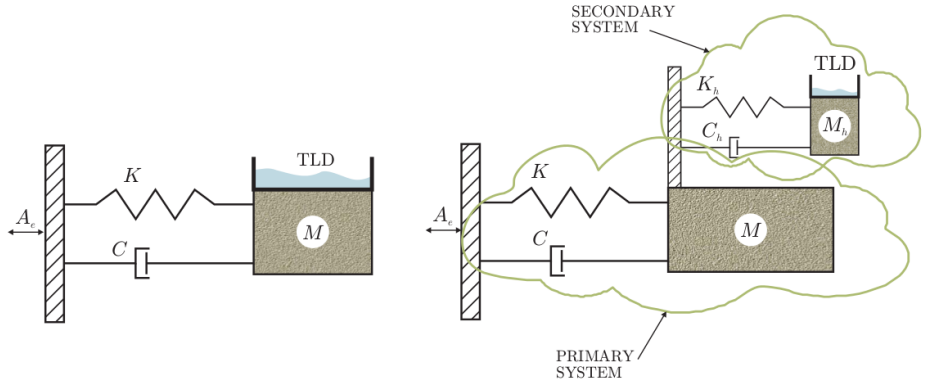

Figure 11.1.: Sketch of the two dynamical systems TLD (left) and HMLD (right) from Banerji and Samanta 2011. The aim is to dampen the motion of M induced by an external acceleration A_e.

partially filled with a liquid, energy is supplied to the whole system by a mass sliding along a linear guide fixed on the tank. The mechanical system and the resulting sloshing flow are coupled in a very complex non-linear manner.

This chapter is organised as follows: first, the frame of reference, notation and elements of the coupled system are presented, the torques and main energy terms affecting the dynamics are identified and an analogy with TLD and HMLD systems is provided. The dynamics of the empty tank is then described prior to developing the theoretical model representing the fluid action. The loads of the fluid on the tank during sloshing are theoretically and numerically investigated by varying both the frequency and the amplitude of the roll motion. Theoretical considerations are done on the scaling of the energy dissipation by the fluid. The numerical investigation is conducted using a Smoothed Particle Hydrodynamics numerical model, widely validated (see Antuono et al. 2012b; Bouscasse et al. 2013b) in the context of violent free surface fragmentation. The chosen model is further adapted to simulate the coupled dynamics, allowing for a non linear analysis of the coupled system behaviour in the frequency domain. Conclusions are drawn and an experimental validation analysis with three different liquids is left for chapter 12.

11.2 A PENDULUM TUNED LIQUID DAMPER

The pendulum TLD (see Fig. 11.2) is composed of three coupled sub-systems:

1. the sliding mass,
2. the moving parts of the sloshing rig including the empty tank but excluding the sliding mass; this sub-system will be hereafter referred to as the tank; the energy balances will refer to this sub-system.

3. the fluid.

The sloshing tank is assumed to be 2D, perfectly rigid, and rotating in the vertical plane about a fixed horizontal axis passing through a fixed pivot $\mathbf{O}$. Although the findings herein are of general value, in order to conform with the experimental data of chapter 12, the tank length L is set equal to 0.9 m and the width B, normal to the plane of motion, is 0.062 m.

The length $l = 0.1$ m is taken as a characteristic length of the system. The filling height h adopted and the sliding mass motion amplitude will be of this order.

The distance H between the center of rotation and the tank bottom is set equal to 0.47 m.

The moment of inertia around $\mathbf{O}$ is I_0 and the static moment S_G of the rigid system around $\mathbf{O}$ is the product of the mass, m_{tank}, and the distance, η_G, between the center of gravity of the tank and the point $\mathbf{O}$, thus $S_G = m_{tank}\eta_G$. I_0 is set equal to $I_0 = 26.9$ kg.m^2 and the static moment to $S_G = -29.2$ kg.m (see chapter 12). The rotation center is above the center of gravity of the whole system, implying that the system is stable in the absence of external forcing.

Since the system is purely rotational, the dynamics can be described in terms of variations in angular position and through balances of angular momentum (torques) contributions. The different torques acting on the tank derive from the following four external forces: one given by the fluid $\mathbf{F}_{fluid/tank}$, another stemming from the sliding mass $\mathbf{F}_{mass/tank}$, the third being the weight of the tank $\mathbf{F}_{static} = m_{tank}\,\mathbf{g}$ ($\mathbf{g}$ is the gravity acceleration) and the last one being the reaction of the holding structure $\mathbf{R}_{axis/tank}$ on the hinge $\mathbf{O}$. A scheme of these forces is provided in Fig. 11.2.

The inertial frame of reference is indicated by $(\mathbf{O}\,\mathbf{i}\,\mathbf{j})$ and the velocity $\mathbf{u}$ of a generic point P on the tank is

$$\mathbf{u}(P) = \dot{\phi}\,\mathbf{k} \times \mathbf{r},$$

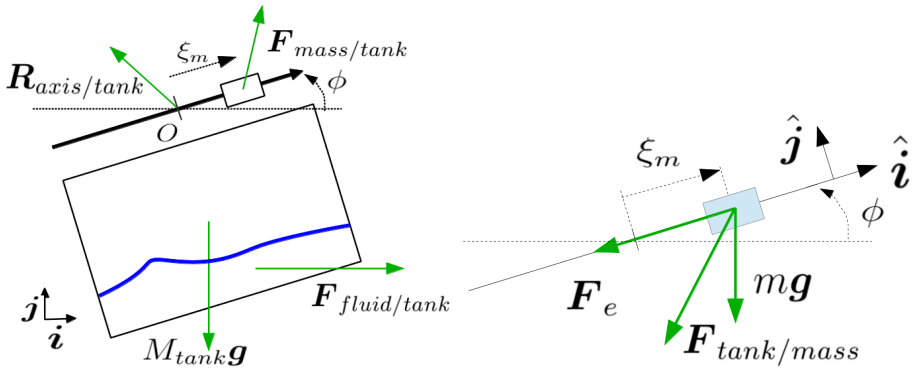

Figure 11.2.: Tank and oscillating mass (arrows are vector representation of forces).

where $\mathbf{k} = \mathbf{i} \times \mathbf{j}$ and is the normal vector orthogonal to the rotating plane, ϕ is the angular displacement, $\dot{\phi}$ is the angular velocity and $\mathbf{r}$ is the position vector of the generic point $\mathbf{P}$ with respect to the pivot $\mathbf{O}$.

The sliding mass $m = 4.978$ kg moves along the linear guide with $\xi_m(t)$ being the coordinate along the slide. This sliding mass is forced under a defined harmonic motion:

$$\xi_m(t) = A_m \sin(2\pi t/T), \tag{11.1}$$

where A_m is the amplitude of the oscillating mass along the linear guide, T is the oscillation period. The sliding mass motion amplitude A_m is set to 0.05, 0.10, 0.15 and 0.20 m. Since ξ_m is imposed, the state of the dynamical system can be defined as a function of the angle ϕ and its derivatives.

The mass moves along the axis defined by the pivot $\mathbf{O}$ and the vector $\hat{\mathbf{i}}$. The non-inertial frame of reference indicated by $(\mathbf{O}\,\hat{\mathbf{i}}\,\hat{\mathbf{j}})$ is defined in Fig. 11.2.

The forces on the sliding mass are: its weight $m\mathbf{g}$, the force given by the electric motor $\mathbf{F}_e$ and the force exerted by the tank on the mass $\mathbf{F}_{tank/mass}$. From the momentum equation in the inertial reference system $(\mathbf{O}\,\mathbf{i}\,\mathbf{j})$ an expression of $\mathbf{F}_{tank/mass}$ is given as a function of the sliding mass acceleration $\mathbf{a}_m$:

$$\mathbf{F}_{tank/mass} = -m\mathbf{g} - \mathbf{F}_e + m\,\mathbf{a}_m, \tag{11.2}$$

where $\mathbf{a}_m$ is given in $(\mathbf{O}\,\mathbf{i}\,\mathbf{j})$ frame by:

$$\mathbf{a}_m = (\ddot{\xi_m} - \xi_m\,\dot{\phi}^2)\,\hat{\mathbf{i}} + (2\dot{\xi_m}\dot{\phi} + \xi_m\,\ddot{\phi})\,\hat{\mathbf{j}}. \tag{11.3}$$

The torque about $\mathbf{O}$ on the tank, due to the sliding mass, is:

$$\begin{aligned} M_{mass/tank} &= \xi_m\hat{\mathbf{i}} \times \mathbf{F}_{mass/tank} \cdot \mathbf{k} = \\ &= -m\xi_m g\cos(\phi) - m(2\xi_m\dot{\xi}_m\dot{\phi} + \xi_m^2\ddot{\phi}). \end{aligned} \tag{11.4}$$

This expression comprises a term due to the weight of the sliding mass plus inertia terms originating from the mass motion on a rotating beam.

This equation mixes together the exciting term ξ_m with the roll angle ϕ, the latter being the main output of the dynamical system. For a sufficiently small roll angle ϕ, a good approximation of $M_{mass/tank}$ can be given by $-m\xi_m g$. The linear behaviour with respect to ξ_m should be dominant for $M_{mass/tank}$, thus simplifying the analysis of the system. This hypothesis is checked with the conditions studied herein.

Following Bulian et al. 2010 a friction torque is included in the mechanical model:

$$M_{friction} = -B_\phi\dot{\phi} - K_{df}\mathrm{sgn}(\dot{\phi}), \tag{11.5}$$

with $K_{df} = 0.54$ N.m and $B_\phi = 0.326$ N.m.$(\mathrm{rad/s})^{-1}$. These values have been determined in Bulian et al. 2010 using a set of inclining and decay tests on the experimental set-up adopted in chapter 12 of this series.

The natural frequency of the rigid system:

$$\omega_1^m = \sqrt{\frac{-g\,S_g}{I_0}} \tag{11.6}$$

is equal to $3.263\,(\mathrm{rad/s})$ and the corresponding period is $T_1 = 1.925\,\mathrm{s}$.

11.2.1 Angular momentum and energy balances

Considering the terms cited above, the angular momentum equation for the roll motion of the tank reads:

$$I_0\ddot{\phi} - gS_g\sin(\phi) - M_{friction} - M_{fluid/tank} = M_{mass/tank}, \tag{11.7}$$

where the first two terms of the left-hand side represent a classical non-linear pendulum equation (the static moment S_g has a negative value), and the right-hand side $M_{mass/tank}$ is the forcing term of the system.

Substituting the expressions reported above, the ODE (11.7) can be rewritten in an expanded form as:

$$(I_0 + m\xi_m^2)\ddot{\phi} + (B_\phi + 2\,m\xi_m\dot{\xi}_m)\dot{\phi} + K_{df}\mathrm{sgn}(\dot{\phi}) - gS_g\sin(\phi) + m\xi_m g\cos(\phi) = M_{fluid/tank}. \tag{11.8}$$

The torque $M_{fluid/tank}$ is given, for a Newtonian fluid, by:

$$M_{fluid/tank} = -\int_{\partial\Omega_B} \mathbf{r}\times p\,\mathbf{n}\,dS + 2\mu\int_{\partial\Omega_B}\mathbf{r}\times\mathbb{D}\,\mathbf{n}\,dS \tag{11.9}$$

where the two addends represent the contribution of the pressure and the viscosity forces, $\partial\Omega_B$ is the internal surface of the tank, $\mathbf{n}$ is the normal vector to this surface pointing away from the fluid, $\mathbb{D}$ is the fluid velocity strain rate tensor and μ the dynamic viscosity of the fluid. For an ideal fluid in absence of breaking, it is generally possible to find an analytical or semi-analytical expression for eq. (11.9) (see *i.e.* section 11.4), while for the more general case, $M_{fluid/tank}$ can only be found through a numerical solver (see *i.e.* subsection 11.4.4). A proper choice of the fluid characteristics and filling height should allow for a fluid response $M_{fluid/tank}$ that can suppress unwanted tank oscillations excited by external forces.

Equation 11.7 can be multiplied by the angular velocity $\dot{\phi}$ and integrated over an oscillation period to obtain the following energy balance:

$$[E_{tank}^{mech}]_t^{t+T} - \Delta E_{friction} - \Delta E_{fluid/tank} = \Delta E_{mass/tank} \tag{11.10}$$

in which:

1. $\Delta E_{mass/tank}$ accounts for the energy transfer between the sliding mass and the tank in one cycle; it is defined as:

$$\Delta E_{mass/tank} = \int_t^{t+T} M_{mass/tank}(s)\,\dot{\phi}\,ds. \tag{11.11}$$

   The sliding mass is the driving element of the system and $\Delta E_{mass/tank}$ is therefore expected to be positive. In reality, if the damping phenomena are not energetic enough, there may be cycles for which there is a net transfer of energy from the tank to the moving mass, as shown in the next sections.

2. $[E^{mech}_{tank}]^{t+T}_t$ is the variation of the mechanical energy of the tank during one oscillation cycle; it is defined as:

$$[E^{mech}_{tank}]^{t+T}_t := \int_t^{t+T} \left(I_0\ddot{\phi} - gS_g\sin(\phi)\right)\,\dot{\phi}\,ds, \tag{11.12}$$

3. $\Delta E_{friction}$, always negative, is the energy variation of the tank due to the mechanical friction for one cycle; it is defined as:

$$\Delta E_{friction} := \int_t^{t+T} M_{friction}(s)\,\dot{\phi}\,ds, \tag{11.13}$$

4. $\Delta E_{fluid/tank}$ is the energy transfer between the fluid and the tank during one cycle; it is defined as:

$$\Delta E_{fluid/tank} := \int_t^{t+T} M_{fluid/tank}(s)\,\dot{\phi}\,ds. \tag{11.14}$$

   This term is linked to the sloshing phenomena induced by the tank motion. In order to dampen such a motion, $\Delta E_{fluid/tank}$ should be negative, that is, in one period of oscillation the tank exerts a positive work on the fluid and not vice versa; this issue will further be discussed in detail in the rest of the paper.

The energy variation $\Delta E_{fluid/tank}$ is characterised by two components:

1. $[E^{mech}_{fluid}]^{t+T}_t$ is the mechanical energy balance of the fluid in one oscillation cycle.

2. $\Delta E^{dissipation}_{fluid}$ is the energy dissipated by the fluid in one cycle and is always negative (see *e.g.* Aris 1989).

The energy $\Delta E^{dissipation}_{fluid}$ involves different phenomena: (i) the fluid friction on the tank walls, (ii) water impacts against the vertical walls, (iii) breaking waves. The magnitudes of these different components depend on the nature

of the fluid. For example, when using water, breaking waves are expected to be the main source of fluid dissipation.

The energy balance for the fluid hence reads:

$$\Delta E_{fluid/tank} = -[E^{mech}_{fluid}]^{t+T}_{t} + \Delta E^{dissipation}_{fluid} \tag{11.15}$$

and therefore equation (11.10) becomes:

$$[E^{mech}_{tank}]^{t+T}_{t} + [E^{mech}_{fluid}]^{t+T}_{t} - \Delta E_{friction} - \Delta E^{dissipation}_{fluid} = \Delta E_{mass/tank} \tag{11.16}$$

The work done by the sliding mass, when positive, increases the mechanical energy of the tank and fluid, but is partially dissipated by the mechanical friction and fluid dissipation mechanism.

All the energy contributions are represented in Fig. 11.3, where the direction of the arrow indicates the positive sign contribution.

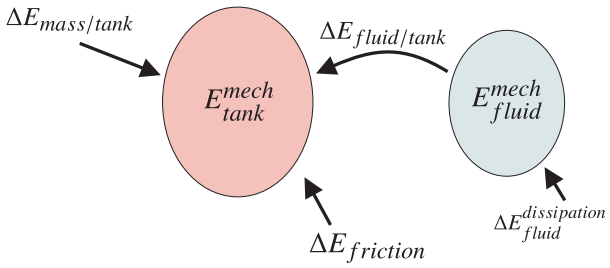

Figure 11.3.: Energy balance between the sliding mass, the tank and the fluid; the direction of the arrow corresponds to positive contributions.

11.2.2 Analogies between the present system, a TLD and a HMLD

TLD

The amplitude of the roll angle ϕ is the main indicator of the performance of a TLD system with angular motion. For a given excitation A_m, the lower the ϕ the more effective the TLD is considered to be. An analogy can be established between the present system and an angular motion TLD. Looking at the left panel of Fig. 11.1, mass M can be thought of as tank for the system described herein, the TLD being the fluid, K being the restoring term of the moment equation, C the friction term, and A_e the moment due to the moving mass.

However, this analogy falls short because, as will later be seen, if the excitation is above a certain threshold, the roll angle may not be reduced even if the system is dissipating a large amount of energy. This property suggests the idea of looking at the system as a hybrid mass liquid damper (HMLD).

HMLD

A large proportion of the analysis for the present system is in the energy transfer between the moving mass and the tank, $\Delta E_{mass/tank}$. Looking at the right panel of Fig. 11.1, the present system can be seen as the secondary system (with mass M_h) and may experience a larger amplitude motion than permitted if attached to the main structure. Under this large motion scenario, high levels of energy transfer may be induced from the primary damper M through the term $\Delta E_{mass/tank}$, finally being dissipated on the secondary system with the large angular motion sloshing flows.

11.2.3 Definition of envelopes and phase lags functions

In this subsection, useful quantities are defined in order to properly analyze the present system. These quantities are not used to obtain analytical solutions but only to extract important information from the numerical simulations and experimental results. As an example, the solution of equation (11.8), $\phi(t)$, can be approximated as:

$$\phi(t) = \Phi_{env}(t) \sum_{n=1}^{\infty} \sin\left[n\,\omega\,t + \delta_n(t)\right], \tag{11.17}$$

provided that the envelope function $\Phi_{env}(t)$ and phase shift functions $\delta_n(t)$ each have slow dynamics with respect to the period $T = 2\pi/\omega$. As will be shown later, the first harmonic component is largely dominant in the roll motion. Therefore, $\phi(t)$ can be described with a good approximation by:

$$\phi(t) \approx \Phi_{env}(t)\,\sin\left[\,\omega\,t + \delta(t)\right]. \tag{11.18}$$

Due to their slow dynamics, the envelope function $\Phi_{env}(t)$ can be approximated as:

$$\Phi(t) = \frac{\pi}{2T}\int_t^{t+T} |\phi(s)|\,ds\,, \tag{11.19}$$

and the shift function $\delta(t)$ can be approximately evaluated looking at the maximum values of $\phi(t)$ and $\xi_m(t)$ in a moving $T-$time window, and measuring the relative time shift in order to evaluate the phase lag.

Due to the existence of dissipative terms, equation (11.8) may admit a a "time-periodic solution" and equation (11.18) becomes:

$$\phi(t) = \Phi\sin[\omega t + \delta] \tag{11.20}$$

This is true for a large number of conditions, however, it is known Bouscasse et al. 2013b that shallow water sloshing can lead to subharmonics, in particular with low amplitude oscillations. Regarding the torque $M_{fluid/tank}$, at time-

periodic state, equation (11.8) shows that even considering the approximation (11.20) for the roll angle, the non-linear terms induce non-negligible effects on the time behaviour and the torque exerted by the fluid on the tank needs to be expressed as:

$$M_{fluid/tank} = \sum_{n=1}^{\infty} M_n \sin[n(\omega t + \delta) + \Psi_n] \tag{11.21}$$

where Ψ_n is the phase lag between the torque n–harmonic component and the roll angle $\phi(t)$ and in which, the first harmonic component is expected to play a lead role in the time-periodic state balance.

Prior to the time-periodic state, and similarly to what is done with $\delta(t)$, it is possible to extract a function $\Psi(t)$ from the time histories of $M_{fluid/tank}(t)$, looking for the local maximum. Indeed, this phase lag function evolves with slow time dynamics with respect to the period T.

Summarizing, in the time-periodic state, it is possible to define phasors on a complex plane using the modulus and phases of the different quantities. The origin for the phases is given by the sliding-mass motion. In order to help in assimilating the notation and in identifying the main actors of the dynamics under study, a typical configuration at time-periodic state is sketched in Fig. 11.4.

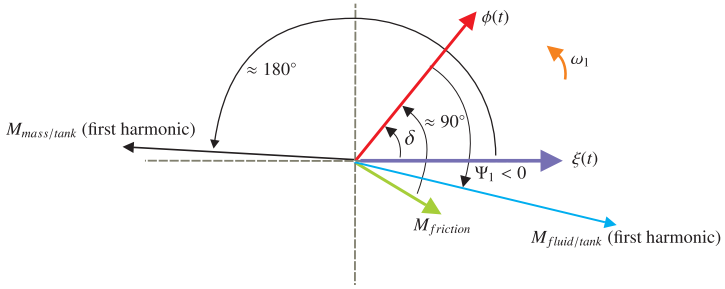

Figure 11.4.: Complex plane: main torques and motions involved in the analysis.

The following observations can be made:

1. Typically, the tank motion, $\phi(t)$, is lagged with respect to the sliding mass motion, $\xi(t)$, with an angle, δ, smaller than 90°.

2. The torque created by the sliding mass, $M_{mass/tank}$, is lagged approximately 180° with respect to the sliding mass motion $\xi(t)$.

3. The torque due to the friction term is advanced approximately 90° with respect to the tank motion $\phi(t)$.

4. The optimum condition in order to damp the tank motion takes place when the torque $M_{fluid/tank}$ acts in counter-phase with respect to the

torque $M_{mass/tank}$. Fulfillment of this condition is discussed in section 11.4.

11.3 DYNAMICS OF THE SYSTEM WITH THE EMPTY TANK

11.3.1 General

In this section the system is studied without fluid, focusing on the dependencies of the moving mass amplitude A_m and the effect of friction on the dynamics.

Considering an empty tank and null friction term, equation (11.8) can be reduced to:

$$\left[1 + \frac{mA_m^2}{I_0}\sin^2(\omega t)\right]\ddot{\phi} + \frac{mA_m^2}{I_0}\omega\sin(2\omega t)\,\dot{\phi} + {\omega_{1m}}^2\sin(\phi) + \frac{mgA_m}{I_0}\sin(\omega t)\cos(\phi) = 0 \tag{11.22}$$

As previously mentioned, equation (11.22) has practically the same behaviour as a driven non-linear pendulum. The dynamics of the empty tank condition is explored numerically looking at this ODE (11.22). The accuracy of this model of the "empty-tank" behavior was demonstrated in Bulian et al. 2010.

In Fig. 11.5, the solid line refers to the solution of equation (11.22) using the largest amplitude of excitation $A_m = 0.20$ m for the sliding mass and ω_1^m as excitation frequency. The solution shows the classical beating characteristic of a driven non-linear pendulum (see *e.g.* Butikov 2008).

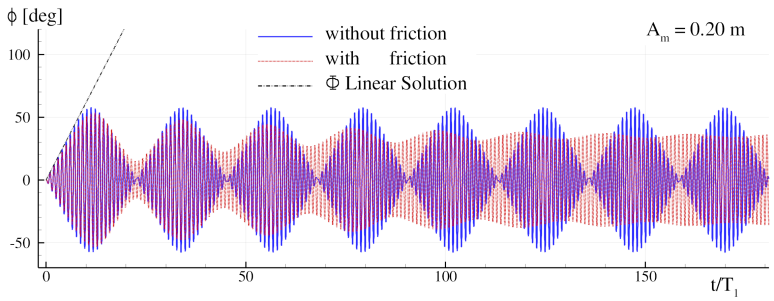

Figure 11.5.: Empty tank model: Roll angle ϕ plotted as a function of time using an excitation amplitude $A_m = 0.20$ m, $\omega = \omega_1^m$. Solid line: without friction, dashed line: with the friction model.

The energy exchanged between the tank and the sliding mass periodically changes in sign during the beating periods.

In the initial part of the time histories plotted in Fig. 11.5, $\phi(t)$ essentially follows the linear resonant solution:

$$\phi_{Lin}(t) = \frac{m\, g\, A_m}{I_0} \frac{t\, \cos(\omega_1^m\, t)}{2\omega_1^m} \tag{11.23}$$

in which the amplitude $\Phi(t)$ grows linearly with time and $\phi_{Lin}(t)$ is in quadrature (i.e. 90 degrees out of phase) with the sliding mass $\xi_m(t)$.

When considering the friction of the system, the solution (see dashed line in Fig. 11.5) shows that ϕ reaches a time-periodic state after a long transient. A similar behaviour is expected when the fluid is in the tank. Indeed, the dissipation mechanisms of the fluid added to the friction mechanism should generate a time-periodic state in a shorter time range.

Figure 11.6 shows the shift function $\delta(t)$ plotted as a function of time in the empty tank condition ($A_m = 0.20$ m with and without friction terms). Without friction, the phase lag oscillates periodically between 90° and −90° (solid line). With friction, the oscillations of $\delta(t)$ decrease in time towards a constant value (8°).

For positive values of δ, the mass is transmitting energy to the tank whilst for negative δ, the tank gives back some energy to the sliding mass (*i.e.* $\Delta E_{mass/tank} < 0$). The behaviour of $\Delta E_{mass/tank}$, Φ and δ in time is better depicted by the plots in Fig. 11.7.

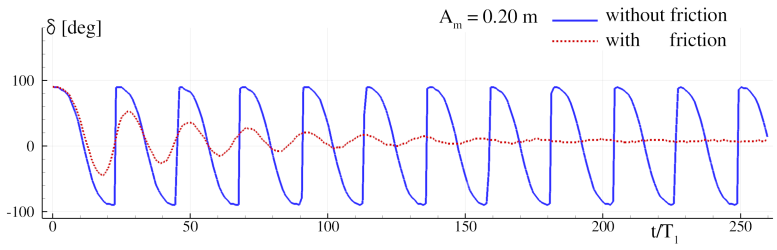

Figure 11.6.: Empty tank model: shift function δ plotted as a function of time using an excitation amplitude $A_m = 0.20$ m,$\omega = \omega_1^m$. Solid line: without friction, dashed line: with the friction model.

Fig. 11.8 shows the frequency behaviour of $[\Phi, \delta, \Delta E_{mass/tank}]$ at time-periodic state. This plot highlights the non-linearity of the mechanical system with the typical bifurcation phenomenon on Φ when varying the frequency ω (see *e*.g. Butikov 2008). Also, when increasing A_m, the frequency at which the maximum Φ appears (*i.e.* at which $\delta = 90°$) moderately decreases and is lower than ω_1^m . This "soft spring" behaviour is well documented in the literature.

Table 11.1 reports the value of $[\,\Phi\,,\delta\,,\Delta E_{mass/tank}\,]$ reached at a time-periodic state using $\omega = \omega_1^m$. Those values are to be used as reference data for chapter 12 where the tank is filled with a liquid.

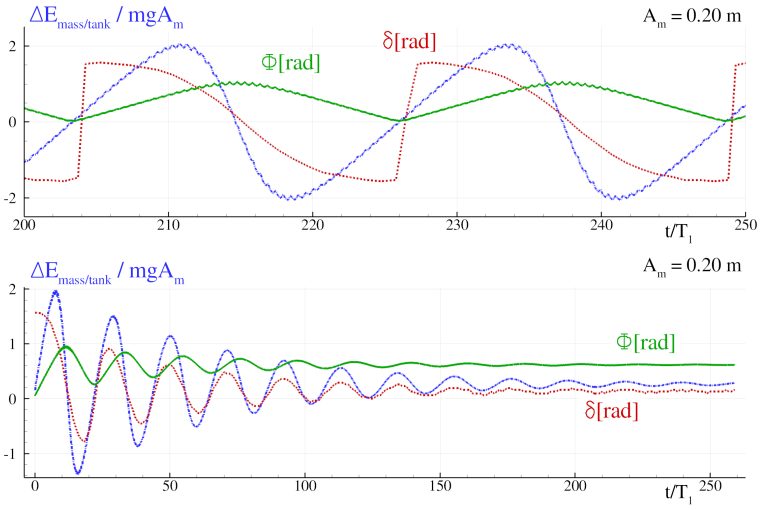

Figure 11.7.: Empty tank model: $\Delta E_{mass/tank}$ plotted as a function of time using an excitation amplitude $A_m = 0.20$ m, $\omega = \omega_1^m$. Top: without friction terms, bottom: with friction terms.

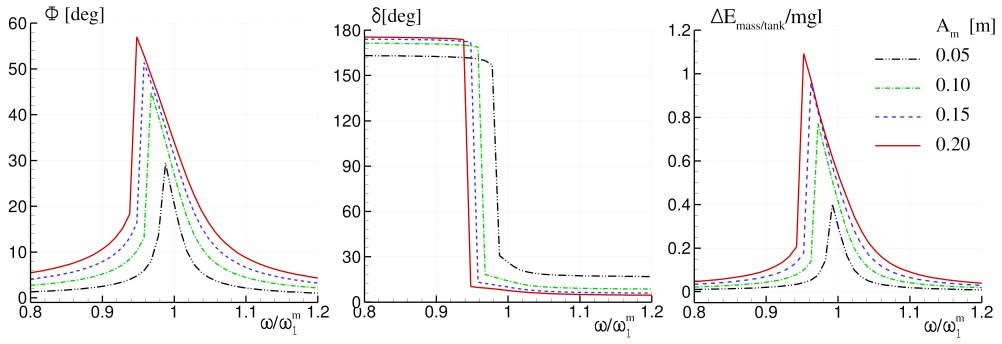

Figure 11.8.: Empty tank model with friction terms: roll angle Φ, phase lag δ and $\Delta E_{mass/tank}$ reached at a time-periodic state for different excitation frequencies.

A_m [m]	0.05	0.10	0.15	0.20
Φ [degree]	20	27	31	34
δ [degree]	26	14	10	8
$\Delta E_{mass/tank}/mgl$	0.30	0.42	0.50	0.54

Table 11.1.: Empty tank model: values of the main quantities reached at time-periodic state for the excitation amplitudes: A_m= 0.05, 0.10, 0.15 and 0.20 m and using the excitation frequency $\omega = \omega_1^m$.

11.3.2 Torque exerted by the sliding mass on the empty tank

Figure 11.9 shows $M_{mass/tank}/mgA_m$ as a function of time for $\omega = \omega_1^m$ at a time-periodic state (when the time-periodic state is met). This torque is a non-linear function of $\xi(t)$, $\phi(t)$ and their derivatives (see eq. 11.4).

The mentioned figure highlights the effect of increasing A_m. For the lowest $A_m = 0.05$ m, the torque is almost sinusoidal. When increasing the excitation amplitude it remains in phase with the sliding mass motion $\xi(t)$. It is also noticeable from the figure that a saturation effect takes place on the upper/lower parts of the signal when A_m is increased.

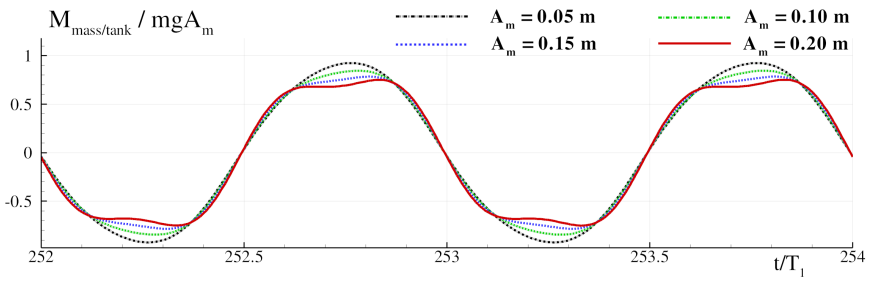

Figure 11.9.: Empty tank model: $M_{mass/tank}$ is plotted as a function of time during a time-periodic state where $\omega = \omega_1^m$ for four excitation amplitudes.

11.4 THEORETICAL AND NUMERICAL PREDICTIONS OF THE TORQUE EXERTED BY THE FLUID AND THE ASSOCIATED DISSIPATION

11.4.1 General

The resonance characteristics of a sloshing tank subjected to swaying and rolling have been thoroughly investigated over the years. The torque $M_{fluid/tank}$ (see equation 11.9) depends on the value of the pressure and velocity fields. It is not possible to find a general formulation in closed form for the Navier Stokes equations, especially when free surface breaking occurs.

Figure 11.10 shows a typical frequency behaviour of the wave amplitude during periodic sloshing in a rectangular tank for shallow water conditions. Increasing the excitation frequency raises the wave elevation until a frequency ω_b where a bifurcation is observed. For frequencies $\omega > \omega_b$ the wave elevation is drastically reduced. In shallow water condition ω_b is always larger than ω_1^f (see Faltinsen and Timokha 2002 and Bouscasse et al. 2013b), where ω_1^f is the first natural sloshing frequency:

$$\omega_1^f = \sqrt{g\,\pi/L\tanh(\pi h/L)}. \tag{11.24}$$

Therefore, the sloshing flow intensity has a "hard spring" type amplitude response, the opposite of the "soft spring" behaviour of Φ discussed in section 11.3 for the empty tank condition. In Fig. 11.10, small peaks are visible on the

wave amplitude measurements when $\omega < \omega_b$. Those are related to secondary resonance effects, which are typical phenomena in shallow water sloshing dynamics (for more details see Chester 1968, Chester and Bones 1968).

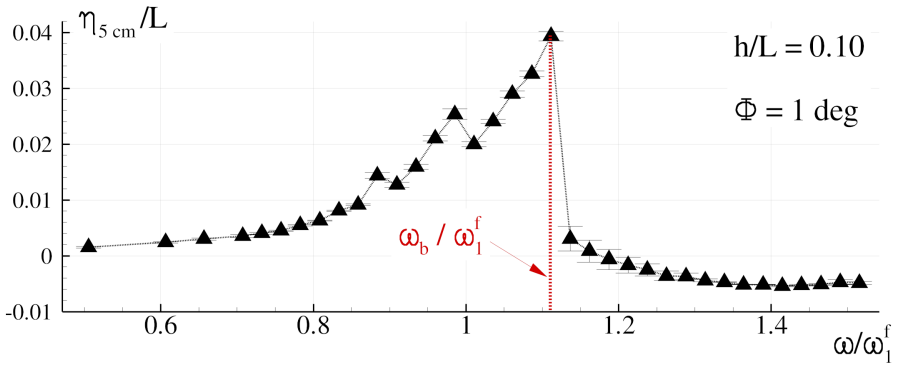

Figure 11.10.: Maximum wave elevation measured at 0.05 m from the left vertical wall obtained during the time-periodic state varying the excitation frequency ω. The roll angle amplitude is set to $\Phi = 1°$.

11.4.2 Torque from Verhagen and Van Wijngaarden analysis

In the pioneer work of Verhagen and Van Wijngaarden 1965, the non-linear inviscid problem is solved for a shallow water regime using hydraulic jump solutions on a tank forced in roll motion with a harmonic time history:

$$\phi(t) = \Phi \sin(\omega t + \delta),$$

with a constant Φ and an arbitrary phase δ.

According to Verhagen and Van Wijngaarden 1965, hydraulic jumps travelling back and forth between the walls of the tank exist in the following range of excitation frequencies:

$$\left(\omega - \omega_1^f\right)^2 < \frac{24\, g\, \Phi}{L}. \tag{11.25}$$

$M_{fluid/tank}$ can be expressed with Fourier series:

$$M_{fluid/tank} = \rho g \left(\frac{L}{2}\right)^3 B \sum_{n=1}^{\infty} \tilde{M}_n \sin[n(\omega t + \delta) + \Psi_n], \tag{11.26}$$

with Ψ_1 being the phase lag between the first harmonic component of the torque and the roll angle $\phi(t)$ (see Fig. 11.4).

In the vicinity of the resonance frequency ω_1^f, the first harmonic component in equation 11.26 is given by:

$$\begin{cases} \tilde{M}_1 &= \left(\frac{2}{3}\right)^{\frac{3}{2}} \left(\frac{4}{\pi}\right)^4 \left(\frac{\Phi\, h}{L}\right)^{\frac{1}{2}} \left[1 - \frac{L(\omega - \omega_1^f)^2}{32\, g\, \Phi}\right] \\ \Psi_1 &= -\frac{\pi}{2} - 2\arcsin\left[\frac{L(\omega - \omega_1^f)^2}{24\, g\, \Phi}\right]^{\frac{1}{2}} + \arcsin\left[\frac{L(\omega - \omega_1^f)^2}{96\, g\, \Phi - 3L\,(\omega - \omega_1^f)^2}\right]^{\frac{1}{2}} \end{cases}. \tag{11.27}$$

Therefore, in the Verhagen and Van Wijngaarden 1965 analysis, the torque magnitude is proportional to $\sqrt{\Phi}$ and its maximum value is achieved for $\omega = \omega_1^f$, i.e. when the system is forced with the fluid resonance frequency.

From equation (11.27) and for values of ω in accordance with equation (11.25), Ψ_1 decreases from 0 to $-180°$. Specifically for $\omega = \omega_1^f$, $\Psi_1 = -90°$, which implies that the first harmonic of $M_{fluid/tank}$ is in quadrature with the tank motion (see equation 11.26).

11.4.3 Theoretical fluid dissipation

A theoretical approximation of the fluid energy dissipation has now been developed similar to Verhagen and Van Wijngaarden 1965, where hydraulic jump solutions for an inviscid flow are used. Following Stoker 1957, the energy loss dissipated across a hydraulic jump between water heights h_0 and h_1 moving with velocity u over a wave period is:

$$\Delta E_{fluid}^{dissipation} \approx -B\rho g h_0 u \frac{(h_1 - h_0)^3}{4 h_0 h_1} T. \tag{11.28}$$

Over one period the total distance that the wave must propagate down the length of the tank and back again, is $uT = 2L$. Therefore, the above expression becomes:

$$\Delta E_{fluid}^{dissipation} \approx -2BL\rho g h_0 \frac{(h_1 - h_0)^3}{4 h_0 h_1}. \tag{11.29}$$

All of the energy given to the fluid comes from the motion of the tank's walls. For an inviscid fluid this can be approximated to the work done by pistons acting against the net difference between the (approximately hydrostatic) pressure distributions at the two end walls. For an elementary angle rotation $d\phi$ the work is:

$$dW_p = -\frac{\rho g B}{2}(h_1^2 - h_0^2)\sqrt{H^2 + (L/2)^2}\, d\phi \tag{11.30}$$

Integrating over an oscillation period and since this value should be equal to $\Delta E_{fluid}^{dissipation}$, on one hand $(h_1 - h_0)$ is obtained combining above expres-

sions, on the other hand $h_1 + h_0 \approx 2h$, and subsequently the following estimation for $\Delta E_{fluid}^{dissipation}$ can be given:

$$\begin{aligned} \Delta E_{fluid}^{dissipation} &= -[(2H/L)^2 + 1]^{3/4} (4\rho g B L h^2) \Phi^{\frac{3}{2}} = \\ &= -[(2H/L)^2 + 1]^{3/4} (4 m_{liquid} g h) \Phi^{\frac{3}{2}} \end{aligned} \tag{11.31}$$

where m_{liquid} is the mass of the sloshing liquid contained in the tank. Since for the present system $2H/L \simeq 1$, the above expression reduces to:

$$\frac{\Delta E_{fluid}^{dissipation}}{(4 m_{liquid} g h \Phi^{\frac{3}{2}})} = -2^{3/4} \approx -1.68 \tag{11.32}$$

This dissipation rate is constant in time, which is generally not the case for a real sloshing flow where a breaking wave front develops only on limited time ranges and is not present during the whole oscillation cycle. This is the reason why equation (11.32) tends to over-predict the fluid dissipation as shown in the next subsection.

This non-dimensional coefficient linked to the energy dissipated by the fluid is referred to hereinafter as:

$$\alpha := -\frac{\Delta E_{fluid}^{dissipation}}{4 m_{liquid} g h \Phi^{\frac{3}{2}}}. \tag{11.33}$$

Being α of order unity, the reference energy, $4 m_{liquid} g h \Phi^{\frac{3}{2}}$ models that part of the mechanical fluid energy (kinetic plus gravitational potential) which is available to be dissipated in breaking.

11.4.4 Numerical predictions of the torque exerted by the fluid and the associated dissipation

The theoretical model presented in section 11.4 is not expected to be valid for large oscillation amplitudes, as is the case for some used in the present work, or for very small oscillations where hydraulic jumps do not occur. For this reason, numerical simulations in a 2D framework are performed using the Smoothed Particle Hydrodynamics model discussed and validated for sloshing flows in Bouscasse et al. 2013b and in Antuono et al. 2012b.

The filling height adopted is equal to $h = 0.092$ m. This choice is motivated by the points discussed in section 11.5.

Plots in Fig. 11.11 show the maximum torque $M_{fluid/tank}$ recorded in the time-periodic regime for five different roll amplitudes Φ: 1, 2, 10, 20 and 35 degrees and a range of exciting frequencies ω close to ω_1^f.

The peak values of $M_{fluid/tank}$ in each oscillation cycle have a very different frequency behaviour for small and large roll angles. Furthermore, for

small roll amplitudes, the associated standard deviation across these cycles is very low. This result indicates repeatability, a characteristic of non-breaking sloshing flows. For a roll angle greater than 2 degrees, breaking waves occur, inducing a standard deviation on the evaluated $M_{fluid/tank}$ that increases with Φ.

The analytical prediction of $M_{fluid/tank}$ in the proximity of ω_1^f (see equation (11.27)) is $M_1 \simeq 0.457\sqrt{\Phi}$. The theoretical model tends to exceed the SPH predictions, however, the agreement between the theory and the numerics on the maximum torque remains fair for all investigated roll angles.

Fig. 11.12 depicts the α coefficient defined in equation 11.33 for the five previously defined roll amplitudes Φ. For the lowest roll amplitudes, the obtained α-values present a complex frequency behaviour with different peaks linked to secondary resonance effects. Besides this, for Φ equal to 1 and 2 degrees, α is very close to the value 1.68 predicted by the analytical expression(11.32) when ω is close to the frequency ω_1^f. These results are compatible with those found in Landrini et al. 2007 where the energy dissipated by breaking waves, when simulating hydraulic jumps with SPH, was shown to be similar to analytical results.

Increasing the roll amplitude, SPH predicts a reduction of the viscous coefficient α which remains in the range of variation $\alpha \in (0.8, 1.8)$ for all the five amplitudes studied. This reduction is also confirmed by the experimental measurements presented in the chapter 12.

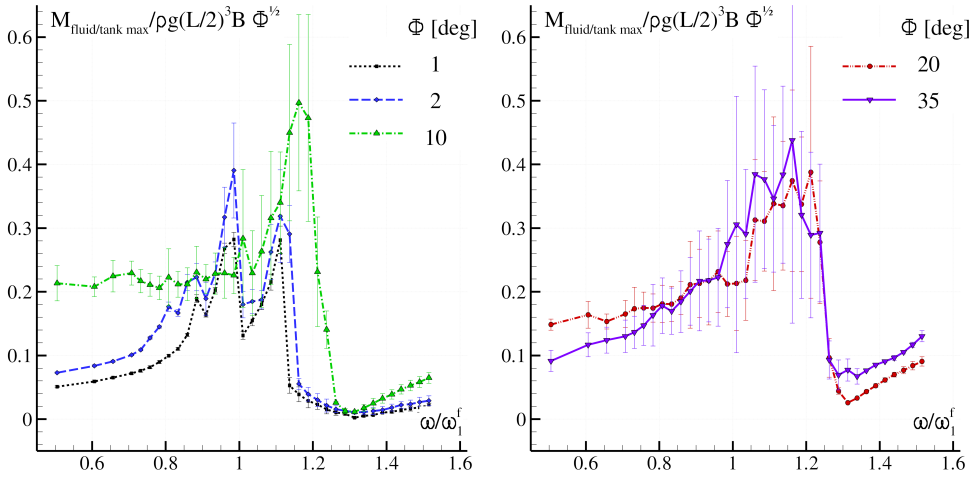

Figure 11.11.: Maximum value for the torque $M_{fluid/tank}$ predicted by the SPH method during the time-periodic state varying the excitation frequency ω. The maximum values plotted are the average of those obtained for the simulated periods. The error bars indicate the associated standard deviation. Left: roll amplitude Φ = 1,2, 10 degrees. Right: Φ = 20 and 35 degrees.

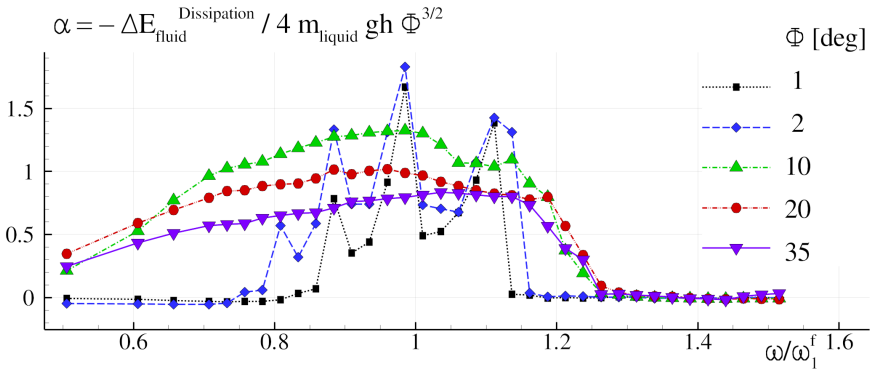

Figure 11.12.: The energy $\Delta E_{fluid}^{dissipation}$ predicted by the SPH method during the time-periodic state is plotted for an excitation frequencies range $(0.4 < \omega/\omega_1^f < 1.5)$ and for five different roll amplitudes Φ.

11.5 THE FULLY COUPLED ANGULAR MOTION SYSTEM

11.5.1 General

Once the empty tank mechanical system and the fluid system have been independently analyzed, it is relevant to observe them coupled.

If the fluid is considered "frozen", considering a filling height $h = 0.092$ m and a "frozen" liquid with density $\rho = 1000\,Kg/m^3$, the moment of Inertia I_0 has an 8% variation. However, since S_g also varies, the effect on the mechanical resonance frequency ω_1^m is limited to a decrease of 0.5%. Therefore, the effects of the presence of a liquid inside the tank, are mainly due to the induced sloshing flows and not so much to the liquid mass added in the system.

In the previous sections the non-linear empty tank and the forced sloshing dynamics have been described. To analytically study the frequency behaviour of the coupled fluid/rig TLD system the methodology described in the works of Frandsen Frandsen 2005 or Alemi Ardakani et al Ardakani et al. 2012 should be followed.

In other articles (e.g. Tait'sTait 2008), the sloshing dynamics of the TLD system is approximated as a simple secondary mass-spring system. This allows (as with the model of Frandsen Frandsen 2005) the selection of an optimal mass of fluid in order to reduce the oscillation amplitude at the resonance frequency of the mechanical system ω_1^m.

In the case studied here for the pendulum-TLD, the roll motion makes these analytical approaches more complex. Furthermore, for the large range of excitation amplitudes A_m investigated here the linearised approach fails.

The optimal choices for the mass of fluid found in the linearised approaches are in the neighborhood of $\omega_1^f/\omega_1^m \approx 1$ and this can be explained by the following simple considerations:

1. As discussed in section 11.4.2, if the system is forced at $\omega = \omega_1^f$ then $\Psi_1 = -90°$ (the first harmonic of $M_{fluid/tank}$ is in quadrature with the tank motion).
2. The largest counteraction expected is when $M_{fluid/tank}$ is lagged 180° with respect to $M_{mass/tank}$. Looking at Fig. 11.4, this case corresponds to $\delta + \Psi_1 = 0$.
3. For the smallest forcing ($A_m = 0.05$m, see section 11.3.1), the roll motion of the mechanical system with an empty tank is in quadrature ($\delta = 90°$) with the sliding mass motion when the system is forced at the mechanical resonance ($\omega = \omega_1^m$).
4. From the above considerations, when the first sloshing frequency is equal mechanical resonance frequency of the system:

$$\omega_1 := \omega_1^f = \omega_1^m \qquad \Rightarrow \qquad g\,\pi/L \tanh(\pi h/L) = -g\,S_g/I_0, \tag{11.34}$$

which allows identifying the filling height $h = 0.092$ m.

Summarizing the above considerations for all the different torques, it is possible to define phasors on a complex plane using the modulus and phases of the first harmonic components obtained by a Fourier decomposition (as in equation 11.21).

The phasors expected for an idealised system are sketched in Fig. 11.13. The inertial and static components are defined respectively as $M_{inertial} = -I_0\ddot{\phi}$ and $M_{static} = gS_g \sin\phi$. The origin of the phases is given by the sliding-mass motion.

In real cases, the dynamic system moves away from this ideal condition. As a consequence, the optimum choice for the filling height, h^*, is not necessarily obtained by (11.34) since h^* also varies due to non-linearities with respect to the forcing amplitude A_m or to the nature of the fluid. These non linearities are the subject of the present study, where the filling height h is therefore set to 0.092 m and this choice is tested across a range of frequencies using a suitable numerical solver to get the fluid reaction $M_{fluid/tank}$.

11.5.2 Pendulum TLD: numerical simulation with SPH

In this section, the Smoothed Particle Hydrodynamics model presented is applied to simulate the fully coupled angular motion system. The two-dimensional hypothesis is still maintained mainly for computational costs.

Fig. 11.14 depicts the sloshing flow predicted by the SPH model. For the frequency $\omega = \omega_1$, two different excitation amplitudes A_m of the sliding mass are used: $A_m = 0.05$ m and $A_m = 0.20$ m. For the smallest amplitude, a train wave develops inside the tank and no breaking wave phenomena are predicted;

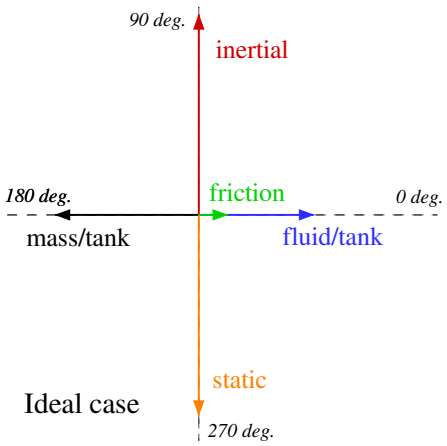

Figure 11.13.: Torque modulus and phase. Phasor expected for a tank filled with an inviscid liquid at oscillating with small amplitude angle, for resonance condition of both liquid and mechanical system.

the motions of the sliding mass and the rolling tank are almost in quadrature. The agreement with the experimental results is very good as it can be seen comparing with the results of chapter 12.

Conversely, using the highest $A_m = 0.20$, the sloshing flow becomes very violent, with an intense free surface fragmentation process; for this case, the sliding mass and the roll tank are far away from the quadrature condition. The SPH prediction of the flow presents no negligible discrepancies with respect to the experiments. Indeed, because of the violent sloshing condition, the flow comprises air entrapment, turbulence processes and significant three-dimensional effects; they are not modeled by the numerical method.

For both amplitudes A_m, the roll angle and the phase lags predicted by the numerical model agree with the experimental results reported in chapter 12 of this work. In Fig. 11.15 the roll angle $\phi(t)$ predicted by the SPH is plotted as a function of time. For $A_m = 0.05$ m an almost time-periodic state is reached after almost ten periods. Even if a small sub-harmonic develops, the roll-angle amplitude Φ stabilizes at a value of around 2 degrees. The largest A_m requires more periods of oscillation to reach a a time-periodic state, for which a value of 35 degrees is attained. Comparing the maximum roll angles with the ones evaluated with the empty tank conditions in the case with $A_m = 0.05$ m (see section 11.3), the presence of liquid induces a drastic reduction of the roll motion and the system thus behaves like a classical TLD.

This is not the case for the largest amplitude $A_m = 0.20$ m. Indeed, in such a condition the final roll angle with water inside the tank is practically the same as obtained with the empty tank condition. Fig. 11.15 shows the phase lags δ and Ψ predicted by SPH and plotted as a function of time. Since the

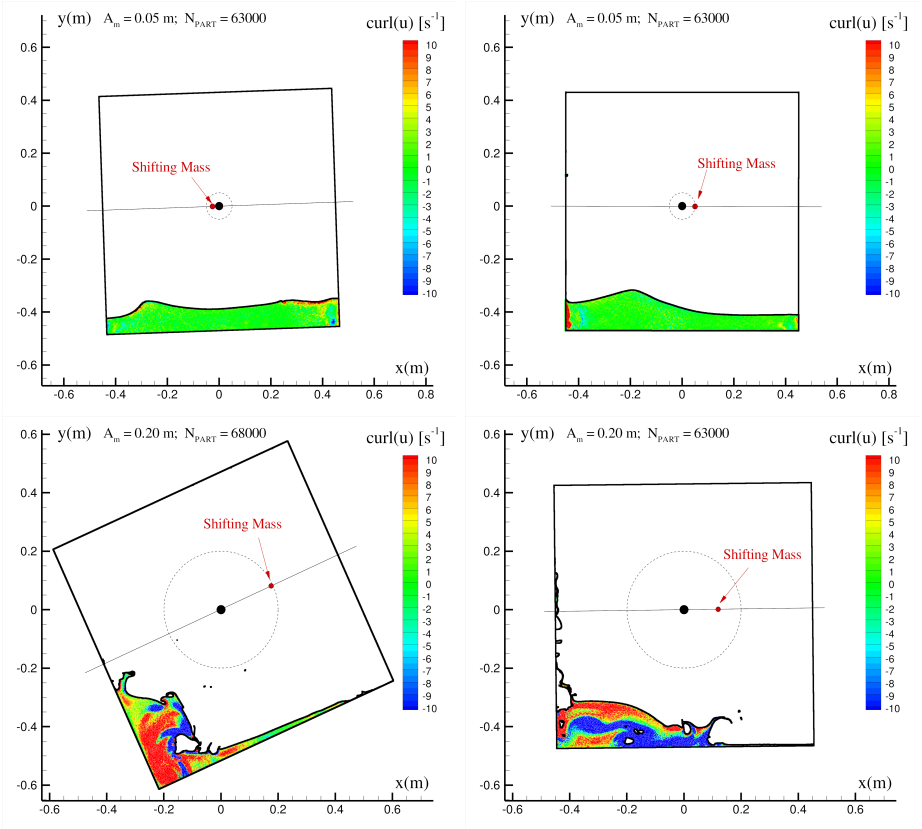

Figure 11.14.: Tank filled with water: Sloshing flow predicted by the SPH model using two excitation amplitudes of the sliding mass: $A_m = 0.05$ m (top) $A_m = 0.20$ m(bottom). Particles are colored according to their vorticity.

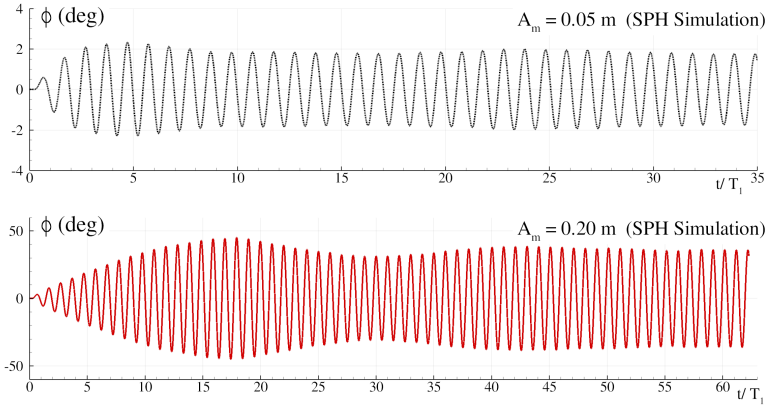

Figure 11.15.: Tank filled with water: roll angle plotted as a function of time using $A_m = 0.05$ m (top) and $A_m = 0.2$ m (bottom) obtained through the SPH model.

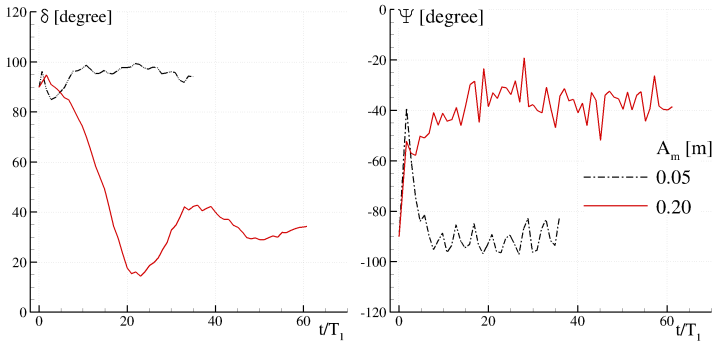

Figure 11.16.: Tank filled with water: phase lags δ and Ψ are plotted as a function of time using four different excitation amplitudes A_m obtained through the SPH model.

roll motion $\phi(t)$ is not affected by super-harmonics, δ presents a smooth time behaviour. Conversely, $\Psi(t)$ displays a noisy time history, which is linked to the more complex numerical treatment of $M_{fluid/tank}$ (see 11.2.3)

For $A_m = 0.05$ m, δ and Ψ are close to 90 degrees and -90 degrees respectively. The system is therefore close to the ideal condition discussed in section 11.5.1. For $A_m = 0.20$ m the time history of δ is more complicated and only begins to stabilize after 60 periods of oscillation at around 35 degrees. This condition gives an indication of how the non-linearities of the dynamical system play a relevant role for this second case. This unique behaviour will be discussed in greater detail in chapter 12 of the manuscript.

11.5.3 Pendulum TLD: frequency behaviour

Since the SPH model seems to predict the time evolution of the coupled system with sufficient accuracy, it is also used to study the frequency behaviour.

For the smallest amplitude ($A_m = 0.05$ m, Fig. 11.17 shows the roll angle Φ reached at time-periodic state for a range of frequencies. $\Phi(\omega)$ presents four peaks while the analysis proposed in Frandsen 2005 shows a classical TLD system which presents only two peaks around the mechanical resonant condition. However, the reduction of Φ in the neighborhood of ω_1, is also maintained in the present system.

Fig. 11.18 shows the frequency operators on the roll angle Φ, the phase lag δ and the energy transfer between the moving mass and the tank, $\Delta E_{mass/tank}$, reached at time-periodic state for two different excitation amplitudes ($A_m = 0.05, 0.20$ m). The operators for the empty tank condition presented in section 11.3.1 are reported in this plot to highlight the differences induced by the sloshing liquid.

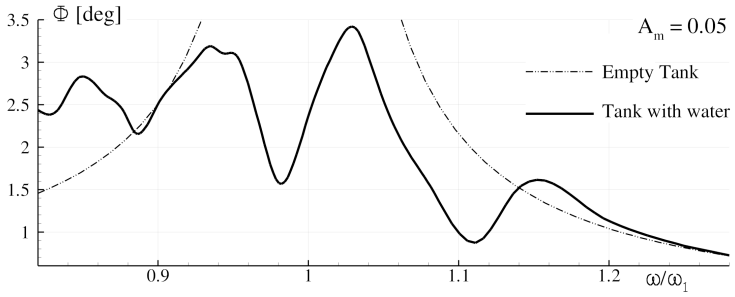

Figure 11.17.: Fully coupled angular motion system. Frequency operators evaluated through the SPH model, for Roll angle Φ, reached at periodic state for the excitation amplitude A_m= 0.05 m

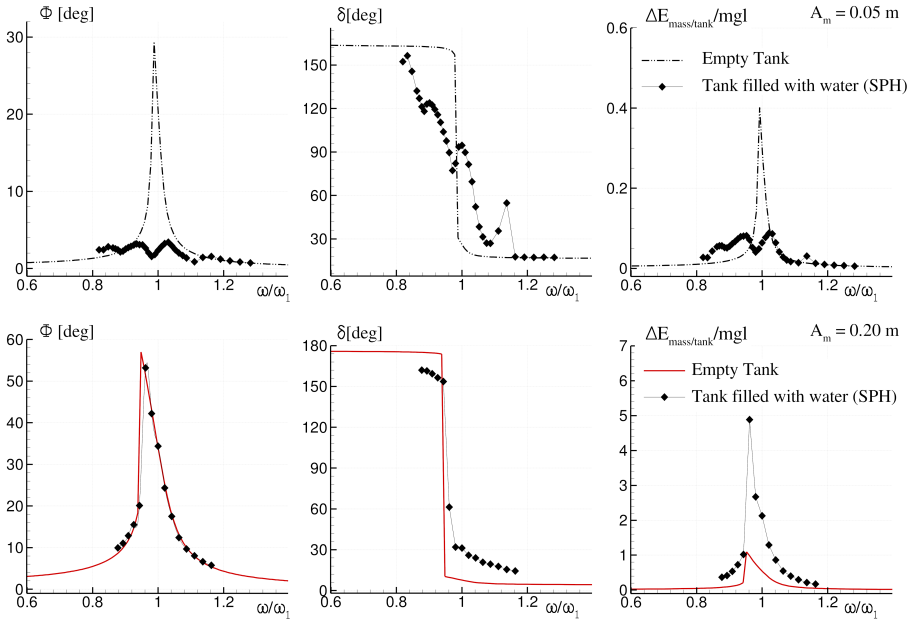

Figure 11.18.: Fully coupled angular motion system. Frequency operators evaluated through the SPH model, for the Roll angle Φ, the phase lag δ and energy transfer between the moving mass and the tank, $\Delta E_{mass/tank}$, reached at periodic state for two different excitation amplitude A_m: 0.05 m (top panel), 0.20 m (bottom panel).

For $A_m = 0.05$ m the frequency behaviour of the phase lag δ is very complex as a result of the shallow water sloshing dynamics. However, for $\omega = \omega_1$ the coupled system confirms that it is close to a quadrature condition. Since the rolling motion is highly reduced in the presence of water, the work done by the sliding mass $\Delta E_{mass/tank}$ is smaller than in the empty tank condition.

Conversely, for A_m equal to 0.20 m, the Φ angles reached at time-periodic state are practically not affected by the presence of the water, and although

there are some visible effects on the phase lag δ, the main differences appear on $\Delta E_{mass/tank}$. Indeed, when water is present inside the tank and for a large A_m, the sloshing flow is not able to reduce the roll motion and the system does not perform as an efficient TLD. However, the work exerted by the sliding mass, $\Delta E_{mass/tank}$, increases up to a factor of five. This phenomenon will be further described in chapter 12.

11.6 SUMMARY OF THIS CHAPTER

The kinematics, dynamics and energy dissipation mechanisms of a pendulum-TLD system have been analyzed.

The pendulum-TLD is composed of three coupled sub-systems: first, a sliding mass whose weight excites the motion, second, the moving parts, including the empty tank, of an angular motion sloshing rig, and third, the fluid which partially fills that tank.

An analogy with TLD and HMLD systems has been provided. Differently from other TLDs studied in the literature, the Pendulum-TLD involves large motions and complex flows, which do not permit the use of an analytical fluid dynamic model.

The nonlinear dynamics of the Pendulum-TLD has been documented both for the empty tank and for the tank partially filled with water. The frequency behaviour of the roll angles, phase lags and energy transfer has been discussed.

The energy dissipated by the sloshing flow has been quantified through a simple theoretical model based on hydraulic jump solutions. This model allows for an evaluation of the mechanical energy available to be dissipated in breaking. Furthermore, a scaling factor for the energy available to be dissipated in breaking has been obtained from this analysis. This scaling factor has been used to make non dimensional in a meaningful way the numerical results obtained by an SPH model (and the experimental data of part II).

From the numerical simulations, the complex kinematics and dynamics of the flow has been discussed: low amplitude traveling waves occur for the small excitation cases while breaking waves and violent fluid-structure impacts develop for large excitations.

Through the SPH model the complete frequency behaviour of the fully coupled system has been obtained. Interesting features have been identified. Specifically, for small excitations, the system behaves like a classical TLD. The frequency response changes drastically with large excitations.

12 MECHANICAL ENERGY DISSIPATION INDUCED BY SLOSHING AND WAVE BREAKING IN A FULLY COUPLED ANGULAR MOTION SYSTEM. II. EXPERIMENTAL INVESTIGATION.

12.1 INTRODUCTION

Much work has been done in order to assess the sloshing related loads that occur during forced harmonic motions (see e.g. Bass 1998; Diebold et al. 2011; Souto-Iglesias et al. 2006). Concerning the coupling between a mechanical system and fluid dynamics, one of the most interesting experimental work is due to Cooker 1994 who carried out decay experiments with a free oscillating tank suspended as a bifilar pendulum in the shallow-water limit. The most attractive feature of this system is that friction effects are negligible. Herczyński and Weidman 2012 also tested several shapes for a free swaying tank. Marsh et al. 2011; So and Semercigil 2004 present other decay tests with egg shaped forms, claiming that they are close to optimum in motion dampening for a range of filling heights.

Experiments for coupled roll motion in waves are found in e.g. Armenio et al. 1996a; Nasar et al. 2010. The effects of screens and baffles placed inside the tank, have been studied experimentally in the works of e.g. Firoozkoohi and Faltinsen 2010; Tait 2008; Tait et al. 2005. The extra dissipation is achieved when viscous boundary layers separate from the many solid edges of a screen. There is a rapid generation of vorticity, and therefore an associated high rate of dissipation of mechanical energy by the viscous forces. Pirner and Urushadze 2007 carried out experimental tests to assess the efficiency of a rolling and translating tank to dampen external vibrations. They performed a frequency analysis of the device, testing different filling levels and liquids with different viscosities.

In the present chapter, the Pendulum-TLD, described in chapter 11 and in Bulian et al. 2010, is experimentally studied. Only one frequency of excitation is considered, forcing the system to roll at the mechanical linear resonant frequency (see discussion in chapter 11). In the designed system, forces and

energy are retrieved from kinematic quantities. This avoids the use of sensors for the measurement of force and torque which introduces practical difficulties and measurement uncertainties. The accuracy of these results could make this work interesting for the validation of numerical models as well as to provide useful information for TLD or HMLD designers.

In order to investigate viscosity effects, three fluids are considered: water, sunflower oil and glycerine. They have a similar density but a very different viscosity. Using these three liquids makes possible the investigation of the influence of Reynolds number for both the time-periodic state dissipation and the transient dynamics of the motion. Particular attention is given to the dissipation linked to wave breaking.

This chapter is organised as follows: the second section is dedicated to the experimental setup, the third section presents experimental results for the empty tank, and in the fourth the results for water are discussed. This is a relevant case since it is the closest to an inviscid case, for which a theoretical model was developed in chapter 11. In the fifth section, results for more viscous liquids are analyzed. A summary of the energy dissipation measurements is presented considering the scales developed in chapter 11. Finally, a novel damping device, the hybrid pendulum mass liquid damper (HPMLD), is discussed before presenting conclusions.

This case is a benchmark for the SPHERIC SPH community and all data is available for reanalysis by third parties. See http://canal.etsin.upm.es/papers/bouscasseetal2013 for videos of the experiments. Watching them across together with reading the paper is recommendable.

12.2 EXPERIMENTAL SETUP

The experiments were conducted with the tank testing device of the CEHINAV - UPM research group. It is a single degree of freedom angular motion sloshing rig used for a number of experimental campaigns documented in the literature, e.g. Brizzolara et al. 2011; Degroote et al. 2010; Delorme et al. 2009; Idelsohn et al. 2008 and described thoroughly in Souto-Iglesias et al. 2011. The tank chosen for the simulations is depicted with its dimensions in Fig. 12.1. In particular, the tank length L is 0.90 m, and the width B is 0.062 m. The length $l = 0.1$ m is defined as a characteristic length of the system, indeed, the filling height adopted will be of this magnitude (almost shallow water regime) as well as the amplitude of the sliding mass motion. The distance H between the center of rotation and the tank bottom is set equal to 0.47 m. The rotation center is above the center of gravity of the whole system, implying that the system is stable at the equilibrium position.

The tank is intentionally narrow along the z-direction, i.e. the direction perpendicular to the paper, in comparison with the horizontal and vertical

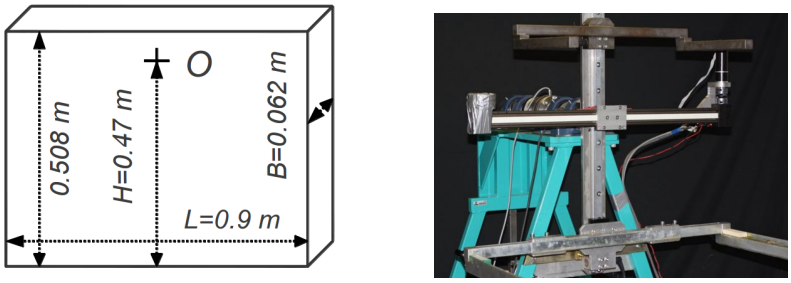

Figure 12.1.: Tank dimensions and sliding device

dimensions, in order to have a predominantly two dimensional flow. A 0.60 m long linear guide is mounted parallel to the tank bottom passing though the rotation center. A controllable electrical engine slides a mass, $m = 4.978\,kg$, along the guide with a specified motion. The weight and inertia of the mass generates a torque that acts as the external excitation to the system, and gives energy to the tank, which begins to roll. Consequently, sloshing is induced and influences the dynamics of the rigid body angular motion.

The sloshing tank rotates on a fixed plane around the fixed pivot **O**. The moment of inertia around **O** is $I_0 = 26.9\ kg.m^2$ and the static moment of the rigid system around **O** is $S_G = m_{tank}\eta_G = -29.2kg.m$. The sliding mass moves with a defined harmonic motion $\xi_m(t)$,

$$\xi_m(t) = A_m \sin(\omega t)$$

where A_m is the amplitude of the mass oscillation and ω is the oscillation frequency. T is the related period set equal to the resonance period of the mechanical system $T_1 = 1.925\,s$. The sliding mass motion amplitude A_m is set to 0.05, 0.10, 0.15 and 0.20 m. Since ξ_m is imposed, the state of the dynamical system can be defined as a function of the angle ϕ and its derivatives.

In order to understand how this system works, the reader is referred to the video presented as supplementary material for Fig. 12.2. On the left part of this figure, sample cases with the empty tank and the tank partially filled with water are presented. In the top panel the angular motion of the tank is presented for these two cases. The influence of the fluid on the tank motion time history can be appreciated. Finally, in the bottom panel, the motion of the exciting sliding mass, which is the same for both cases, is plotted.

12.3 DYNAMICS OF THE SYSTEM WITH THE EMPTY TANK

As shown in chapter 11, the dynamics of the system with the empty tank is not a straightforward problem due to the strong non-linear features. The analysis of chapter 11 focused mainly on the time-periodic state, and results

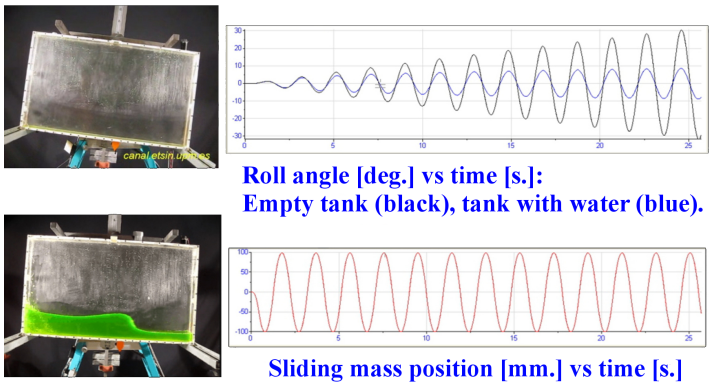

Figure 12.2.: Experimental device in action, top: empty tank, bottom: tank partially filled with water. Videos available as supplementary materials at http://canal.etsin.upm.es/papers/bouscasseetal2013/.

were obtained through a numerical integration of equation (III.22) in chapter 11. The transient dynamics was shown to lead to very large angles.

In order to remain within the safety operational margins of the sloshing rig, the experiments are stopped when the roll angle ϕ exceeds 35° (see Fig. 12.3). This constraint impedes the time-periodic state showed in chapter 11 to be reached. In the early phase of the test, $\Delta E_{mass/tank}$ is converted in $[E^{mech}_{tank}]^{t+T}_{t}$ and partially in $\Delta E_{friction}$. The system can be said to behave linearly with A_m in that early phase.

The primarily linear behaviour seen on the experimental plots is confirmed in Fig. 12.4, where the lag function $\delta(t)$ (see definition in chapter 11 section II.C) is plotted as a function of time. δ remains close to 90° (meaning that the roll motion is in quadrature with the sliding mass) for all amplitudes A_m.

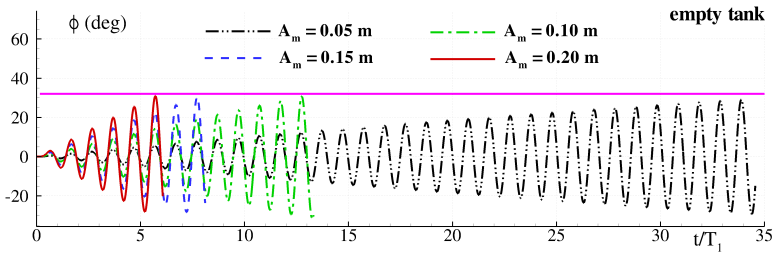

Figure 12.3.: Empty tank: experimental roll angle ϕ plotted as a function of time for different A_m value using the excitation frequency $\omega = \omega_1$. The horizontal purple line indicates the safety margins of the sloshing rig (35 degrees).

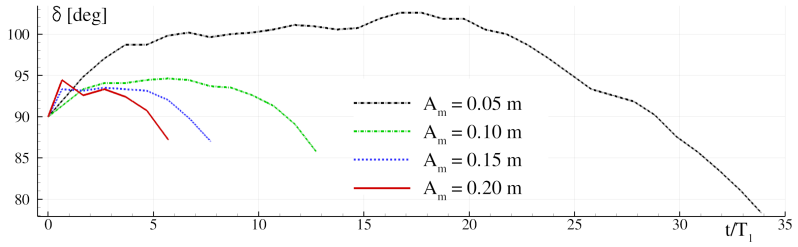

Figure 12.4.: Empty tank: shift function δ obtained from experiments plotted as a function of time for different A_m value using the excitation frequency $\omega = \omega_1^m$.

12.4 ANALYSIS OF THE DYNAMICAL SYSTEM: TANK FILLED WITH WATER.

In this section, the analysis of the dynamical system is considered when the tank is partially filled with water. The filling level is set equal to $h = 0.092$ m and has been chosen so that the first sloshing period matches the resonance period of the structure $T_1 = 1.925$ s (see chapter 11). The period for the motion of the sliding mass T has been set equal to T_1, and the excitation amplitudes A_m are again $0.05\,, 0.10\,, 0.15\,, 0.20$ m, labeled respectively as Series 1,2,3,4.

A discussion is presented for the four excitation amplitudes since distinct features in the sloshing regimes are observed; these are summarised in Table 12.1. In order to illustrate them, some pictures of the flow are presented in Fig. 12.5 for each of the Series. Two instants are selected for each case, one with the maximum angle and one with a flat angle.

	A_m (m)	motion regime	developed flow
Series 1	0.05	weak	wave train without breaking event
Series 2	0.10	moderate	plunging breaker in the middle of the tank
Series 3	0.15	strong	strong hydraulic jump flow
Series 4	0.20	very strong	an almost dam-break flow

Table 12.1.: Sloshing regime induced in the oscillating tank when using water.

For the first Series, only a wave train without breaking events takes place. For the second Series, a plunge breaking event develops towards the middle of the tank. For the most violent case, Series 4, when the maximum roll angle is reached, almost all the water accumulates on the tank side and a quasi dam-break type flow occurs.

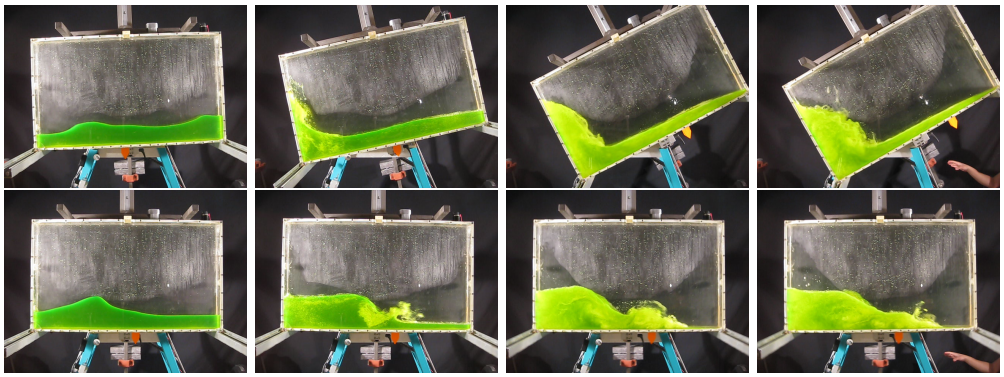

Figure 12.5.: Sloshing wave in tank filled with water from left to right $A_m = 0.05, 0.1, 0.15, 0.2$ m. Videos available from http://canal.etsin.upm.es/papers/bouscasseetal2013/.

12.4.1 Roll angle

The experimentally obtained roll angles are plotted as a function of time in Fig. 12.6. For the first three Series, the system reaches an approximate time-periodic state within 40 periods; the duration of the experiment is not long enough for Series 4 to reach such state.

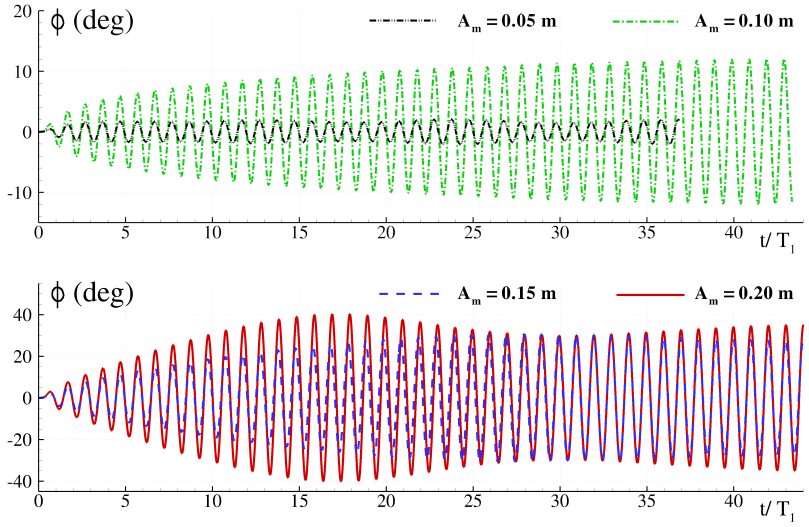

Figure 12.6.: Tank filled with water: roll angle plotted as a function of time using $A_m = 0.05$ m, $A_m = 0.1$ m (top), $A_m = 0.15$ m, $A_m = 0.2$ m (bottom), excitation frequency $\omega = \omega_1^m$.

Fig. 12.7 depicts the envelope function Φ defined in equation 11.19 as:

$$\Phi(t) = \frac{\pi}{2T} \int_t^{t+T} |\phi(s)| \, ds \tag{12.1}$$

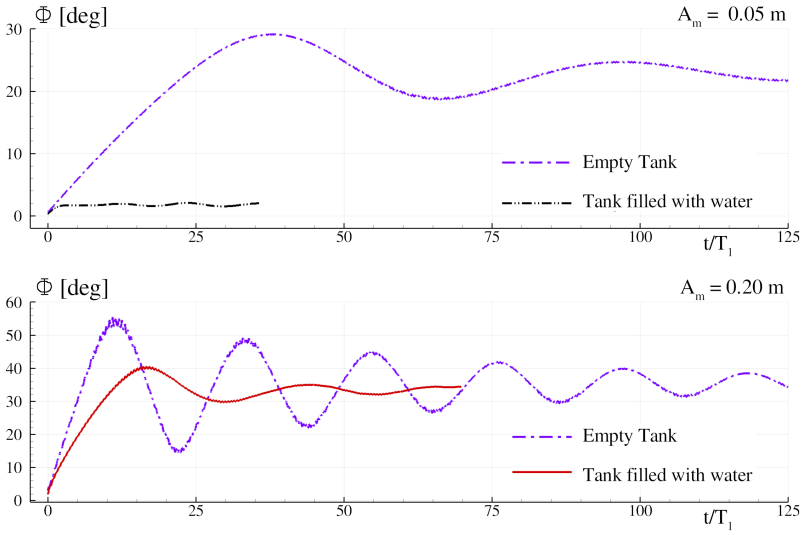

Figure 12.7.: Envelope function Φ plotted as a function of time, using excitation amplitudes $A_m = 0.05$ m (top) and $A_m = 0.20$ m (bottom) for the empty tank and for the water filled tank.

obtained with the empty tank and with the tank filled with water for both Series 1 and 4.

The top plot is obtained for the smallest excitation amplitude $A_m = 0.05$ m. In this case, the system behaves like a classical TLD, i.e. when water is present, Φ is drastically reduced. In the transient stage and for the largest excitation, $A_m = 0.20$ m, the angle Φ is lower when water is present (maximum angle 52° with the empty tank against 40° with water), as can be seen in the same figure. On the other hand, at time-periodic state, the roll angle is similar for the two different configurations (empty / filled with water).

This behaviour is partially explained by the fact that $M_{mass/tank}$ is approximately proportional to A_m (see equation (II.4) of chapter 11) while $M_{fluid/tank}$ is approximately proportional to $\sqrt{\Phi}$ (see equation (IV.27) of chapter 11). The behaviour of the coupled system is further influenced by the phase lags between the different torques.

12.4.2 Phase lags analysis of the coupled system

The results of the time evolution of δ (phase lag between the sliding mass motion and roll angle) and Ψ (phase lag between $M_{fluid/tank}$ and the roll

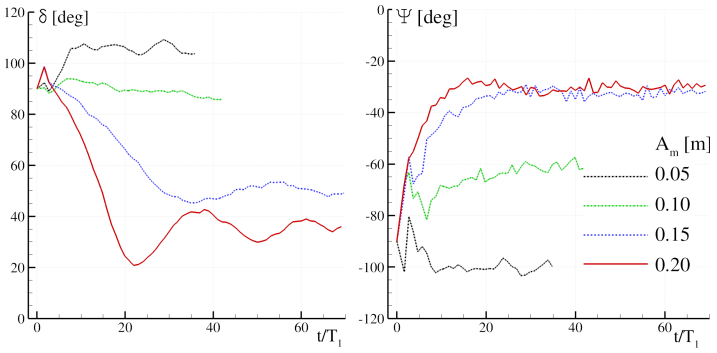

Figure 12.8.: Tank filled with water: phase lags δ and Ψ plotted as a function of time using the four different excitation amplitudes A_m mentioned in section 12.2.

angle) are shown in Fig. 12.8. The torque $M_{fluid/tank}$ is evaluated through (Eq. II.8 of chapter 11):

$$M_{fluid/tank} = I_0\ddot{\phi} - gS_g\sin(\phi) + B_\phi\dot{\phi} + K_{df}sgn(\dot{\phi}) + m\xi_m gcos(\phi) + m(2\xi_m\dot{\xi}_m\dot{\phi} + \xi_m^2\ddot{\phi}) \tag{12.2}$$

where the motions of the sliding mass $\xi_m(t)$ and of the tank $\phi(t)$ are experimentally recorded.

For the smallest value of A_m, the torque $M_{fluid/tank}$ (see 12.2) is approximately in quadrature with the tank motion ($\Psi \approx -90°$) during the time evolution. The roll motion is also approximately in quadrature with the sliding mass motion ($\delta \approx 90°$). For larger A_m, the phase lag Ψ measured at the time-periodic state moves to $\Psi = -30°$ for Series 3). δ also changes accordingly with the net outcome being that $M_{fluid/tank}$ remains approximately in counter-phase with $M_{mass/tank}$ at time-periodic state. Indeed, the fluid helps the system to reduce the effect of the external excitation.

This can be appreciated in the phasors' graphs, corresponding to the time-periodic state, of Fig. 12.9. For the smallest value of A_m (top panel), the system behaves basically like the ideal TLD system presented in chapter 11. For the largest value of A_m (bottom panel), the behaviour is completely different from what expected in a ideal TLD.

In chapter 11, the dissipation properties of the Pendulum-TLD excited with large values of A_m was discussed and the analogy of the present system with a hybrid mass liquid damper was established. With such an analogy it is important that the damper does not return energy to the external system. As it shown in chapter 11, this is not always the case with the empty tank. This implies that it is necessary to analyze energy transfers during the process in order to establish the practical interest of the present system.

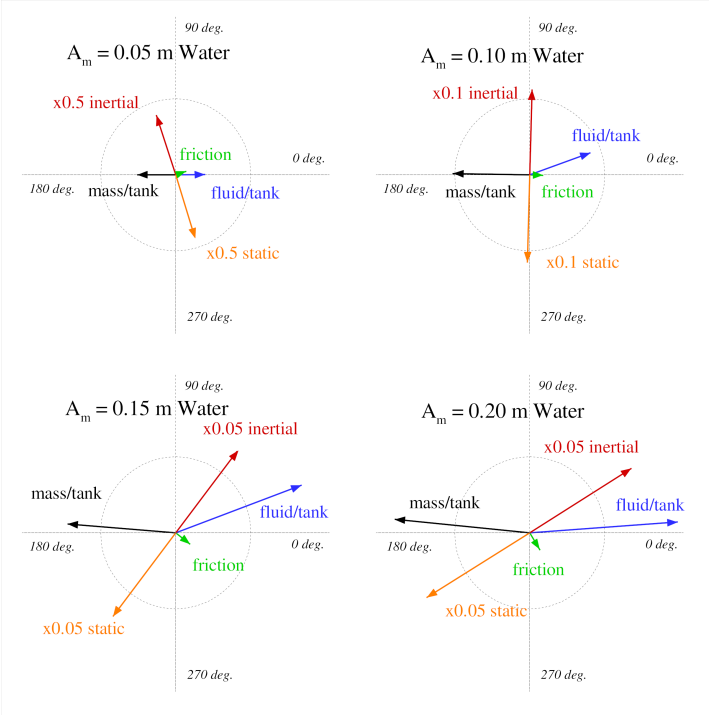

Figure 12.9.: Phasors obtained for the tank filled with water (see definition in chapter 11). Torque modulus and phase are retrieved as the first harmonic at time-periodic state.

12.4.3 Energy transfer from tank to fluid

The time history of the energy transfer between the sliding mass and the tank in one cycle, $\Delta E_{mass/tank}$, can be calculated with equation:

$$\Delta E_{mass/tank} = \int_{t}^{t+T} M_{mass/tank}(s)\,\dot{\phi}\,ds, \tag{12.3}$$

This variable is depicted in Fig. 12.10 for the extreme sliding mass motion amplitudes (the reader is referred to chapter 11 for all the torque and energy term definitions and sign conventions).

For Series 1, when the tank is empty, $\Delta E_{mass/tank}$ is always positive and the value largely oscillates before ending in a time-periodic state. When water is in the tank, $\Delta E_{mass/tank}$ is drastically reduced and so is the roll angle amplitude. The low level of $\Delta E_{mass/tank}$ is continuously transferred to the gentle sloshing flow regime.

For Series 4, when the tank is empty, $\Delta E_{mass/tank}$ periodically changes in sign; in other words, the sliding mass exerts work on the tank during some parts of the process but also receives work from the tank in others. This is a major concern, assuming that the goal is to retrieve energy from the exciting sys-

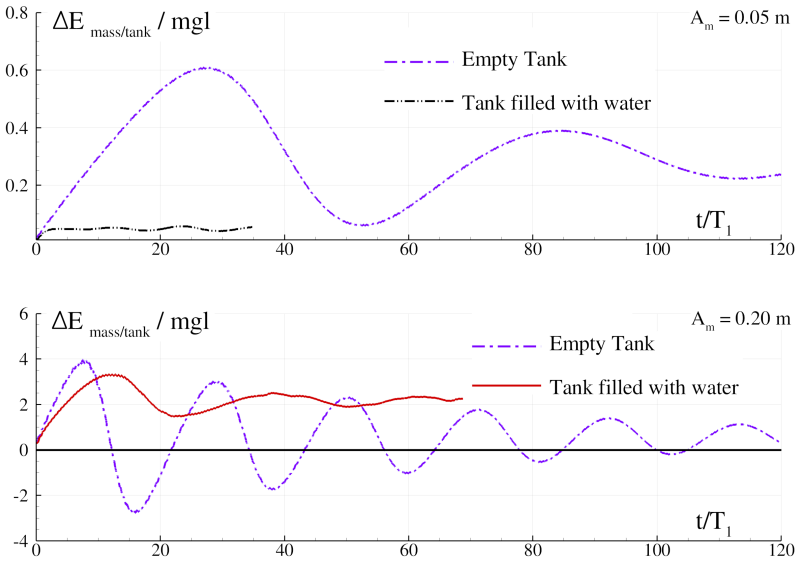

Figure 12.10.: $\Delta E_{mass/tank}$ plotted as a function of time, using excitation amplitudes $A_m = 0.05$ m (top) and $A_m = 0.20$ m (bottom) for the empty tank and for the tank filled with water.

tem. With this amplitude and the empty tank, the sign only stabilizes as positive after many periods. On the other hand, in presence of water, $\Delta E_{mass/tank}$ remains positive; the sliding mass always makes a positive and intense work on the tank which is then transferred to the fluid through $-\Delta E_{fluid/tank}$. At time-periodic state this work is fully dissipated by the fluid. This dissipation can be quantified, as discussed hereafter.

12.4.4 Wave breaking and energy dissipation

The energy transfer between the fluid and the tank, $\Delta E_{fluid/tank}$, is obtained as:

$$\Delta E_{fluid/tank} := \int_t^{t+T} M_{fluid/tank}(s)\,\dot{\phi}\,ds, \tag{12.4}$$

where $M_{fluid/tank}(s)$ is computed from experiments using eq. (12.2). Fig. 12.11 plots $\Delta E_{fluid/tank}$ as a function of time for the four Series. This term comprises the fluid mechanical energy variation and a dissipation term (see also chapter 11):

$$\Delta E_{fluid/tank} = -[E^{mech}_{fluid}]_t^{t+T} + \Delta E^{dissipation}_{fluid} \tag{12.5}$$

On these plots a dissipated energy per cycle, $\Delta E^{dissipation}_{fluid}$, time history plot

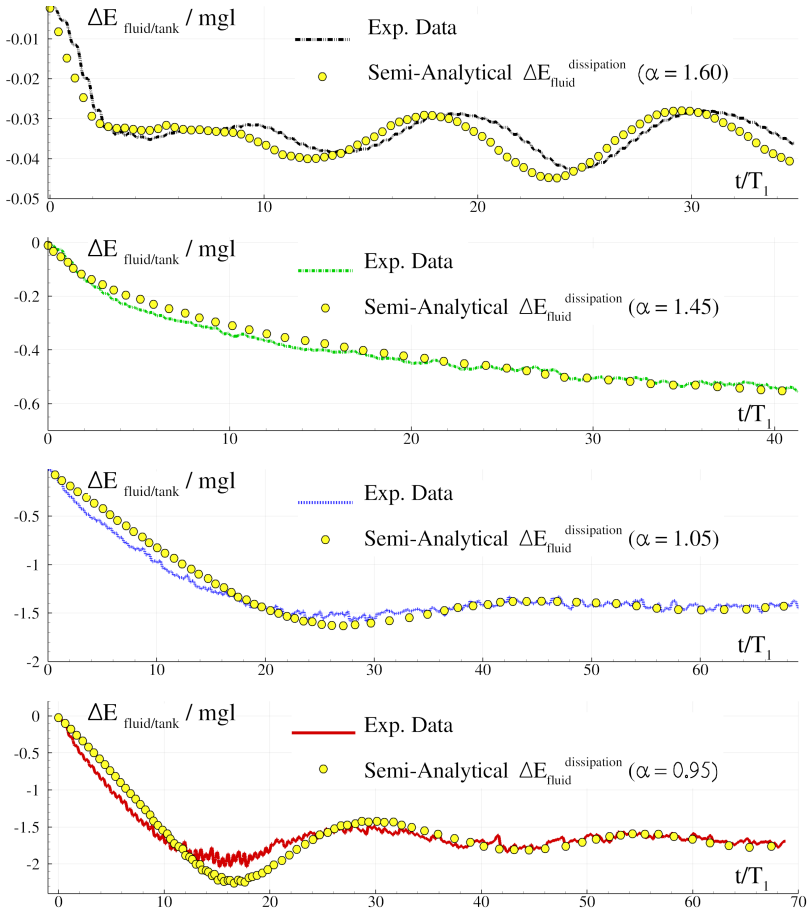

Figure 12.11.: Energy transfer $\Delta E_{fluid/tank}$ plotted as a function of time, using excitation amplitudes $A_m = 0.05$, 0.10, 0.15 and 0.20 m (from top to bottom).

is also included computing it with the following semi-analytical expression (see eq. 11.33):

$$\Delta E_{fluid}^{dissipation}(t) = -\alpha \left[4\, m_{liquid}\, g\, h\, \Phi^{\frac{3}{2}}(t) \right], \tag{12.6}$$

in which $\Phi(t)$ is the recorded envelope (see eq. (11.19)) and α is a constant coefficient α tuned in order to match the curves on the final part of the time histories. The range of α adopted is in agreement with what was obtained in the numerical analysis for forced motion performed in chapter 11. Indeed, for the smaller excitation amplitude cases, $A_m = 0.05$ m, the coefficient α is close to the theoretical value 1.68 found in chapter 11. By increasing the amplitude, α is progressively reduced as predicted by the SPH model discussed in chapter 11.

Even if these "semi-analytical" curves may be a crude approximation, the fine match with the experimental data indicates:

1. the predicted values for the dissipation in time-periodic state for water are within the range found in chapter 11.
2. that for moderate and large amplitude cases, the large increases in dissipation are linked to the breaking wave phenomena, that dominate the flow dynamics.
3. the component $[E^{mech}_{fluid}]^{t+T}_{t}$ seems to be much smaller than $\Delta E^{dissipation}_{fluid}$ along the whole process, except for the very early stage. This is also confirmed by other results shown in section 12.5.5.

It is observed that a perfect time-periodic state is not reached for Series 1 and a sub-harmonic behaviour appears. However, the amplitudes of the sub-harmonics are small and the phenomenon can be ignored in the present analysis.

Using the results of the previous subsection, it can be stated that the dissipation associated with intense breaking wave phenomena stabilizes the sign of the energy $\Delta E_{mass/tank}$ for Series 2, 3 and 4. For Series 1 the low level of energy involved only induces the development of wave trains inside the tank.

12.4.5 Summary of results for the water case

To summarize the results of this section, the value of the main quantities at time-periodic state are reported in table 12.2. It can be noted that the energy transfers $\Delta E_{fluid/tank}$ and $\Delta E_{mass/tank}$ for the case $A_m = 0.20$ m are almost 50 times higher than the one with $A_m = 0.05$ m, while the external work ratio $\Delta E^{water}_{mass/tank}/\Delta E^{empty}_{mass/tank}$ increases by a factor of 25.

Finally, in Fig. 12.12 the torque $M_{mass/tank}$ is plotted as a function of time for the excitation amplitude $A_m = 0.20$ m for both the empty tank and for the tank filled with water. This plot confirms that even when the water is present, $M_{mass/tank}$ remains in phase opposition with the sliding mass motion. It also confirms that the torque amplitude is practically unaffected by the presence of water (*i.e.* the differences induced by the roll motion $\phi(t)$ on the torque $M_{mass/tank}$ are negligible).

12.5 EFFECTS OF THE LIQUID ADOPTED: VISCOSITY AND DENSITY.

In the performed experiments, the influence of the viscosity of the fluid is explored. Table 12.3 records the physical properties of the three liquids used:

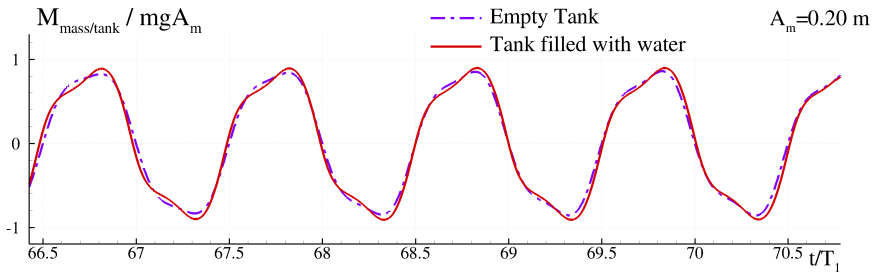

Figure 12.12.: Torque $M_{mass/tank}$ plotted as a function of time, using excitation amplitude $A_m = 0.20$ m for the empty tank and for the water filled tank.

A_m [m]	0.05	0.10	0.15	0.20
Φ [deg]	1.7	12	28	33
δ [deg]	105	85	50	35
Ψ [deg]	-100	-60	-33	-30
$\Delta E_{mass/tank}/mgl$	0.05	0.65	1.8	2.2
$\Delta E_{fluid/tank}/mgl$	-0.035	-0.52	-1.42	-1.68
$\Delta E_{friction}/mgl$	-0.015	-0.13	-0.38	-0.52
$\Phi^{water}/\Phi^{empty}$	0.085	0.43	0.90	0.97
$\Delta E^{water}_{mass/tank}/\Delta E^{empty}_{mass/tank}$	0.17	1.55	3.6	4.07

Table 12.2.: Tank filled with water: values of the main quantities reached at time-periodic state for the excitation amplitudes: A_m= 0.05, 0.10, 0.15 and 0.20 m.

water, sunflower oil, and glycerine. The total mass of fluid in the tank, the surface tension coefficient, and the density, all differ little among the three liquids. But the three values of the kinematic viscosity vary such that the oil is fifty times more viscous than water, and the glycerine is 740 times more viscous than water.

	$\nu(m^2 \cdot s^{-1})$	$\sigma(mN/m)$	$\rho(kg \cdot m^{-3})$	$m_{liquid}(Kg)$
Glycerine	$7.4 \cdot 10^{-4}$	64	1261	6.474
Sunflower Oil	$5 \cdot 10^{-5}$	33	900	4.620
Water	10^{-6}	72	998	5.123

Table 12.3.: kinematic viscosity, surface tension, density and mass inserted inside the tank for the studied fluids.

In Table 12.4 the different Reynolds numbers, defined as $Re = \sqrt{gh}\,A_m/\nu$, and Weber number, defined as $We = \rho\, gh\, A_m/\sigma$, are reported, assuming $\sqrt{gh}$ is the characteristic flow velocity in shallow water condition.

	A_m (m)	Re^{water}	Re^{oil}	$Re^{glycerine}$	We^{water}	We^{oil}	$We^{glycerine}$
Series 1	0.05	47500	950	64	625	1230	890
Series 2	0.10	95000	1900	128	1250	2460	1780
Series 3	0.15	142500	2850	193	1880	3690	2670
Series 4	0.20	190000	3800	256	2500	4920	3560

Table 12.4.: Reynolds and Weber numbers for the sloshing flows induced in the oscillating tank when using water, sunflower oil and glycerine inside the tank.

As shown hereinafter, when using sunflower oil and glycerine, the roll angle obtained is generally larger than the one recorded with water. As a consequence and for safety reasons, the tests for Series 3 and Series 4 are stopped during the transient, before a time-periodic state could be reached.

12.5.1 Series 1

Two pictures, representative of the flow evolution at time-periodic state for Series 1, are shown in Fig. 12.13 for all three fluids. The wave train obtained with water has already been discussed. For the oil case, the viscosity damps out the wave train and wave steepness is drastically reduced. When using glycerine, the free surface remains almost flat.

The left plot of Fig. 12.14 shows the roll angle amplitude Φ as a function of time for $A_m = 0.05$ m with water, sunflower oil and glycerine. An almost time-periodic state is achieved for all cases within about 20 periods. The time-periodic state angles are 2, 3 and 7° for water, oil and glycerine, respectively. Therefore, the least viscous fluid (water) leads to the lowest roll angles, and the most viscous (glycerine) to the largest ones. The time-periodic state angle obtained with glycerine is more than twice the one obtained with oil and more than three times that of water. These results are in agreement with those reported in Pirner and Urushadze 2007 who found a similar behaviour with methanol, water and glycerine. This means that, if the dynamical system is considered as a TLD, the use of water allows for the best reduction of the roll angle for a given harmonic torque at ω_1.

The right plot of Fig. 12.14 depicts the energy transfer $\Delta E_{fluid/tank}$ as a function of time. This plot shows that using water, the response of the energy transfer is accelerated, whereas using glycerine $\Delta E_{fluid/tank}$ takes more time to stabilize.

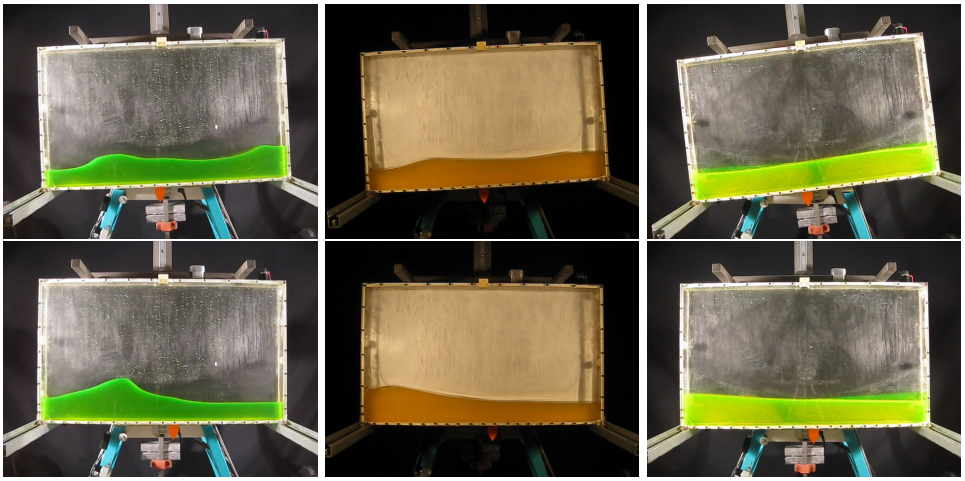

Figure 12.13.: Sloshing wave in tank: filled with water, oil and glycerine $A_m = 0.05m$. See supplementary materials from http://canal.etsin.upm.es/papers/bouscasseetal2013/.

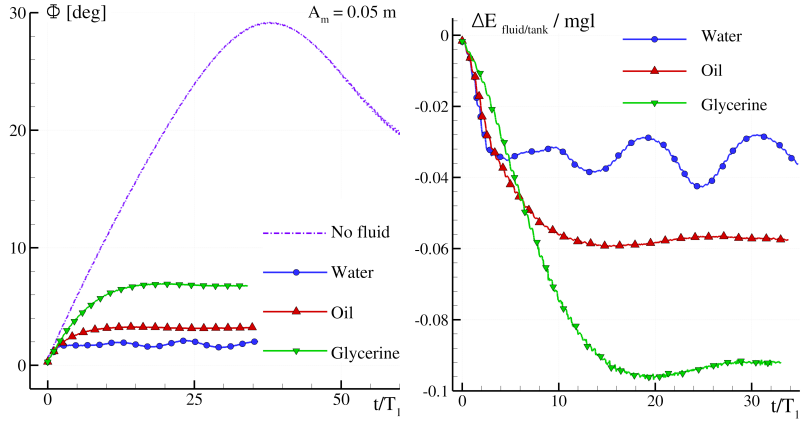

Figure 12.14.: Envelope function Φ (left) and energy transfer $\Delta E_{fluid/tank}$ (right) plotted as a function of time, with an excitation amplitude $A_m = 0.05$ m, using water, sunflower oil and glycerine inside the tank.

Liquid	water	oil	glycerine
Φ [degree]	1.7	3.2	6.8
δ [degree]	105	110	125
Ψ [degree]	-100	-103	-127
$\Phi^{liquid}/\Phi^{empty}$	0.085	0.16	0.34
$\Delta E^{liquid}_{mass/tank}/\Delta E^{empty}_{mass/tank}$	0.17	0.29	0.52

Table 12.5.: Tank filled with water, oil, glycerine: values of the main quantities reached at time-periodic state for the excitation amplitude A_m= 0.05 m.

The main quantities at time-periodic state using the three different liquids are reported in table 12.5. From these measurements, it is observed that by increasing the viscosity, the moduli of δ (positive) and Ψ (negative) also increase, as shown with the phasors of the various torques plotted in Fig. 12.15. The phasor plane obtained with water has the closest behaviour to an ideal TLD such as the one discussed in chapter 11. This justifies why using water is a more efficient option for the reduction of the roll angle than using other liquids.

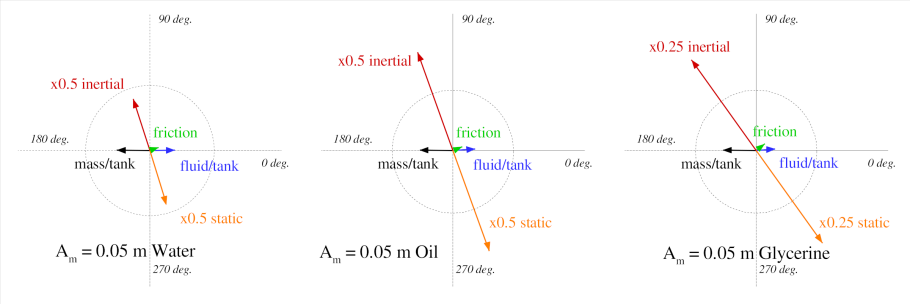

Figure 12.15.: Phasors obtained for the tank filled with water $A_m = 0.05m$. Torque modulus and phases are retrieved as the first harmonic at time-periodic state.

12.5.2 Series 2

Typical pictures of the sloshing flow at time-periodic state for Series 2 are shown in Fig. 12.16 for all three fluids. For Series 2 and with water, an energetic plunger develops in the middle of the tank. When oil is present, a spilling breaking phenomena develops. When using glycerine, the high viscosity inhibits the formation of steep waves.

The left plot of Fig. 12.17 shows the roll angle amplitude Φ plotted as a function of time for the amplitude $A_m = 0.10$ m using water, sunflower oil, and glycerine. The attainment of the time-periodic state requires more oscillations than in Series 1. Indeed, at least 50 periods are needed for all three liquids. The experimental records are too short to take the system to the time-periodic state regime. Experimental data can only be extrapolated upon in order to get the value of Φ for longer time ranges. The time-periodic state angles are approximatively 12, 16 and 20 degrees for water, oil and glycerine respectively. The least viscous fluid (water) leads to the lowest roll angles and the most viscous (glycerine) to the largest ones as in the previous Series. However, the relative differences between the liquids are smaller than those observed in Series 1.

The right plot of Fig. 12.14 depicts the energy transfer $\Delta E_{fluid/tank}$ plotted as a function of time. Considering the steepness of these curves during the

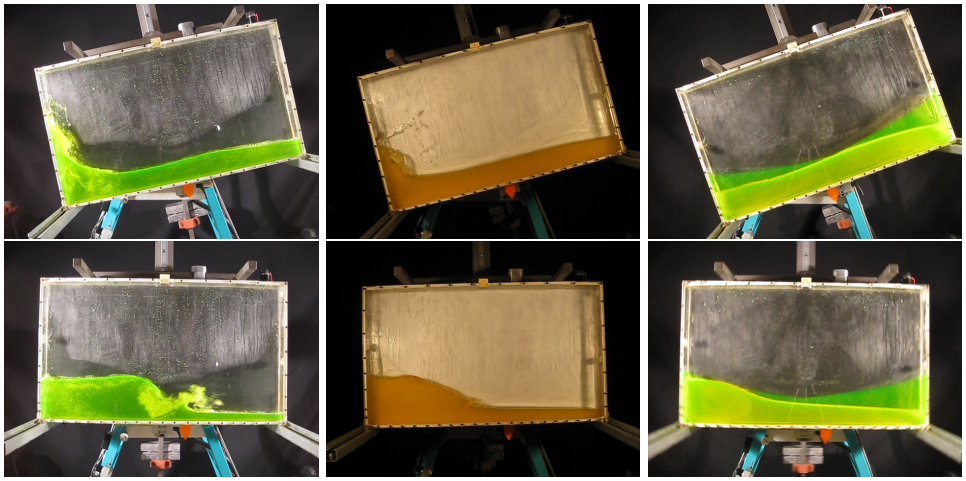

Figure 12.16.: $A_m = 0.1m$; sloshing wave in tank: filled with water, oil and glycerine. See supplementary materials from at http://canal.etsin.upm.es/papers/bouscasseetal2013/.

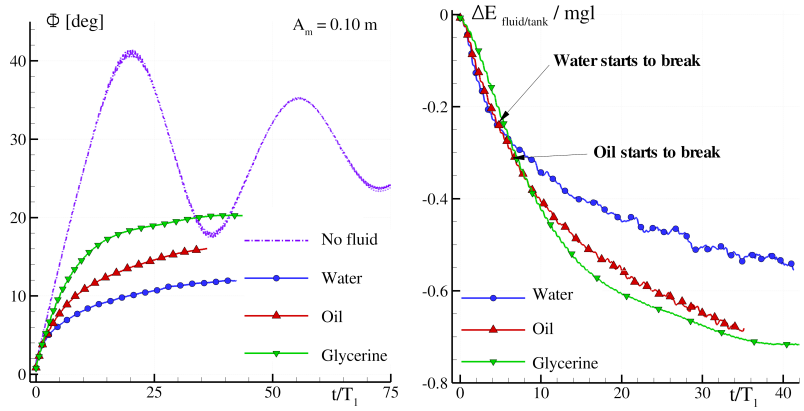

Figure 12.17.: Envelope function Φ (left) and energy transfer $\Delta E_{fluid/tank}$ (right) plotted as a function of time, with an excitation amplitude $A_m = 0.10$ m, using water, sunflower oil and glycerine inside the tank.

initial stage, it can be inferred that water has a faster response with respect to energy transfer. Fig. 12.14 also reports the time instants when the first breaking of the free surface is observed. Using water, the breaking appears earlier than with oil, that is, after just four periods. When the breaking develops, the slope of $\Delta E_{fluid/tank}$ is reduced and the curve related to water crosses the curves corresponding to oil and glycerine. In the early stages, the increase of $\Delta E_{fluid/tank}$ is affected by the mechanical energy component (see eq. (11.15)). Water and oil increase their mechanical energy quickly as a result of the tank motion. The breaking process then induces a large increase of the dissipation component $\Delta E_{fluid}^{dissipation}$; it is the only one present at time-periodic state. Due to the breaking processes for water and oil, and to the high viscosity

of the glycerine, the value of $\Delta E_{fluid/tank}$ increases one order of magnitude with respect to the measurements in Series 1.

The phasors of the various torques are plotted in Fig. 12.18. With water and oil, the phasor plane keeps close to the ideal TLD of chapter 11.

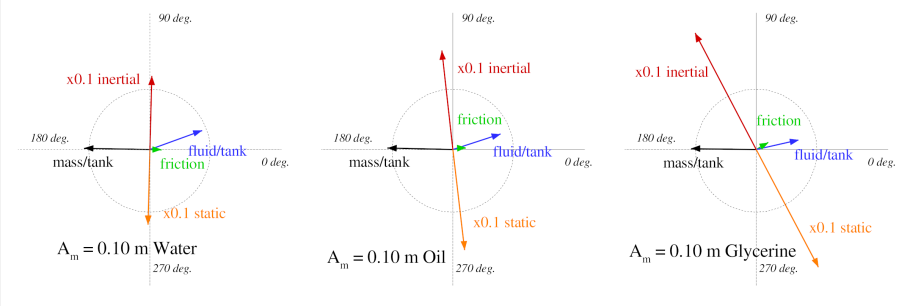

Figure 12.18.: Phasors obtained for the tank filled with water $A_m = 0.1m$.

Liquid	water	oil	glycerine
Φ [degree]	12	16	20
δ [degree]	85	96	120
Ψ [degree]	-60	-80	-110
$\Phi^{liquid}/\Phi^{empty}$	0.43	0.57	0.71
$\Delta E^{liquid}_{mass/tank}/\Delta E^{empty}_{mass/tank}$	~ 1.7	~ 2.3	~ 2.3

Table 12.6.: Tank filled with water, oil, glycerine: values of the main quantities reached at time-periodic state for the excitation amplitude A_m= 0.05 m.

For this Series 2, an estimation of the main quantities at time-periodic state using the three different liquids are reported in table 12.6. The work done by the sliding mass on the tank, $\Delta E_{mass/tank}$, is very similar when using glycerine or oil, although the pair of values (δ,Φ) are different. The phase lags δ and Ψ increase in modulus together with viscosity.

12.5.3 Series 3

The sloshing flows for the Series 3 cases are visualised with several photographs (see Fig. 12.19). The selected pictures correspond to an oscillation angle of about 30°, which is extremely large for roll motion sloshing. With water, almost the entire side wall is covered, and the successive evolution shows a large plunging wave with a splash-up producing air entrapment. For the oil, the elevation on the wall is similar, whilst the breaking wave is less violent. With the glycerine, a spilling breaker develops, a salient feature to be found in a liquid 740 times more viscous than water.

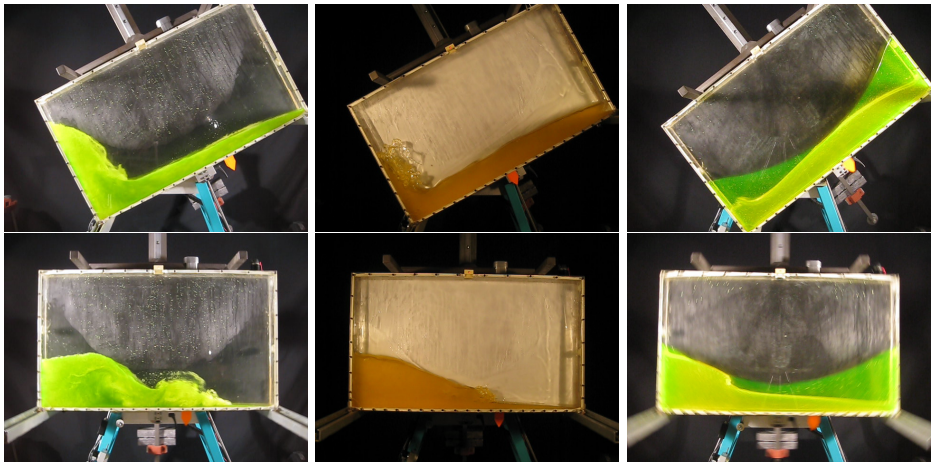

Figure 12.19.: Sloshing wave in tank: filled with water, oil and glycerine $A_m = 0.15m$. See supplementary materials from http://canal.etsin.upm.es/papers/bouscasseetal2013/.

The left plot of Fig. 12.20 shows the time histories for the envelope function Φ. When oil and glycerine are used, the roll angle exceeds 35° and the experiment is stopped in order to avoid risking the integrity of the rig. This reduces the possibilities of the analysis, but the time history of Φ suggests that with oil and glycerine the roll angle at time-periodic state can be higher than the one reached with the empty tank.

The large roll motion induces an intense energy transfer $\Delta E_{fluid/tank}$ (see right plot of Fig. 12.20), almost three times larger than in Series 2. The time instants when the breaking phenomena start to develop are reported in Fig. 12.20. The first breaking event occurs during the first four periods of oscillations for oil and water. Glycerine shows an extended transient phase; the first breaking event appears after 15 periods.

Fig. 12.21 shows the phase lags δ and Ψ plotted as a function of time for Series 3. Large time ranges are needed to stabilize the phase lag δ (left panel) between the sliding mass and the roll angle. However, even if the dynamical system is far from a time-periodic state, Ψ (right panel) is almost stable after 20 periods. The increase of viscosity generates an increase in modulus for both δ and Ψ, at least in the time range covered by the experiments, similar to what was obtained in previous Series. These results also show that when using oil in the tank, the torque $M_{fluid/tank}$ is in quadrature with the roll motion. This affects the energy transfer between the fluid and the tank. Indeed, the $\Delta E_{fluid/tank}$ obtained with oil is almost the same as the one obtained with glycerine, even though the roll angle with oil is lower.

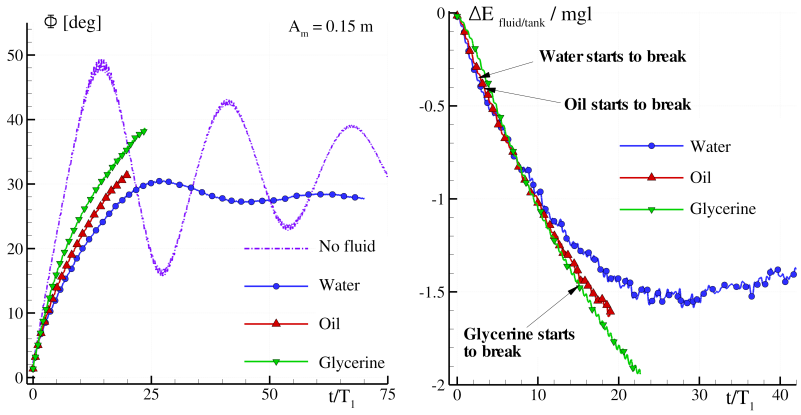

Figure 12.20.: Envelope function Φ (left) and energy transfer $\Delta E_{fluid/tank}$ (right) plotted as a function of time, with an excitation amplitude $A_m = 0.15$ m, using water, sunflower oil and glycerine inside the tank.

12.5.4 Series 4

Very little information is available for the last Series, mainly because after a few periods the roll angles induced are larger than allowed by the rig, and therefore the experimental time records are too short for a complete analysis of the system's dynamics.

The left plot of Fig. 12.22 shows the envelope function for the roll angle Φ obtained for the first eight periods. The angles relative to the three different liquids manifest small differences. Again, as already shown for the first three Series, the roll angle attained is smallest when using water. The energy transfer $\Delta E_{fluid/tank}$ is also very similar for the three liquids in the transient stage. In these first eight oscillations, the phase lag δ remains close to 90° (left plot of Fig. 12.23) whilst the phase lag Ψ has a more complex time behaviour. When using oil, Ψ shows a tendency to remain closer to a quadrature configuration 90° whilst, when using water, Ψ decreases in modulus until the value of $-30°$. Contrarily, when using glycerine, Ψ increases in modulus, finally settling on the value $-120°$.

Fig. 12.24 depicts $M_{mass/tank}$, $M_{fluid/tank}$ and ϕ in the transient stage, as a function of time. $M_{fluid/tank}$ quickly opposes $M_{mass/tank}$ (*i*.e. $\delta + \Psi \approx 0$). Conversely $M_{fluid/tank}$ increases in amplitude very slowly, indicating that, in the first 10 periods of oscillation, the system is quite far from the time-periodic state, as confirmed by the increase of the roll angle $\phi(t)$. Furthermore, $M_{mass/tank}$ shows a small non-linear behaviour resulting from the large amplitude A_m, as already commented upon in section 12.4.

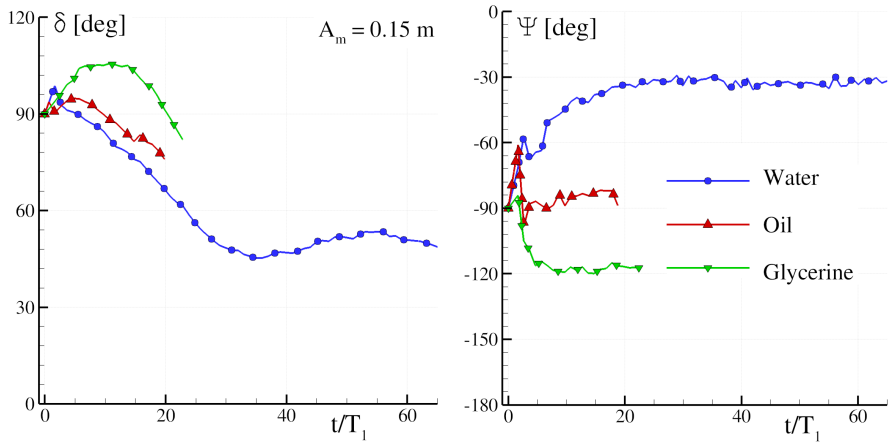

Figure 12.21.: Phase lags δ (left) and Ψ (right) plotted as a function of time, with an excitation amplitude $A_m = 0.15$ m (Series 3), using water, sunflower oil and glycerine.

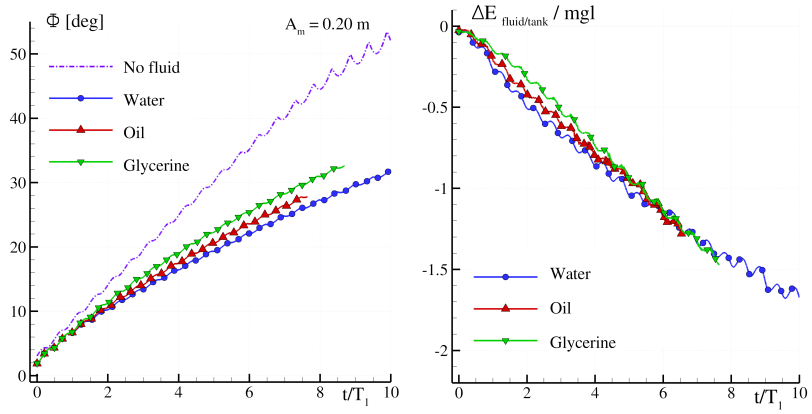

Figure 12.22.: Envelope function Φ (left) and energy transfer $\Delta E_{fluid/tank}$ (right) plotted as a function of time, with an excitation amplitude $A_m = 0.20$ m, using water, sunflower oil and glycerine.

12.5.5 Summary of dissipation results for the different liquids

Putting together all the data recorded in the four Series, some conclusions can be drawn about the influence of dissipation induced by sloshing on the system's dynamics. Fig. 12.25 shows the time histories for Φ and $\Delta E_{mass/tank}$ for the four Series using the three different liquids. According to this figure, increasing the viscosity of the liquid drives both Φ and $\Delta E_{mass/tank}$ to increase.

However, a more detailed analysis can be achieved for the performance of the sloshing liquid using the theoretical findings introduced in sections IV and

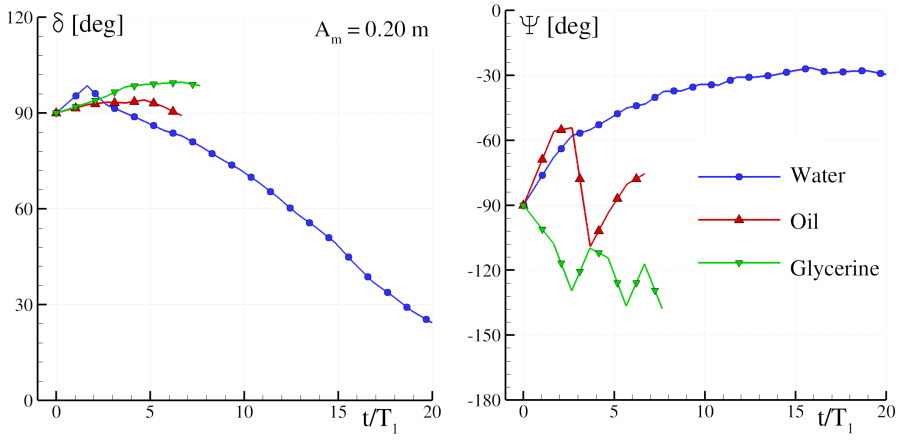

Figure 12.23.: Phase lags δ (left) and of Ψ (right) plotted as a function of time, with an excitation amplitude $A_m = 0.20$ m, using water, sunflower oil and glycerine.

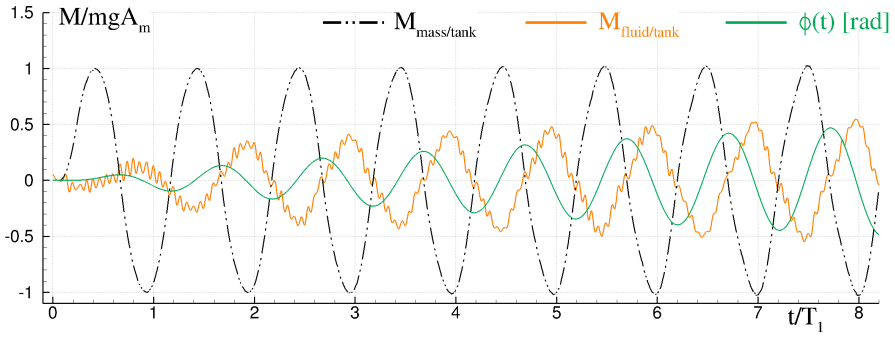

Figure 12.24.: Torque $M_{mass/tank}$ and $M_{fluid/tank}$ as a function of time recorded during the first period of oscillation with an excitation amplitude $A_m = 0.20$ m and using sunflower oil.

V of chapter 11 and the evaluation of the viscosity coefficient α (see equation (11.33) expected to be close to the theoretical value 1.68.

Fig. 12.26 shows the energy transfer $\Delta E_{fluid/tank}$ for the four Series obtained experimentally. This energy is made non dimensional using the coefficient $(4\, m_{liquid}\, g\, h\, \Phi^{\frac{3}{2}})$. Since the energy transfer between the fluid and the tank, $\Delta E_{fluid/tank}$, is fully dissipative at a time-periodic state, the ratio $\Delta E_{fluid/tank}/(4\, m_{liquid}\, g\, h\, \Phi^{\frac{3}{2}})$ is expected to converge to $-\alpha$ over time.

The left plot of Fig. 12.26 concerns the Series with water. For the first two Series, the α coefficient oscillates around the theoretical value but tends to diminish when A_m increases. This means that for the most energetic case, the sloshing flow decreases its dissipation efficiency. Sunflower oil shows a similar behaviour, but with much smaller variations. Glycerine shows a more

regular behaviour but this time the coefficient α is very low with respect to the theoretical one. This can be linked to the fact that its high viscosity inhibits the formation of hydraulic jumps and their associated dissipation. Furthermore, α rises with the glycerine only when increasing the excitation amplitude A_m. Even if the glycerine presents a smaller α value, this is partially compensated by its larger density, which, in absolute terms, induces a certain increase on $\Delta E_{fluid}^{dissipation}$.

Another way to read the above results is to directly plot the experimental results on the $[\Delta E_{fluid/tank}$ vs $\Phi^{3/2}]$ graph. Fig. 12.27 shows this same result with the energy made non-dimensional by the factor $4 m_{liquid}\, g\, h$. On this plot the time dependence disappears and points related to the transitory stages are plotted together with those related to the periodic conditions. This confirms that $\Delta E_{fluid/tank}$ is essentially a dissipative contribution for the sloshing conditions studied in this work. The data related to all three liquids lie on curves where the steepness is linked to the α coefficient. As shown previously for water, α decreases as the roll angle Φ increases. Water and sunflower oil exhibit a similar behaviour. Considering the mass m_{liquid} of the three liquids (see table 12.3) $\Delta E_{fluid/tank}$ is comparable for large Φ.

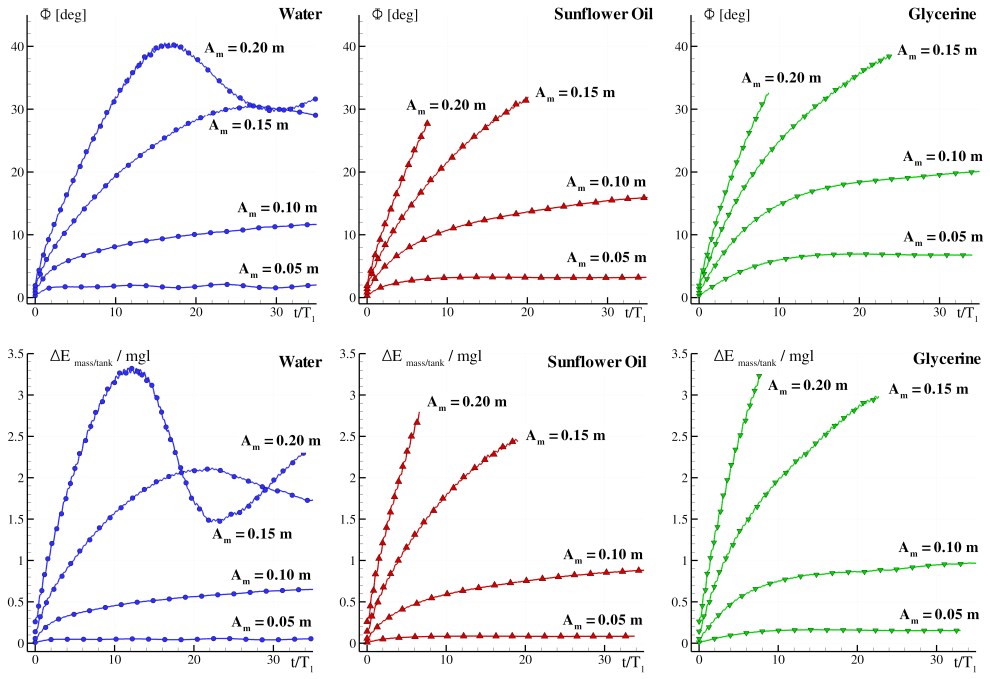

Figure 12.25.: Roll angle $\phi(t)$ (top) and of energy transfer $\Delta E_{mass/tank}$ (bottom) plotted as a function of time for all the excitation amplitudes, varying the liquid present inside the tank.

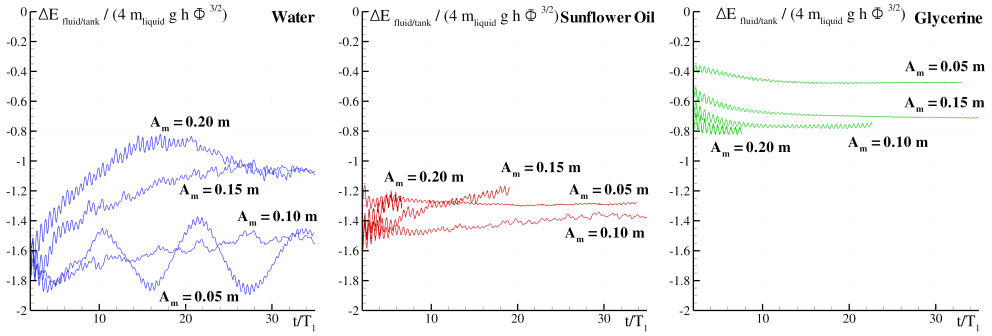

Figure 12.26.: Energy transfer $\Delta E_{fluid/tank}$ plotted as a function of time for all the excitation amplitudes, using water (left), sunflower oil (middle) and glycerine (right) inside the tank.

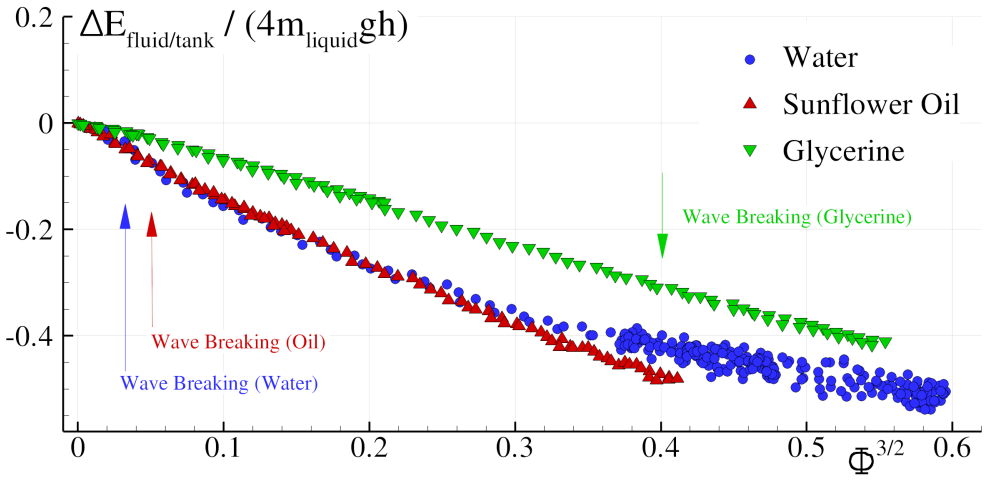

Figure 12.27.: Energy transfer $\Delta E_{fluid/tank}$ plotted as a function of $\Phi^{3/2}$, using water, sunflower oil and glycerine.

12.6 PRACTICAL APPLICATION

From the analysis performed in previous sections, it can be seen that the effective roll angle Φ reached by the system depends not only on the amplitude of the sliding mass motion but on the phase lags δ and Ψ, which in turn depend on the fluid, the filling height h, and the excitation frequency ω.

In Part II of this paper series, the analysis has been limited to one filling height and one frequency of excitation $\omega = \omega_1$. The analysis performed also shows that the energy dissipation capability with this system can be large. Indeed, the system first transforms the external energy given by the sliding mass into mechanical energy, making the tank move. Then, the large roll motion induces violent sloshing and its associated dissipation which prevent the energy accumulated by the tank to be sent back to the sliding mass.

Considering this analysis and noting that the forcing term in a horizontally driven pendulum Lourenco 2011 is analogous to the forcing term of the present system (equation (II.4) of chapter 11), a novel damping system is proposed. It is named here a hybrid pendulum mass liquid damper (HPMLD). The mechanical sketch of such a system is shown in Fig. 12.28. Its principle is that of a HMLD, (see section 11.2.2 in chapter 11), but the secondary damping system is a pendulum partially filled with liquid.

The idea to transfer energy from horizontal motions into pendular ones (with a mass and no liquid) was already presented by Tedesco et al. 1999, and a full analysis of a such a device, a Pendulum Tuned Mass Damper (PTMD), is carried out by Lourenco 2011. For an analysis of an oscillating structure containing liquid and coupled with a horizontal motion device, see the work of Pirner and Urushadze 2007.

The system proposed herein incorporates both ideas. Its capability to dissipate large amounts of energy through sloshing and wave breaking has been discussed in this paper. An in-depth analysis of its full potential as a HPMLD is still left for future work.

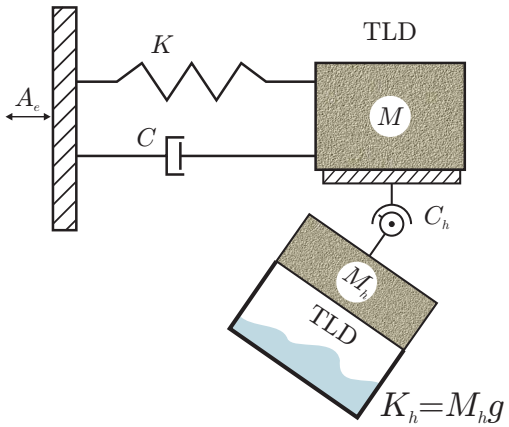

Figure 12.28.: Mechanical sketch of the use of the pendulum has a hybrid pendulum mass liquid damper (HPMLD).

12.7 SUMMARY OF THIS CHAPTER

A Pendulum-TLD system has been analyzed in terms of its kinematics, dynamics and energy dissipation mechanisms.

It is composed of three coupled sub-systems: a sliding mass, the moving part of an angular motion sloshing rig, including an empty tank, and the fluid which partially fills that tank. The data from a set of experiments in which the sliding mass is excited with harmonic motions is discussed.

The experimental analysis of this system has been performed at the mechanical system resonance frequency. This choice together with the filling height adopted, both stem from chapter 11 of the present paper series. The experimental analysis of other frequencies and other filling heights is left for future work. The test matrix has included fluids of different densities and viscosities, namely water, sunflower oil and glycerine, and four different exciting amplitudes.

The kinematics and dynamics of the flow are complex and extremely nonlinear. Low amplitude traveling waves occur for the small excitation cases, while large breaking waves are found for large excitations.

The different physical quantities can be evaluated with great accuracy since the experimental set-up allows for the computation of all terms from the roll angle time history and its derivatives. In particular, the time evolution of energy balances between the fluid and the tank can be evaluated. At time-periodic state this balance becomes the energy dissipated by the fluid.

The experiments have been analyzed considering modulus and phase for the different torques acting on the system. The phase lags between the sliding mass motion, roll angle, and torque exerted by the fluid allows for the understanding of the time-periodic state reached by the system in terms of roll amplitude and work done by the sliding mass.

The fluid dissipation measured during the experiments has been compared to the theoretical model described in chapter 11. The predictions obtained with this model match those corresponding to the water cases. Since the energy dissipation in such a model is obtained though a hydraulic jump solution, the conclusion is that the dissipation source for these cases is mostly due to breaking.

The influence of the nature of the liquid on the system has been studied for a set of excitation amplitudes. At the time-periodic state, the most viscous liquid, glycerine, leads to the largest oscillation amplitude. On the contrary, using the least viscous liquid, water, leads to the smallest oscillation amplitude. The liquid choice is shown to greatly influence the phase lags between the different torques. During the early transient stage, the least viscous fluid (water) is shown to have a faster increase of the roll counteracting effect, and to reach a time periodic state within a smaller number of periods.

When correctly scaled using the theoretical model, the fluid dissipation value for a fixed roll angle diminishes as viscosity increases. However, since the time-periodic state roll angle is larger when increasing viscosity, the net dissipation is also larger. This is another conclusion from this research and it implies that the choice of liquid when obtaining the best damping performance is not straightforward.

For the empty tank condition, the system may return energy to the sliding mass; this does not happen when fluid is present, even when similar angles are found at time-periodic state. This idea inspires a novel damping device, named

hybrid pendulum mass liquid damper (HPMLD), which is introduced here. This system may be able to take advantage of the intense mechanical response of the structure in order to pump the initial energy and later dissipate it with the violent sloshing flow generated. Its proper development and analysis is left for future work.

Part V

CONCLUSIONS AND PERSPECTIVES

13 CONCLUSIONS AND PERSPECTIVES

A meshless technique based on the Smoothed Particle Hydrodynamics has been further developed and has been found to be able to correctly reproduce the dynamics of a viscous flow interacting with a rigid body in the presence of a free surface. Special attention has been paid to energy conservation properties of the numerical scheme, with emphasis on accurate evaluation of power and energy balances with fragmented free-surface and breaking waves. The choice of the numerical technique has some consequences, the most important ones being not to use any turbulence model nor any resolution adaptivity methods in order to avoid as much as possible the dissipation linked to other sources than the Navier-Stokes equations.

The numerical method has been benchmarked and validated, and some physical investigations conducted. Firstly, a cylinder under the free surface has been simulated at a relatively high Froude number, keeping the Reynolds number relatively low. This has allowed for identification of charateristic patterns and in some cases retrieved already-known flow behaviours. Particular attention was paid to the interaction between the wake of the cylinder and the free-surface, and some interesting new instability types have been found.

Secondly, sloshing in a rectangular tank caused by a horizontal sinusoidal excitation has been extensively studied in the case of low-filling ratios. The characteristic wave systems have been identified and allowed for a more complete picture of the phenomena.

Finally, the analysis of the TLD-like system has been done, focusing on the dissipation mechanism and the non-linear behaviour of the coupled system. Some key behaviours have been identified and the different viscosities of the fluids tested have allowed for a better undestanding of the dissipation capacity of such a system.

13.1 MAJOR FINDINGS

13.1.1 Computing the energy dissipation using SPH

An energy decomposition technique for viscous free-surface flows has been presented and applied to the δ-SPH modelling of a standing wave. For this topic, a matrix of test cases covering a large range of Reynolds numbers and wave amplitudes, has been set. For the high Reynolds and large amplitude

case, wave breaking appears. Its influence in mechanical energy dissipation has been discussed. It has been found that:

1. The dissipated mechanical energy can be written as the sum of two terms: the enstrophy volume integral and a surface integral along the free surface.
2. Applying energy conservation, a double-checking of the free surface term is developed and applied, confirming the quality of the surface integral SPH evaluation, even in the presence of moderately fragmented free surface.
3. For low amplitude cases the free-surface contribution to dissipation is substantially larger than the enstrophy one.
4. For large amplitude cases, the flow becomes very energetic, eventually leading to steep and/or breaking waves.
5. In the case with wave breaking, the related vorticity generation in the first breaking event, induces a mechanical energy dissipation of around 8% of the initial energy.

13.1.2 Explicit algorithm for fluid/body interaction using SPH

A SPH solver is developed for applications in the framework of NWT (Numerical Wave Tanks) and floating bodies. To this aim, a complete algorithm able to compute viscous and fully-coupled Fluid-Solid interactions is described.

A no-slip boundary condition is enforced on the solid surface through a ghost-fluid technique. For the considered problem, the intersection between the free surface and the solid profile has to be carefully addressed. The details of a specific treatment regarding the ghost fluid close to the free surface are described. Further, a formula for the evaluation of forces and torque is also provided in the ghost-fluid framework. The assessment of loads acting on bodies is validated through a difficult diffraction test case with satisfactory results.

An explicit synchronous algorithm is developed for the full coupling between fluid and rigid bodies. Stability, convergence and conservation properties are tested on several freely-floating test cases and a final validation of the full algorithm is performed for the interaction between a 2D box and an incoming wave packet.

13.1.3 Flow past a submerged cylinder

Two-dimensional monophasic flow past a horizontal circular cylinder intersecting or close to a free surface at low Reynolds number, 180, and at low, mod-

erate and large Froude number (between 0.3 and 2.0 based on the cylinder diameter), has been investigated numerically using Smoothed Particle Hydrodynamics. The variety of case studied cover a larger range than the previous studies on the topic.

The detached flow patterns dependence with the submergence of the cylinder and the Froude number has been investigated. Vorticity, mixing processes, vortex generation patterns, free-surface breaking and drag and lift coefficient behaviour have been discussed. Mixing processes have been documented with more detail than previous studies, taking advantage of the Lagrangian nature of the solver.

An analysis varying the cylinder submergence has been carried out fixing successively the Froude number to a value of one and two. At Froude one, for large submergences, the flow has been found to behave similarly to unbounded flows, with von Kármán street of vortices developing at a frequency comparable to classic unbounded flows literature. As the submergence is reduced, certain mixing with the free surface occurs and substantial breaking takes place. Moreover, it has been found that below certain distance to the free surface the classical von Kármán street of shedding vortices does not take place while moderate vortex shedding departs from vorticity generated at the free surface. In some of these cases, consecutive vortices may merge, leading to the formation of a large meta-vortex which is advected downstream, a previously unreported form of wake instability, to the authors' knowledge.

Within the submergence dependence analysis, computations have been carried out until the cylinder being in contact with the undisturbed free surface as well as half submerged. For these configurations, the vorticity layer remains fixed, placed between the cylinder and the free surface and a recirculating area at the wake develops.

Regarding the dependence of the flow on Froude number, the analysis has been carried out for a fixed submergence, 0.55, which had been given some attention in previous literature at low and moderate Froude numbers. That range has been extended here reaching up to a value of 2. For this submergence, up to Froude number 1.6, the von Kármán vortex shedding is blocked, but that is not the case when Froude number reaches a value of 2. This transitional effect is in agreement with stability analysis of half submerged cylinder existing in literature.

13.1.4 Shallow water sloshing on a rectangular tank

An extensive study of the shallow water sloshing problems has been done using both experimental and numerical data. Different configurations (Series) of sway motion have been considered in detail, spreading from small-amplitude excitations ($A/h = 0.033, 0.065$) to moderate ($A/h = 0.500$) and large excitations ($A/h = 0.800, 2.333$). For each Series, wave amplitude operators have

been computed by varying the frequency of the excitation. Specific cases have been selected among the broad range of simulations to describe the main features of the sloshing motion (wave trains, wave breaking, jet run-up/run-down at the vertical walls, etc.). The results have been analyzed according to the classification proposed by Olsen & Johnsen Olsen and Johnsen 1975, proving the existence of a novel sloshing configuration, namely *Conf. VI*.

Finally, a summary has been done for two filling ratios, describing the wave scenarios and the wave amplitude operators for a large range of frequencies and inspecting the influence of the excitation amplitude.

13.1.5 Pendulum-TLD, and dissipation in a coupled fluid-body problem

The kinematics, dynamics and energy dissipation mechanisms of a pendulum-TLD system have been analyzed.

The pendulum-TLD is composed of three coupled sub-systems: first, a sliding mass whose weight excites the motion, second, the moving parts, including the empty tank, of an angular motion sloshing rig, and third, the fluid which partially fills that tank.

An analogy with TLD and HMLD systems has been provided. Differently from other TLDs studied in the literature, the Pendulum-TLD involves large motions and complex flows, which do not permit the use of an analytical fluid dynamic model.

The nonlinear dynamics of the Pendulum-TLD has been documented both for the empty tank and for the tank partially filled with water. The frequency behaviour of the roll angles, phase lags and energy transfer has been discussed.

The energy dissipated by the sloshing flow has been quantified through a simple theoretical model based on hydraulic jump solutions. This model allows for an evaluation of the mechanical energy available to be dissipated in breaking. Furthermore, a scaling factor for the energy available to be dissipated in breaking has been obtained from this analysis. This scaling factor has been used to make non dimensional in a meaningful way the numerical results obtained by an SPH model (and the experimental data of part II).

From the numerical simulations, the complex kinematics and dynamics of the flow has been discussed: low amplitude traveling waves occur for the small excitation cases while breaking waves and violent fluid-structure impacts develop for large excitations.

Through the SPH model the complete frequency behaviour of the fully coupled system has been obtained. Interesting features have been identified. Specifically, for small excitations, the system behaves like a classical TLD. The frequency response changes drastically with large excitations.

The data from a set of experiments is also discussed.

The test matrix has included fluids of different densities and viscosities, namely water, sunflower oil and glycerine, and four different exciting amplitudes.

The kinematics and dynamics of the flow are complex and extremely nonlinear. Low amplitude traveling waves occur for the small excitation cases, while large breaking waves are found for large excitations.

The different physical quantities can be evaluated with great accuracy since the experimental set-up allows for the computation of all terms from the roll angle time history and its derivatives. In particular, the time evolution of energy balances between the fluid and the tank can be evaluated. At time-periodic state this balance becomes the energy dissipated by the fluid.

The experiments have been analyzed considering modulus and phase for the different torques acting on the system. The phase lags between the sliding mass motion, roll angle, and torque exerted by the fluid allows for the understanding of the time-periodic state reached by the system in terms of roll amplitude and work done by the sliding mass.

The fluid dissipation measured during the experiments has been compared to the theoretical model described in Part I. The predictions obtained with this model match those corresponding to the water cases. Since the energy dissipation in such a model is obtained though a hydraulic jump solution, the conclusion is that the dissipation source for these cases is mostly due to breaking.

The influence of the nature of the liquid on the system has been studied for a set of excitation amplitudes. At the time-periodic state, the most viscous liquid, glycerine, leads to the largest oscillation amplitude. On the contrary, using the least viscous liquid, water, leads to the smallest oscillation amplitude. The liquid choice is shown to greatly influence the phase lags between the different torques. During the early transient stage, the least viscous fluid (water) is shown to have a faster increase of the roll counteracting effect, and to reach a time periodic state within a smaller number of periods.

When correctly scaled using the theoretical model, the fluid dissipation value for a fixed roll angle diminishes as viscosity increases. However, since the time-periodic state roll angle is larger when increasing viscosity, the net dissipation is also larger. This is another conclusion from this research and it implies that the choice of liquid when obtaining the best damping performance is not straightforward.

For the empty tank condition, the system may return energy to the sliding mass; this does not happen when fluid is present, even when similar angles are found at time-periodic state. This idea inspires a novel damping device, named hybrid pendulum mass liquid damper (HPMLD), which is introduced here. This system may be able to take advantage of the intense mechanical response of the structure in order to pump the initial energy and later dissipate it with

the violent sloshing flow generated. Its proper development and analysis is left for future work.

13.2 PERSPECTIVE

In some aspects, the work covered by this thesis is an invitation to pursue with these methods of Lagrangian modelling. It proves that it is possible to model a viscous flow interacting with a floating body with a nice accuracy. It proves also that some very complex physical problems like TLDs are very well modelled by this kind of techniques.

On the other hand all the problems shown are in reality 3D, and all the best conservation properties for the numerical model have been demonstrated for moderate Reynolds.

In order to be able to transfer this technology to a very large set of industrial or environnmental problems, some work has to be performed to increase the accuracy of the method in problems with larger Reynolds number. Diminishing the viscosity the stability puts the particle system at risk and the parameters of the simulation, like the particle size, have to be further modified, increasing the computational effort.

It remains as future work to apply the methodology presented in the thesis to more complex fragmented free-surface flows for which, the dissipated energy may influence the external dynamics of a building, vehicle, etc.. It remains also to compare the results with those of mesh-based methods and to incorporate gas phase and surface tension in the analysis.

Some questions have been, for different reasons, left open, but could be a follow to the present work:

1. Extend the conservation study to more complex problems. It could be also interesting to compare with other numerical methods.

2. Extend the detailed analysis of the freely floating problem to the 3D case.

3. A coupled model of the flow around the cylinder and corresponding forces with a dynamic model such as that used by Ding et al. 2013, overcoming its limitations when close to a free surface, is an interesting future research goal.

4. The same kind of extensive analysis of sloshing could be extended for larger filling height, or for the 3D case.

5. For the PTLD, various interesting studies could be conducted varying the natural frequencies of the tank and the sloshing.

14 PUBLICATIONS LINKED WITH THIS THESIS

14.1 REFEREED PAPERS

Bouscasse, B and Colagrossi, A and Marrone, S and Antuono, M. Nonlinear water wave interaction with floating bodies in SPH. Journal of Fluids and Structures, Vol. 42, 112-129, 2013

Bouscasse, B; Antuono, M; Colagrossi, A; Lugni, C. Numerical and experimental investigation of nonlinear shallow water sloshing. Int. J. Nonlinear Sci. Numer. Simul. Vol .14, 2, 123-138, 2013

Bouscasse, B; Colagrossi, A; Souto-Iglesias, A; Cercos-Pita, JL. Mechanical energy dissipation induced by sloshing and wave breaking in a fully coupled angular motion system. I. Theoretical formulation and numerical investigation. Physics of Fluids (1994-present), Vol. 26, 3, 33103, 2014.

Bouscasse, B; Colagrossi, A; Souto-Iglesias, A; Cercos-Pita, JL. Mechanical energy dissipation induced by sloshing and wave breaking in a fully coupled angular motion system. II. Experimental investigation, Physics of Fluids (1994-present), Vol. 26, 3, 33104, 2014.

Antuono, M; Bouscasse, B; Colagrossi, A; Marrone, S. A measure of spatial disorder in particle methods, Computer Physics Communications, Vol. 185, 10, 2609-2621, 2014.

Antuono, M; Marrone, S; Colagrossi, A; Bouscasse, B. Energy balance in the δ-SPH scheme, Computer Methods in Applied Mechanics and Engineering, 2015

Colagrossi, A; Marrone, S; Bouscasse, B; Broglia, R; Numerical Simulations of the Flow Past Surface-Piercing Objects, International Journal of Offshore and Polar Engineering, 25(01), 13-18, 2015

14.2 CONFERENCE PAPERS

Bouscasse, B; Colagrossi, A; Marrone, S; Souto-Iglesias, A. Viscous flow past a circular cylinder below a free surface, ASME 2014 33rd International Conference on Ocean, Offshore and Arctic Engineering, 2014

Bouscasse, B; Colagrossi, A; Souto-Iglesias, A, Energy decomposition analysis in free-surface flows: road-map for the direct computation of wave breaking dissipation, SPHERIC, 2014.

Bouscasse, B; Colagrossi, A; Antuono, M; Lugni, C; A Classification of Shallow Water Resonant Sloshing in a Rectangular Tank, ASME 2013, 32nd International Conference on Ocean, Offshore and Arctic Engineering, 2013

Bouscasse, B, Colagrossi, A; Marrone, S; Souto-Iglesias, A. High froude number viscous flow past a circular cylinder, ASME 2015 34th International Conference on Ocean, Offshore and Arctic Engineering, 2015

14.3 PAPERS UNDER PREPARATION

Bouscasse, B; Colagrossi, A; Marrone, S; Souto-Iglesias, A. Viscous flow past a half-submerged or close to a free surface circular cylinder; Submitted

Colagrossi, A; Bouscasse, B; Marrone, S; Energy decomposition analysis for viscous free-surface flows, Submitted

A USEFUL RELATIONS

$$(\mathbf{a} \times \mathbf{b}) \cdot \mathbf{c} = \mathbf{a} \cdot (\mathbf{b} \times \mathbf{c}) \tag{A.1}$$

therefore in the present framework:

$$(\mathbf{u} \times \boldsymbol{\omega}) \cdot \mathbf{n} = \mathbf{u} \cdot (\boldsymbol{\omega} \times \mathbf{n}) \tag{A.2}$$

$$\begin{aligned} \mathbb{D} &:= \frac{1}{2}\left(\nabla \mathbf{u} + \nabla^{\mathsf{T}} \mathbf{u}\right) \\ \mathbb{W} &:= \frac{1}{2}\left(\nabla \mathbf{u} - \nabla^{\mathsf{T}} \mathbf{u}\right) \end{aligned} \tag{A.3}$$

$$\begin{aligned} \nabla \mathbf{u} &= \mathbb{D} + \mathbb{W} \\ 2\mathbb{W}\,\mathbf{a} &= \boldsymbol{\omega} \times \mathbf{a} \end{aligned} \tag{A.4}$$

$$\mathbb{A}\,\mathbf{u} \cdot \boldsymbol{v} = \mathbf{u} \cdot \mathbb{A}^{\mathsf{T}} \boldsymbol{v} \tag{A.5}$$

B TRANSPORT THEOREM

Considering the case where $V_c(t)$ is not the a material fluid volume but a generic control volume.

$$\frac{D}{Dt}\int_{V_c(t)} f dV = \int_{V_c(t)} \frac{\partial f}{\partial t} dV + \int_{\partial V_c(t)} (\mathbf{v}^b \cdot \mathbf{n}) f dS \tag{B.1}$$

substituting $f \to (\rho f)$

$$\frac{D}{Dt}\int_{V_c(t)} (\rho f) dV = \int_{V_c(t)} \rho \frac{\partial f}{\partial t} dV + \int_{V_c(t)} f \frac{\partial \rho}{\partial t} dV + \int_{\partial V_c(t)} (\mathbf{v}^b \cdot \mathbf{n}) (\rho f) dS \tag{B.2}$$

$$\frac{Df}{Dt} = \frac{\partial f}{\partial t} + \mathbf{u} \cdot \nabla f \tag{B.3}$$

$$\frac{D}{Dt}\int_{V_c(t)} (\rho f) dV = \int_{V_c(t)} \rho \frac{Df}{Dt} dV + \int_{V_c(t)} \left(f \frac{\partial \rho}{\partial t} - \rho \mathbf{u} \cdot \nabla f \right) dV + \int_{\partial V_c(t)} (\mathbf{v}^b \cdot \mathbf{n}) (\rho f) dS \tag{B.4}$$

$$\operatorname{div}(\rho f \mathbf{u}) = \operatorname{div}(\mathbf{u}) (\rho f) + f \nabla \rho \cdot \mathbf{u} + \rho (\nabla f) \cdot \mathbf{u} \tag{B.5}$$

$$\begin{aligned} \frac{D}{Dt}\int_{V_c(t)} (\rho f) dV \;=\; & \int_{V_c(t)} \rho \frac{Df}{Dt} dV + \\ & \int_{V_c(t)} \left[f \left(\frac{\partial \rho}{\partial t} + \operatorname{div}(\mathbf{u}) \rho + (\nabla \rho) \cdot \mathbf{u} \right) - \operatorname{div}(\rho f \mathbf{u}) \right] dV + \\ & \int_{\partial V_c(t)} (\mathbf{v}^b \cdot \mathbf{n}) (\rho f) dS \end{aligned} \tag{B.6}$$

$$\begin{aligned} \frac{D}{Dt}\int_{V_c(t)} (\rho f) dV \;=\; & \int_{V_c(t)} \rho \frac{Df}{Dt} dV + \int_{V_c(t)} f \left[\frac{D\rho}{Dt} + \rho \operatorname{div}(\mathbf{u}) \right] dV + \\ & - \int_{V_c(t)} \operatorname{div}(\rho f \mathbf{u}) dV + \int_{\partial V_c(t)} (\mathbf{v}^b \cdot \mathbf{n}) (\rho f) dS \end{aligned} \tag{B.7}$$

$$\begin{aligned}\frac{D}{Dt}\int_{V_c(t)}(\rho f)dV &= \int_{V_c(t)}\rho\frac{Df}{Dt}dV+\int_{V_c(t)}f\left[\frac{D\rho}{Dt}+\rho\,\mathrm{div}(\mathbf{u})\right]dV+\\ &- \int_{\partial V_c(t)}(\mathbf{u}\cdot\mathbf{n})\,(\rho f)dS+\int_{\partial V_c(t)}(\mathbf{v}^b\cdot\mathbf{n})\,(\rho f)dS\end{aligned} \tag{B.8}$$

$$\begin{aligned}\frac{D}{Dt}\int_{V_c(t)}(\rho f)dV &= \int_{V_c(t)}\rho\frac{Df}{Dt}dV+\int_{V_c(t)}f\left[\frac{D\rho}{Dt}+\rho\,\mathrm{div}(\mathbf{u})\right]dV\\ &+ \int_{\partial V_c(t)}(\mathbf{v}^b-\mathbf{u})\cdot\mathbf{n}\,(\rho f)dS\end{aligned} \tag{B.9}$$

using the continuity equation 2.1:

$$\frac{D}{Dt}\int_{V_c(t)}(\rho f)dV=\int_{V_c(t)}\rho\frac{Df}{Dt}dV+\int_{\partial V_c(t)}(\mathbf{v}^b-\mathbf{u})\cdot\mathbf{n}\,(\rho f)dS \tag{B.10}$$

If $\mathbf{v}^b=\mathbf{u}$ this means that the control volume is a material volume and the equation (B.10) becomes:

$$\frac{D}{Dt}\int_{\Omega}(\rho f)dV=\int_{\Omega}\rho\frac{Df}{Dt}dV \tag{B.11}$$

C DETAILED CALCULATIONS

C.1 DETAIL 1

The term $\mathcal{P}_{wall}$ can be combined with $\mathcal{P}_{ext}$ which can be rewritten as:

$$\begin{aligned} -\mathcal{P}_{ext} + \mathcal{P}_{wall} &= \int_{\partial\Omega_B} \mathbb{T}\mathbf{n}\cdot\mathbf{u}_B \, dS - 2\mu \int_{\partial\Omega_B} (\nabla\mathbf{u}\,\mathbf{u}_B)\cdot\mathbf{n}\, dS + 2\mu \int_{\partial\Omega_B} \mathrm{div}(\mathbf{u})(\mathbf{u_B}\cdot\mathbf{n}) dS \\ &= \int_{\partial\Omega_B} (\mathbb{T} - 2\mu\nabla\mathbf{u})\,\mathbf{u}_B \cdot \mathbf{n}\, dS + 2\mu \int_{\partial\Omega_B} \mathrm{div}(\mathbf{u})(\mathbf{u_B}\cdot\mathbf{n}) dS \end{aligned} \tag{C.1}$$

using the constitutive equation (2.3)

$$\begin{aligned} \mathcal{P}_{Body} = \mathcal{P}_{ext} + \mathcal{P}_{wall} &= \int_{\partial\Omega_B} -p\,\mathbf{u}_B \cdot \mathbf{n}\, dS + (\lambda + 2\mu) \int_{\partial\Omega_B} \mathrm{div}(\mathbf{u})\,\mathbf{u}_B \cdot \mathbf{n}\, dS \\ &+ 2\,\mu \int_{\partial\Omega_B} (\mathbb{D} - \nabla\mathbf{u})\,\mathbf{u}_B \cdot \mathbf{n}\, dS \\ &= \int_{\partial\Omega_B} -p\,\mathbf{u}_B \cdot \mathbf{n}\, dS + (\lambda + 2\mu) \int_{\partial\Omega_B} \mathrm{div}(\mathbf{u})\,\mathbf{u}_B \cdot \mathbf{n}\, dS \\ &- \mu \int_{\partial\Omega_B} (\boldsymbol{\omega} \times \mathbf{u}_B)\cdot\mathbf{n}\, dS \\ &= \int_{\partial\Omega_B} -p\,\mathbf{u}_B \cdot \mathbf{n}\, dS + (\lambda + 2\mu) \int_{\partial\Omega_B} \mathrm{div}(\mathbf{u})\,\mathbf{u}_B \cdot \mathbf{n}\, dS \\ &+ \mu \int_{\partial\Omega_B} (\boldsymbol{\omega} \times \mathbf{n})\cdot\mathbf{u}_B\, dS \end{aligned} \tag{C.2}$$

C.2 DETAIL 2

$$\mathcal{P}_{FS}^{Pres} + \mathcal{P}_{FS}^{\lambda B} + \mathcal{P}_{FS}^{Visc} = \int_{\partial\Omega_F} (-p\mathbf{u}\cdot\mathbf{n} + \lambda \mathrm{div}(\mathbf{u})\,\mathbf{u}\cdot\mathbf{n} + \mu(\boldsymbol{\omega}\times\mathbf{n})\cdot\mathbf{u})\, dS \tag{C.3}$$

The boundary condition equation (2.8) applied on the free surface gives:

$$[-p\mathbf{u} + \lambda\,\mathrm{div}(\mathbf{u})\mathbf{u}]\,\mathbf{n} + \mu\,(\mathbf{n}\times\boldsymbol{\omega})\mathbf{u} = -2\mu\,(\nabla\mathbf{u})\mathbf{n}\cdot\mathbf{u} \tag{C.4}$$

$$\begin{aligned}
\mathcal{P}_{FS}^{Pres} + \mathcal{P}_{FS}^{\lambda B} + \mathcal{P}_{FS}^{Visc} &= \int_{\partial\Omega_F} [2\mu(\boldsymbol{\omega} \times \mathbf{n}) - 2\mu\,(\nabla\mathbf{u})\mathbf{n}] \cdot \mathbf{u} dS \\
&= \int_{\partial\Omega_F} 2\mu\,[-(\boldsymbol{\omega} \times \mathbf{u}) \cdot \mathbf{n} - (\nabla\mathbf{u})\mathbf{n} \cdot \mathbf{u}]\,dS \\
&= \int_{\partial\Omega_F} 2\mu\left[-(2\,\mathbb{W}\mathbf{u}) \cdot \mathbf{n} - (\nabla^T\mathbf{u})\mathbf{u} \cdot \mathbf{n}\right] dS \\
&= \int_{\partial\Omega_F} 2\mu\left[-((\nabla\mathbf{u} - \nabla^T\mathbf{u})\mathbf{u}) \cdot \mathbf{n} - (\nabla^T\mathbf{u})\mathbf{u} \cdot \mathbf{n}\right] dS \\
&= \mathcal{P}_{FS}
\end{aligned} \tag{C.5}$$

C.3 ALTERNATIVE DECOMPOSITION

Using equation (2.4) in equation (3.11):

$$\mathcal{P}_M - \mathcal{P}_{NC} = \int_\Omega \left(-\nabla p + \mu\nabla^2\mathbf{u} + (\lambda + \mu)\nabla(\nabla \cdot \mathbf{u})\right) \cdot \mathbf{u}\,dV \tag{C.6}$$

$$\begin{aligned}
\int_\Omega (\nabla p) \cdot \mathbf{u}\,dV &= \int_\Omega (\nabla p) \cdot \mathbf{u}\,dV \\
&= \int_\Omega [\mathrm{div}\,(p\mathbf{u}) - p\mathrm{div}(\mathbf{u})]\,dV \\
&= \int_{\partial\Omega} (p\mathbf{u}) \cdot \mathbf{n} dS - \int_\Omega p\mathrm{div}(\mathbf{u})\,dV
\end{aligned} \tag{C.7}$$

$$\begin{aligned}
\int_\Omega \nabla(\mathrm{div}\mathbf{u}) \cdot \mathbf{u}\,dV &= \int_\Omega \left[\mathrm{div}(\mathrm{div}(\mathbf{u}) \cdot \mathbf{u}) - \mathrm{div}^2(\mathbf{u})\right] dV \\
&= \int_{\partial\Omega} \mathrm{div}(\mathbf{u})(\mathbf{u} \cdot \mathbf{n}) dS - \int_\Omega \mathrm{div}^2(\mathbf{u})\,dV
\end{aligned} \tag{C.8}$$

Using the formula $\nabla^2\mathbf{u} \cdot \mathbf{u} = \mathrm{div}(\mathbf{u} \times \omega) - |\omega|^2 + \nabla\mathrm{div}(\mathbf{u}) \cdot \mathbf{u}$

$$\begin{aligned}
\int_\Omega \nabla^2\mathbf{u} \cdot \mathbf{u}\,dV &= \int_\Omega \left[\mathrm{div}(\mathbf{u} \times \omega) - |\omega|^2 + \nabla\mathrm{div}(\mathbf{u}) \cdot \mathbf{u}\right] dV \\
&= \int_{\partial\Omega} (\mathbf{u} \times \omega) \cdot \mathbf{n} - \int_\Omega |\omega|^2\,dV + \int_\Omega \nabla\mathrm{div}(\mathbf{u}) \cdot \mathbf{u}\,dV \\
&= \int_{\partial\Omega} (\mathbf{u} \times \omega) \cdot \mathbf{n} - \int_\Omega |\omega|^2\,dV + \int_{\partial\Omega} \mathrm{div}(\mathbf{u})(\mathbf{u} \cdot \mathbf{n}) dS - \int_\Omega \mathrm{div}^2(\mathbf{u})\,dV
\end{aligned} \tag{C.9}$$

Each expression is composed of a volume integral and a boundary integral.

$$\mathcal{P}_M - \mathcal{P}_{NC} + \mathcal{P}_C = \int_{\partial\Omega} \left[-p\mathbf{u} + (\lambda+\mu)\mathrm{div}(\mathbf{u})\mathbf{u} + \mu(\mathbf{u}\times\omega)) \right] \cdot \mathbf{n} dS + \mathcal{P}_B^{(\lambda+2\mu)} + \mathcal{P}_\omega \tag{C.10}$$

The decomposition of the boundary integral on the free surface and on the body will lead to the same balance of equation (3.37)

BIBLIOGRAPHY

Abramson, H.M. (1966). *The Dynamic Behavior of Liquids in Moving Containers*. Tech. rep. NASA National Aeronautics and Space Administration, Washington D.C.

Amini, Azin et al. (2008). "Dynamics of low-viscosity oils retained by rigid and flexible barriers". In: *Ocean Engineering* 35.14–15, pp. 1479–1491. ISSN: 0029-8018. DOI: 10.1016/j.oceaneng.2008.06.010. URL: http://www.sciencedirect.com/science/article/pii/S0029801808001327.

Anderson, J.G. et al. (2000). "A standing-wave-type sloshing absorber to control transient oscillations". In: *Journal of Sound and Vibration* 232.5, pp. 839–56.

Antuono, M. and A. Colagrossi (2012). "The damping of viscous gravity waves". In: *Wave Motion* 50.0, pp. 197–209. ISSN: 0165-2125. DOI: 10.1016/j.wavemoti.2012.08.008. URL: http://www.sciencedirect.com/science/article/pii/S0165212512001060.

Antuono, M. et al. (2010). "Free-surface flows solved by means of SPH schemes with numerical diffusive terms". In: *Computer Physics Communications* 181.3, pp. 532–549. ISSN: 0010-4655. DOI: 10.1016/j.cpc.2009.11.002.

Antuono, M. et al. (2011). "Propagation of gravity waves through an SPH scheme with numerical diffusive terms". In: *Computer Physics Communications* 182.4, pp. 866–877. ISSN: 0010-4655. DOI: 10.1016/j.cpc.2010.12.012. URL: http://www.sciencedirect.com/science/article/B6TJ5-51PRYCS-1/2/b69f4a14370f08b80c197c90035b226a.

Antuono, M. et al. (2012a). "Numerical diffusive terms in weakly-compressible SPH schemes". In: *Computer Physics Communications* 183.12, pp. 2570–2580. DOI: 10.1016/j.cpc.2012.07.006.

Antuono, M. et al. (2012b). "Two-dimensional modal method for shallow-water sloshing in rectangular basins". In: *Journal of Fluid Mechanics* 700, pp. 419–440. ISSN: 1469-7645. DOI: 10.1017/jfm.2012.140.

Antuono, M. et al. (2013). "Conservation of circulation in SPH for 2D free-surface flows". In: *International Journal for Numerical Methods in Fluids* 72.5, pp. 583–606. ISSN: 1097-0363. DOI: 10.1002/fld.3757.

Antuono, M et al. (2015). "Energy balance in the δ-SPH scheme". In: *Computer Methods in Applied Mechanics and Engineering* 289.

Ardakani, H Alemi and TJ Bridges (2010). "Dynamic coupling between shallow-water sloshing and horizontal vehicle motion". In: *European Journal of Applied Mathematics* 21.6, pp. 479–517.

Ardakani, H Alemi et al. (2012). "Resonance in a model for Cooker's sloshing experiment". In: *European Journal of Mechanics-B/Fluids* 36, pp. 25–38.

Aris, R. (1989). *Vectors, Tensors, and the Basic Equations of Fluid Mechaniscs*. Dover Books on Mathematics Series. Dover Publications, Mineola, New York. ISBN: 9780486661100. URL: http://books.google.es/books?id=W1tiFsxDedMC.

Armenio, V. and M. La Rocca (1996). "On the analysis of sloshing of water in rectangular containers: numerical study and experimental validation". In: *Journal of Ocean Engineering* 23.8, pp. 705–39.

Armenio, V. et al. (1996a). "On the roll motion of a ship partially filled unbaffled and baffled tanks - Part I: Mathematical model and experimental setup". In: *Int. Journ. of Offshore and Polar Eng.* 6.4, pp. 278–282.

— (1996b). "On the roll motion of a ship partially filled unbaffled and baffled tanks - Part II: Numerical and experimental analysis". In: *Int. Journ. of Offshore and Polar Eng.* 6.4, pp. 283–290.

Banerji, Pradipta and Avik Samanta (2011). "Earthquake vibration control of structures using hybrid mass liquid damper". In: *Engineering Structures* 33.4, pp. 1291–1301.

Barkley, Dwight and Ronald D. Henderson (1996). "Three-dimensional Floquet stability analysis of the wake of a circular cylinder". In: *Journal of Fluid Mechanics* 322, pp. 215–241. ISSN: 1469-7645. DOI: 10.1017/S0022112096002777. URL: http://journals.cambridge.org/article_S0022112096002777.

Bass, D.W. (1998). "Roll stabilization for small fishing vessels using paravanes and anti-roll tanks". In: *Marine Technology* 35.2, pp. 74–84.

Benz, W. (1989). "Smooth Particle Hydrodynamics: A Review". In: *Harvard-Smithsonian Center for Astrophysics* Preprint No. 2884.

Bouscasse, B. et al. (2007). "Numerical and experimental investigation of sloshing phenomena in conditions of low filling ratios". In: *10th Numerical Towing Tank Symposium (NuTTS 07)*. Hamburg, Germany. URL: http://dx.doi.org/.

Bouscasse, B. et al. (2013a). "Nonlinear water wave interaction with floating bodies in SPH". In: *Journal of Fluids and Structures* 42, pp. 112–129.

Bouscasse, B. et al. (2013b). "Numerical and Experimental Investigation of Nonlinear Shallow Water Sloshing". In: *International Journal of Nonlinear Sciences and Numerical Simulation* 14.2, pp. 123–138.

Bridges, Thomas J. (1986). "Cnoidal standing waves and the transition to the traveling hydraulic jump". In: *Physics of Fluids* 29.9, pp. 2819–2827. DOI: 10.1063/1.865480. URL: http://link.aip.org/link/?PFL/29/2819/1.

Brizzolara, S. et al. (2011). "Comparison of experimental and numerical sloshing loads in partially filled tank". In: *Ships and Offshore Structures* 6.1,2, pp. 15–43.

Broglia, Riccardo et al. (2009). "Experimental and numerical analysis of the roll decay motion for a patrol boat". In: *The Nineteenth International Offshore and*

Polar Engineering Conference. International Society of Offshore and Polar Engineers.

Brøns, M. et al. (2014). "Vorticity generation and conservation for two-dimensional interfaces and boundaries". In: *Journal of Fluid Mechanics* 758, pp. 63–93. ISSN: 1469-7645. DOI: 10.1017/jfm.2014.520. URL: http://journals.cambridge.org/article_S0022112014005205.

Buchner, B. (2002). "Green Water on Ship-type Offshore Structures". PhD thesis. Delft University of Technology.

Bulian, G. et al. (2010). "SPH simulation of a Tuned Liquid Damper with angular motion". In: *Journal of Hydraulic Research* 48.Extra Issue, pp. 28–39. ISSN: 0022-1686. DOI: 10.3826/jhr.2010.0014.

Butikov, Eugene I (2008). "Extraordinary oscillations of an ordinary forced pendulum". In: *European Journal of Physics* 29.2, p. 215.

Carberry, Josie (2002). "Wake states of a submerged oscillating cylinder and of a cylinder beneath a free-surface". PhD thesis. Monash University, Melbourne, Australia. URL: http://arrow.monash.edu.au/hdl/1959.1/7678.

Cariou, A. and G. Casella (1999). "Liquid sloshing in ship tanks: a comparative study of numerical simulation". In: *Marine structures* 12, pp. 183–88.

Celebi, M.S. and H. Akyildiz (2002). "Nonlinear modeling of liquid sloshing in a moving rectangular tank". In: *Ocean Engineering* 29.12, pp. 1527–1553.

Chester, W (1968). "Resonant oscillations of water waves. I. Theory". In: *Proceedings of the Royal Society of London. Series A. Mathematical and Physical Sciences* 306.1484, pp. 5–22.

Chester, W and JA Bones (1968). "Resonant oscillations of water waves. II. Experiment". In: *Proceedings of the Royal Society of London. Series A. Mathematical and Physical Sciences* 306.1484, pp. 23–39.

Colagrossi, A. (2005). "A meshless lagrangian method for free-surface and interface flows with fragmentation". PhD thesis. Università di Roma La Sapienza.

Colagrossi, A. and M. Landrini (2003). "Numerical Simulation of Interfacial Flows by Smoothed Particle Hydrodynamics". In: *J. Comp. Phys.* 191, pp. 448–475.

Colagrossi, A. et al. (2010). "A study of violent sloshing wave impacts using an improved SPH method". In: *Journal of Hydraulic Research* 48.Extra Issue, pp. 94–104. ISSN: 0022-1686. DOI: 10.3826/jhr.2010.0014.

Colagrossi, A. et al. (2011). "Theoretical analysis and numerical verification of the consistency of viscous smoothed-particle-hydrodynamics formulations in simulating free-surface flows". In: *Physical Review E* 84, p. 026705.

Colagrossi, A. et al. (2012). "Particle packing algorithm for SPH schemes". In: *Computer Physics Communications* 183.2, pp. 1641–1683.

Colagrossi, A. et al. (2014). "Particles for fluids: SPH vs Vortex methods". In: *Journal of Mathematics and Mechanics of Complex Systems* 2.1, pp. 45–70.

Colagrossi, Andrea et al. (2009). "Theoretical considerations on the free-surface role in the Smoothed-particle-hydrodynamics model". In: *Physical Review E* 79.5, 056701, p. 056701. DOI: 10.1103/PhysRevE.79.056701.

Colagrossi, Andrea et al. (2013). "Smoothed-particle-hydrodynamics modeling of dissipation mechanisms in gravity waves". In: *Phys. Rev. E* 87 (2), p. 023302.

Cooker, MJ (1994). "Water waves in a suspended container". In: *Wave Motion* 20.4, pp. 385–395.

— (1996). "Wave energy losses from a suspended container". In: *Physics of Fluids* 8, p. 283.

Cox, E.A. et al. (2005). "Nonlinear sloshing and passage through resonance in a shallow water tank". English. In: *Zeitschrift für angewandte Mathematik und Physik ZAMP* 56 (4), pp. 645–680. ISSN: 0044-2275. DOI: 10.1007/s00033-004-3125-9. URL: http://dx.doi.org/10.1007/s00033-004-3125-9.

De Leffe, M. et al. (2011). "A modified no-slip condition in weakly-compressible SPH". In: *6th ERCOFTAC SPHERIC workshop on SPH applications*. Hamburg, Germany, pp. 291–297.

Dean, R.G. and R.A. Dalrymple (1991). *Water wave mechanics for engineers and scientists*. Advanced series on ocean engineering. World Scientific. ISBN: 9789810204211. URL: http://books.google.es/books?id=9-M4U_sfin8C.

Degroote, J. et al. (2010). "Partitioned simulation of the interaction between an elastic structure and free surface flow". In: *Computer Methods in Applied Mechanics and Engineering* 199.33-36, pp. 2085–2098.

Delorme, L. et al. (2006). "Coupling between sloshing and ship roll motion: Comparison between nonlinear potential theory and SPH". In: *26th Symposium on Naval Hydrodynamics, Rome, Italy*.

Delorme, L. et al. (2009). "A set of canonical problems in sloshing. Part I: Pressure field in forced roll. Comparison between experimental results and SPH". In: *Ocean Engineering* 36.2, pp. 168–178. DOI: 10.1016/j.oceaneng.2008.09.014.

Demirbilek, Zeki (1983a). "Energy dissipation in sloshing waves in a rolling rectangular tank - III. Results and applications". In: *Ocean Engineering* 10.5, pp. 375–382. ISSN: 0029-8018. DOI: 10.1016/0029-8018(83)90006-9.

— (1983b). "Energy dissipation in sloshing waves in a rolling rectangular tank-I. Mathematical theory". In: *Ocean Engineering* 10.5, pp. 347–358. ISSN: 0029-8018. DOI: 10.1016/0029-8018(83)90004-5.

— (1983c). "Energy dissipation in sloshing waves in a rolling rectangular tank-II. Solution method and analysis of numerical technique". In: *Ocean Engineering* 10.5, pp. 359–374. ISSN: 0029-8018. DOI: 10.1016/0029-8018(83)90005-7.

Di Mascio, A et al. (2008). "Numerical simulations of viscous flow around a naval combatant in regular head waves". In: *Proceedings of the 6th Osaka Colloquium on Seakeping and Stability of Ships*.

Diebold, L. et al. (2011). "Experimental and Numerical Investigations of Internal Global Forces for Violent Irregular Excitations in LNGC Prismatic Tanks". In: *21st International Offshore and Polar Engineering Conference (ISOPE)*. The International Society of Offshore and Polar Engineers (ISOPE). Hawaii, USA: ISOPE.

Dimas, Athanassios A. (1998). "Free-surface waves generation by a fully submerged wake". In: *Wave Motion* 27.1, pp. 43–54. ISSN: 0165-2125. DOI: 10.1016/S0165-2125(97)00034-6. URL: http://www.sciencedirect.com/science/article/pii/S0165212597000346.

— (2007). "Large-wave simulation of microscale breaking waves induced by a free-surface drift layer". In: *Wave Motion* 44.5, pp. 355–370. ISSN: 0165-2125. DOI: 10.1016/j.wavemoti.2006.12.003. URL: http://www.sciencedirect.com/science/article/pii/S0165212507000029.

Dimas, Athanassios A. and George S. Triantafyllou (1994). "Nonlinear interaction of shear flow with a free surface". In: *Journal of Fluid Mechanics* 260, pp. 211–246. ISSN: 1469-7645. DOI: 10.1017/S0022112094003496. URL: http://journals.cambridge.org/article_S0022112094003496.

Ding, Lin et al. (2013). "2-D URANS vs. experiments of flow induced motions of two circular cylinders in tandem with passive turbulence control for 30,000<Re<105,000". In: *Ocean Engineering* 72.0, pp. 429–440. ISSN: 0029-8018. DOI: 10.1016/j.oceaneng.2013.06.005. URL: http://www.sciencedirect.com/science/article/pii/S0029801813002448.

Doring, Mathieu et al. (2004). "Sph simulations of floating bodies in waves". In: *Proceedings of the 19th International Workshop on Water Waves and Floating Bodies*.

Duncan, James H. (1983). "The breaking and non-breaking wave resistance of a two-dimensional hydrofoil". In: *Journal of Fluid Mechanics* 126, pp. 507–520. ISSN: 1469-7645. DOI: 10.1017/S0022112083000294. URL: http://journals.cambridge.org/article_S0022112083000294.

Faltinsen, O. M. and A. N. Timokha (2002). "Asymptotic modal approximation of nonlinear resonant sloshing in a rectangular tank with small fluid depth". In: *Journal of Fluid Mechanics* 470, pp. 319–357. ISSN: 1469-7645. DOI: 10.1017/S0022112002002112. URL: http://journals.cambridge.org/article_S0022112002002112.

— (2009). *Sloshing*. Cambridge University Press, Cambridge, UK. ISBN: 13: 9780521881111.

Faltinsen, O. M. et al. (2000). "Multidimensional modal analysis of nonlinear sloshing in a rectangular tank with finite water depth". In: *Journal of Fluid Mechanics* 407, pp. 201–234.

Faltinsen, O. M. et al. (2006). "Transient and steady-state amplitudes of resonant three-dimensional sloshing in a square base tank with a finite fluid depth". In: *Physics of Fluids* 18.1, 012103, p. 012103. DOI: 10.1063/1.2160522. URL: http://link.aip.org/link/?PHF/18/012103/1.

Faltinsen, Odd M (1977). "Numerical solution of transient nonlinear free-surface motion outside or inside moving bodies". In: *Proceedings 2nd Int. Conf. on Num. Ship Hydrodynamics, UC Berkeley*, pp. 257–266.

Faltinsen, O.M and A.N. Timokha (2001). "An adaptive multimodal approach to nonlinear sloshing in a rectangular tank". In: *Journal of Fluid Mechanics* 432.1, pp. 167–200.

Faltinsen, O.M. et al. (2004). "Slamming in marine applications". In: *Journal of Engineering Mathematics* 48.3-4, pp. 187–217. DOI: 10.1023/B:engi.0000018188.68304.ae. URL: http://www.ingentaconnect.com/content/klu/engi/2004/00000048/F0020003/05147594.

Fani, Andrea and François Gallaire (2015). "The motion of a 2D pendulum in a channel subjected to an incoming flow". In: *Journal of Fluid Mechanics* 764, pp. 5–25. ISSN: 1469-7645. DOI: 10.1017/jfm.2014.670. URL: http://journals.cambridge.org/article_S0022112014006703.

Federico, I et al. (2012). "Simulating 2D open-channel flows through an SPH model". In: *European Journal of Mechanics-B/Fluids* 34, pp. 35–46.

Ferrand, M. et al. (2013). "Unified semi-analytical wall boundary conditions for inviscid, laminar or turbulent flows in the meshless SPH method". In: *International Journal for Numerical Methods in Fluids* 71.4, pp. 446–472. ISSN: 1097-0363. DOI: 10.1002/fld.3666. URL: http://dx.doi.org/10.1002/fld.3666.

Ferrant, P (2000). "Fully Nonlinear Interactions of Long-Crested Wave Packets with a three dimensional body". In: *Twenty-Second Symposium on Naval Hydrodynamics*. National Academies Press, p. 403.

Ferrari, Angela et al. (2009). "A new 3D parallel SPH scheme for free surface flows". In: *Computers & Fluids* 38.6, pp. 1203–1217. ISSN: 0045-7930. DOI: 10.1016/j.compfluid.2008.11.012.

Firoozkoohi, R. and O. M. Faltinsen (2010). "Experimental and numerical investigation of the effect of swash bulkhead on sloshing". In: *International Offshore and Polar Engineering Conference (ISOPE)*. The International Society of Offshore and Polar Engineers (ISOPE). Beijing, China.

Fornberg, Bengt (1985). "Steady viscous flow past a circular cylinder up to reynolds number 600". In: *Journal of Computational Physics* 61.2, pp. 297–320. ISSN: 0021-9991. DOI: 10.1016/0021-9991(85)90089-0. URL: http://www.sciencedirect.com/science/article/pii/0021999185900890.

Frandsen, J.B. (2005). "Numerical predictions of tuned liquid tank structural systems". In: *Journal of Fluids and Structures* 20.3, pp. 309–329. ISSN: 0889-9746. DOI: 10.1016/j.jfluidstructs.2004.10.003.

Fries, T.P. and H.G. Matthies (2004). "Classification and Overview of Meshfree Methods". In: *Scientific Computing, Informatikbericht*. Ed. by Brunswick Germany Technical University Braunschweig.

Gingold, R.A. and J.J. Monaghan (1977). "Smoothed Particle Hydrodynamics: theory and application to non-spherical stars". In: *Mon. Not. Roy. Astron. Soc. (MNRAS)* 181, pp. 375–389.

Gomez-Gesteira, M. et al. (2012). "SPHysics - development of a free-surface fluid solver - Part 1: Theory and formulations". In: *Computers & Geosciences* 48.0, pp. 289–299. ISSN: 0098-3004. DOI: 10.1016/j.cageo.2012.02.029. URL: http://www.sciencedirect.com/science/article/pii/S0098300412000854.

Goodrich, G.J. (1968). "Development and design of passive roll stabilisers". In: *Transactions of the Royal Institution of Naval Architects, London*.

Graham, E.W. and A.M. Rodriguez (1952). "The characteristics of fuel motion which affects airplane dynamics". In: *J. Applied Mechanics* 19, pp. 381–388.

Greco, Marilena (2001). "A two-dimensional study of green-water loading". PhD thesis. Norwegian University of Science and Technology (NTNU) - Dept of Marine Hydrodynamics, Trondheim, Norway.

Hadžić, I et al. (2005). "Computation of flow-induced motion of floating bodies". In: *Applied mathematical modelling* 29.12, pp. 1196–1210.

Hashemi, MR et al. (2012). "A modified SPH method for simulating motion of rigid bodies in Newtonian fluid flows". In: *International Journal of Non-Linear Mechanics* 47.6, pp. 626–638.

Havelock, TH (1927). "The method of images in some problems of surface waves". In: *Proceedings of the Royal Society of London. Series A, Containing Papers of a Mathematical and Physical Character*, pp. 268–280.

Herczyński, Andrzej and Patrick D Weidman (2012). "Experiments on the periodic oscillation of free containers driven by liquid sloshing". In: *Journal of Fluid Mechanics* 1.1, pp. 1–27.

Hill, D. F. (2003). "Transient and steady-state amplitudes of forced waves in rectangular basins". In: *Physics of Fluids* 15.6, pp. 1576–1587. DOI: 10.1063/1.1569917. URL: http://link.aip.org/link/?PHF/15/1576/1.

Hirt, C. W. and B. D. Nichols (1981). "Volume of fluid (VOF) method for the dynamics of free boundaries". In: *Journal of Computational Physics* 39.1, pp. 201–225. ISSN: 0021-9991. DOI: 10.1016/0021-9991(81)90145-5.

Hu, Changhong and Masashi Kashiwagi (2009). "Two-dimensional numerical simulation and experiment on strongly nonlinear wave–body interactions". In: *Journal of marine science and technology* 14.2, pp. 200–213.

Iafrati, A. (2009). "Numerical study of the effects of the breaking intensity on wave breaking flows". In: *Journal of Fluid Mechanics* 622, pp. 371–411. ISSN: 1469-7645. DOI: 10.1017/S0022112008005302. URL: http://journals.cambridge.org/article_S0022112008005302.

Iafrati, A (2011). "Energy dissipation mechanisms in wave breaking processes: Spilling and highly aerated plunging breaking events". In: *Journal of Geophysical Research: Oceans (1978–2012)* 116.C7.

Ibrahim, R. A. (2005). *Liquid sloshing dynamics : theory and applications*. New York: Cambridge University Press, p. 948. ISBN: 0-521-83885-1; 978-0-521-838856.

Idelsohn, S. et al. (2008). "Interaction between an elastic structure and free-surface flows: experimental versus numerical comparisons using the PFEM". In: *Computational Mechanics* 43.1, pp. 125–132.

Ikeda, T. and N. Nakagawa (1997). "Non-linear vibrations of a structure caused by water sloshing in a rectangular tank". In: *Journal of Sound and Vibration* 201.1, pp. 23–41.

Kajtar, Jules and JJ Monaghan (2008). "SPH simulations of swimming linked bodies". In: *Journal of Computational Physics* 227.19, pp. 8568–8587.

Kareem, A. et al. (1999). "Mitigation of motions of tall buildings with special examples of recent applications". In: *Journal on Wind and Structures* 2.3, pp. 201–251.

Keulegan, Garbis H. (1959). "Energy dissipation in standing waves in rectangular basins". In: *Journal of Fluid Mechanics* 6.01, pp. 33–50. DOI: 10.1017/S0022112059000489. eprint: http://journals.cambridge.org/article_S0022112059000489. URL: http://dx.doi.org/10.1017/S0022112059000489.

Kiger, Kenneth T. and James H. Duncan (2012). "Air-Entrainment Mechanisms in Plunging Jets and Breaking Waves". In: *Annual Review of Fluid Mechanics* 44.1, pp. 563–596.

Koshizuka, S. et al. (1998). "Numerical analysis of breaking waves using the moving particle semi-implicit method". In: *International Journal for Numerical Methods in Fluids* 26.7, pp. 751–769.

Landrini, M. et al. (2007). "Gridless simulations of splashing process and near-shore bore propagation". In: *Journal of Fluid Mechanics* 591, pp. 183–213.

Lepelletier, T. and F. Raichlen (1988). "Nonlinear Oscillations in Rectangular Tanks". In: *Journal of Engineering Mechanics* 114.1, pp. 1–23. DOI: 10.1061/(ASCE)0733-9399(1988)114:1(1). eprint: http://ascelibrary.org/doi/pdf/10.1061/\%28ASCE\%290733-9399\%281988\%29114\%3A1\%281\%29. URL: http://ascelibrary.org/doi/abs/10.1061/%28ASCE%290733-9399%281988%29114%3A1%281%29.

Lewis, E. V. (1989). *Principles of naval architecture (vol. II)*. Principles of Naval Architecture. Society of Naval Architects and Marine Engineers. URL: http://books.google.es/books?id=bWwZAQAAIAAJ.

Lighthill, J. (2001). *Waves in fluids*. English. Cambridge University Press.

Lobovský, L. et al. (2014). "Experimental investigation of dynamic pressure loads during dam break". In: *Journal of Fluids and Structures* 48, pp. 407–434. ISSN: 0889-9746. DOI: 10.1016/j.jfluidstructs.2014.03.009.

Longuet-Higgins, Michael S and ED Cokelet (1976). "The deformation of steep surface waves on water. I. A numerical method of computation". In: *Proceedings of the Royal Society of London. A. Mathematical and Physical Sciences* 350.1660, pp. 1–26.

Lourenco, Richard (2011). "Design, Construction and Testing of an Adaptive Pendulum Tuned Mass Damper". MA thesis. University of Waterloo, Ontario, Canada.

Lucy, L.B. (1977). "A numerical approach to the testing of the fission hypothesis". In: *Astronomical Journal* 82, pp. 1013–1024.

Lugni, C. et al. (2010a). "Evolution of the air cavity during a depressurized wave impact. I. The kinematic flow field". In: *Physics of Fluids* 22.5, 056101, p. 056101. DOI: 10.1063/1.3407664. URL: http://link.aip.org/link/?PHF/22/056101/1.

Lugni, C. et al. (2010b). "Evolution of the air cavity during a depressurized wave impact. II. The dynamic field". In: *Physics of Fluids* 22.5, 056102, p. 056102. DOI: 10.1063/1.3409491. URL: http://link.aip.org/link/?PHF/22/056102/1.

Lundgren, T. and P. Koumoutsakos (1999). "On the generation of vorticity at a free surface". In: *Journal of Fluid Mechanics* 382, pp. 351–366. URL: http://dx.doi.org/10.1017/S0022112098003978.

Macià, Fabricio et al. (2011). "Theoretical Analysis of the No-Slip Boundary Condition Enforcement in SPH Methods". In: *Progress of Theoretical Physics* 125.6, pp. 1091–1121. DOI: 10.1143/PTP.125.1091. URL: http://ptp.ipap.jp/link?PTP/125/1091/.

Macià, Fabricio et al. (2012). "A boundary integral SPH formulation. Consistency and applications to ISPH and WCSPH". In: *Progress of Theoretical Physics* 128.3.

Madsen, P.A. and H.A. Schaffer (2006). "A discussion of artificial compressibility". In: *Coastal Engineering* 53.1, pp. 93–98. ISSN: 0378-3839. DOI: 10.1016/j.coastaleng.2005.09.020. URL: http://www.sciencedirect.com/science/article/pii/S0378383905001250.

Marrone, S (2011). "Enhanced SPH modeling of free-surface flows with large deformations". PhD thesis. PhD thesis, University of Rome, La Sapienza.

Marrone, S. et al. (2010). "Fast free-surface detection and level-set function definition in SPH solvers". In: *Journal of Computational Physics* 229.10, pp. 3652–3663. ISSN: 0021-9991. DOI: 10.1016/j.jcp.2010.01.019. URL: http://www.sciencedirect.com/science/article/pii/S0021999110000343.

Marrone, S. et al. (2011a). "A 2D+t {SPH} model to study the breaking wave pattern generated by fast ships". In: *Journal of Fluids and Structures* 27.8, pp. 1199–1215. ISSN: 0889-9746. DOI: 10.1016/j.jfluidstructs.2011.08.003. URL: http://www.sciencedirect.com/science/article/pii/S0889974611001241.

Marrone, S. et al. (2011b). "Delta-SPH model for simulating violent impact flows". In: *Computer Methods in Applied Mechanics and Engineering* 200.13-16, pp. 1526–1542. ISSN: 0045-7825. DOI: 10.1016/j.cma.2010.12.016.

Marrone, S. et al. (2012). "Study of ship wave breaking patterns using 3D parallel {SPH} simulations". In: *Computers and Fluids* 69, pp. 54–66. ISSN: 0045-7930. DOI: 10.1016/j.compfluid.2012.08.008. URL: http://www.sciencedirect.com/science/article/pii/S0045793012003131.

Marrone, S. et al. (2013). "An accurate SPH modeling of viscous flows around bodies at low and moderate Reynolds numbers". In: *Journal of Computa-*

tional Physics 245, pp. 456–475. ISSN: 0021-9991. DOI: 10.1016/j.jcp.2013.03.011.

Marrone, S. et al. (2015). "Prediction of energy losses in water impacts using incompressible and weakly compressible models". In: *Journal of Fluids and Structures* 54, pp. 802–822.

Marsh, Adam P et al. (2011). "An investigation and modelling of energy dissipation through sloshing in an egg-shaped shell". In: *Journal of Sound and Vibration* 330.26, pp. 6287–6295.

May, D.A. and J.J. Monhagan (2003). "Can a single bubble sink a ship". In: *Am. J. Phys.* 71.8.

Melville, WK (1996). "The role of surface-wave breaking in air-sea interaction". In: *Annual review of fluid mechanics* 28.1, pp. 279–321.

Meunier, Patrice (2012). "Stratified wake of a tilted cylinder. Part 1. Suppression of a von Kármán vortex street". In: *Journal of Fluid Mechanics* 699, pp. 174–197. ISSN: 1469-7645. DOI: 10.1017/jfm.2012.92. URL: http://journals.cambridge.org/article_S0022112012000924.

Miyata, H. et al. (1990). "Forces on a circular cylinder advancing steadily beneath the free-surface". In: *Ocean Engineering* 17.1-2, pp. 81–104. ISSN: 0029-8018. DOI: 10.1016/0029-8018(90)90016-Y. URL: http://www.sciencedirect.com/science/article/pii/002980189090016Y.

Modi, V.J. and M.L. Seto (1997). "Suppression of flow-induced oscillations using sloshing liquid dampers: analysis and experiments". In: *Journal of Wind Engineering and Industrial Aerodynamics* 67.1-3, pp. 611–626.

Molteni, D. and A. Colagrossi (2009). "A simple procedure to improve the pressure evaluation in hydrodynamic context using the SPH". In: *Computer Physics Communications* 180, pp. 861–872.

Monaghan, J. and R. A. Gingold (1983). "Shock Simulation by the particle method SPH". In: *Journal of Computational Physics* 52.2, pp. 374–389.

Monaghan, J.J. (1985). "Particle methods for hydrodynamics". In: *Computer-physics-reports* 3.2, pp. 71–124.

— (1994). "Simulating Free Surface Flows with SPH". In: *J. Comp. Phys.* 110.2, pp. 39–406.

— (2012). "Smoothed Particle Hydrodynamics and Its Diverse Applications". In: *Annual Review of Fluid Mechanics* 44.1, pp. 323–346.

Monaghan, J.J. and A. Kos (1999). "Solitary waves on a Cretan Beach". In: *J. Waterway, Port, Coastal, and Ocean Eng.* 125.3, p. 145.

— (2000). "Scott Russell's Wave Generator". In: *Phys. of Fluids* 12.3, p. 622.

Monaghan, J.J. et al. (2003). "Fluid motion generated by impact". In: *Journal of waterway, port, coastal, and ocean engineering* 129.6, pp. 250–259.

Morris, Joseph P. et al. (1997). "Modeling Low Reynolds Number Incompressible Flows Using SPH". In: *Journal of Computational Physics* 136, pp. 214–226. DOI: 10.1006/jcph.1997.5776.

Naito, Shigeru and Makoto Sueyoshi (2002). "A numerical analysis of violent free surface flow by particle method". In: *Fifth ISOPE Pacific/Asia Offshore Mechanics Symposium, Daejeon, Korea*.

Nasar, T. et al. (2010). "Motion responses of barge carrying liquid tank". In: *Ocean Engineering* 37.10, pp. 935–946. ISSN: 0029-8018. DOI: 10.1016/j.oceaneng.2010.03.006. URL: http://www.sciencedirect.com/science/article/pii/S0029801810000703.

Nguyen, Hai-Dang Tam et al. (2013). "A miniature pneumatic energy generator using Karman vortex street". In: *Journal of Wind Engineering and Industrial Aerodynamics* 116.0, pp. 40–48. ISSN: 0167-6105. DOI: 10.1016/j.jweia.2013.03.002. URL: http://www.sciencedirect.com/science/article/pii/S0167610513000524.

Novo, T. et al. (2014). "Tuned liquid dampers simulation for earthquake response control of buildings". English. In: *Bulletin of Earthquake Engineering* 12.2, pp. 1007–1024. ISSN: 1570-761X. DOI: 10.1007/s10518-013-9528-2. URL: http://dx.doi.org/10.1007/s10518-013-9528-2.

Oger, G. et al. (2006). "Two-dimensional SPH simulations of wedge water entries". In: *J. Comp. Phys.* 213 (2), pp. 803–822.

Olsen, H. A. and K. Johnsen (1975). *Nonlinear sloshing in rectangular tanks. a pilot study on the applicability of analytical models*. Tech. rep. 74-72-5, Vol. 2. Hovik, Norway: Det Norske Veritas (DNV).

Perlin, Marc et al. (2013). "Breaking Waves in Deep and Intermediate Waters". In: *Annual Review of Fluid Mechanics* 45.1, pp. 115–145. DOI: 10.1146/annurev-fluid-011212-140721.

Peskin (1977). "Numerical analysis of blood flow in the heart". In: *J. Comp. Phys.* 25, pp. 220–252.

Pirner, M. and S. Urushadze (2007). "Liquid damper for suppressing horizontal and vertical motions-parametric study". In: *Journal of Wind Engineering and Industrial Aerodynamics* 95.9-11, pp. 1329–1349. ISSN: 0167-6105. DOI: 10.1016/j.jweia.2007.02.010.

Popov, G. et al. (1993). "Dynamics of Liquid Sloshing in Baffled and Compartmented Road Containers". In: *Journal of Fluids and Structures* 7.7, pp. 803–821.

Randles, P.W. and L.D. Libersky (1996). "Smoothed Particle Hydrodynamics: some recent improvements and applications". In: *Computer methods in applied mechanics and engineering* 39, pp. 375–408.

Reed, Dorothy et al. (1998). "Investigation of tuned liquid dampers under large amplitude excitation". In: *Journal of Engineering Mechanics* 124.4, pp. 405–413.

Reichl, P. (2001). "Flow past a cylinder close to a free surface". PhD thesis. Department of Mechanical Engineering - Monash University, Melbourne, Australia. URL: http://dx.doi.org/.

Reichl, P. et al. (2005). "Flow past a cylinder close to a free surface". In: *Journal of Fluid Mechanics* 533, pp. 269–296. ISSN: 1469-7645. DOI: 10.1017/S0022112005004209.

Reichl, P. J. et al. (2001). "Metastable wake states for flow past a cylinder close to a free surface". In: *14th Australasian Fluid Mechanics Conference*. Adelaide University. Adelaide, Australia.

Reichl, Paul et al. (2003). "The Unsteady Wake of a Circular Cylinder near a Free Surface". English. In: *Flow, Turbulence and Combustion* 71.1-4, pp. 347–359. ISSN: 1386-6184. DOI: 10.1023/B:APPL.0000014926.99751.b1. URL: http://dx.doi.org/10.1023/B%3AAPPL.0000014926.99751.b1.

Rossi, E et al. (2015). "The Diffused Vortex Hydrodynamics method". In: *Communications in Computational Physics* 18.2, pp. 351–379.

Sames, P.C. et al. (2002). "Sloshing in Rectangular and Cylindrical Tanks". In: *Journal of Ship Research* 46.3, pp. 186–200.

Scullen, D. C. and E. O. Tuck (1995). "Nonlinear Free-Surface Flow Computations for Submerged Cylinders". In: *Journal of Ship Research* 39.3, pp. 185–193.

Scullen, David C (1998). "Accurate computation of steady nonlinear free-surface flows". PhD thesis. The University of Adelaide.

Sethian, J.A. (1999). *Level Set Methods and Fast Marching Methods : Evolving Interfaces in Computational Geometry, Fluid Mechanics, Computer Vision, and Materials Science*. Cambridge University Press.

Shao, Songdong and Hitoshi Gotoh (2004). "Simulating coupled motion of progressive wave and floating curtain wall by SPH-LES model". In: *Coastal Engineering Journal* 46.02, pp. 171–202.

Sheridan, J. et al. (1995). "Metastable states of a cylinder wake adjacent to a free surface". In: *Physics of Fluids (1994-present)* 7.9, pp. 2099–2101. DOI: 10.1063/1.868458. URL: http://scitation.aip.org/content/aip/journal/pof2/7/9/10.1063/1.868458.

— (1997). "Flow past a cylinder close to a free surface". In: *Journal of Fluid Mechanics* 330, pp. 1–30. ISSN: 1469-7645. DOI: 10.1017/S002211209600328X.

So, Gavin and S.Eren Semercigil (2004). "A note on a natural sloshing absorber for vibration control". In: *Journal of Sound and Vibration* 269.3-5, pp. 1119–1127. ISSN: 0022-460X. DOI: 10.1016/S0022-460X(03)00388-2. URL: http://www.sciencedirect.com/science/article/pii/S0022460X03003882.

Souto-Iglesias, A. et al. (2006). "Liquid moment amplitude assessment in sloshing type problems with smooth particle hydrodynamics". In: *Ocean Engineering* 33.11-12, pp. 1462–1484.

Souto-Iglesias, A. et al. (2011). "A set of canonical problems in Sloshing. Part 0: Experimental setup and data processing." In: *Ocean Engineering* 38.16, pp. 1823–1830.

Souto-Iglesias, A. et al. (2013). "On the consistency of MPS". In: *Computer Physics Communications* 184.3, pp. 732–745. ISSN: 0010-4655. DOI: 10.1016/j.

cpc.2012.11.009. URL: http://www.sciencedirect.com/science/article/pii/S0010465512003852?v=s5.

Souto-Iglesias, Antonio et al. (2014). "Addendum to On the consistency of MPS [Comput. Phys. Comm. 184 (3) (2013) 732-745]". In: *Computer Physics Communications* 185.2, pp. 595–598. ISSN: 0010-4655. DOI: 10.1016/j.cpc.2013.10.018. URL: http://www.sciencedirect.com/science/article/pii/S0010465513003469.

Stoker, J.J. (1957). *Water Waves: The Mathematical Theory With Applications*. Wiley Classics Library. John Wiley & Sons, Hoboken, New Jersey. ISBN: 9780471570349. URL: http://books.google.es/books?id=xwJ94ZsdUnYC.

Sun, L. M. and Y. Fujino (1994). "A Semi-Analytical Model for Tuned Liquid Damper (TLD) with Wave Breaking". In: *Journal of Fluids and Structures* 8.5, pp. 471–488.

Tait, M.J. (2008). "Modelling and preliminary design of a structure-TLD system". In: *Engineering Structures* 30.10, pp. 2644–2655. ISSN: 0141-0296. DOI: 10.1016/j.engstruct.2008.02.017.

Tait, M.J. et al. (2005). "Numerical flow models to simulate tuned liquid dampers (TLD) with slat screens". In: *Journal of Fluids and Structures* 20.8, pp. 1007–1023. ISSN: 0889-9746. DOI: 10.1016/j.jfluidstructs.2005.04.004. URL: http://www.sciencedirect.com/science/article/pii/S0889974605000587.

Tamura, Yukio et al. (1995). "Effectiveness of tuned liquid dampers under wind excitation". In: *Engineering Structures* 17.9, pp. 609–621. ISSN: 0141-0296. DOI: 10.1016/0141-0296(95)00031-2.

Tedesco, Joseph W et al. (1999). *Structural dynamics*. Addison Wesley, Boston, MA.

Triantafyllou, George S. and Athanassios A. Dimas (1989). "Interaction of two-dimensional separated flows with a free surface at low Froude numbers". In: *Physics of Fluids A: Fluid Dynamics (1989-1993)* 1.11, pp. 1813–1821. DOI: 10.1063/1.857507. URL: http://scitation.aip.org/content/aip/journal/pofa/1/11/10.1063/1.857507.

Tuck, E. O. (1965). "The effect of non-linearity at the free surface on flow past a submerged cylinder". In: *Journal of Fluid Mechanics* 22 (02), pp. 401–414. ISSN: 1469-7645. DOI: 10.1017/S0022112065000836. URL: http://journals.cambridge.org/article_S0022112065000836.

Turner, MR and TJ Bridges (2013). "Nonlinear energy transfer between fluid sloshing and vessel motion". In: *Journal of Fluid Mechanics* 719, pp. 606–636.

Ulrich, Christian and Thomas Rung (2012). "Multi-Physics SPH Simulations of Launching Problems and Floating Body Interactions". In: *ASME 2012 31st International Conference on Ocean, Offshore and Arctic Engineering*. American Society of Mechanical Engineers, pp. 685–694.

Van Den Bosch, J.J. and J.H. Vugts (1966). "On Roll Damping by Free-Surface Tanks". In: *Trans. RINA*.

Vanden-Broeck, Jean-Marc (1987). "Free-surface flow over an obstruction in a channel". In: *Physics of Fluids (1958-1988)* 30.8, pp. 2315–2317. DOI: 10.1063/1.866121. URL: http://scitation.aip.org/content/aip/journal/pof1/30/8/10.1063/1.866121.

Verhagen, J.H.G. and L. Van Wijngaarden (1965). "Non-linear oscillations of fluid in a container". In: *Journal of Fluid Mechanics* 22.4, pp. 737–751.

Vinje, T and P Brevig (1981). "Nonlinear ship motions". In: *Proc. 3rd Int. Symp. Num. Ship Hydrodyn., Paris*.

Violeau, D. (2009). "Dissipative forces for Lagrangian models in computational fluid dynamics and application to smoothed-particle hydrodynamics". In: *Phys. Rev. E* 80 (3), p. 036705. DOI: 10.1103/PhysRevE.80.036705. URL: http://link.aps.org/doi/10.1103/PhysRevE.80.036705.

Vugts, JH (1968). *The hydrodynamic coefficients for swaying, heaving and rolling cylinders in a free surface*. Tech. rep.

Wehausen, John V and Edmund V Laitone (1960). *Surface waves*. Springer.

Wicks, M. (1969). "Fluid Dynamics of Floating Oil Containment by Mechanical Barriers in the Presence of Water Currents". In: *International Oil Spill Conference*. Vol. 1969. 1, pp. 55–106.

Williamson, C.H.K. and R. Govardhan (2004). "Vortex-induced vibrations". In: *Annual Review of Fluid Mechanics* 36.1, pp. 413–455. DOI: 10.1146/annurev.fluid.36.050802.122128. eprint: http://www.annualreviews.org/doi/pdf/10.1146/annurev.fluid.36.050802.122128. URL: http://www.annualreviews.org/doi/abs/10.1146/annurev.fluid.36.050802.122128.

Yabe, Takashi et al. (2001). "The constrained interpolation profile method for multiphase analysis". In: *Journal of Computational Physics* 169.2, pp. 556–593.

Yamamoto, Masashi and Takayuki Sone (2014). "Behavior of active mass damper (AMD) installed in high-rise building during 2011 earthquake off Pacific coast of Tohoku and verification of regenerating system of AMD based on monitoring". In: *Structural Control and Health Monitoring* 21.4, pp. 634–647. ISSN: 1545-2263. DOI: 10.1002/stc.1590. URL: http://dx.doi.org/10.1002/stc.1590.

Yang, Jianming and Frederick Stern (2012). "A simple and efficient direct forcing immersed boundary framework for fluid–structure interactions". In: *Journal of Computational Physics* 231.15, pp. 5029–5061.

Yu, Jin-Kyu et al. (1999). "A non-linear numerical model of the tuned liquid damper". In: *Earthquake Engineering and structural dynamics* 28.6, pp. 671–686.

Zhong, Z. et al. (1998). "A Numerical Study of U-Tube Passive Anti-Rolling Tanks". In: *8th International Offshore and Polar Engineering Conference, Montreal, Canada*.

Zhou, Z. Q. et al. (1999). "A nonlinear 3D approach to simulate green water dynamics on deck". In: *Seventh international conference on numerical ship hydrodynamics*, pp. 1–4.